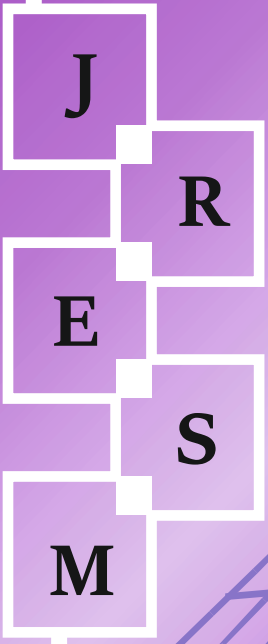




# Research on Engineering Structures & Materials

P-ISSN: 2148-9807 E-ISSN: 2149-4088

Volume 7 Issue 4 December 2021



[www.jresm.org](http://www.jresm.org)

The International Journal of **Research on Engineering Structures and Materials (RESM)** is a peer-reviewed open access journal (p-ISSN: 2148-9807; o-ISSN: 2149-4088) published by MIM Research Group. It is published in February, June, September, and December.

The main objective of RESM is to provide an International academic platform for researchers to share scientific results related to all aspects of mechanical, civil and material engineering areas.

RESM aims the publication of original research articles, reviews, short communications technical reports, and letters to the editor on the latest developments in the related fields.

All expenditures for the publication of the manuscripts are most kindly reimbursed by *MIM Research Group*. Thus, authors do not need to pay for publishing their studies in the journal.

The scope of the journal covers (but not limited to) behavior of structures, machines and mechanical systems, vibration, impact loadings and structural dynamics, mechanics of materials (elasticity, plasticity, fracture mechanics), material science (structure and properties of concrete, metals, ceramics, composites, plastics, wood, etc.), nano-materials performances of new and existing buildings and other structural systems, design of buildings and other structural systems, seismic behavior of buildings and other structural systems, repair and strengthening of structural systems, case studies and failure of structural systems, safety and reliability in structural and material engineering, use of new and innovative materials and techniques in energy systems and mechanical aspects of biological systems (biomechanics and biomimetics).

**The topics covered in JRESM include:**

- Structural Engineering
- Mechanical Engineering
- Material Engineering
- Earthquake Engineering
- Nano-technology
- Energy Systems
- Biomechanics and Biomimetics

**Abstracting and Indexing**

Please visit <http://www.jresm.org> for more information.

**Graphics and Design**

Yunus Demirtaş

[ydemirtas@jresm.net](mailto:ydemirtas@jresm.net)



**RESEARCH on  
ENGINEERING STRUCTURES &  
MATERIALS**



Published by MIM Research Group

# RESEARCH on ENGINEERING STRUCTURES & MATERIALS

## Editorial Board

---

<b>Editor in Chief</b>		
Hayri Baytan Özmen	Usak University	Turkey
<b>Editor (Energy, Thermodynamics)</b>		
Canan Kandilli	Usak University	Turkey
<b>Editor (Physics, Fluid Dynamics)</b>		
Antonio F. Miguel	University of Evora	Portugal
<b>Editor (Earthquake Eng., Structural Eng.)</b>		
Michele Barbato	University of California Davis	USA
<b>Editor (Mechanics, Biosystems, Meta-materials)</b>		
Alp Karakoç	Aalto University	Finland
<b>Editor (Applied Mechanics, Manufacturing, Design)</b>		
Faris Tarlochan	Qatar University	Qatar
<b>Editor (Civil Engineering)</b>		
Mehmet Palancı	Arel University	Turkey

---

## Editorial Office

---

<b>Publishing Assistant</b>		
Yunus Demirtaş	Eskişehir Technical University	Turkey

---

---

**Editorial Board Members**

---

Farid Abed-Meraim	Arts et Metiers ParisTech	France
P. Anbazhagan	Indian Institute of Science	India
Raffaele Barretta	University of Naples Federico II	Italy
R.S. Beniwal	Council of Scientific and Industrial Research	India
Antonio Caggiano	University of Buenos Aires	Argentina
Noel Challamel	University of South Brittany	France
Abdulkadir Çevik	Gaziantep University	Turkey
J. Paulo Davim	University of Aveiro	Portugal
Hom Nath Dhakal	University of Portsmouth	UK
Ali Faghidian	Islamic Azad University	Iran
S. Amir M. Ghannadpour	Shahid Beheshti University	Iran
Ali Goodarzi	Harvard University	USA
Jian Jiang	National Institute of Standards and Technology	USA
Ramazan Karakuzu	Dokuz Eylül University	Turkey
Arkadiusz Kwiecien	Cracow University of Technology	Poland
Stefano Lenci	Universita Politecnica delle Marche	Italy
Silva Lozančić	University of Osijek	Croatia
Fabio Mazza	University of Calabria	Italia
Yuan Meini	North University of China	China
Stergios A. Mitoulis	University of Surrey	UK
Vinayagam Mohanavel	Anna University	India
Ehsan Noroozinejad Farsangi	Kerman Graduate University of Technology	Iran
Alaa M. Rashad	Shaqra University	Saudi Arabia
Mohammad Mehdi Rashidi	University of Tongji	China
Pier Paolo Rossi	University of Catania	Italy
Neritan Shkodrani	Polythecnic University of Tirana	Albania



---

**Advisory Board Members**

---

Mohammad Afrazi	Tarbiat Modares University	Iran
Mohammad Al Biajawi	Universiti Malaysia Pahang	Malaysia
Mohammed Gamal Al-Hagri	Konya Technical University	Turkey
Saber Alizadeh	Bu-Ali-Sina University	Iran
Ibrahim Almeshal	Universiti Sains Malaysia	Malaysia
Gabriel Arce	Louisiana State University	USA
Evren Ariöz	Eskisehir Technical University	Turkey
Saeed Asiri	King Abdulaziz University	Saudi Arabia
Olumoyewa Atoyebi	Landmark University	Nigeria
Levent Aydin	-	Turkey
Yurdakul Aygormez	Yıldız Technical University	Turkey
Kemal Aydin	Gumushane University	Turkey
Ameer Baiee	University of Babylon	Iraq
Huseyin Ersen Balcioglu	-	Turkey
Mateusz Barczewski	Poznan University of Technology	Poland
Emin Bayraktar	Supméca Institute of Mechanics of Paris	France
Rohan Bhasker	Indian Institute of Technology Madras	India
David Bigaud	University of Angers	France
Huseyin Bilgin	Epoka University	Albania
Mehmet Bulut	Hakkari University	Turkey
Engin Burgaz	Ondokuz Mayıs University	Turkey
Ziya Cakici	Bayburt University	Turkey
Tanik Bayram Cayci	Pamukkale University	Turkey
Daniel Cruze	Mohamed Sathak A.J. College of Engineering	India
Jebasingh Daniel	Hawassa University	Ethiopia
Mehmet Hakan Demir	Iskenderun Technic University	Turkey
Cengiz Görkem Dengiz	Ondokuz Mayıs University	Turkey

---

**Advisory Board Members**

---

Elif Begüm Elcioglu	Eskişehir Technical University	Turkey
Emre Esener	Bilecik Seyh Edebali University	Turkey
S. Ali Faghidian	Islamic Azad University	Iran
Abdullah Fettahoglu	Usak University	Turkey
Berker Fıçıcılar	Ondokuz Mayıs University	Turkey
Saeid Foroughi	Konya Technical University	Turkey
Chithambar Ganesh	Kalasalingam University	India
Mehmet Cemal Genes	Eastern Mediterranean University	North Cyprus
Can Gonenli	Ege University	Ege University
Orhan Gülcan	General Electric Aviation	USA
Ersin Asım Güven	Kocaeli University	Turkey
Kadir Gunaydın	GE Aviation	Turkey
Marijana Hadzima-Nyarko	University of Osijek	Croatia
Dulce Franco Henriques	Instituto Politécnico de Lisboa	Portugal
Qing Hong	Midwestern University	USA
Manuel Horta	Universidade do Porto	Portugal
Halit Levent Hosgun	Bursa Technical University	Bursa Technical University
Bulent Imamoglu	Gedik University	Turkey
Ercan Isik	Bitlis Eren University	Turkey
Khairul Nizar Ismail	Universiti Malaysia Perlis	Malaysia
Sahar Ismail	Saint Joseph University of Beirut	Beirut
Berrin İkizler	Ege University	Turkey
Atike İnce Yardımcı	Usak University	Turkey
Liyana Jamaludin	Universiti Malaysia Perlis	Malaysia
Saifulnizan Jamian	Universiti Tun Hussein Onn Malaysia	Malaysia
Md. Salim Kaiser	Bangladesh University of Engineering and Technology	Bangladesh
Sreevani Kannan	Chennai Institute of Technology	India

---

**Advisory Board Members**

---

Gökhan Kaplan	Atatürk University	Turkey
Altug Karabey	Yuzuncu Yil University	Turkey
Abdulhalim Karasin	Dicle University	Turkey
Mehmet Kaya	Yozgat Bozok University	Turkey
Dogan Kaya	Cukurova University	Turkey
Deniz Kaya	Dokuz Eylul University	Turkey
Jibran Khaliq	Northumbria University	United Kingdom
Kadir Kılınç	Kırklareli University	Turkey
Abiodun Kilani	Federal University Oye Ekiti	Nigeria
Sedat Kömürcü	Istanbul Technical University	Turkey
A. Suresh	Kalasalingam Academy of Research and Education	India
Salmabanu Luhar	Universiti Malaysia Perlis	Malaysia
Lomesh Mahajan	Dr. Babasaheb Ambedkar Technological University	India
Waqas Ahmed Mahar	University of Liege	Belgium
Yelda Mert	Iskenderun Technical University	Turkey
Seyede Mahdiah Miralami	University of Rahman	Iran
Jinxu Mo	Yangtze University	China
Nebab Mokhtar	Hassiba Benbouali University of Chlef	Algeria
Nahida Nazim Musayeva	Azerbaijan National Academy of Sciences	Azerbaijan
Elango Natarajan	UCSI University	Malaysia
Muhammed Yasin Naz	Universiti Teknologi Petronas	Malaysia
Samson Olalekan Odeyemi	Kwara State University	Nigeria
Osama Mohamed Omar	Beirut Arab University	Lebanon
Mehmet Orhan	Pamukkale University	Turkey
Hayri Baytan Ozmen	Usak University	Turkey
Zehra Özçelik	Ege University	Turkey
Alp Özdemir	Eskisehir Technical University	Turkey

---

**Advisory Board Members**

---

Yasin Onuralp Özkılıç	Necmettin Erbakan University	Turkey
Partheeban Pachaivannan	Chennai Institute of Technology	India
Ozer Pamuk	Usak University	Turkey
Krishna Murari Pandey	National Institute of Technology	India
Narasimha Reddy Panga	Sri Venkateswara College of Engineering Technology	India
Chitaranjan Pany	Vikram Sarabhi Space Center	India
Vikas Patel	National Council for Cement and Building Materials	India
Dhirendra Patel	Kalaniketan Polytechnic College	India
Fatma Ülker Peker	Turgut Özal University	Turkey
Ramon Peña-Garcia	Federal University of Pernambuco	Brazil
Amin Moslemi Petrucci	Tehran University	Iran
Majid Pouraminian	Islamic Azad University	Iran
K. Venkatesh Raja	Sona College of Technology	India
Alaa M. Rashad	Housing and Building National Research Center	Egypt
Badrinarayan Rath	Wollega University	Ethiopia
Mahesh Raut	Rungta Group of Colleges	India
T.V. Reshma	Gandhi Institute of Technology and Management	India
Pier Paola Rossi	University of Catania	Italy
Behnam Rosti	Shiraz University of Technology	Iran
Vahid Saberi	University of Eyvanekey	Iran
Hamid Saberi	University of Eyvanekey	Iran
Abbasali Sadeghi	Islamic Azad University	Iran
Mohammed A. Sakr	Tanta University	Egypt
S. Reza Salimbahrami	Semnan University	Iran
Tamer Saracyakupoglu	Istanbul Gelisim University	Turkey
Gözde Sari	Celal Bayar University	Turkey

---

**Advisory Board Members**

---

Mehmer Sarıkanat	Ege University	Turkey
Hakan Sarıkaya	Usak University	Turkey
Mohammed M. Shabat	Islamic University of Gaza	Palestine
Ahmed Y. Shash	Cairo University	Egypt
Brijesh Singh	National Council for Cement & Building Material	India
Ozgur Solmaz	Celal Bayar University	Turkey
Emrah Sozumert	Swansea University	UK
V.G. Sridhar	VIT University	India
Hossein Taghipoor	Semnan University	Iran
Hamide Tekeli	Süleyman Demirel University	Turkey
Sezen Tekin	Çankırı Karatekin University	Turkey
Raja Thandavamoorthy	Institute of Science and Technology	India
Adem Ugurlu	Kırklareli University	Turkey
Hasan Ulus	Selcuk University	Turkey
Sergio Velazquez	Universidad Panamericana Sede Guadalajara	Mexico
Gustavo Bosel Wally	Federal University of Rio Grande do Sul	Brazil
Hexiang Wang	Berkshire Hathaway Specialty Insurance	USA
Qinhua Wang	Shantou University	China
Suiwen Wu	University of Nevada	USA
Wei Xu	Northeastern University	USA
Jhair Yacila	Pontifical Catholic University of Peru	Peru
Saeed Yaghoubi	Islamic Azad University	Iran
Omid Aminoroayai Yamani	K. N. Toosi University of Technology	USA
Seda Yeşilmen	Çankaya University	Turkey
Salih Hakan Yetgin	Kütahya Dumlupınar University	Turkey
Ferhat Yıldırım	Çanakkale Onsekiz Mart University	Turkey
Ceyhun Yılmaz	Afyon Kocatepe University	Turkey

---

## In This Issue

### Review Article

- 481 **Ismail Luhar, Salmabanu Luhar**  
Valorization of geopolymer paste containing wastes glass

### Research Article

- 505 **P.N. Ojha, Amit Trivedi, Brijesh Singh, Adarsh Kumar N. S., Vikas Patel, R.K. Gupta**  
High performance fiber reinforced concrete – for repair in spillways of concrete dams

### Research Article

- 523 **Giovanni Falsonea, Gabriele La Valle**  
Dynamic and buckling of functionally graded beams based on a homogenization theory

### Research Article

- 539 **Al Montazer Mandong, Abdullah Uzum**  
Fresnel calculations of double/multi-layer antireflection coatings on silicon substrates

### Research Article

- 551 **Sahar Ismail, Wassim Raphael, Emmanuel Durand**  
Case study of the Beirut port explosion using 3D laser scan and nonlinear finite element model

### Research Article

- 579 **Warda Abdulla, Craig Menzemer**  
Fatigue life prediction of steel bridge connections using fracture mechanics models

### Research Article

- 595 **Anjeza Gjini, Hektor Cullufi, Enio Deneko, Princ Xhika**  
Behavior of structure type 82/2 (RC frame), during the earthquake of 26 November 2019 in Durrës, Albania

### Research Article

- 617 **Olatunji Oladimeji Ojo**  
Macro-/micro-mechanical interlocking modification on the performance of hybrid friction stir spot welded aluminum/acrylonitrile butadiene styrene joints

Technical Note

- 635 **Akshansh Mishra, Devarrishi Dixit, Raheem Al-Sabur**  
Development of specially reinforced magnesium composites  
prepared by squeeze casting process

Research Article

- 647 **Juho Kerminen, Jenny Wiklund, Alp Karakoç, Kalle Ruttik, Riku Jäntti, Hüseyin Yiğitler**  
Characterization of low-cost inkjet printed-photonic cured strain  
gauges for remote sensing and structural monitoring applications

Research Article

- 661 **Selale Elcin Sungur, Umit Turgay Arpacioğlu, Mustafa Ozgunler**  
London the Shard analysis in the context of parametric and  
sustainable skyscraper design

Free access to tables of content, abstracts and full text of papers for web visitors.

Copyright © 2021

Research on Engineering Structures & Materials  
MIM Research Group Publications  
P-ISSN: 2148-9807  
E-ISSN: 2149-4088  
<http://www.jresm.org>



## ABSTRACTING / INDEXING

The international journal of Research on Engineering Structures and Materials (RESM) is currently Abstracted/Indexed by Asos Indeks, CiteFactor, Cosmos, CrossRef, Directory of Research Journal Indexing, Engineering Journals (ProQuest), EZB Electronic Journal Library, Global Impact Factor, Google Scholar, International Institute of Organized Research (I2OR), International Scientific Indexing (ISI), Materials Science & Engineering Database (ProQuest), Open Academic Journals Index, Publication Forum, Research BibleScientific Indexing Service, Root Indexing, Scopus, Ulakbim TR Index (Tubitak), Universal Impact Factor and under evaluation by many other respected indexes.

Check web site for current indexing info, [www.jresm.org](http://www.jresm.org)

# Scopus®



Publication  
Forum



Review Article

## Valorization of geopolymers containing waste glass

Ismail Luhar<sup>1,a</sup>, Salmabanu Luhar<sup>\*2,3,b</sup>

<sup>1</sup>Shri Jagdishprasad Jhabarmal Tibrewala University, Rajasthan, India

<sup>2</sup>Frederick Research Center, Frederick University, Nicosia 1036, Southern Cyprus

<sup>3</sup>Center of Excellence Geopolymer and Green Technology, School of Materials Engineering, Universiti Malaysia Perlis (UniMAP), Perlis 01000, Malaysia

### Article Info

#### Article history:

Received 13 Dec 2020

Revised 12 Apr 2021

Accepted 03 May 2021

#### Keywords:

Glass waste;  
Compressive strength;  
Microstructure;  
Geopolymer technology

### Abstract

"More industrial developments equals more generation of wastes". Wastes of glasses are blameworthy for the grave issue of pollution of environments chiefly in virtue of their profound accessibility and inconsistency of this stream. With mounting environmental pressure to trim them down and to recycle them as much as possible, the concrete industry has lent a hand to incorporate them with the manufacturing of inorganic, user, and eco-benevolent innovative Geopolymer construction composites. The current review paper studies the most striking points in the context of the production of waste glass integrated Geopolymer paste stressing its valorization in lights of its properties. More often than not, the center of attention here is to embrace the "conversion of wastes into wealth" strategy. That is why, this article reviews with an objective of its confined literature to comprehend its characteristics viz., workability, compressive strength, thermal, microstructure, etc. As a final point, the paper pigeonholes research work challenges, endorsement of potential utilization for this promising brand-new, green valorized Geopolymeric building material in order to establish it as a cost-effective, sustainable, durable construction material as a "futures toolkit".

© 2021 MIM Research Group. All rights reserved.

## 1. Introduction

An upsurge in industrial developments brought forth the generation of several wastes from industries cropping up a gigantic dilemma for their well-thought-out disposal. Copious landfills of solid glass waste (WG) from a lot more sources are liable to not only environmental but also health jeopardy. Nowadays, glass production is in great demand due to its employment in extensive practical, technological, traditional and decorative applications with the characteristic easiness of formability into any kind of shape viz., packaging, pharmaceuticals, cosmetics; dining tableware, housing and building interior decoration, window panes, optics, etc. Depending upon the resources of generation, the diverse waste glass may be found in the form of solar panel-WG, cullet of WG, modern E-WG from E-waste, etc. Often, glass is transparent and a non-crystalline amorphous type solid whereby the atomic structure is deficient of the long-range periodicity as visible crystallized ones. The historically oldest and well-known kinds of brittle but extremely durable manufactured glasses are coined as "silicate glasses" based on their enclosure of the primary component of sand, i.e., Silica [Quartz - Silicon Dioxide (SiO<sub>2</sub>)]; as well as "Soda-lime glass" having roughly 70% Silica Glass is regarded as inert material in a usual environment that can undergo recycling through an assortment of techniques sans leaving any impression on its chemistry. The different oxide additives bring about diverse colors into the glass. The color in glass may be achieved by supplement homogeneously dispersed color centers or ions that are electrically charged. Also, glass can be colored through the

\*Corresponding author: [ersalmabanu.mnit@gmail.com](mailto:ersalmabanu.mnit@gmail.com)

<sup>a</sup>orcid.org/0000-0002-9032-0483; <sup>b</sup>orcid.org/0000-0002-1129-2825

DOI: <http://dx.doi.org/10.17515/resm2020.240st1213>

Res. Eng. Struct. Mat. Vol. 7 Iss. 4 (2021) 481-504

addition of metal salts to use it like stained glass windows, glass art objects, etc. Glasses can be poured, formed, extruded, and molded with ease into flat sheets to extremely intricate shapes during production. It is solvable at alkaline pH values amazingly. More often than not, it is strongly resistant to chemical attacks; however, it can be corroded or dissolved under a few specific conditions. Surprisingly, it is found stronger than most metals with a significant tensile strength owing to its capability to experience reversible compression with no fracture. Thus, the glass is very hard and possesses very inferior thermal expansion with brilliant thermal shock resistance. For these reasons, it is competent enough to survive on immersing in the water when it was red hot resisting elevated temperatures ranging from 1000° to 1500 °C as well as chemical weathering. The fused quartz is employed for applications at towering temperatures like furnace and lighting tubes, melting crucibles, etc. Not only have that, the non-biodegradable nature of WG is also a challenge to contaminate soil and waters. However, WG can be subjected to recycling to use it for concrete manufacturing as a replacement of natural restricted aggregate resources helping to protect for their conservation. Recently, WG has attracted researchers to manufacture Geopolymeric composites as an add-on recycled material in Geopolymer paste, mortar, and concretes not only to lower operational energy and CO<sub>2</sub> emissions as compared to cement-system, which in turn, lower the challenges of a titanic dilemma of global warming. Having high regard for innovative Geopolymer technology, this has long been documented to offer the potential for incorporation of wastes in producing Geopolymer construction composites. It extends a systematic solution for their disposal dilemma. This is the core reason why geopolymers are dexterous of valorizing quite a lot of pozzolanic wastes from diverse resources of glass rich in Alumina plus Silica. Various researchers have worked on various wastes to be utilized for preparing diverse pastes to apply for construction industries [1-4]. Significantly, the geopolymer emits nine-fold low carbon footprint and six times lesser operational energy in comparison to the contemporary cement production process, saving natural limited mineral resources as fuels to achieve towering temperatures for calcination of Limestones – an essential raw material for cement as well as slimming down the earth-heating [6-8]. Little preceding investigations are easy to get to on geopolymer paste with WG- valorization. To date, highly limited investigations have conducted on geopolymerization of pastes integrated with WG or WG-powder or WG- mixes blended with Slag, Fly ash, etc. Momentously, the viability and acceptance of such WG blended Geopolymeric paste must be confirmed by verifying its significant parameters to establish it as a 'sustainable' structural material. For this reason, the present scientometric review aspires to valorize and stimulate the application of waste glass integrated manufacturing of novel geopolymer paste making it over as a "'class' material keeping an eye on its attributes viz., workability, compressive strength, thermal, microstructure, etc. along with challenges and applications to encourage their application as low carbon, reduced operational energy, affordable, durable, sustainable and user-benevolent inorganic polymerized composite in construction and infrastructure industries.

## **2. Properties of Geopolymer Composites Incorporated with Glass Wastes**

### **2.1. Workability**

Wang et al. [13] have investigated on a study of the engineering attributes of Geopolymer material containing WG and its setting times as represented by Fig.1 that when the alkaline solution is taken as 0.5% and the liquid: solid ratio is escalated from 0.50 to 0.55, the early and final setting times are extended by 87 and 131 minutes respectively. If the liquid: solid ratio is augmented to 0.60, the initial and final setting times are made longer by 159 and 227 min. Correspondingly. On account of the higher liquid: solid ratio, the alkaline solution is diluted via the water of the alkali metal silicate solution, and hence, the setting time is

lengthened. When the liquid: solid ratio is 0.55, and the alkaline solution is kept at 0.5%, the early and final setting times found are 300 min and 595 min in that order.

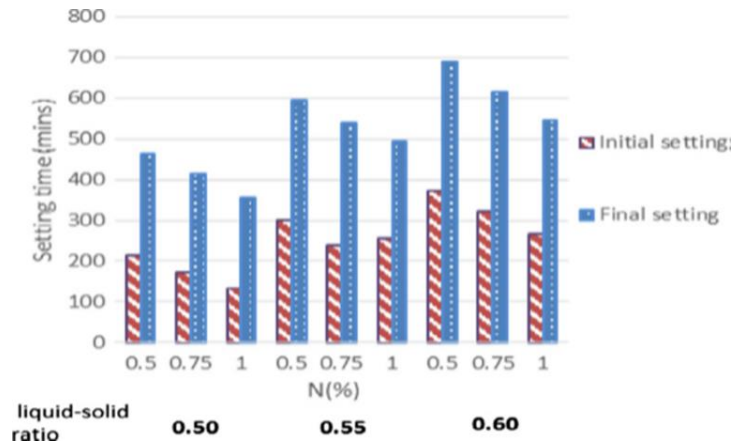


Fig. 1 Setting time of alkali-activated waste glass material [13]

When the alkaline solution boosts to 1%, the early and final setting times are cut down by 45 min. and 100 min. respectively, signaling to an enhance in the alkaline solution that can condense the setting time. Fig. 2 displays that when the alkaline solution is kept at 0.75%, the liquid: solid ratio is 0.50, and the glass sand substitution level is 0%, the early and final setting times are 171 min. and 413 min., correspondingly. When the glass sand substitution is accelerated to 20 %, the initial and final setting times are 321 min. and 616 min., in that order. The upshot reveals that the setting time enhances as the glass Sand substitution escalates. For a reason, the glass sand is water repellent when the glass sand substitution accelerates, the glass sand cannot swiftly submit itself to a poly-reaction with Slag and OH ions, so the setting time has got extended.

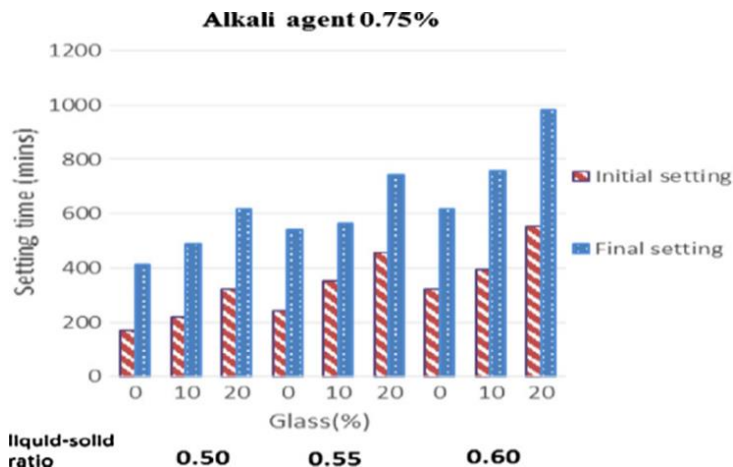


Fig. 2 Impact of glass waste on setting time of geopolymer paste [13]

The study by Torres-Carrasco and Puertas [14], unearthed that the nature of the activator has significantly affected the development of paste strength. Of the solutions they investigated, the least performance was displayed by NaOH: Na<sub>2</sub>CO<sub>3</sub> having pH = 13.3, with values of 29 MPa as portrayed in Fig. 3, which dropped to 17.1 MPa when 25 g of WG

was supplemented to that solution as an option to commercial Sodium Silicate, extending a pH of 13.4. Because pH controls Alumino-Silicate dissolution that encourages nucleation or condensation and polymerization, it plays an important role in the activation of the said materials. Even so, while a commercial Sodium Silicate, i.e., water glass, along with a SiO<sub>2</sub>:Na<sub>2</sub>O modulus of 0.86, as well as pH of 13.8, was employed, the strength measured was 54 MPa. As the liquid: solid ratio, i.e., L/S = 0.4, was the same in every one of the systems, though, when the commercial Sodium Silicate solution was employed, the paste showed a lower consistency. This may have partly described the enhanced mechanical strength monitored [15].

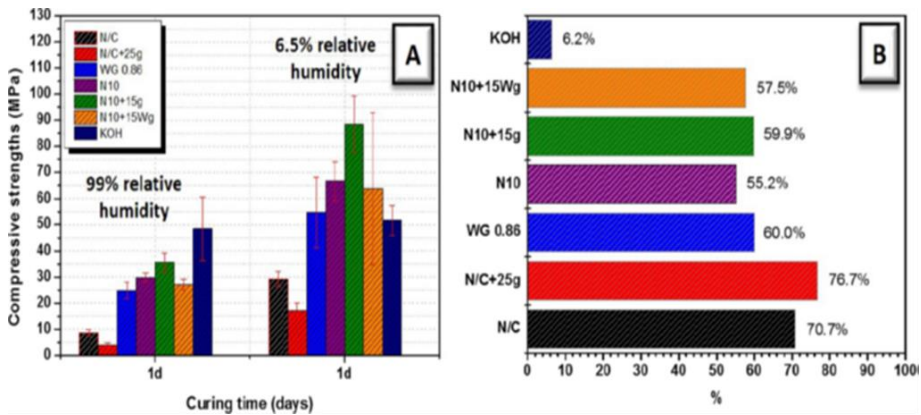


Fig. 3 Compressive strength for waste glass activated with different activating solutions [14]

What is more, the reactivity of Si from a commercial Sodium Silicate is superior to the dissolve Si from WG. While the glass pastes were activated with a high OH<sup>-</sup> concentration eg. typically utilized to activate Fly ash, mechanical strength has increased. The optimum outcomes were monitored for the WG-NaOH solution (N10 + 15g), which exhibited the strength of 88 MPa.

Torres-Carrasco and Puertas [16] have noticed the identical strength performance concerning Fly ash activated with this option to commercial Sodium Silicate, made by dissolving the WG through heating [6]. Ultimately, by taking 10M KOH solution as an activator, the WG obtained strength roughly of 50 MPa, which is a smaller value than that of the Na<sup>+</sup> ion-containing system. Since the K<sup>+</sup> cation dissolves less of the Ca and Mg present in the preliminary material, a reduced amount of reaction yield precipitates [18, 19].

Lin et al., [20] have investigated the setting time of WG incorporated Metakaolin-based Geopolymers and recorded that the setting time experiment was employed to investigate the early and final fresh paste setting times. The early setting time displayed that the fresh paste lost the workability, and the final setting time pointed out that mechanical strength enhanced. Fig. 4 illustrate the setting time experiment outcomes.

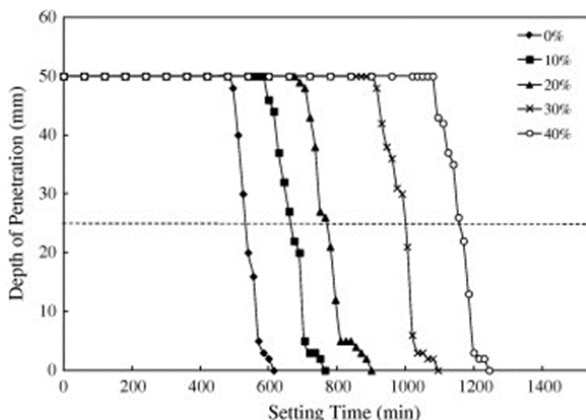


Fig. 4 Setting times of waste-glass metakaolin-based geopolymers [20]

Fig. 4 depicts that the setting time ascended as the Metakaolin (MK) was substituted with WG of TFT-LCD. The early and final setting times of the MK-based Geopolymers were around 533 min. and 615 min., correspondingly. Since more MK was substituted with WG of TFT-LCD, the early and final setting times are augmented. When 10% of the MK was substituted by WG of TFT-LCD, the early and final setting times were about 666 min. and 765 min., in that order. While 40% of MK was substituted with WG of TFT-LCD, the early and final setting times boosted to 1158 min and 1245 min correspondingly. The upshots are represented that the Valorization WG of TFT-LCD enhanced the workability.

## 2.2. Compressive Strength

The study by Torres-Carrasco and Puertas [14], unearthed that the nature of the activator has affected significantly. Kastiukas and Zhou, [21] studied the influence of WG addition on the mechanical performance of Geopolymer binders accompanied by Tungsten Mining Wastes (TMW). The average compressive strength of the four poles apart compositions of Geopolymer binders with the substitution of TMW by WG for up to 40 % by weight is summed up in Fig. 5.

The upshots achieved for only TMW-Geopolymer binders are also taken into account. Fig. 5 has pointed out that the compressive strength boosted with an enhancement of WG content across all ages. Substitution of 40 % by weight of WG, i.e., specimens 60TMW40WG, have shown 16% of augment in  $\text{SiO}_2$  molar content and demonstrated the highest 28<sup>th</sup> day compressive strength of 41 MPa; a 127% enhancement comparative to the 100TMW control specimen. The compressive strength at the initial age was also monitored to enhance with the boost in WG content. Commencing with the control specimen of 100TMW, the compressive strength on the first day is merely 12.3% of the final 28th-day strength.

Nevertheless, for 20, 30, and 40 % substitution of TMW by weight with WG, the first-day strength enhances to 48.6, 67.8, and 72% of the ultimate 28th-day strength. To investigate the latter strength enhancements, SEM micrographs of Geopolymer binders unearthing the micro-structural divergences in specimens manufactured incorporating WG are depicted in Fig. 6.

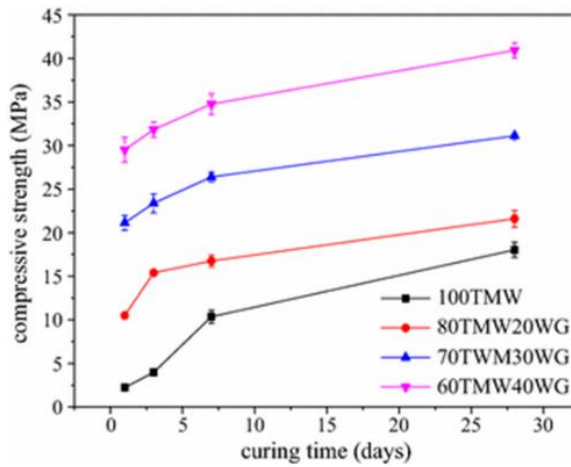


Fig. 5 Effects of WG on compressive strength [21]

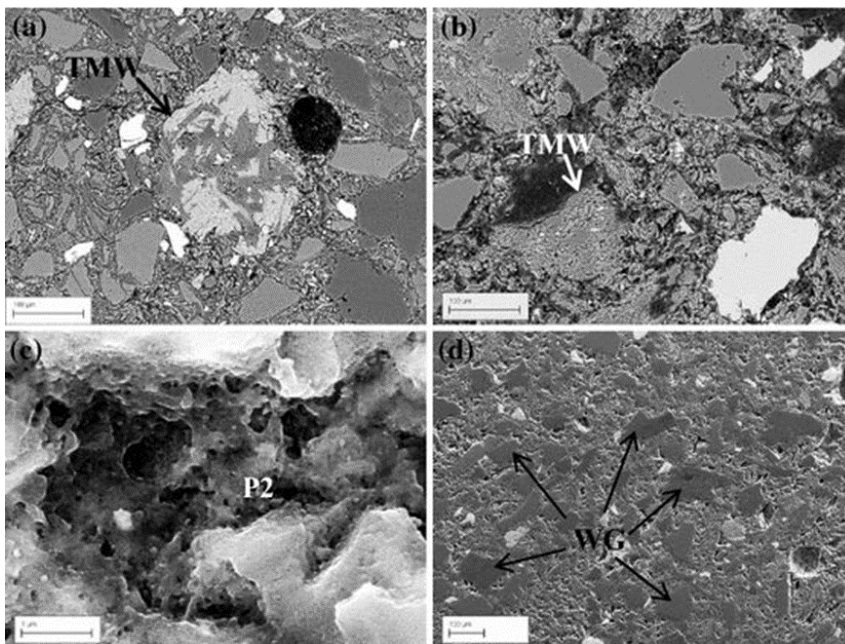


Fig. 6 SEM images of a 60TMW40WG, b 100TMW, c amorphous reaction products in 60TMW40WG and d unreacted WG particles [21]

Particles of TMW on the first day (60TMW40WG specimen) (Fig. 6a) displayed more zones of the Muscovite crystal with a laminated structure, which is shown as lighter areas that can be deduced as an augment in the echelon of Al and Si leaching. On the other side, the particles of Muscovite on the first day 100TMW specimens (Fig. 6b) stayed comparatively unaffected. The structure of specimens of 60TMW:40WG seems to have a smaller number of voids, whereas the reaction products emerge as denser and with more permanence, i.e., they are not composed of remote areas such as the case of 100TMWspecimens.

Dense amorphous gel formations were also observed in the 60TMW:40WG as illustrated in Fig. 6c). Also, fig. demonstrates how WG particles are partly converting into amorphous reaction yields propping up the suggestion that an enlarged substitution of WG contributes a means of escalating reactive Silica and, in this manner, growing the Si: Al ratio. In other words, less dependence on employing more expensive and less sustainable soluble Silica met within commercial  $\text{Na}_2\text{SiO}_3$  (Sodium Silicate) solution. Subsequent to 28 days, a lot of bulky particles of  $\text{SiO}_2$  were found entrenched in the matrix of Geopolymer binders as given away in Fig. 6d.

Nevertheless, it was not easy to establish the amount which came from the TMW and WG. However, it can be concluded that the enhanced WG content might not have merely contributed reactive Silica to the mixture but also encouraged to strengthen the Geopolymer binders as inert filler, most probably by the coarser portion of WG. The compressive strength results with the optimum substitution by WG, i.e., 40 % by weight are comparable with the outcomes of Pacheco- Torgal et al.[22], who achieved 39.6 MPa at 28 days for TMW incorporated Geopolymer mortar. Though, the achievement was only subsequent to an energy-intensive Calcination of the TMW at 950°C for 2 hours.

A study by Rivera et al., [23] leads to the upshots of the compressive strength examinations on the synthesized Alkaline cement cured for 7 days, which are illustrated in Fig. 7. Even though the composition of the WG is extremely analogous, the compressive strength at 7 days, for the three alkaline-activated residues is very dissimilar.

The bottle residues represented the greatest resistance of 56 MPa at low concentrations of the activator solution NaOH which was only 4 molar. The lower percentage of NaOH necessitated for the activation of the residue is not only cost-effective but also environmentally benign. This is attributed to the enhanced percentage of dissolution in alkaline condition, which is an index of the better reactivity, irrespective of the bulky size of the particle as the action of the medium could take place on the surface of the particles which stay entrenched in the alkaline activated matrix performing as a reinforcement that limits the propagation of cracks and augments the resistance. It has been chronicled that an elevated concentration of MOH activator where,  $M = \text{Na}^+$  or  $\text{K}^+$  generates a high pH in the liquid phase, and results in an enhanced percentage of ionic species, that limits the mobility of ions and therefore, hinders the process of polymerization [24,25].

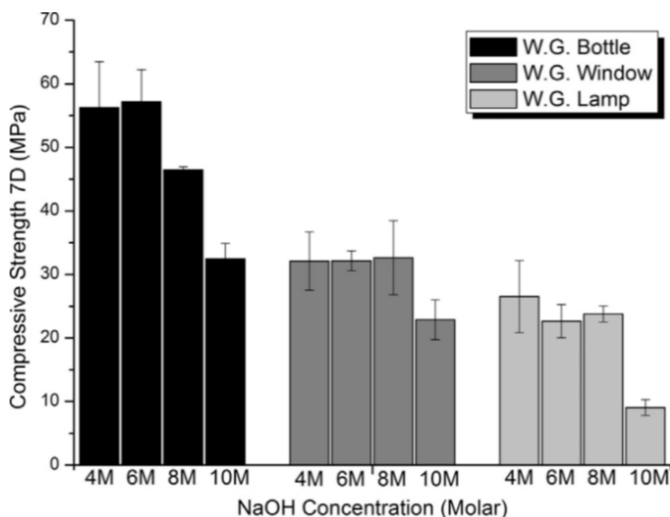


Fig. 7 Effect of waste glass (W.G) on Compressive strength at 7 days[23]

What's more, Silica from the WG has a better solubility at higher concentrations of NaOH and at the reaction temperature which was 70° C, extended its amorphous nature, and this surplus of soluble Silica in the mix is predicted to augment the viscosity of the network [26], by this means declining the mobility of Silicate chains in the formulation and providing to the loss of mechanical strength in the trial piece. A few researchers assigned this dwindle to an advanced attack on particles of WG by the alkali, which forms an outside layer on the particles which delays the reaction [27,28]. The said outcomes put forward the survival of a restricting value of the concentration of NaOH, in particular, taking into account the contribution of Sodium from the WG.

The study of Rivera et al., [22] has obtained the value as 4 Molar, keeping the compressive strength almost constant or drop off considerably, as shown in Fig. 7. The referred result coincides with that recorded by Pascual et al. [27].

Fig. 8, the upshots of compressive strength of the Geopolymer samples employing NaOH of 4 M as an activator are compared, at the ages of 7 and 28 days of curing. A drop in the context of the mechanical resistance at 28 days is monitored, of about 4% for bottle glass waste, 8% for window glass waste, and 32% for lamp glass waste. The falls in strength noticed between 7 and 28 days could be owing to the phase modifications taking place for the duration of ageing, though, shrinkage and cracking [26].

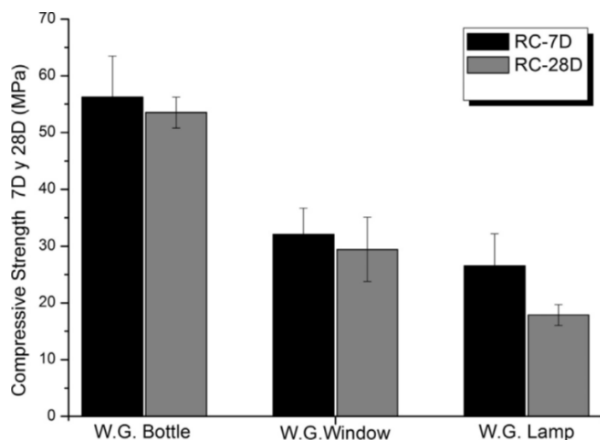


Fig. 8 Effect of waste glass (W.G) on Compressive strength at 7 and 28 days [23]

Haji Mohammadi et al. [28] have reported on the behavior of drying shrinkage of the Geopolymer pastes over time, which is demonstrated in Fig. 9. The control group with no aggregates possess the uppermost rate of shrinkage, which is supposed owing to the higher quantity of gel production for the analogous amount of binder paste as there are no aggregates present. The aggregates do not shrink, and hence influences the ultimate percentage of shrinkage of the system. Consequently, the quantity of aggregate content is significant for a reduction in shrinkage [29]. The Sand group displays a noticeably high proportion of shrinkage than the glass grouping. Mortars are well-known to exhibit low shrinkage in comparison with the pure paste, on account of the enclosing aggregates [30]. It is also identified that the size enhances of aggregates accelerates the drying shrinkage of the mortars [30,31].

For that reason, the behavior monitored in Fig. 9 is logical i.e., a decline in shrinkage from the control grouping to the Sand group and a further fall in shrinkage from the sand group to the glass group having finer WG particles. It is quite attention-grabbing to make a note that the glass group designates amazingly low shrinkage on the 7<sup>th</sup> day and 14<sup>th</sup> day;

however, the shrinkage out of the blue quadruples on the 21st day! It stems from the fact that the WG-fine is fundamentally pozzolanic, and it will ultimately play a role in the kinetics of the Geopolymerization process. The quantity percentage of Silica dissolution from WG at ambient temperature is identified to be trifling [32].

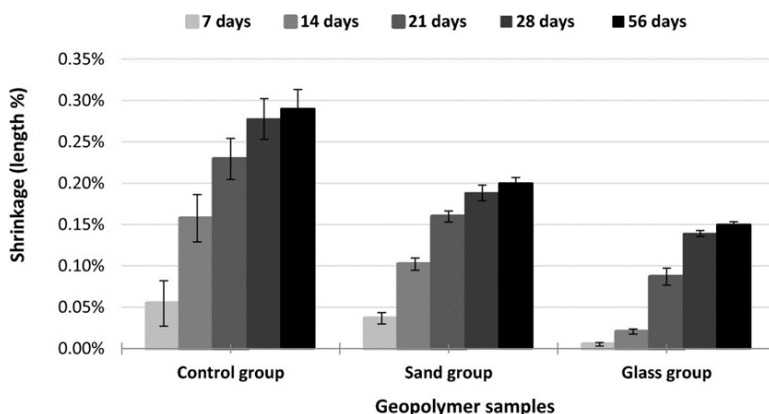


Fig. 9 Drying shrinkage of geopolymer binders [28]

Also, another study by Puertas and Torres-Carrasco [33], has flashed lights on the mechanical performance of the pastes, which is depicted in Fig. 10. Fig. exhibits that compressive strength ascended with curing time in every one of the pastes. The least values of strength were noted down, at all ages, for paste Slag-Geopolymer with NaOH/Na<sub>2</sub>CO<sub>3</sub>. N/C, i.e., the paste made with NaOH/Na<sub>2</sub>CO<sub>3</sub> as the activator, and the highest for a paste of slag Geopolymer with water glass solution, manufactured with water glass activator. The graph also displays that the greater the content of WG in the activator solution in the Slag-Geopolymer N/C family of pastes, the superior was their mechanical strength, though neither was as strong as a paste of WG-Slag Geopolymer. In the range of 100–0.01 μm, the total porosity and pore size distribution for the pastes are correspondingly made known in Fig. 11, whereby the porosity values are demonstrated in the percentage of the entire specimen volume. The total porosity was highest in the paste of Slag-Geopolymer prepared with N/Cat all ages, varying from 18 to 24%. While in the case of pastes made with Si possessing activators, total porosity was considerably low: 4 to 9% in WG-Slag Geopolymer and 7 to 9% in paste Slag Geopolymer made with N/C-25. Pore size distribution pursued an analogous pattern as shown in Fig.11, with a higher proportion of micro and mesopores in the pastes manufactured with the silicon-activators. The paste made with 25 g/100 mL WG had a bigger fraction of pores lesser than 0.01 μm. These total porosity and pore size distribution outcomes are constant with the compressive strength obtained for the materials examined, as demonstrated in Fig. 10.

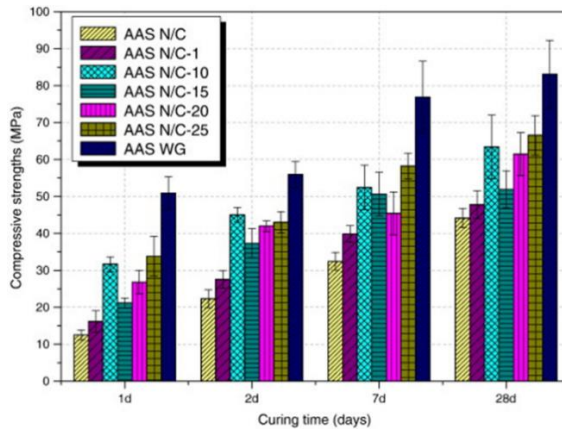


Fig. 10 Compressive strength of AAS pastes [11]

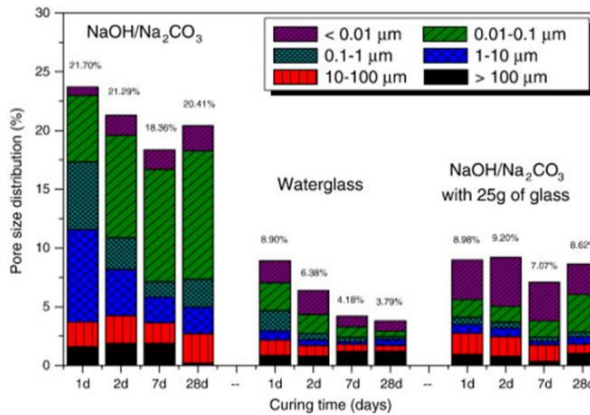


Fig. 11 Pore size distribution in pastes [33]

Martinez-Lopez and Escalante-Garcia, [34] have also studied concerning the compressive strength of the Geopolymer paste evolution from 1 to 28 days for the pastes grouped by the quantity percentage of WG. The compressive strength generally enhanced with the period, and the greatest strength at 28 days was for specimen CN1 with 4% Na<sub>2</sub>O employing NaOH as an activator, 0%WG, and curing at 20°C. Paste CN17 demonstrated a strength reduce following 14 days owing to the long-termed curing at a higher temperature, following Puertas [35], who talked about the strength decline that it is owing to the slimming down of Silica gel phase developed at early ages, Silica gel encloses water not bound chemically and it evaporates readily at elevated temperature, this reduction results into formation of cracks in strength detriment. It is discernible that in trials of 0 to 25% WG, i.e., with a low percentage of WG, the strength mitigated with the boost of percentage quantity of Na<sub>2</sub>O; the enhance of Na<sub>2</sub>O contents in blast furnace slag (BFS) has been recorded to trim down the strength [36,37].

Wang [38] designated that 2 to 8 % of Na<sub>2</sub>O was enough to acquire higher strength in BFS pastes, some other researchers have also signified that a surplus of Alkalis directed to Carbonation and strength loses owing to the referred phenomenon[37,39]. On the other side, the pastes with 50 % WG demonstrated inferior strength for 4 to 8% of Na<sub>2</sub>O that points that the Slag and class contested for an inadequate quantity of activator, it also

seems that the strength enhanced with a grouping of elevated curing temperature, enhanced quantity percentage of  $\text{Na}_2\text{O}$  along with the presence of  $\text{Na}_2\text{CO}_3$ ; however, the on the whole attitude of these composites designate that there was no apposite percentage of content of  $\text{Na}_2\text{O}$ , i.e., lower content of  $\text{Na}_2\text{O}$ , were not as much as essential for the activation of WG, and a high percentage of  $\text{Na}_2\text{O}$  had a pessimistic impact on the activation of BFS, as reported in the micro-structures as shown in Fig. 12, whereby the quantity of non-reacted WG particles was elevated in comparison with other trials. It was accounted that the advanced percentage of WG advantaged from the amalgamation of  $\text{Na}_2\text{CO}_3$ , as demonstrated by trials CN6, CN15, CN17, and CN25 with 25%, 50%, 75%, and 100 % of WG respectively.

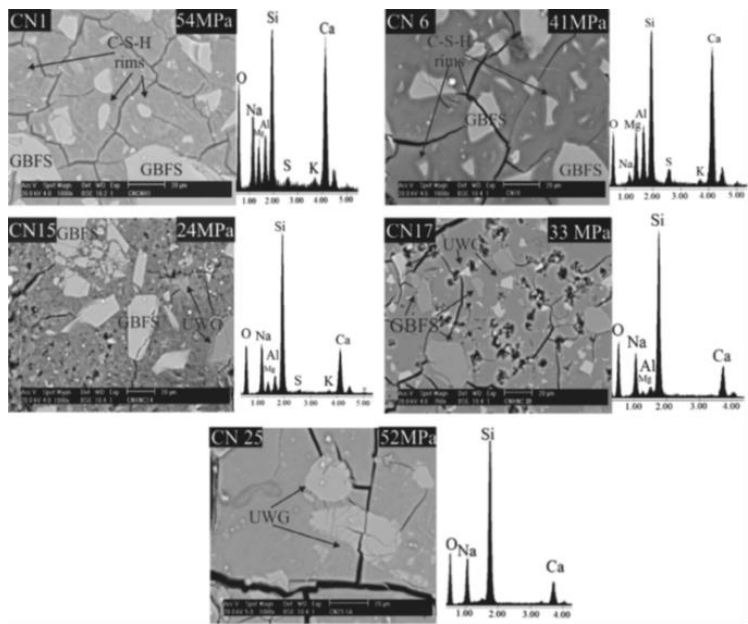


Fig. 12 Scanning electron micrograph of the samples CN1, CN6, CN15, CN17 and CN25 at 28 days [34]

Ruiz-Santaquiera [40] found that the solubility of glass was found more employing an activation solution of  $\text{NaOH} : \text{Na}_2\text{CO}_3$  at the ratio of 50:50, and Sodium Carbonate functions as a pH stabilizer in Alkaline solution; i.e., for merely  $\text{NaOH}$ , the Ions of Hydroxide  $[\text{OH}]$  declined as the Silica dissolved, on making the adding together of  $\text{Na}_2\text{CO}_3$  permitted the  $\text{OH}^-$  ions to stay quite constant with time, permitting the split of more  $\text{Si-O}$  bonds. The temperature for curing also had a powerful impact on strength; elevated temperatures supported the early strength; this was in harmony with accounts on BFS binders [41–43]. The author also mentioned the WG necessitates a prolonged curing time to build up higher mechanical characteristics.

Tho-In et al., [44] 'What's more to add, the compressive strengths of the Fly Ash based Geopolymer pastes with diverging substitutions of Fly Ash by WG. The upshots fingers towards the substitution levels of both fluorescent lamp glass powder (FP) and ground container glass powder (CP) have imperative impacts on the compressive strengths of Geopolymer pastes. The best possible performances for FP and CP substitutions are attained from the 10FP and 20CP samples with compressive strengths of 41.1 MPa and 47.6 MPa, correspondingly, whereas the reference paste displays a compressive strength of 45.7 MPa. With substitution by FP, the compressive strength inclines to reduce as the

substitution level is enhanced. Samples 10FP,20FP, 30FP and 40FP demonstrate compressive strengths of 41.1, 40.7, 39.6, and 33.3 MPa, in that order, while 100 FA has a compressive strength of 45.7 MPa. The decline in compressive strength may be assigned to the substitution with FP, altering the Silicon: Aluminum ratio on account of its elevated Silicon content. The attributes of Geopolymers are considerably modified with comparatively little alterations in Silicon and Aluminum contents during the Geopolymerization of Alumino-Silicates [45]. Higher Silicon: Aluminum ratios persuade the development of low cross-linked Alumino-Silicate materials with reduced strengths[46, 47].

Davidovits [48], as well as Chindaprasirt et al. [49], have pointed out that the optimum Silicon: Aluminum ratio for a good-strength Geopolymer was among 3.5 to 4.0. Nevertheless, the geopolymer samples employing 10 to 30%FPdemonstrated compressive strengths of 87 to 90% that of the reference paste owing to the higher fineness of the FP-particles. The fine FP- particles play the role of micro-fillers for the Geopolymer paste, inducing matrix densification. The compressive strengths of Geopolymer paste incorporating CP are also mitigated, analogous to those amalgamating FP, on account of the enhanced Silicon: Aluminum ratios. Nevertheless, the compressive strengths of the CP-pastes are superior to FP-pastes at the constant substitution levels. This is for the reason that the CaO content of 12.80% in CP is greater than in FP, which was7.43%. High CaO levels in Geopolymer pastes have been accounted to form supplementary Calcium-Silicate-Hydrate or Calcium Alumino-Silicate Hydrate phases along with other Geopolymerization yields, consequently, producing denser structures and enhanced strengths [50, 51]. The Geopolymer paste is incorporating 20%CP demonstrates the greatest compressive strength of 47.6 MPa, a little more than that of the reference paste. This may be due to the amalgamation of a correct quantity of fine CP-particles with a higher content of CaO.

### 2.3. Thermal

Badanoiu et al. [52], have examined thermal attributes in the context of mass changes, porosity, and compressive strength. They reported that the mass alterations evaluated on the cubic paste samples treated at diverse temperatures are represented in Fig. 13.

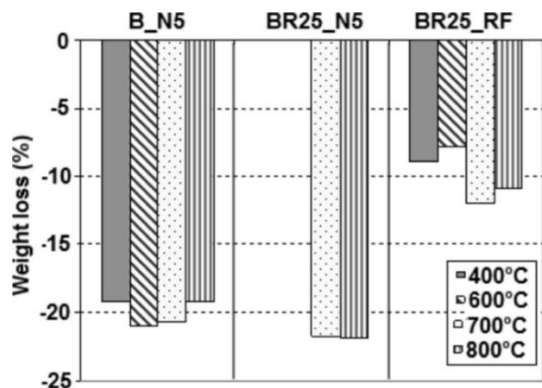


Fig. 13 Mass loss of pastes after thermal treatment at different temperatures [52]

The mass losses noted down for B\_N5 (NaOH 5 M), and BR25\_N5 (NaOH 5 M) pastes subsequent to thermal treatment at temperatures among 400 and 800°C is consisted among 19% and 22%; this significant weight loss is chiefly owing to the dehydration and transformation of Sodium Silicate (Aluminate) Hydrates which confirms the foaming of the material. For the BR25\_RF (Red mud slurry filtrate (RF) pastes, the mass losses are smaller with 8 to 12% mostly owing to the low-quantity of Sodium Silicate (Aluminate) Hydrates developed when filtrate RF with low alkalinity in comparison with NaOH 5 M was employed as the liquid ingredient. Two B\_N5 pastes – one treated at 600°C and another at 800°C, possess the apparent density values smaller than 0.866 g/cm<sup>3</sup>. For the BR25\_N5 pastes, apparent density the values trim down with the augment of temperature for thermal treatment. The said data are in good agreement with the enhancement of open porosity, which also evaluated visually as depicted in Fig. 17. The greatest values for open porosities are documented for BR25\_RF paste prior to and subsequent to thermal treatment at 400°C and 600°C. The referred values can be compared with the loose and heterogeneous micro-structure specific for the said samples, as exemplified in Figs. 14, 15, and 16. Thermal treatment at 700°C, which is exceeding the melting point of brown glass, confirms paste reduction and densification of the micro-structure as portrayed in Fig.-18 in comparison with Fig.-15c and 15d.

As a result, the open porosity sharply declines to 1.64%. The enhancement in temperature for thermal treatment to 800 °C trims down the viscosity of the melt stage, and the gases generated by Sodium Silicate (Aluminate, Ferrite) stages develop bubbles in the material; thus, the micro-structure represents abundant pores of a variety of sizes Fig. 19e and 19f, and the open porosity value enhances again. Fig. 19 illustrates the evolution of verses temperature values of compressive strength. For B\_N5 paste, the values of the compressive strength declines with the escalation of thermal treatment temperature, in fine correlation with the augment of porosity. Even so, the compressive strength of 2 to 5 MPa is fine for foamed materials [53]. Densification of the micro-structure of BR25\_RF paste treated at 700°C confirms an imperative augment of compressive strength, which is found at 25 MPa. Expectedly, the enhancement of open porosity, for pastes treated at 800°C determines to dwindle in compressive strength, but the value found of 8.6 MPa is still higher.

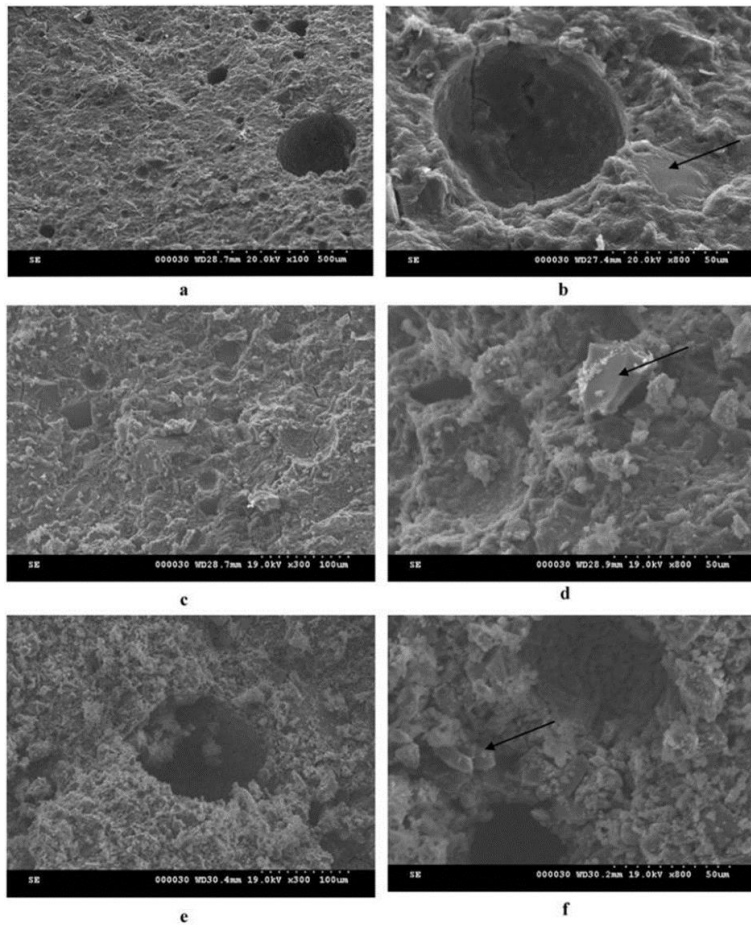


Fig. 14 SEM micrographs of B\_N5 (a and b), BR25\_N5 (c and d), and BR25\_RF (e and f) paste before thermal treatment [52]

Zhang et al., [54] have clarified that as an ingredient in Geopolymer concrete the surface of the WG-aggregates can react with Alkaline solution over time and good binding with the Geopolymer paste in bulk. Furthermore, the development of compressive strength of paste mixes with escalating waste glass powder (GP) as powder coal fly ash (PCFA) substitution from 0% to 30% is displayed in Fig. 21.

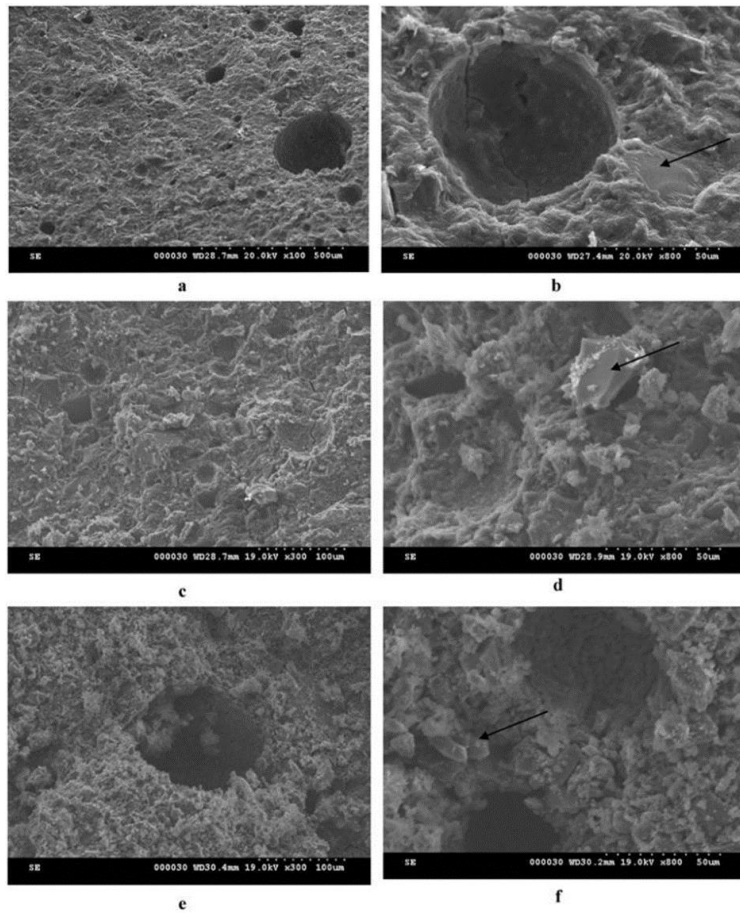


Fig. 15 SEM micrographs of B\_N5 (a and b), BR25\_N5 (c and d) and BR25\_RF (e and f) paste after thermal treatment at 400 °C for 1 h [52]

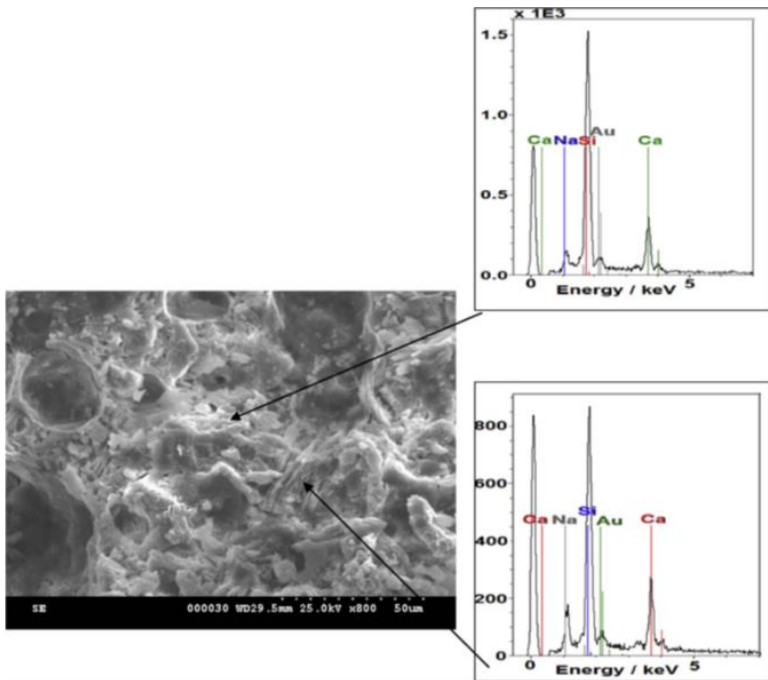


Fig. 16 SEM micrograph and EDX analysis B\_N5 paste treated at 400 °C for 1 h [52]



Fig. 17The visual aspect of BR25\_RF pastes after thermal treatment for 1 h at temperatures between 400 and 800 °C [52]

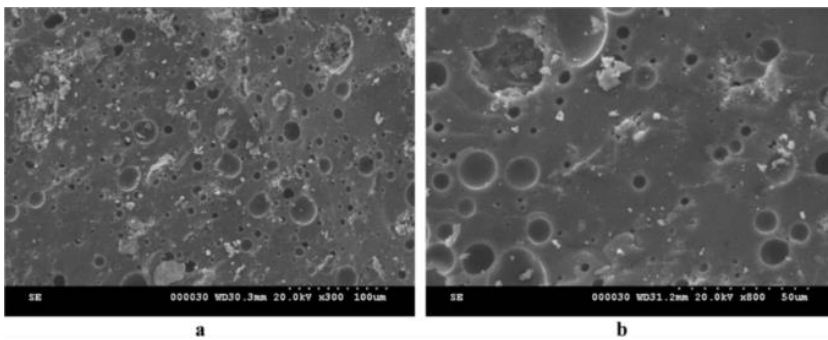


Fig. 18 SEM micrographs of BR25\_RF paste after thermal treatment at 700 °C for 1 h [52]

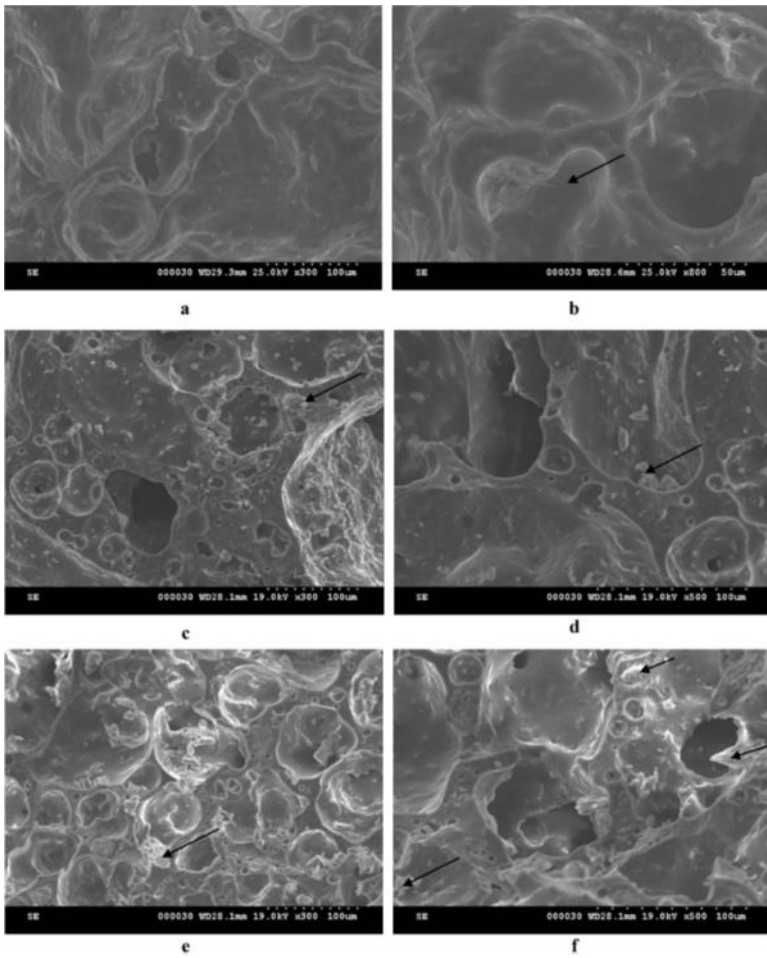


Fig. 19 SEM micrographs of B\_N5 (a and b), BR25\_N5 (c and d) and BR25\_RF (e and f) paste after thermal treatment at 800 °C for 1 h [52]

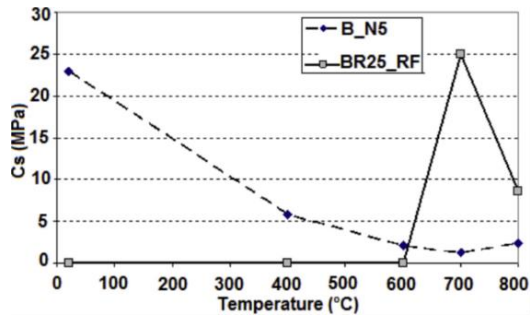


Fig. 20 Compressive strengths of pastes before and after thermal exposure [52]

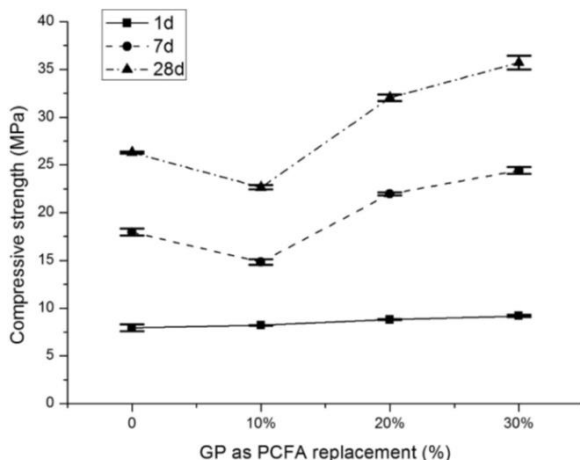


Fig. 21 Compressive strength development of paste with GP as PCFA [54]

The compressive strength of one day is identical within all mixes while the compressive strength accelerates considerably at 7 and 28 days with a greater quantity of GP substitution. In comparison with R [0% substitution], up to 35% strength enhance is monitored in G30 [30% GP as PCFA substitution]. The said augment could be assigned to the advanced GP reactivity and accessibility of soluble Silica contributed by the reaction among GP and NaOH that encourages the Geopolymerization procedure and directs to elevated quantity of gel development. The international activation course is comparable to the conjugational impact of employing Sodium Silicate and Sodium Hydroxide as alkali activator. Preceding investigations also determined that this conjugational impact consequences in supplementary accessible Silica in the system and escalates the gel Polycondensation [55], which provides improved mechanical attributes. More than that, Fly ash is well-known to possess Hollow Cenospheres and Plerospheres that are susceptible to surface opening within dissolution course of action. For that reason, the production of reaction yields is supposed to be stimulated on the internal PCFA surface [56,57]. This occurrence has also been determined in PCFA cement paste mixtures, where reacted hollow PCFA-particles offer additional room for the reaction yields [58]. The opening of the "closed" voids in PCFA was investigated by alkaline solution treatment to validate that the PCFA in the study may also hold reaction yields. A comparison of the pore structure of with and without treated PCFA through 4 M NaOH solutions for 2 hours uncovers palpable disparities. As given away in Fig. 22 (a), the total porosity of the without treated original ash was 5.69% while it got enhanced to 17.42% subsequent to treatment.

Not only that, Fig. 22(b) designates that the pore size range expands from 3 to 6  $\mu\text{m}$  towards 2 to 10  $\mu\text{m}$  following treatment with an alkaline solution. Consequently, all the referred facts suggested that the surface opening of hollow PCFA may amplify the ease of access of the finer pores, and that's why endorse the reaction yields production within PCFA-particles.

Nevertheless, they inefficiently offer the bonding of particles that directs to reduce compressive strength. This impact inclines to be diluted on escalating the content of GP since the diminished potential for the PCFA to have room for reaction yields. For that reason, they are augmenting the quantity of GP, finally pilots to augmentation of the compressive strength. On the other hand, a substantial strength decline is met within the case of G10 10% of GP in comparison to R at 7 and 28 days, which entails that dissimilar

mechanisms are engaged at lower substitution levels. This unforeseen propensity may be induced by the finer size of the particle distribution of GP in comparison with PCFA.

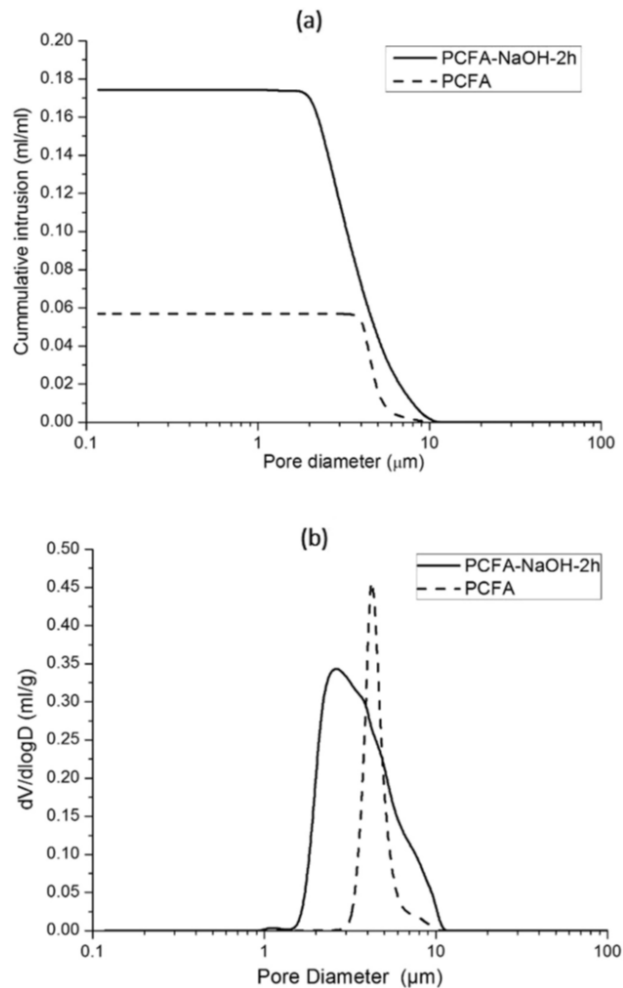


Fig. 22(a) cumulative pore-size distribution and (b) differential pore size distribution [54]

The diminutive size of a particle of GP and its angular shape may have a pessimistic effect on the stuffing density of the mix [59] that could escort to a compressive strength drop off. For the moment, the low density of mix with GP substitution may also contribute to the strength reduction. It is worthless that the impacts are merely predominant on the compressive strength development at low GP substitution levels [ $\leq 10\%$ ]. With advanced GP substitution levels [ $\geq 20\%$ ], the governing feature may progressively alter from the physical impact to a chemical one. Compared with R mix, merely a slight augment of gel development is found in G10 whereas a noteworthy augment is monitored in G20 and G30 (20%, and 30% of GP) mixes.

## 2.4. Microstructural

Kastiukas and Zhou [60] explored the impact of WG supplement of WG on microstructural attributes of Geopolymer binders incorporated with Tungsten Mining Wastes (TMW). The initial age reaction product development in the 100 TMW (100% tungsten mining waste) specimens is publicized in Fig. 23a. The outcomes from the SEM imaging illustrate sites of N-A-S-H gel reaction products, say P1, with dissimilar cation and anion replacement of Fe, Mg, and K that possess the structure of amorphous type and point up branch-like formulations bridging the reaction products collectively. The same reaction yields can also be observed integrating with the particles of Quartz from the TMW, developing the gel system. Fig. 23b encompasses crystals of Muscovite (M) into TMW incorporating Geopolymer binders is shown to form a thickly laminated structure for the duration of Alkali activation indicative of uptake of hydroxyl (OH) ions on account of rehydroxylation. Through EDX micro-analyses, the Al: Si ratio for non-reacted Muscovite was confirmed as 1.0 when readings recorded subsequent to one day of reaction with the Alkali activator noticed the latter value plunge to 0.65, representing an obvious signal of the discharge of Aluminium cations into the solution.

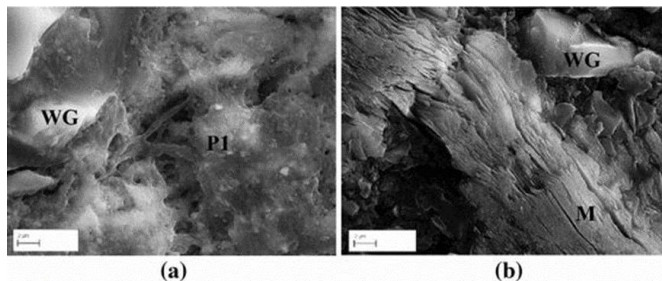


Fig. 23 SEM image of TMW incorporating geopolymer binder [60]

## 3. Conclusion and discussion

This paper reviews the valorization of the applications of WG incorporation for the development of geopolymer paste and discussed the previous few studies on workability, strength, thermal, and microstructural properties. This review included the possibility of employing WG in a geopolymer as a precursor for alkaline cement. The review reveals that it is wholly possible to blend these wastes in construction and building materials, sans any further makeover beyond crushing to develop innovative Geopolymer building materials. Geopolymer paste with a lightweight glass waste aggregate can be used as foam concrete. Glass can be ground easily to very fine particles that can replace fine sand in lightweight geopolymer foams. Over the time, the surface of the glass particles reacts with the paste and forms stronger bonds with the geopolymer binder. These inimitable features make glass fines a suitable substitute for fine sand in geopolymer foam applications. To sum up, the application of WG has been established as a valuable material in making Geopolymers with excellent and acceptable attributes that valorize it as an economical and sustainable construction material. This is a valuable step putting a step forward towards the “Green Concept” and in the direction of its valorization.

## References

- [1] Luhar S, Cheng TW, Nicolaidis D, Luhar I, Pnias D, Sakkas K. Valorisation of glass wastes for the development of geopolymer composites - Durability, thermal and microstructural properties: A review. *Construction and Building Materials* 2019, 222, 673-687. <https://doi.org/10.1016/j.conbuildmat.2019.06.169>
- [2] Luhar S, Cheng TW, Nicolaidis D, Luhar I, Pnias D, Sakkas K. Valorisation of glass waste for development of Geopolymer composites - Mechanical properties and rheological characteristics: A review. *Construction and Building Materials* 2019, 220, 547-564. <https://doi.org/10.1016/j.conbuildmat.2019.06.041>
- [3] Shaikh FUA, Luhar S, Arel HŞ, Luhar I. Performance evaluation of Ultrahigh performance fibre reinforced concrete - A review. *Construction and Building Materials* 2020, 232. <https://doi.org/10.1016/j.conbuildmat.2019.117152>
- [4] Luhar S, Cheng TW, Luhar I. Incorporation of natural waste from agricultural and aquacultural farming as supplementary materials with green concrete: A review. *Composites Part B: Engineering* 2019, 175. <https://doi.org/10.1016/j.compositesb.2019.107076>
- [5] Chao JY. Manufacturing and properties of alkali-activated waste glass cement (Master thesis). National Cheng Kung University, 2008.
- [6] Luhar S, Chaudhary PS, Luhar I. Influence of Steel Crystal Powder on Performance of Recycled Aggregate Concrete. *IOP Conference Series: Materials Science and Engineering* 2018, 431. <https://doi.org/10.1088/1757-899X/431/10/102003>
- [7] Luhar S, Dave UV, Chaudhary S. A Brief Review On Geopolymer Concrete. 5th Nirma University International Conference On Engineering, Ahmedabad, 2015.
- [8] Luhar S, Dave U. Investigations On Mechanical Properties Of Fly Ash And Slag Based Geopolymer Concrete. *Indian Concrete Journal* 2016, 34-41.
- [9] Luhar S, Chaudhary S. Effect Of Elevated Temperatures On Rubberized Geopolymer Mortar. *International Journal Of Civil, Structural, Environmental And Infrastructure Engineering Research And Development* 2016, 79-86.
- [10] Luhar S. Fly, Ash And Slag Based Geopolymer Concrete: Experimental Facts. Lap Lambert Academic Publishing, 2016.
- [11] Luhar S. Performance Evaluation Of Rubberized Geopolymer Concrete And Fly Ash-Based Geopolymer Mortar. (Thesis), 2018.
- [12] Luhar S, Luhar I. Potential application of E-wastes in construction industry: A review. *Construction and Building Materials* 2019, 203, 222-240. <https://doi.org/10.1016/j.conbuildmat.2019.01.080>
- [13] Wang WC, Chen BT, Wang HY, Chou HC. A study of the engineering properties of alkali-activated waste glass material (AAWGM). *Construction and Building Materials* 2016, 112, 962-969. <https://doi.org/10.1016/j.conbuildmat.2016.03.022>
- [14] Torres-Carrasco M, Puertas F. Waste glass as a precursor in alkaline activation: Chemical process and hydration products. *Construction and Building Materials* 2017, 139, 342-354. <https://doi.org/10.1016/j.conbuildmat.2017.02.071>
- [15] Yang KH, Song JK. Workability Loss and Compressive Strength Development of Cementless Mortars Activated by Combination of Sodium Silicate and Sodium Hydroxide. *Journal of Materials in Civil Engineering* 2009, 21, 119-127. [https://doi.org/10.1061/\(ASCE\)0899-1561\(2009\)21:3\(119\)](https://doi.org/10.1061/(ASCE)0899-1561(2009)21:3(119))
- [16] Torres-Carrasco M, Puertas F. Waste glass in the geopolymer preparation. Mechanical and microstructural characterisation. *Journal of Cleaner Production* 2015, 90, 397-408. <https://doi.org/10.1016/j.jclepro.2014.11.074>
- [17] Carrasco M, Puertas F. Sodium silicate solutions from dissolution of glass wastes. Statistical analysis. *Materiales de Construcción* 2014, 64. <https://doi.org/10.3989/mc.2014.05213>

- [18] Fernández-Jiménez, A.; Palomo, A.; Criado, M. Alkali activated fly ash binders. A comparative study between sodium and potassium activators. *Materiales de Construcción* 2006, 56, 51-65.
- [19] Xu H, van Deventer JSJ. The effect of alkali metals on the formation of geopolymeric gels from alkali-feldspars. *Colloids and Surfaces A: Physicochemical and Engineering Aspects* 2003, 216, 27-44. [https://doi.org/10.1016/S0927-7757\(02\)00499-5](https://doi.org/10.1016/S0927-7757(02)00499-5)
- [20] Lin KL, Shiu HS, Shie JL, Cheng TW, Hwang CL. Effect of composition on characteristics of thin film transistor liquid crystal display (TFT-LCD) waste glass-metakaolin-based geopolymers. *Construction and Building Materials* 2012, 36, 501-507. <https://doi.org/10.1016/j.conbuildmat.2012.05.018>
- [21] Pacheco-Torgal F, Jalali S, Castro Gomes JP. 13 - Utilization of mining wastes to produce geopolymer binders. In: Geopolymers. Provis, J.L.; van Deventer, J.S.J. Eds. Woodhead Publishing: 2009; pp. 267-293. <https://doi.org/10.1533/9781845696382.2.267>
- [22] Rivera JF, Cuarán-Cuarán ZI, Vanegas-Bonilla N, Mejía de Gutiérrez R. Novel use of waste glass powder: Production of geopolymeric tiles. *Advanced Powder Technology* 2018, 29, 3448-3454. <https://doi.org/10.1016/j.apt.2018.09.023>
- [23] Alonso S, Palomo A. Alkaline activation of metakaolin and calcium hydroxide mixtures: influence of temperature, activator concentration and solids ratio. *Materials Letters* 2001, 47, 55-62. [https://doi.org/10.1016/S0167-577X\(00\)00212-3](https://doi.org/10.1016/S0167-577X(00)00212-3)
- [24] Novais RM, Ascensão G, Seabra MP, Labrincha JA. Waste glass from end-of-life fluorescent lamps as raw material in geopolymers. *Waste Management* 2016, 52, 245-255. <https://doi.org/10.1016/j.wasman.2016.04.003>
- [25] Panias D, Giannopoulou IP, Perraki T. Effect of synthesis parameters on the mechanical properties of fly ash-based geopolymers. *Colloids and Surfaces A: Physicochemical and Engineering Aspects* 2007, 301, 246-254. <https://doi.org/10.1016/j.colsurfa.2006.12.064>
- [26] Cyr M, Idir R, Poinot T. Properties of inorganic polymer (geopolymer) mortars made of glass cullet. *Journal of Materials Science* 2012, 47, 2782-2797. <https://doi.org/10.1007/s10853-011-6107-2>
- [27] Pascual A, Tognonvi M, Tagnit-Hamou A. Waste glass powder-based alkali-activated mortar. *International Journal of Research in Engineering and Technology* 2014, 03, 32-36. <https://doi.org/10.15623/ijret.2014.0325006>
- [28] Hajimohammadi A, Ngo T, Kashani A. Sustainable one-part geopolymer foams with glass fines versus sand as aggregates. *Construction and Building Materials* 2018, 171, 223-231. <https://doi.org/10.1016/j.conbuildmat.2018.03.120>
- [29] Abdollahnejad Z, Zhang Z, Wang H, Mastali M. Comparative Study on the Drying Shrinkage and Mechanical Properties of Geopolymer Foam Concrete Incorporating Different Dosages of Fiber, Sand and Foam Agents. In: *Proceedings of High Tech Concrete: Where Technology and Engineering Meet*, Cham, 2018; pp. 42-48. [https://doi.org/10.1007/978-3-319-59471-2\\_6](https://doi.org/10.1007/978-3-319-59471-2_6)
- [30] Grassl P, Wong HS, Buenfeld NR. Influence of aggregate size and volume fraction on shrinkage induced micro-cracking of concrete and mortar. *Cem. Concr. Res.* 2010, 40, 85-93. <https://doi.org/10.1016/j.cemconres.2009.09.012>
- [31] Rao GA. Long-term drying shrinkage of mortar - influence of silica fume and size of fine aggregate. *Cement and Concrete Research* 2001, 31, 171-175. [https://doi.org/10.1016/S0008-8846\(00\)00347-1](https://doi.org/10.1016/S0008-8846(00)00347-1)
- [32] Carrasco, M.; Puertas, F.; Varga, C.; Torres, J.J.; Moreno, E.; Palomo, J.G. Re-use of urban and industrial glass waste to prepare alkaline cements. 2012.
- [33] Puertas F, Torres-Carrasco M. Use of glass waste as an activator in the preparation of alkali-activated slag. Mechanical strength and paste characterisation. *Cement and Concrete Research* 2014, 57, 95-104. <https://doi.org/10.1016/j.cemconres.2013.12.005>

- [34] Martinez-Lopez R, Ivan Escalante-Garcia J. Alkali activated composite binders of waste silica soda lime glass and blast furnace slag: Strength as a function of the composition. *Construction and Building Materials* 2016, 119, 119-129. <https://doi.org/10.1016/j.conbuildmat.2016.05.064>
- [35] Puertas F. Cementos de escorias activadas alcalinamente: Situación actual y perspectivas de futuro. *Mater. Constr.* 1995, 45, 53-64. <https://doi.org/10.3989/mc.1995.v45.i239.553>
- [36] Escalante García JI, Campos-Venegas K, Gorokhovskiy A, Fernández A. Cementitious composites of pulverised fuel ash and blast furnace slag activated by sodium silicate: effect of Na<sub>2</sub>O concentration and modulus. *Advances in Applied Ceramics* 2006, 105, 201-208. <https://doi.org/10.1179/174367606X120151>
- [37] Burciaga-Díaz O, Magallanes-Rivera RX, Escalante-García JI. Alkali-activated slag-metakaolin pastes: strength, structural, and microstructural characterization. *Journal of Sustainable Cement-Based Materials* 2013, 2, 111-127. <https://doi.org/10.1080/21650373.2013.801799>
- [38] Wang SD, Scrivener KL, Pratt PL. Factors affecting the strength of alkali-activated slag. *Cement and Concrete Research* 1994, 24, 1033-1043. [https://doi.org/10.1016/0008-8846\(94\)90026-4](https://doi.org/10.1016/0008-8846(94)90026-4)
- [39] Burciaga-Díaz O, Escalante-García JI. Structure, Mechanisms of Reaction, and Strength of an Alkali-Activated Blast-Furnace Slag. *Journal of the American Ceramic Society* 2013, 96, 3939-3948. <https://doi.org/10.1111/jace.12620>
- [40] Técnica E, De Edificación S. Politécnica, U. Workshop on Environmental Impact of Buildings. 2013.
- [41] Bagheri A, Nazari A. Compressive strength of high strength class C fly ash-based geopolymers with reactive granulated blast furnace slag aggregates designed by Taguchi method. *Materials & Design (1980-2015)* 2014, 54, 483-490. <https://doi.org/10.1016/j.matdes.2013.07.035>
- [42] Nazari A, Riahi S, Bagheri A. Designing water resistant lightweight geopolymers produced from waste materials. *Materials & Design* 2012, 35, 296-302. <https://doi.org/10.1016/j.matdes.2011.09.016>
- [43] Bakharev T, Sanjayan JG, Cheng YB. Effect of admixtures on properties of alkali-activated slag concrete. *Cement and Concrete Research* 2000, 30, 1367-1374. [https://doi.org/10.1016/S0008-8846\(00\)00349-5](https://doi.org/10.1016/S0008-8846(00)00349-5)
- [44] Tho-In T, Sata V, Boonserm K, Chindaprasirt P. Compressive strength and microstructure analysis of geopolymer paste using waste glass powder and fly ash. *Journal of Cleaner Production* 2018, 172, 2892-2898. <https://doi.org/10.1016/j.jclepro.2017.11.125>
- [45] Silva PD, Sagoe-Crenstil K, Sirivivatnanon V. Kinetics of geopolymerization: Role of Al<sub>2</sub>O<sub>3</sub> and SiO<sub>2</sub>. *Cement and Concrete Research* 2007, 37, 512-518. <https://doi.org/10.1016/j.cemconres.2007.01.003>
- [46] Fletcher RA, MacKenzie KJD, Nicholson CL, Shimada S. The composition range of aluminosilicate geopolymers. *Journal of the European Ceramic Society* 2005, 25, 1471-1477. <https://doi.org/10.1016/j.jeurceramsoc.2004.06.001>
- [47] Rattanasak U, Chindaprasirt P, Suwanvitaya P. Development of high volume rice husk ash aluminosilicate composites. *International Journal of Minerals, Metallurgy, and Materials* 2010, 17, 654-659. <https://doi.org/10.1007/s12613-010-0370-0>
- [48] Davidovits J. Geopolymers: Inorganic Polymeric New Materials. *Journal of Thermal Analysis and Calorimetry* 1991, 37, 1633-1656. <https://doi.org/10.1007/BF01912193>
- [49] Chindaprasirt P, Rattanasak U, Vongvoradit P, Jenjirapanya S. Thermal treatment and utilization of Al-rich waste in high calcium fly ash geopolymeric materials. *International Journal of Minerals, Metallurgy, and Materials* 2012, 19, 872-878. <https://doi.org/10.1007/s12613-012-0641-z>

- [50] Temuujin J, van Riessen A, Williams R. Influence of calcium compounds on the mechanical properties of fly ash geopolymer pastes. *Journal of Hazardous Materials* 2009, 167, 82-88. <https://doi.org/10.1016/j.jhazmat.2008.12.121>
- [51] Saha S, Rajasekaran C. Enhancement of the properties of fly ash based geopolymer paste by incorporating ground granulated blast furnace slag. *Construction and Building Materials* 2017, 146, 615-620. <https://doi.org/10.1016/j.conbuildmat.2017.04.139>
- [52] Badanoiu AI, Al Saadi THA, Stoleriu S, Voicu G. Preparation and characterization of foamed geopolymers from waste glass and red mud. *Construction and Building Materials* 2015, 84, 284-293. <https://doi.org/10.1016/j.conbuildmat.2015.03.004>
- [53] Guo Y, Zhang Y, Huang H, Meng K, Hu K, Hu P, Wang X, Zhang Z, Meng X. Novel glass ceramic foams materials based on red mud. *Ceramics International* 2014, 40, 6677-6683. <https://doi.org/10.1016/j.ceramint.2013.11.128>
- [54] Zhang S, Keulen A, Arbi K, Ye G. Waste glass as partial mineral precursor in alkali-activated slag/fly ash system. *Cement and Concrete Research* 2017, 102, 29-40. <https://doi.org/10.1016/j.cemconres.2017.08.012>
- [55] Ravikumar D, Neithalath N. Effects of activator characteristics on the reaction product formation in slag binders activated using alkali silicate powder and NaOH. *Cement and Concrete Composites* 2012, 34, 809-818. <https://doi.org/10.1016/j.cemconcomp.2012.03.006>
- [56] Kutchko BG, Kim AG. Fly ash characterization by SEM-EDS. *Fuel* 2006, 85, 2537-2544. <https://doi.org/10.1016/j.fuel.2006.05.016>
- [57] Dudas MJ, Warren CJ. Submicroscopic model of fly ash particles. *Geoderma* 1987, 40, 101-114. [https://doi.org/10.1016/0016-7061\(87\)90016-4](https://doi.org/10.1016/0016-7061(87)90016-4)
- [58] Yu Z. Microstructure development and transport properties of portland cement-fly ash binary systems, *View of Service Life Predictions*. TU Delft, Delft University of Technology, 2015.
- [59] Peronius N, Sweeting TJ. On the correlation of minimum porosity with particle size distribution. *Powder Technology* 1985, 42, 113-121. [https://doi.org/10.1016/0032-5910\(85\)80043-7](https://doi.org/10.1016/0032-5910(85)80043-7)
- [60] Kastiukas G, Zhou X. Effects of waste glass on alkali-activated tungsten mining waste: composition and mechanical properties. *Materials and Structures* 2017, 50. <https://doi.org/10.1617/s11527-017-1062-2>



Research Article

## High performance fiber reinforced concrete – for repair in spillways of concrete dams

P.N. Ojha<sup>1,a</sup>, Amit Trivedi<sup>1,b</sup>, Brijesh Singh<sup>1,c</sup>, Adarsh Kumar N. S.<sup>1,d</sup>, Vikas Patel<sup>\*1,e</sup>, R.K. Gupta<sup>2,f</sup>

<sup>1</sup>National Council for Cement and Building Materials, India

<sup>2</sup>NHPC Limited, India

### Article Info

#### Article history:

Received 28 Jan 2021

Revised 16 May 2021

Accepted 26 May 2021

#### Keywords:

Fiber reinforced concrete;  
High performance concrete;  
Polypropylene fibers;  
Spillways;  
Concrete dams;  
Abrasion resistance

### Abstract

Hydraulic structures like spillways, glacis, etc. undergoes abrasion-erosion due to impact & cavitation losses due to the flowing water action. To overcome the deterioration of the concrete in such structures, addition of fibers to the concrete can be viable solution as it is known to increase the structural integrity of the concrete. A comparative study of various engineering characteristics using high strength concrete by incorporating steel fibers and micro polypropylene fibers has been carried out. Water/binder ratio of 0.23 has been kept constant for the study. Dosage for steel fibers is kept as 1, 1.25 and 1.5% by volume while for polypropylene fibers were kept as 1, 2 & 3 kg/m<sup>3</sup>. Engineering properties such compressive strength, flexural strength, toughness, energy absorption, splitting tensile strength, drying shrinkage, abrasion resistance, and water and air permeability of high-performance concrete with & without fibers in its fresh & hardened state are investigated in this paper. Based on the study, the steel fibers with 1.5% dosage are found to be more effective in countering the abrasive and repetitive loading which can be more effective in the repairs of spillways and glacis of concrete dams.

© 2021 MIM Research Group. All rights reserved.

## 1. Introduction

The abrasive action of waterborne solid particles such as boulders, debris etc. at high velocity is one of the major issues while design of the hydraulic structures like spillways, glacis etc. Therefore, it is desired to develop a high-performance concrete that can provide high abrasion-erosion & cavitation resistance to sustain the high velocities & impact containing silt and rolling boulders over the hydraulic structures. This in turn will also reduce operation and maintenance cost of the structures.

Liu & Donald [1], Holland [2], Papenfus [3], Galvao, Portella & Kormann [4] reported that abrasion erosion resistance of concrete increases with the increase in compressive strength. Liu & Donald [1], Holland [2], Wu, Yen, Liu & Hsu [5] reported water-to-cement ratio as an important factor and recommended to adopt the lowest practical water-cement ratio where abrasion-erosion is of major concern. Liu & Donald [1], Holland [2], Kryzanowski, Mikos, Sustersic & Planinc [6], Papenfus [3] investigated the abrasion erosion resistance using different types of coarse aggregates in concrete composite. The test results indicate that abrasion erosion resistance of concrete increases with the increase in the hardness of coarse aggregates when the water to-cement ratio and compressive strength are kept constants and concluded that the hardest available

\*Corresponding author: [vikas.patel299@gmail.com](mailto:vikas.patel299@gmail.com)

<sup>a</sup> [orcid.org/0000-0003-1754-4488](http://orcid.org/0000-0003-1754-4488); <sup>b</sup> [orcid.org/0000-0002-2594-4679](http://orcid.org/0000-0002-2594-4679); <sup>c</sup> [orcid.org/0000-0002-6512-1968](http://orcid.org/0000-0002-6512-1968);

<sup>d</sup> [orcid.org/0000-0001-6125-4408](http://orcid.org/0000-0001-6125-4408); <sup>e</sup> [orcid.org/0000-0002-2251-3849](http://orcid.org/0000-0002-2251-3849); <sup>f</sup> [orcid.org/0000-0001-5021-3774](http://orcid.org/0000-0001-5021-3774)

DOI: <http://dx.doi.org/10.17515/resm2021.252ma0128>

Res. Eng. Struct. Mat. Vol. 7 Iss. 4 (2021) 505-522

aggregate should be used in new construction or repair of stilling basins or other hydraulic structures.

Holland [2] & Papenfus [3], ACI 546.R [7] & ACI 210.R [8] Committee reported that the concrete containing silica fume & high range water reducing agent has better abrasion erosion resistance where hard aggregate was not available to develop very high strength concrete. Liu & Donald [1], Holland [2], Papenfus [3], Galvao, Portella & Kormann [4] reported that impregnation of Polymer & Epoxy in concrete mix and Surface treatment with coatings like polyurethane improves abrasion-erosion resistance. Kryzanowski, Mikos, Sustersic & Planinc [6], Galvao, Portella & Kormann [4] investigated and found that the introduction of granular rubber/waste rubber with complementary polymer binder increases the abrasion-erosion resistance of concrete.

It is important to note the difference between erosion caused by impact forces such as cavitation caused by rocks and debris impacting at high velocity and type of erosion that occurs due to wearing action of low velocity particles. Contradictory data are available regarding the performance of SFRC on abrasion-erosion & cavitation. Liu & Donald [1], Holland [2] reported that FRC is less resistant to abrasion-erosion due to smaller particles at lower velocities when compared with concrete without fibers. This is because of the adjustments in the mixture proportions to accommodate the fiber requirement which reduces coarse aggregate content and increases the paste content. As per the ACI 544.4R [9] committee report both laboratory tests and full-scale field trials have shown Steel Fiber Reinforced Concrete (SFRC) has high resistance to cavitation's forces resulting from high-velocity water flow and the damage caused by the impact of large waterborne debris at high velocity.

Lin & Cheng [10] studied the performance of inclusion of steel fibers and silica fume in the concrete composite and found that abrasion resistance of concrete is improved by 8-15%. Hu & Yin [11] studied the impact angle of abrasion and found that steel fibers improve erosion resistance at low impact angle ( $\theta=15$  degree). Stig Ostfjord [12], Papenfus [3] & ACI 544.1R [13] reported that adding fibers in concrete can enhance toughness, moment capacity, tensile strength, stiffness and brittleness of concrete. Stig Ostfjord [12], ACI 544.1R [13], Shah & Jenq [14], Gopalaratnam & Shah [15], Kamal, Kassimi & Ghoddousi [16] concluded that steel fibers can absorb the deformation energy of concrete and reduce the risk of cracking. While designing the abrasion resistant concrete, abrasion resistance alone should not be emphasized rather the abrasion resistance of concrete should be assessed based on different parameters that defines the mechanical properties of concrete. Mechanical properties such as compressive strength, tensile strength, aggregate strength, modulus of elasticity, toughness, impact strength, chemical Admixtures, surface polishing & coatings, curing and other additives (Silica Fume and fibers) must be assessed in order to assess the abrasion-erosion & cavitation resistance [17].

Satish Sharma et.al. [18-19] concluded that the addition of 5% silica fume shows significant improvement in compressive strength, flexural strength, static modulus of elasticity, split tensile strength, drying shrinkage and water permeability. Inclusion of steel fiber increases the abrasion resistance of concrete. The inclusion of silica fume might have enhanced the bond between steel fibers and paste. Bond strength between fibers and paste is another important factor, associated with abrasion resistance. Based on the results, the recycled concrete and recycled fiber concrete with the proposed mix design have a high compressive strength, and due to relatively high porosity of the recycled aggregate concrete, its density has decreased by 2.48% and its water absorption increased by 54% compared to the natural concrete [20].

The exceptional characteristics of high-performance fiber reinforced concrete in comparison to conventional concrete make it a very good choice for long- span bridges and

high-rise buildings (21) and in recent many attempts have been made to characterize the behavior of fiber-reinforced concrete (FRC) both experimentally and numerically in various conditions (22, 23, 24, 25). Various types of fibers such as natural and polymeric, e.g. polypropylene (PP) may be used to enhance the performance of concrete for different applications. The enhancement of different types of fibers on the flexural strengths and toughness is mainly attributed to the fiber crack-bridging and load-carrying capacities wherein the fibers alter the failure pattern and results in the ductile failure of concrete. Specimens with hooked-end fibers show the best flexural performance. An increase in volume fractions of both steel and polypropylene fibers leads to an increase in the compressive, splitting tensile and flexural strengths of concrete (26, 27). The post-peak ductility of concrete is improved and the strength degradation is alleviated with increasing fiber volume fraction and steel fiber aspect ratio (28, 29, 30). In addition, specimens with corrugated and hooked-end fibers exhibit a better failure behavior than specimens with straight fibers, with multiply micro-cracks induced by mechanical interlocks of deformed steel fibers observed at the main cracks (31, 32, 33).

The research program presented herein sets out to test a comprehensive number of HPC specimens with substantially varied parameters to expand the database of test results of the developed HPC. The subsequent objective is to study and quantify the material's post-cracking characteristics of SFRC specimen, to improve or sustain abrasion-erosion & cavitation problems associated with hydraulic structures.

## **2. Experimental Program**

### **2.1. Constitutive Materials**

Following concrete making materials have been used for the investigations on high performance concrete:

- Ordinary Portland Cement (OPC) 53 Grade satisfying to the specification of IS:12269-2013[34] [Table 1]
- Silica Fume (SF) satisfying to the specification of IS:15388-2003[35], [Table 1]
- Fine (Zone-II) & Coarse aggregate (20mm downsize) satisfying to the specifications as per IS: 383-1970[36] [Table 2],
- Potable water
- Polycarboxylic Ether (PCE) based super plasticizer satisfying to the specification of IS:9103[37]
- Fibers: (i) Hooked end steel fibers of 0.55mm diameter with an aspect Ratio of 63 satisfying to the specification of ASTM A 820[38]. The Material test certificate of tensile strength provided by manufacturer is 1468.99N/mm<sup>2</sup> where minimum requirement is 345 N/mm<sup>2</sup> as per ASTM A 820.
- (ii) Micro Polypropylene with properties as given in table 3 were used.

Table 1. Physical, Chemical and Strength Characteristics of Cement

Characteristics	OPC -53 Grade	Silica Fume
Physical Tests:		
Fineness (m <sup>2</sup> /kg)	320.00	22000
Soundness Autoclave (%)	00.05	-
Soundness Le Chatelier (mm)	1.00	-
Setting Time Initial (min.) & (max.)	170.00 & 220.00	-
Specific gravity	3.16	2.24
Chemical Tests:		
Loss of Ignition (LOI) (%)	1.50	1.16
Silica (SiO <sub>2</sub> ) (%)	20.38	95.02
Iron Oxide (Fe <sub>2</sub> O <sub>3</sub> ) (%)	3.96	0.80
Aluminium Oxide (Al <sub>2</sub> O <sub>3</sub> )	4.95	-
Calcium Oxide (CaO) (%)	60.73	-
Magnesium Oxide (MgO) (%)	4.78	-
Sulphate (SO <sub>3</sub> ) (%)	2.07	-
Alkalis (%) Na <sub>2</sub> O & K <sub>2</sub> O	0.57 & 0.59	0.73 & 2.96
Chloride (Cl) (%)	0.04	-
IR (%)	1.20	-
Moisture (%)	-	0.43

Table 2. Properties of Aggregates

Property	Granite		Fine Aggregate
	20 mm	10 mm	
Specific gravity	2.70	2.69	2.64
Water absorption (%)	0.32	0.35	0.72
Sieve Analysis Cumulative Percentage Passing (%)	40 mm	100	100
	20 mm	95	100
	10 mm	7	95
	4.75 mm	0	19
	2.36 mm	0	2
	1.18 mm	0	0
	600 μ	0	0
	300 μ	0	0
	150 μ	0	0
	Pan	0	0

Table 3. Properties of Polypropylene Fiber

Properties	Value
Cut length (mm)	12
Effective diameter (micron)	20-40
Specific gravity	0.90-091
Melting point (°C)	160-165
Elongation (%)	20-60
Alkaline stability	Very good
Young's modulus (MPa)	>4000

## 2.2 Mixture Proportion and Concrete Production

The control concrete was designed & optimized using 10% silica fume by weight of cement as per IS: 10262[39]. Mix proportions for fiber reinforced concrete were optimized using different percentages of steel and polypropylene fibers for the desired slump. Since hooked end steel fibers of 1, 1.25 & 1.5% by concrete volume & micro-Polypropylene fiber dose of 1 kg/m<sup>3</sup>, 2 kg/m<sup>3</sup> & 3kg/m<sup>3</sup> was adopted for the study, some adjustments were done in the mix proportions to maintain the required slump. The dose of PCE based superplasticizer is adjusted and the ratio of fine to coarse aggregate is adjusted accordingly. Concrete mix proportions are shown in Table 4.

For conducting studies, the concrete mixes were prepared in pan type concrete mixer. Before use, the moulds were properly painted with mineral oil, casting was done in three different layers and each layer was compacted on vibration table to minimize air bubbles and voids. After 24 hours, the specimens were demoulded from their respective moulds. The laboratory conditions of temperature and relative humidity were monitored during the different ages at 27±2oC and relative humidity 65% or more. The specimens were taken out from the tank and allowed for surface drying and then tested in saturated surface dried condition.

Table 4. Concrete Mix of Control and Fiber Reinforced Concrete

Type of concrete	Designation	Water (kg/m <sup>3</sup> )	OPC (kg/m <sup>3</sup> )	SF (kg/m <sup>3</sup> )	HRWRA (kg/m <sup>3</sup> )	CA (kg/m <sup>3</sup> )	FA (kg/m <sup>3</sup> )	Fibers (kg/m <sup>3</sup> )
Control	CM	131.1	570	64	9.51	1093.0	625.0	0.00
SFRC 1%	S1	131.1	570	64	10.30	1132.2	693.8	78.50
SFRC 1.25 %	S2	131.1	570	64	11.10	1126.6	693.8	98.13
SFRC 1.5%	S3	131.1	570	64	11.89	1126.6	699.5	117.75
PFRC 1kg/m <sup>3</sup>	P1	131.1	570	64	9.51	1093.0	630.7	1.00
PFRC 2kg/m <sup>3</sup>	P2	131.1	570	64	10.30	1160.3	619.3	2.00
PFRC 3kg/m <sup>3</sup>	P3	131.1	570	64	11.10	1160.3	619.3	3.00

\*OPC= Ordinary Portland Cement, SF=Silica fume, CA=Coarse Aggregate, FA=fine Aggregate, HRWRA=High Range Water Reducing Agent/Admixtures, SFRC=Steel fiber reinforced concrete & PFRC= Polypropylene fiber reinforced concrete

The laboratory conditions were maintained as per Indian Standard during casting, placing & testing of concrete specimen i.e.  $27\pm 2^{\circ}\text{C}$  and  $65\pm 5$  RH. The slump, measured as per IS: 1199 [40] of control concrete was 150mm. It was observed that the slump value decreases with the introduction of fibers into the mixture which affects the workability of the concrete. To maintain the required workability slump of 130-150 mm, dose of PCE based HRWRA is adjusted and more fines are added to mix.

The air content of mixes was measured as per ASTM C 231 [41] (pressure method) and it was found that it increases with introduction of steel fibers by 30 to 50%. The wet density of CM and PFRC was around  $2542\text{kg/m}^3$  while slightly more density was observed for SFRC mix i.e.,  $2560\text{kg/m}^3$ . The setting times (both initial and final) of all mixes were determined as per IS:8142 [42] and were found to be fairly similar i.e., 7.5 hours & 9.2 hours respectively.

### **3. Test Setup**

#### **3.1. Mechanical Parameters: Compressive Strength, Flexural Strength and Splitting Tensile Strength**

The compressive and flexural strength tests were carried out at 3, 7 and 28 day's age on cubes (150 mm) and beams ( $100 \times 100 \times 500$  mm) respectively. The test procedure followed during the tests was in conformity with IS: 516 [43] for compressive strength test and ASTM C1609 [44] for flexure strength test. Splitting tensile strength test was carried out at 3, 7 and 28 day's age on cylinder specimen (150 mm diameter & 300 mm length) as per in IS: 5816 [45]. Drying Shrinkage test was carried out on prism ( $75 \times 75 \times 300$  mm) at 28 day's age as per IS: 1199 [40].

#### **3.2. Flexure Toughness Test**

The flexure test apparatus consisting of a three-point bending with pin and roller type supports was used. The specimen size was  $100 \times 100 \times 500$  mm with clear span of 400 mm. Test was carried out as per the provisions of ASTM C 1609 [27]. Test was carried out in displacement control mode in a servo controlled closed-loop system with a bending yoke where Linear Variable Displacement Transducers (LVDT) were mounted on the sides of the yoke around the specimen. These LVDT's were connected to display unit to measure the net deflection at the center of the beam. Experimental setup is shown in Fig. 1. The test facility is specifically developed to study the post cracking behavior of fiber reinforced concrete and measure the flexural toughness of the test specimen.



Fig. 1 Experimental flexure toughness test setup as per ASTM C 1609[27].

### 3.3 Abrasion Resistance Test (Under Water Method) as per ASTM C1138

The abrasion test (under water method) was carried out at 28 days on a concrete specimen with dimensions of 300 mm diameter and 100 mm thickness as per the procedure given in ASTM C-1138. The test set up and specimen of abrasion test (under water method) is shown in Fig. 2.

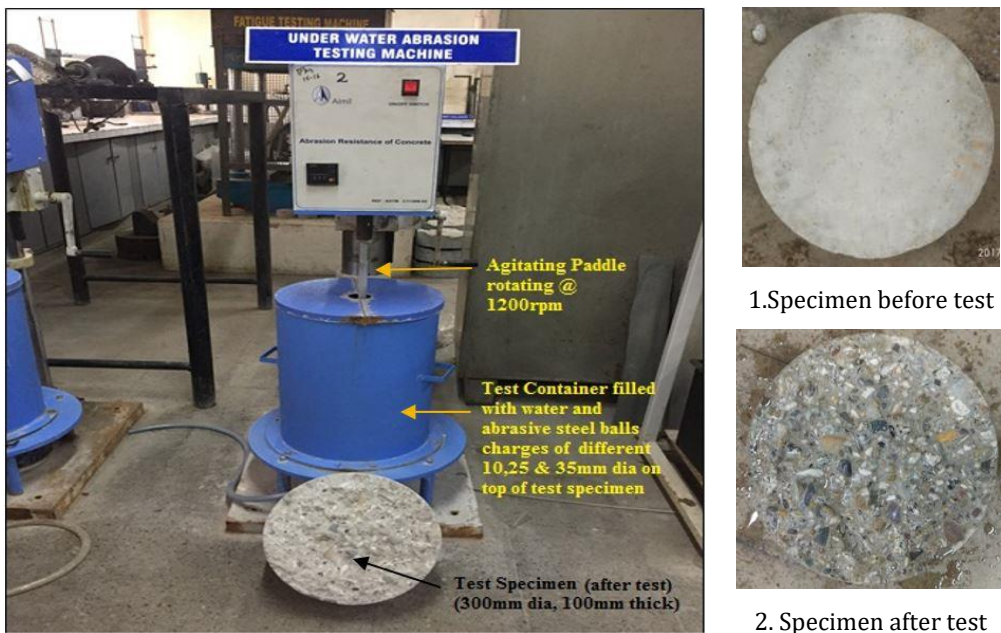


Fig. 2 Abrasion test (Under water method) setup as per ASTM C 1138

The initial mass of the concrete specimen (Diameter  $300\pm 2$  mm & Height  $100\pm 13$  mm) were recorded in air & in water, then the specimen was kept in test container with surface

to be tested facing up on the seating blocks. The agitation paddle was placed such that the bottom of paddle was  $38 \pm 5$  mm above the surface of specimen. The abrasive charges (Steel balls) were placed on the surface of specimen and water was added upto  $165 \pm 5$  mm above surface of specimen. Then the agitating paddle was rotated at the rate of  $1200 \pm 100$  rpm. The specimen was removed from test container at the end of every 12-hours of operation and the abraded material was flushed off & surface of specimen was dried off. The mass of specimen was recorded again in air & water. The test was repeated for six times of 12-hours periods for a total of 72 hours and final mass loss was recorded.

### 3.4 Abrasion Resistance Test (Revolving Disk Method) as per ASTM C 779

The abrasion test was carried out at accelerated 28 days on a concrete slab of size  $300 \times 300$  mm with 100 mm thickness as per the procedure given in ASTM C-779 (46). The test set up and specimen of abrasion test (revolving disk method) is shown in Fig. 3.

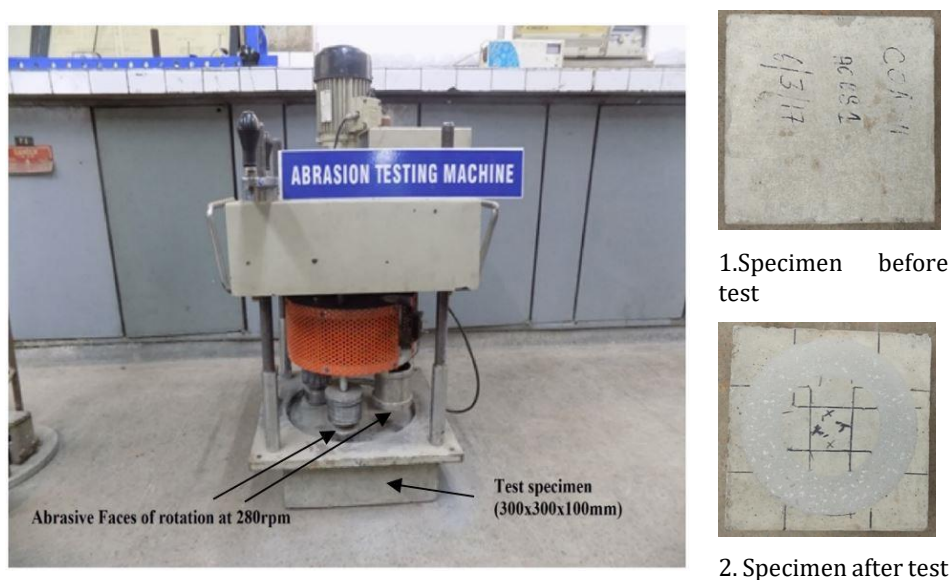


Fig. 3 Abrasion Test (Revolving Disk Method) Setup as per ASTM C 779

### 3.5 Water and Air Permeability

Water permeability test was carried out at the age of 28 day's age on concrete cylinder (150 mm diameter & 150 mm height) as per DIN-1048[47] and Air permeability test at 28 days was carried out on slabs ( $300 \times 300 \times 100$  mm) using Torrent Permeability tester.

## 4. Result and Discussion

### 4.1. Mechanical Parameters: Compressive Strength, Flexural Strength & Splitting Tensile Strength

#### 4.1.1. Compressive Strength

The result of compressive strength at 3, 7 & 28 days of control & fiber reinforced concrete is shown in Fig. 4. Test result indicates that the compressive strength of control concrete and micro polypropylene fiber reinforced concrete specimens are fairly similar. There is a substantial increase in the compressive strength of steel fiber reinforced concrete as

compared to control concrete. The compressive strength of the steel fiber-reinforced concrete is maximum at 1.25 & 1.5% steel fibers with 12 & 14% increment respectively.

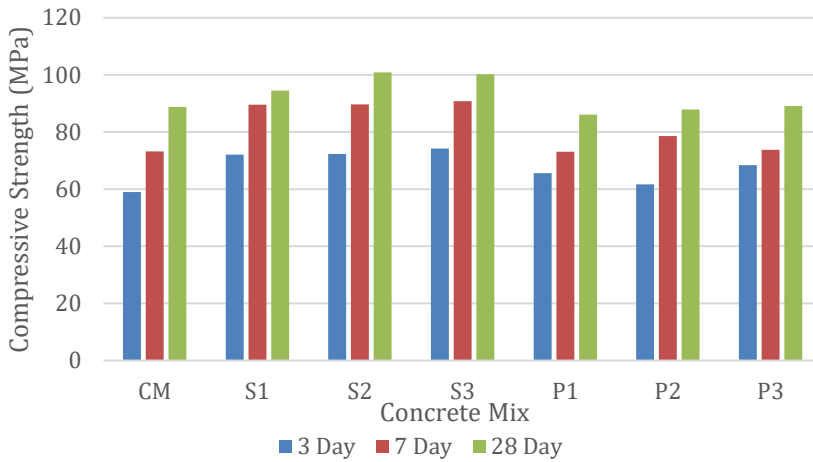


Fig. 4 Compressive Strength at 3, 7 and 28 Days

The significant increase in compressive strength of the concrete with steel fibers is a result of increased concrete integrity wherein steel fibers randomly distributed in concrete matrix binds the composites together and restricts the disintegration upon loading to peak stress.

#### 4.1.2. Flexural Strength

Flexural strength at 3, 7 & 28 days of the mixes (CM, SFRC & PFRC) covered in the study is shown in Fig. 5. From test results it is observed that there is an increase in the flexural strength with the introduction of fibers into the mix. For micro polypropylene fibers reinforced concrete the increments are in the range of 7% to 18% and for steel fiber reinforced concrete it varies from 20% to 42%.

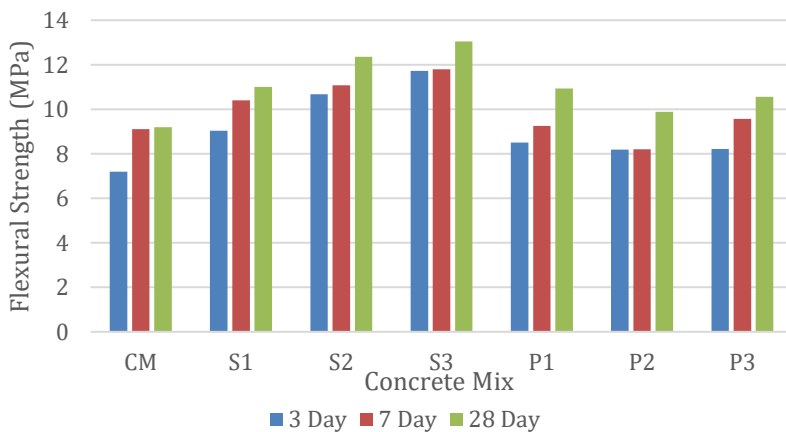


Fig. 5 Flexural Strength at 3, 7 and 28 Days

The increase in the flexural strength of the concrete can be attributed to the bridging action of fibers which acts as a tensile reinforcement and subsequently increases the flexural capacity of the beam. Fibers addresses the tensile strength by two mechanisms wherein first mechanism it reduces the crack propagation by bridging action while in second mechanism it delays the crack initiation by contribution to the loading before initiation of cracks at surface.

#### 4.1.3. Splitting Tensile Strength

Splitting tensile strength at 3, 7 & 28 days of control & fiber reinforced concrete is shown in Fig. 6. Test results indicate that the tensile strength of control and micro polypropylene fiber reinforced concrete specimens are almost similar. In case of SFRC, there is a substantial increase in the tensile strength compared to control by about 40% to 75%. Uniformly distributed Fibers acts as a tensile reinforcement due which this significant increase in splitting tensile strength can be seen. A part of initial load is taken by the steel fibers and full load is transferred to the concrete once the fibers fails by pull out or break out of the fibers from the concrete matrix.

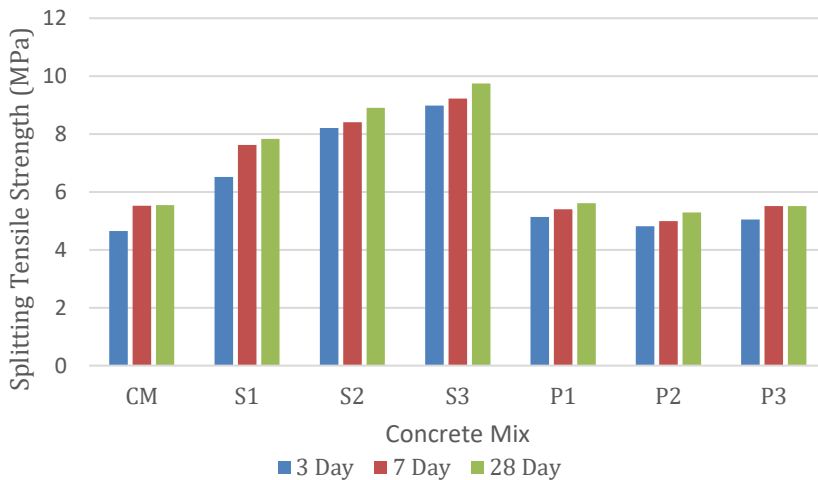


Fig. 6 Splitting Tensile Strength at 3, 7 and 28 Days

#### 4.1.4. Load – Deflection Behavior

Based on test results of SFRC segments (S1, S2 & S3) as shown in Fig. 7 and Fig. 8, addition of steel fibers into the mix result in ductile response in load deflection curve. The load-deflection response of fibre reinforced concrete generally starts by an initial portion that is linearly elastic up to a certain load and then deviates from its linearity. This is often identified as the onset of first cracking in the matrix. If the cement matrix is not reinforced with fibers, first cracking is followed by a sudden drop in the load-deflection curve, and failure occurs which is observed in case of control concrete. The addition of steel fibers mostly influences the response of the concrete mixture after the onset of initial cracks by the bridging action. These fibers reduce the crack propagation by addressing the tensile loads and acts as a tensile reinforcement which results in the ductile failure while the control concrete being brittle in nature undergoes sudden failure.

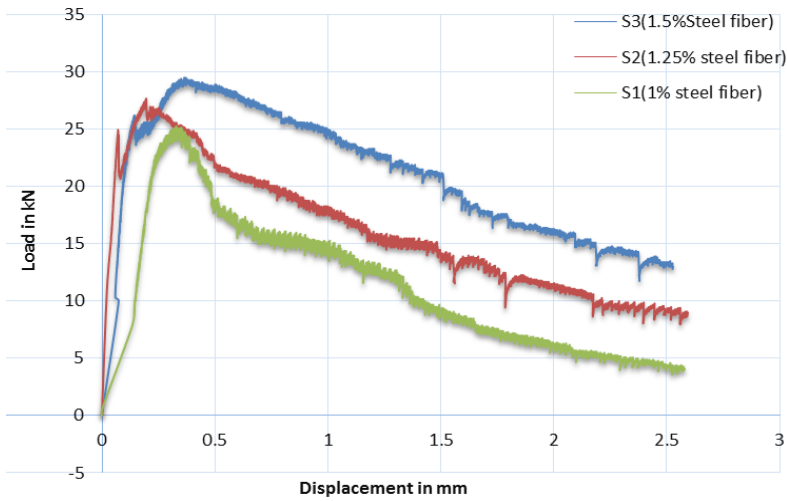


Fig. 7 Load - Displacement Curves of SFRC (S1, S2 & S3) Specimen at 7 Day

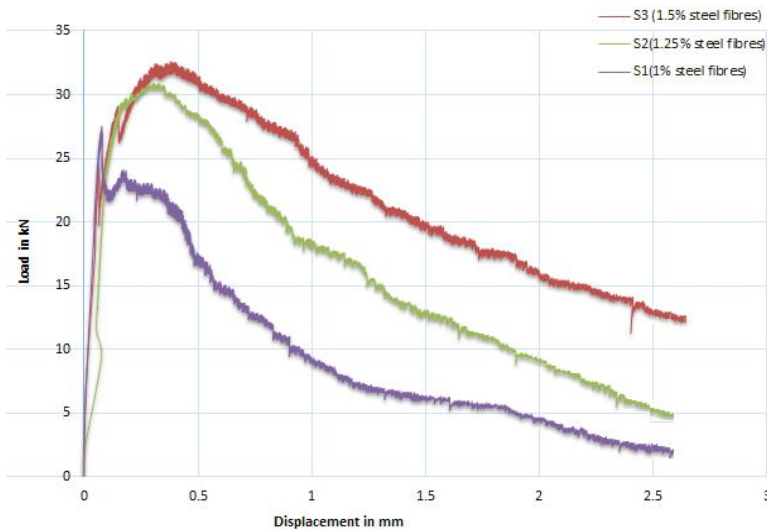


Fig. 8 Load - Displacement Curves of SFRC (S1, S2 & S3) Specimen at 28 Day

#### 4.1.5. Mode of Failure

Steel fibers in concrete allows the bridging of cracks, which aids in increasing the ductility of the concrete after the post cracking stage. The crack behaviour of S1, S2 & S3 also shows different pattern. S1 shows single crack whereas S2 & S3 shows multiples cracks, this maybe because, if the fibre content in the mix is more, it is possible that the load-bearing capacity of the fibers is greater than the load on the composite at the first crack. Additional loading will result in additional cracks, until the matrix is divided into a number of segments separated by cracks. The cracking may stop when the stress transferred to the matrix no longer exceeds the cracking load. For all practical purposes, the load-deflection response of fibre reinforced cement composites can be classified as either "strain-

softening" or "strain-hardening. As per Naaman [31], High performance fiber reinforced cement composites are a class of FRC composites characterized by a strain hardening behavior in tension after first cracking, accompanied by multiple cracking up to relatively high strain levels.

From load-deflection curve of SFRC at 28 days S1 shows strain softening, the load carrying capacity decreases gradually after the onset of first crack load of 27.5 kN, whereas S2 & S3 show strain hardening i.e. even after the onset of first cracks load at 28.3kN & 29.4kN the segment load carrying capacity increases till it reaches ultimate crack load at 30.8kN & 32.3 kN respectively which is tabulated in Table 5.

The area under load- deflection curve from 0 to L/150 (here L=400 mm) is the flexural toughness which is the apparent amount of energy absorbed by the specimen. The toughness of Steel Fibre Reinforced Concrete analyzed as per ASTM C 1609[25] from the load – deflection curve at 28days strength are 27, 43 & 59 Joules respectively for S1, S2 & S3 mix.

Table 5. Summary of Parameters Obtained from Load-Deflection Curve Of SFRC Specimen as per ASTM C 1609<sup>[28]</sup> at 28 Days

Parameters	HS-SFRC		
	S1	S2	S3
Fist peak Load in kN	27.5	28.3	29.4
Peak load in kN	-	30.8	32.3
Fist Peak Strength in MPa	11.0	11.32	11.76
Peak Strength in MPa	-	12.32	12.92
Residual load at net deflection of L/600 in kN	13.8	24.7	29.5
Residual strength at net deflection of L/600 in MPa	5.52	9.88	11.80
Residual load at net deflection of L/150 in kN	3.20	7.20	12.6
Residual strength at net deflection of L/150 in MPa	1.28	2.88	5.04
Area Under the load vs net deflection curve 0 to L/150 in Joules	27.0	43	59

Strength is calculated as  $PL/bd^2$ , where P=load in kN at corresponding displacement. L=length of specimen in mm, b= width of specimen in mm and d =depth of specimen in mm.

## 4.2. Durability Parameters: Drying Shrinkage, Abrasion, Water and Air Permeability

### 4.2.1. Drying Shrinkage

The result of drying shrinkage of control & fiber reinforced concrete is shown in Fig. 9. From the figure, a reduction in drying shrinkage can be observed of 20% to 37% in PFRC as compared to the control while in case of SFRC reduction of 8 to 29% is observed. Fibers incorporated in concrete are known to control cracking arising from drying and/or plastic shrinkage behaviour in the cementitious matrix. The mitigation of drying shrinkage aids the concrete aesthetically and also by controlling and preventing shrinkage cracks the durability of concrete can be enhanced.

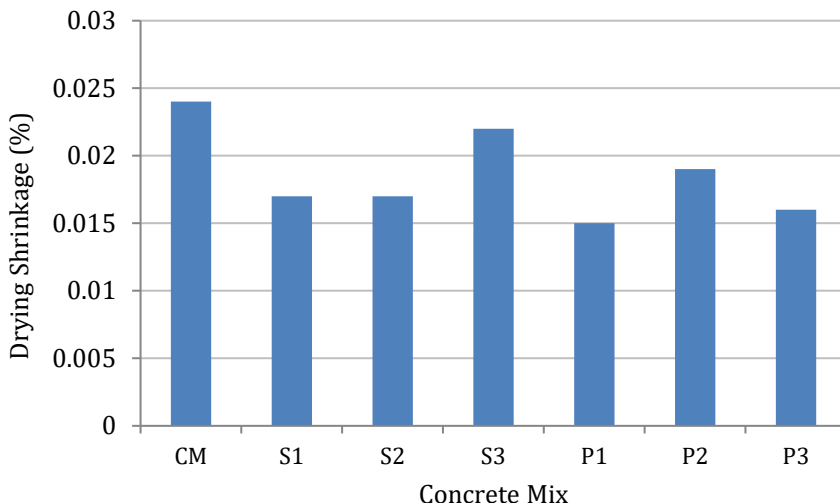


Fig. 9 Drying Shrinkage at 28 Day

4.2.2. Abrasion Resistance Test (Under Water Method) as per ASTM C1138

From the test result (Fig. 10), the 28 days age cumulative abrasion volume loss in m<sup>3</sup> for control mix is  $110 \times 10^{-6}$  m<sup>3</sup> and for Steel fiber reinforced concrete mix of 1 % to 1.5% of steel fibers by volume varies from  $102 \times 10^{-6}$  to  $120 \times 10^{-6}$  m<sup>3</sup> while for concrete mix with polypropylene fibers volume loss varies from  $111 \times 10^{-6}$  to  $109 \times 10^{-6}$  m<sup>3</sup>.

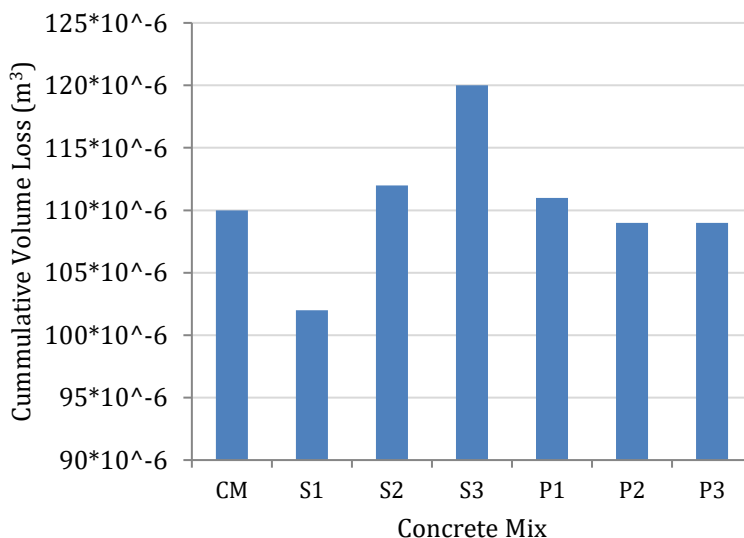


Fig. 10 Abrasion Resistance Test (Under Water Method)

This test result shows varying abrasion loss when steel fibers are introduced into the mix, more abrasion volume loss is observed as compared to control mix. This is primarily due

to abrasion of mortar part of concrete as in SFRC, adjustments were made in the mix proportions to accommodate steel fibers which reduces coarse aggregate content and increases the paste content. It was observed that the coarse aggregates in concrete were not getting abraded in this test.

#### 4.2.3. Abrasion Resistance Test (Revolving Disk Method) as per ASTM C 779

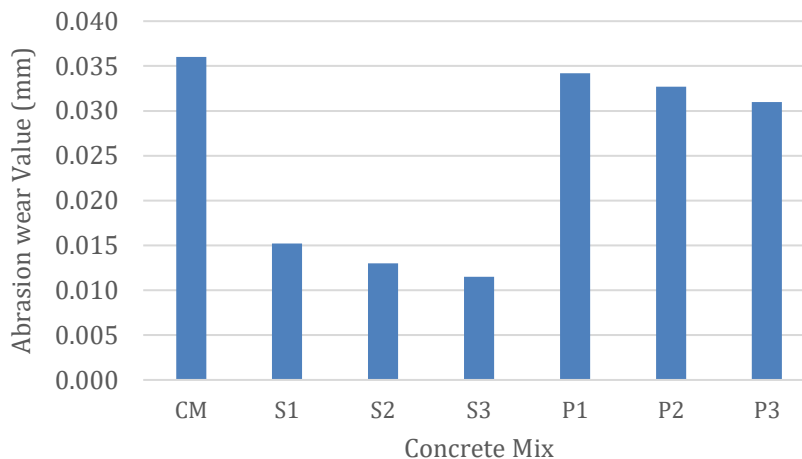


Fig. 11 Abrasion Wear Value at 28 Day

From Fig. 11, the inclusion of fibers produced an improvement in the abrasion resistance of the concrete. In this study, it was found that the most significant improvement was achieved with the optimum inclusion of steel fibers at 1.5 % by volume, it can be also seen that abrasion wear decreases with increase in fibers percentage. The reduction in abrasion wear value of SFRC to that of control concrete is 58 to 68% & 5% to 13.89% for PFRC.

Considering the test results of both methods of abrasion resistance tests, SFRC can be a viable solution for repairs and construction specific elements critical to erosive or abrasive action in hydraulic structures. By increasing the integrity of the concrete, steel fibers hold the composites together and reduces the disintegration of aggregates and thus addresses the problem of cavitation and erosion of concrete constituents.

#### 4.2.4. Water Permeability

Concrete Samples were cast and tested for water permeability after 28 days of water curing. Results of the test from Fig. 12 indicates significant decrease in the permeability of concrete with the addition of steel fibers. Test result shows that in SFRC specimen water penetration is almost negligible as the reduction of water penetration percentages vary from 61% to 99%. This is most likely due to the stitching and multiple cracking effect of the steel fibers. Steel fibers seems more effective as compared to polypropylene fibers as per the experimental results.

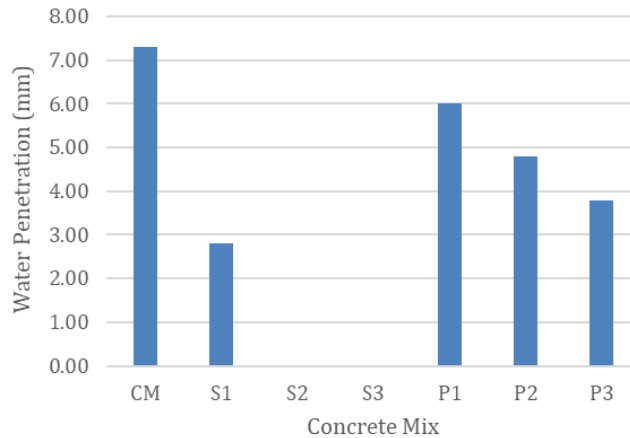


Fig. 12 Water Penetration at 28 Day

#### 4.2.5. Air Permeability

From Fig. 13 it is observed that the air permeability coefficient ( $kT-16m^2$ ) value of SFRC specimens are less than that of control concrete by 80% to 91% and while in case of PFRC specimens values are 14 to 76% less than the control. The result indicates the quality of concrete as good. The permeability coefficient decreases with increase in steel fibers percentage by volume in the mix.

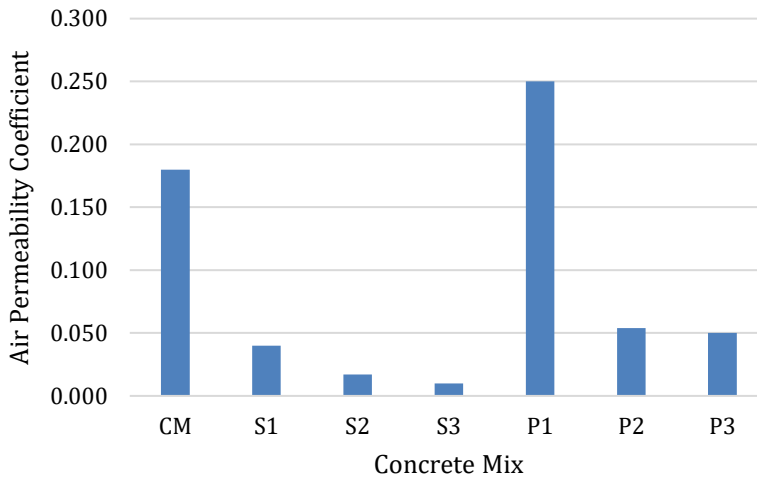


Fig. 13 Air Permeability Coefficient at 28 Day

The reduction in air and water permeability of the SFRC reduces the ingress of chlorides, sulphates, etc. from the constant contact of water. Further, this reduction in permeability can be attributed to the reduced number and depth/width of the micro cracks on the surface of concrete due to incorporation of steel fibers. Bridging action of steel fibers plays an important role in increasing the overall integrity of the concrete.

## **5. Conclusion**

The addition of different fibers affects the different properties and steel fibers have been proven more efficient in addressing the abrasion and erosion in the hydraulic structures. Following conclusions can be drawn with respect to the properties studied:

- High Strength Steel Fiber Reinforced Concrete incorporating 1, 1.25 & 1.5% steel fibers have improved mechanical & durability properties substantially as compared to Control & Polypropylene Fiber Reinforced Concrete of same water to binder ratio. Addition of polypropylene fibers will not be a viable solution wherein abrasive and repetitive loading is applicable.
- Among the three HS-SFRC mix selected for evaluation, the mix with 1.5% steel fibers shows maximum strain hardening behavior in the load deflection curve indicating that the specimen can absorb more energy, comparatively.
- The Toughness or energy absorption & residual strength of HS-SFRC with 1.5% steel fiber content is highest compared to HS-SFRC with 1% & 1.25% steel fibers. Therefore, HS-SFRC with 1.5 % steel fiber can sustain higher impact at higher velocities and will result in lesser deterioration of concrete by flowing water containing large debris, boulders, etc.
- This test result for abrasion resistance test (Under water method) shows varying abrasion loss when steel fibers are introduced into the mix, more abrasion volume loss is observed as compared to control mix. The test results for abrasion resistance test (Revolving Disk method) shows the reduction in abrasion wear value of SFRC compared to that of control concrete in the range of 58 to 68%. Therefore, considering both the results of both tests use of steel fibers will be more efficient and effective against the abrasive action water in hydraulic structures.
- Air and water permeability has been substantially reduced upon addition of steel fibers which will increase the resistance to ingress of chlorides, sulphates and other ions and will enhance the durability of the concrete.
- With the overall improvement in engineering characteristics as reported in this paper, the optimized mix incorporating 1.5% steel fibers is found suitable for application in spillways where cavitation due to impact is of major concern & 1.25% to 1.5% for abrasion-erosion in glacis.

## **6. Acknowledgement**

The Research work presented in this paper was sponsored by NHPC Limited (LoA No: NH/R&D/MOU/366/174, dated 5th December 2013). The authors are thankful to Mr. S P S Kundla and Mrs. Renu Badrasen from NHPC Limited, India for their technical support in this research work.

## **References**

- [1] Tony C, Liu James E, Mc Donald. Abrasion-erosion resistance of fibre reinforced concrete, Structural laboratory U S Army Engineer Waterways, 1981.
- [2] Terrence CH. Abrasion-erosion Evaluation of concrete Mixtures for stilling basin Repairs Kinzua Dam, Pennsylvania, Structural laboratory U S Army Engineer Waterways, 1983.
- [3] Papenfus N. Applying concrete technology to abrasion Resistance. Proceedings of 7th International Conference on Concrete Block Paving, Sun City, South Africa, October 2003.

- [4] Galvao JCA, Portella KF, Kormann ACM. Abrasive effects observed in concrete hydraulic surfaces of dams and application of repair materials, Federal Technological University of Parana, Brazil, March, 2012.
- [5] Wu CH, Yen T, Liu YW, Hsu TH. The Abrasion erosion resistance of Concrete Containing Blast Furnace Slag, Taiwan Power Company Report, 1994.
- [6] Kryzanowski A, Mikos M, Sustersistic J, Plannic I. Abrasion resistance of concrete in hydraulic structures, *ACI Materials Journal*, 2009; 106:4, 349-356. <https://doi.org/10.14359/56655>
- [7] ACI Committee 546.R-2004. Concrete Repair Guide, 2004.
- [8] ACI Committee 210R-1993. Erosion of Concrete in Hydraulic Structures, 1993.
- [9] ACI Committee 544.4R-1988. Design consideration for steel Fibre Reinforced Concrete,
- [10] Lin WT, Cheng An. Abrasion resistance of cement-based composites, 2012. <https://doi.org/10.5772/34798>
- [11] Hu XG, Momber AW, Yin YG. Hydro-abrasive erosion of steel-fibre reinforced hydraulic concrete, Institute of Tribology, Hefei University of Technology, Hefei, China, WOMA Apparatebau GmbH Duisburg, Germany, 2002. [https://doi.org/10.1016/S0043-1648\(02\)00215-6](https://doi.org/10.1016/S0043-1648(02)00215-6)
- [12] Stig O. Lack of practicable Standards & test methods restrict the development of Steel fibre Shotcrete, Steel fibre concrete US-Sweden joint seminar (NSF-STU) Stockholm, Sweden, June, 1985.
- [13] ACI Committee 544.1R-1996. State-of-the-Art Report on Fiber Reinforced Concrete.
- [14] Shah SP, Jeng YS. Fracture Resistance of Steel Fiber Reinforced Concrete, Steel fibre concrete US-Sweden joint seminar (NSF-STU) Stockholm, Sweden, June, 1985.
- [15] Gopalaratnam VS, Shah SP. Strength, Deformation & Fracture Toughness of fiber cement composite at different rates of flexural loading” Steel fibre concrete US-Sweden joint seminar (NSF-STU) Stockholm, Sweden, June, 1985.
- [16] Khayat KH, Kassimi F, Ghoddousi P. Mixture design and testing of fiber-reinforced Self Consolidating concrete. *ACI materials journals*, 2014, 111(2), 143-151. <https://doi.org/10.14359/51686722>
- [17] Naaman AE. Engineered Steel fibers with optimal properties for reinforcement of cement Composite-Advanced concrete technology, Japan Concrete Institute, Japan, November, 2003, 1 (3), 241-252. <https://doi.org/10.3151/jact.1.241>
- [18] Sharma S, Kumar S, Daniel YN, Arora VV. Improvement in abrasion resistance & other engineering characteristics of Concrete using Low Grade Coarse Aggregates Using Silica Fume & Steel Fiber, Proceedings of the NCB seminar on Durability and service life design of Concrete Structure, New Delhi, India, April, 2017.
- [19] Sharma S, Arora V, Kumar S, Daniel Y N, Sharma A. Durability study of high strength steel fiber reinforced concrete, *ACI material Journal*, 2018,115 (2), 219-225. <https://doi.org/10.14359/51701122>
- [20] Salimbahrami SR, Shakeri R. Experimental investigation and comparative machine-learning prediction of compressive strength of recycled aggregate concrete. *Soft Computing*, January, 2021. <https://doi.org/10.1007/s00500-021-05571-1>
- [21] Swamy, RN. High-strength concrete-material properties and structural behavior, Spec. Publications, 1985, 87, 119-146.
- [22] Aslani F, Nejadi S, Samali B. Long-term flexural cracking control of reinforced self-compacting concrete one way slabs with and without fibres, *Comput. Concrete*, (2014a), 14(4), 419-443. <https://doi.org/10.12989/cac.2014.14.4.419>
- [23] Aslani F, Nejadi S, Samali B. Short term bond shear stress and cracking control of reinforced self-compacting concrete one way slabs under flexural loading, (2014b), *Comput. Concrete*, 13(6), 709-737. <https://doi.org/10.12989/cac.2014.13.6.709>
- [24] Kandekar SB, Talikoti R S. Torsional behaviour of reinforced concrete beams retrofitted with aramid fiber, *Advances in concrete construction*, 2020, 9 (1), 1-7. <https://doi.org/10.3390/fib7020011>

- [25] Raj SD, Ganesan N, Abraham, R. Role of fibers on the performance of geopolymer concrete exterior beam column joints, *Advances in concrete construction*, 2020, 115-123.
- [26] Mansouri I, Shahheidari F S, Hashemi, SMA, Farzampour, A. Investigation of steel fiber effects on concrete abrasion resistance, *Adv. Concrete Constr.*, 2020, 9(4), 367-374.
- [26] Li B, Chi Y, Xu L, Shi Y, Li, C. Experimental investigation on the flexural behavior of steel-polypropylene hybrid fiber reinforced concrete, *Constr. Build. Mater.*, 2018, 191, 80-94. <https://doi.org/10.1016/j.conbuildmat.2018.09.202>
- [28] Sharma R, Bansal PP. Efficacy of supplementary cementitious material and hybrid fiber to develop the ultra-high performance hybrid fiber reinforced concrete, *Adv. Concrete Constr.*, 2019, 8(1), 21-31.
- [29] Ojha PN, Singh B, Singh A, Patel V, Arora VV. Experimental study on creep and shrinkage behavior of high strength concrete for application in high rise buildings, *Indian Concrete Journal*, 2021; 95 (2), 30-42.
- [30] Arora V V, Singh B, Jain S. Effect of indigenous aggregate type on mechanical properties of high strength concrete, *Indian Concrete Journal*, 2017, 91 (1), 34-44.
- [31] Arora VV, Singh B, Jain S. Experimental studies on short term mechanical properties of high strength concrete. *Indian Concrete Journal*, 2016, 90 (10), 65-75.
- [32] Singh B, Arora VV, Patel V. Study on stress strain characteristics of high strength concrete". *Indian Concrete Journal*, 2018, 92 (6), 37-43.
- [33] Arora VV, Singh B, Patel V, Daniel YN, Mohapatra BN. Stress-Strain Behaviour and Performance Evaluation of High Strength Steel Fibre Reinforced Concrete, 2019, 93 (12).
- [34] IS: 12269-1987. Specification for 53Grade Ordinary Portland Cement, Bureau of Indian Standard, New Delhi, India.
- [35] IS: 15388-2003. Silica Fume Specification, Bureau of Indian Standard, New Delhi, India.
- [36] IS: 383-1970. Specifications for coarse and fine aggregates from natural sources for concrete, Bureau of Indian Standards, New Delhi, India.
- [37] IS: 9103-1999. Concrete admixture specification", Bureau of Indian Standards, New Delhi, India.
- [38] ASTM A-820-2016. Standard specification for steel fibre reinforced concrete, Annual Books of ASTM Standards.
- [39] IS: 10262-1982. Recommended guidelines for Concrete Mix Design, Bureau of Indian Standards, New Delhi, India .
- [40] IS: 1199-1959, Methods of Sampling and Analysis of Concrete, Bureau of Indian Standards, New Delhi, India.
- [41] ASTM C 231-2010. Standard Test Method for Air Content of Freshly Mixed Concrete by the Pressure Method, Annual Books of ASTM Standards.
- [42] IS: 8142-1976. Method of Test for Determining Setting Time of Concrete by Penetration Resistance, Bureau of Indian Standards, New Delhi, India.
- [43] IS: 516-1959. Methods of Tests for Strength of Concrete, Bureau of Indian Standards, New Delhi, India.
- [44] ASTM C-1609-2012. Flexural Performance of Fiber-Reinforced Concrete (Using Beam with Third Point Loading), Annual Book of ASTM Standards.
- [45] IS: 5816-1999. Splitting Tensile Strength of Concrete Method of Test, Bureau of Indian Standards, New Delhi, India.
- [46] ASTM C 779-2019. Standard Test Method for Abrasion Resistance of Horizontal Concrete Surfaces, Annual Book of ASTM Standards.
- [47] DIN 1048 (part5). Testing of Hardened Concrete (Specimens Prepared in the Mould), June, 1991.



Research Article

## Dynamic and buckling of functionally graded beams based on a homogenization theory

Giovanni Falsone<sup>a</sup>, Gabriele La Valle<sup>\*,b</sup>

*Department of Engineering, University of Messina, Italy.*

### Article Info

### Abstract

#### Article history:

Received 16 Feb 2021

Revised 11 May 2021

Accepted 14 May 2021

#### Keywords:

*Functionally graded beams;*

*Free vibration;*

*Buckling load;*

*Beam theory;*

*Finite element*

*approach*

In this work, the free vibration and the stability problems of functionally graded beams are analysed via the Timoshenko theory through the Navier procedure and via an appropriated finite element (FE) approach. In particular, it is shown how the definition of homogenized/generalized displacements allows to uncouple boundary conditions, obtaining a remarkable advantage in terms of computational effort. Moreover, a unified expression capable to express the buckling load for different constrain conditions is discovered. The latter may be considered the natural extension of the Euler's one derived in the century XVIII. In order to verify the reliability of the proposed method, natural frequencies, buckling loads and static displacements of differently constrained beams are numerically evaluated.

© 2021 MIM Research Group. All rights reserved.

## 1. Introduction

Since the beginning of the actual century, there has been a considerable interest in the study of functionally graded materials (FGMs) due to their ability to satisfy the increasing demands in modern technologies. This class of composites is formed by varying percentage content of materials in any desired direction and, consequently, it owns properties that vary gradually with respect to the spatial coordinates. Compared with the traditional laminated composite materials, the FGMs have no interfaces of material property, so that the phenomena of stress concentration can be reduced greatly. The literature on the topic shows several studies on the structures in both the civil and mechanical engineering. Among these papers, for example, a three dimensional solution for the problem of transversely loaded, all around clamped, rectangular plates, within the linear, small deformation theory of elasticity, is presented by Elishakoff & Gentilini [1]. Theoretical and numerical formulations based on the third-order deformation plate are developed by Reddy [2]. Huang & Shen [3] treat the nonlinear vibration and dynamic response of FGM plates, taking into account conduction and temperature-dependent material properties. Referring to the modelling of functionally graded beams (FGBs), Reddy [4] applies couple stress theories, introduced by Eringen [5] and developed by Yang et al. [6], to describe micro-mono-dimensional structures. Most of the work mentioned have considered variation of the material properties in the thickness direction. A relatively small number of researchers consider the variation of the material properties along the axial direction [7],[8]. Moreover, Zhu & Sankar [9] consider the Euler beam theory in the special case of Young modulus varying following a polynomial law in the thickness direction. Although the presence of papers showing the application of new formulations, only a small number

\*Corresponding author: [gabrielelavallo@gmail.com](mailto:gabrielelavallo@gmail.com)

<sup>a</sup> orcid.org/0000-0003-2668-5100; <sup>b</sup> orcid.org/0000-0003-0664-8740

DOI: <http://dx.doi.org/10.17515/resm2021.259st0216>

Res. Eng. Struct. Mat. Vol. 7 Iss. 4 (2021) 523-538

of them aims to simplify the solution procedures for the FGBs under the Euler-Bernoulli and Timoshenko hypotheses.

In Euler-Bernoulli beam theory, cross sections, perpendicular to the neutral axis before the bending, remain perpendicular to the neutral axis even after the bending. This model is suitable for slender beams and lower modes of vibration, while it is inadequate to characterize the response of short beams, due to lower shear rigidity. To overcome this drawback, the Timoshenko beam theory is largely applied. A useful review of the studies on shear deformable beams and plates can be found in the book by Wang & al. [10]. Furthermore, the work made by Li & al. [11] is also interesting. They show a unified approach for analysing static and dynamic behaviour of both Euler-Bernoulli and Timoshenko FGBs introducing a new variable linked to vertical and rotational degrees of freedom of beams. This type of technique is widely used in literature and it leads to physical speculations based on not local theories [12] and computational advantageous methods [13]. With the same philosophy, Falsone G. & La Valle G. [14] show a new kind of approach that lies on the concept of homogenization of the general beam cross-section and on the introduction of generalized quantities with the aim of simplifying differential equations governing the correspondent elastic equilibrium problem.

The goal of this work is to apply homogenized/generalized displacements, introduced in the last cited paper in static conditions, for dynamic problems and buckling problems. Moreover, a FE formulation, based on the use of the homogenized/generalized displacements, is shown for the Timoshenko FGBs. The paper is organized as follows: first the differential equations governing dynamic equilibrium of FGBs, in terms of homogenized/generalized axial and transversal displacements, are derived. Then, the above cited FE formulation is shown in the details. In section 5, the buckling problem is treated, showing how the use of the above cited displacement leads to a very simple formulation, able to give some exact solutions. Lastly, in section 6, some simple numerical examples are shown to verify the reliability of the reported approach.

## 2. Preliminary Concepts

In this section, some preliminary known concepts are given in order to introduce the notations and the formulations that will be used in the remaining part of the paper.

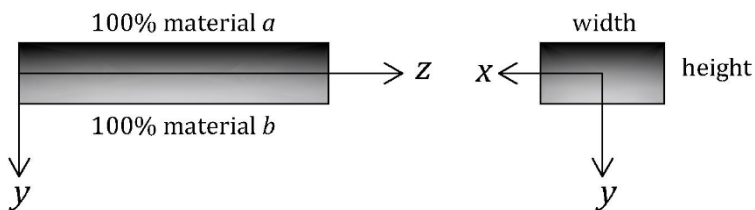


Fig. 1 Geometry of a functionally graded beam

The beams are referred to a Cartesian coordinate system  $(O; x, y, z)$  with the origin  $O$  placed in the geometrical centre of an extreme section; the  $z$ -axis coincides with the beam axis, while the  $y$ -axis coincides with the section principal axis along the thickness. The Young modulus is assumed changing along the thickness in a generic way.

### 2.1. Hamilton's Principle for Timoshenko FGBs.

The Timoshenko theory is based on the following assumptions in the displacement field (see [15], [16], [17], [18] and [19]):

$$u_z(x, y, z, t) = w(z, t) + y\phi(z, t) \tag{1a}$$

$$u_y(x, y, z, t) = v(z, t) \tag{1b}$$

$$u_x(x, y, z, t) = 0 \tag{1c}$$

where  $u_z$  and  $u_y$  are the punctual displacement components, while  $w$ ,  $v$  and  $\phi$  are the displacement variables generalized to the cross-section. The punctual axial and shear deformations,  $\varepsilon_z$  and  $\gamma_{zy}$ , and the punctual axial and shear stresses,  $\sigma_z$  and  $\tau_{zy}$ , can be obtained by the compatibility conditions and constitutive relations that, taking into account Eq. (1a), give:

$$\varepsilon_z(x, y, z, t) = \frac{\partial u_z(x, y, z, t)}{\partial z} = \frac{\partial w(z, t)}{\partial z} + y \frac{\partial \phi(z, t)}{\partial z} \tag{2a}$$

$$\gamma_{zy}(x, y, z, t) = \frac{\partial v(z, t)}{\partial z} + \phi(z, t) \tag{2b}$$

$$\sigma_z(x, y, z, t) = E(y)\varepsilon_z(x, y, z, t) = E(y) \left[ \frac{\partial w(z, t)}{\partial z} + y \frac{\partial \phi(z, t)}{\partial z} \right] \tag{2c}$$

$$\tau_{zy}(x, y, z, t) = G(y)\gamma_{zy}(x, y, z, t) = G(y) \left[ \frac{\partial v(z, t)}{\partial z} + \phi(z, t) \right] \tag{2d}$$

$E(y)$  and  $G(y)$  being the normal and transversal material modulus, respectively. Here, they are assumed to change along the  $y$  axis. The generalized internal actions, the axial one  $N$ , the transversal one  $T$  and the bending moment  $M$ , are given by:

$$N(z, t) = \int_A \sigma_z(x, y, z, t) dA = E_0 \frac{\partial w(z, t)}{\partial z} + E_1 \frac{\partial \phi(z, t)}{\partial z} \tag{3a}$$

$$M(z, t) = \int_A y\sigma_z(x, y, z, t) dA = E_1 \frac{\partial w(z, t)}{\partial z} + E_2 \frac{\partial \phi(z, t)}{\partial z} \tag{3b}$$

$$T(z, t) = \int_A \tau_{zx}(x, y, z, t) dA \approx \frac{G_0}{\chi} \left[ \frac{\partial v(z, t)}{\partial z} + \phi(z, t) \right] \tag{3c}$$

where the following notation has been used:

$$E_i = \int_A y^i E(y) dA \tag{4a}$$

$$i \in \{0,1,2\}$$

$$G_0 = \int_A G(y) dA \tag{4b}$$

and where  $\chi$  is the correction shear factor. In order to obtain the governing equations, the Hamilton's Principle is applied:

$$0 = \int_0^T (\delta K - \delta U - \delta V) dt \tag{5}$$

where  $\delta U$  is the virtual strain energy,  $\delta K$  is the virtual kinetic energy, and  $\delta V$  is the virtual work done by the external forces. Taking into account Eqs.(3), they assume the following form:

$$\delta U = \int_0^L \int_A (\sigma_z \delta \varepsilon_z + \tau_{zy} \delta \gamma_{zy}) dA dz$$

$$= \int_0^L \left\{ E_0 \frac{\partial w}{\partial z} \frac{\partial \delta w}{\partial z} + E_1 \left( \frac{\partial w}{\partial z} \frac{\partial \delta \phi}{\partial z} + \frac{\partial \phi}{\partial z} \frac{\partial \delta w}{\partial z} \right) + \right. \\ \left. + E_2 \frac{\partial \phi}{\partial z} \frac{\partial \delta \phi}{\partial z} + \frac{G_0}{\chi} \left[ \frac{\partial v}{\partial z} \frac{\partial \delta v}{\partial z} + \frac{\partial v}{\partial z} \delta \phi + \phi \frac{\partial \delta v}{\partial z} + \phi \delta \phi \right] \right\} dz \tag{6a}$$

$$\delta K = \int_0^L \left[ m_0 \left( \frac{\partial w}{\partial t} \frac{\partial \delta w}{\partial t} + \frac{\partial v}{\partial t} \frac{\partial \delta v}{\partial t} \right) + m_1 \left( \frac{\partial \phi}{\partial t} \frac{\partial \delta w}{\partial t} + \frac{\partial w}{\partial t} \frac{\partial \delta \phi}{\partial t} + m_2 \frac{\partial \phi}{\partial t} \frac{\partial \delta \phi}{\partial t} \right) \right] dz \tag{6b}$$

$$\delta V = - \int_0^L (q_z \delta w + q_y \delta v) dz \tag{6c}$$

where:

$$m_i = \int_A y^i \rho(y) dA \tag{6d}$$

$q_z$  and  $q_y$  being the axial and transversal external loads, while  $\rho(z)$  is the material mass density of the FGB. Substituting the expressions of  $\delta U$ ,  $\delta K$ ,  $\delta V$  from Eqs. (6a,c) into Eq. (5), integrating by parts with respect to both  $t$  and  $z$  and fixing the following usual dynamic boundary conditions:

$$\delta w(z, 0) = \delta w(z, t_f) = 0 \tag{7a}$$

$$\delta \phi(z, 0) = \delta \phi(z, t_f) = 0 \tag{7b}$$

$$\delta v(z, 0) = \delta v(z, t_f) = 0 \tag{7c}$$

$t_f$  being the final instant of the analysis temporal interval, it is possible to obtain:

$$\delta u: -E_0 \left( \frac{\partial^2 w}{\partial z^2} + \frac{E_1}{E_0} \frac{\partial^2 \phi}{\partial z^2} \right) + m_0 \frac{\partial^2 w}{\partial t^2} + m_1 \frac{\partial^2 \phi}{\partial t^2} - q_z = 0 \tag{8a}$$

$$\delta \phi: -E_2 \left( \frac{\partial^2 \phi}{\partial z^2} + \frac{E_1}{E_2} \frac{\partial^2 w}{\partial z^2} \right) + \frac{G_0}{\chi} \left( \frac{\partial v}{\partial z} + \phi \right) + m_2 \frac{\partial^2 \phi}{\partial t^2} + m_1 \frac{\partial^2 w}{\partial t^2} = 0 \tag{8b}$$

$$\delta v: -\frac{G_0}{\chi} \left( \frac{\partial^2 v}{\partial z^2} + \frac{\partial \phi}{\partial z} \right) - q_y + m_0 \frac{\partial^2 v}{\partial t^2} = 0 \tag{8c}$$

with the boundary conditions:

$$\left[ \left( E_0 \frac{\partial w}{\partial z} + E_1 \frac{\partial \phi}{\partial z} \right) \delta w \right]_0^L = 0 \tag{9a}$$

$$\left[ \left( E_1 \frac{\partial w}{\partial z} + E_2 \frac{\partial \phi}{\partial z} \right) \delta \phi \right]_0^L = 0 \tag{9b}$$

$$\left[ \frac{G_0}{\chi} \left( \frac{\partial v}{\partial z} + \phi \right) \delta v \right]_0^L = 0 \tag{9c}$$

Eqs. (9a,b) show that the static boundary conditions are coupled. This makes not simple the application of the FE method and the solution of some relevant problems, as the analysis of the free vibration frequencies or the buckling loads.

### 2.2. Generalized/Homogenized Displacements

In the above cited authors' work [14], the expressions of the generalized/homogenized axial displacement,  $\bar{w}$ , and rotation,  $\bar{\phi}$ , are given as:

$$\bar{w}(z,t) = w(z,t) + \frac{E_1}{E_0} \phi(z,t) = w(z,t) + y_{GE} \phi(z,t) \tag{10a}$$

$$\bar{\phi}(z,t) = \phi(z,t) + \frac{E_1}{E_2} w(z,t) = \phi(z,t) + \frac{1}{y_{CE}} w(z,t) \tag{10b}$$

The inverse relationships are:

$$w(z,t) = \frac{\bar{w}(z,t) - y_{GE} \bar{\phi}(z,t)}{1 - \frac{y_{GE}}{y_{CE}}} \tag{11a}$$

$$\phi(z,t) = \frac{\bar{\phi}(z,t) - \frac{1}{y_{CE}} \bar{w}(z,t)}{1 - \frac{y_{GE}}{y_{CE}}} \tag{11b}$$

### 3. Hamilton's Principle In Terms Of Generalized/Homogenized Displacements

By replacing Eqs. (10a,b) and Eqs. (11a,b) into Eqs. (8a,c) and (9a,c), it is possible to obtain the governing equations of Timoshenko FGBs. They have the following expressions:

$$\delta w: -E_0 \frac{\partial^2 \bar{w}}{\partial z^2} + m_{11} \frac{\partial^2 \bar{w}}{\partial t^2} + m_{12} \frac{\partial^2 \bar{\phi}}{\partial t^2} - q_z = 0 \tag{12a}$$

$$\delta \phi: -E_2 \frac{\partial^2 \bar{\phi}}{\partial z^2} + \frac{G_0}{\chi} \left( \frac{\partial v}{\partial z} - \Omega_{21} \bar{w} + \Omega_{22} \bar{\phi} \right) + m_{21} \frac{\partial^2 \bar{w}}{\partial t^2} + m_{22} \frac{\partial^2 \bar{\phi}}{\partial t^2} = 0 \tag{12b}$$

$$\delta v: -\frac{G_0}{\chi} \left( \frac{\partial^2 v}{\partial z^2} - \Omega_{21} \frac{\partial \bar{w}}{\partial z} + \Omega_{22} \frac{\partial \bar{\phi}}{\partial z} \right) - q_y + m_0 \frac{\partial^2 v}{\partial t^2} = 0 \tag{12c}$$

with the following boundary conditions:

$$\left[ E_0 \frac{\partial \bar{w}}{\partial z} \delta w \right]_0^L = 0 \tag{13a}$$

$$\left[ E_2 \frac{\partial \bar{\phi}}{\partial z} \delta \phi \right]_0^L = 0 \tag{13b}$$

$$\left[ \frac{G_0}{\chi} \left( \frac{\partial v}{\partial z} + \Omega_{22} \bar{\phi} - \Omega_{21} \bar{w} \right) \delta v \right]_0^L = 0 \tag{13c}$$

in which some useful coefficients have been defined:

$$\Omega_{11} = \frac{1}{1 - \frac{y_{GE}}{y_{CE}}} = \Omega_{22} \tag{14a}$$

$$\Omega_{12} = y_{GE} \Omega_{11} \tag{14b}$$

$$\Omega_{21} = \frac{1}{y_{CE}} \Omega_{22} \tag{14c}$$

$$m_{11} = m_0 \Omega_{11} - m_1 \Omega_{21} \tag{14d}$$

$$m_{12} = -m_0 \Omega_{12} + m_1 \Omega_{22} \tag{14e}$$

$$m_{21} = -m_2 \Omega_{21} + m_1 \Omega_{11} \tag{14f}$$

$$m_{22} = m_2 \Omega_{22} - m_1 \Omega_{12} \tag{14g}$$

It is easy to verify that the introduction of the new kinematic quantities allows to decouple the first two boundary conditions (Eqs.(13a,b)). This simplifies remarkably the application of the FE method, as will be seen in the next section

#### 4. Dynamic and Static Applications of FE Method

##### 4.1 Dynamic Problem

Following the usual FE procedures for the dynamic analysis of beams (see, for example [20], [21], [23] and [24]), it is useful to approximate the kinematic variables as the product of two independent functions, one of the spatial coordinate and one of the time. By applying the same assumption here, the generalized/homogenized displacements are approximated as follows:

$$\bar{w}(z, t) = \bar{W}(z) e^{-i\omega t} \tag{15a}$$

$$\bar{\phi}(z, t) = \bar{\Phi}(z) e^{-i\omega t} \tag{15b}$$

$$v(z, t) = V(z) e^{-i\omega t} \tag{15c}$$

Taking into account these relationships and fixing  $q_y = q_z = 0$ , in order to analyse beam free vibrations, Eqs. (12a,c) become:

$$\delta w: -E_0 \frac{d^2 \bar{W}}{dz^2} - \omega^2 (m_{11} \bar{W} + m_{12} \bar{\Phi}) = 0 \tag{16a}$$

$$\delta \phi: -E_2 \frac{d^2 \bar{\Phi}}{dz^2} + \frac{G_0}{\chi} \left( \frac{dV}{dz} - \Omega_{21} \bar{W} + \Omega_{22} \bar{\Phi} \right) - \omega^2 (m_{21} \bar{W} + m_{22} \bar{\Phi}) = 0 \tag{16b}$$

$$\delta v: -\frac{G_0}{\chi} \left( \frac{d^2 V}{dz^2} - \Omega_{21} \frac{d\bar{W}}{dz} + \Omega_{22} \frac{d\bar{\Phi}}{dz} \right) - \omega^2 m_0 V = 0 \tag{16c}$$

In order to implement a FE approach, let us consider the weak formulation directly to Eqs. (16) (strong and weak formulations are crucial concepts of partial differential equations:

the weak formulation turns a differential equation to an integral one). If a generic FE of length  $h$  is referred to a local axis reference  $0 < \xi < h$ , it is possible to write:

$$\left[ -E_0 \frac{d\bar{W}}{d\xi} v_1 \right]_0^h + \int_0^h E_0 \frac{d\bar{W}}{d\xi} \frac{dv_1}{d\xi} d\xi - \omega^2 \int_0^h m_{11} \bar{W} v_1 + m_{12} \bar{\Phi} v_1 d\xi = 0 \tag{17a}$$

$$\left[ -E_2 \frac{d\bar{\Phi}}{d\xi} v_2 \right]_0^h + \int_0^h E_2 \frac{d\bar{\Phi}}{d\xi} \frac{dv_2}{d\xi} + \frac{G_0}{\chi} \left( \frac{dV}{dz} - \Omega_{21} \bar{W} + \Omega_{22} \bar{\Phi} \right) v_2 d\xi - \omega^2 \int_0^h m_{21} \bar{W} v_2 + m_{22} \bar{\Phi} v_2 d\xi = 0 \tag{17b}$$

$$\left[ -\frac{G_0}{\chi} \left( \frac{dV}{dz} - \Omega_{21} \bar{W} + \Omega_{22} \bar{\Phi} \right) v_3 \right]_0^h + \int_0^h \frac{G_0}{\chi} \left( \frac{dV}{dz} - \Omega_{21} \bar{W} + \Omega_{22} \bar{\Phi} \right) \frac{dv_3}{d\xi} d\xi - \omega^2 \int_0^h m_0 V v_3 d\xi = 0 \tag{17c}$$

where  $v_1$ ,  $v_2$  and  $v_3$  are opportune weight functions. Eqs. (17a,c) allow to evidence primary and secondary variables. The degree of interpolation for the functions  $\bar{W}$ ,  $\bar{\Phi}$  and  $V$  can be generic, but the degree of interpolation of  $V$  must be an unit more than that of  $\bar{\Phi}$  (we define it as Consistent Interpolation Element (CIE)). Then, it is:

$$\bar{W}(\xi) \approx [\underline{\Psi}^{\bar{W}}(\xi)]^T \bar{W}^e [\underline{\Psi}^{\bar{W}}(\xi)]^T = (\psi_1^{\bar{W}}(\xi), \psi_2^{\bar{W}}(\xi), \dots, \psi_n^{\bar{W}}(\xi)) \tag{18a}$$

$$\bar{\Phi}(\xi) \approx [\underline{\Psi}^{\bar{\Phi}}(\xi)]^T \bar{\Phi}^e [\underline{\Psi}^{\bar{\Phi}}(\xi)]^T = (\psi_1^{\bar{\Phi}}(\xi), \psi_2^{\bar{\Phi}}(\xi), \dots, \psi_n^{\bar{\Phi}}(\xi)) \tag{18b}$$

$$V(\xi) \approx [\underline{\Psi}^V(\xi)]^T V^e [\underline{\Psi}^V(\xi)]^T = (\psi_1^V(\xi), \psi_2^V(\xi), \dots, \psi_{n+1}^V(\xi)) \tag{18c}$$

Replacing Eqs. (18a,c) into Eqs. (17a,c) and, with the aim of applying a Ritz-Galerkin FE approach, setting  $v_1(\xi) = \Psi_i^{\bar{W}}(\xi)$  ( $i=1, \dots, n$ ),  $v_2(\xi) = \Psi_i^{\bar{\Phi}}(\xi)$  ( $i=1, \dots, n$ ) and  $v_3(\xi) = \Psi_i^V(\xi)$  ( $i=1, \dots, n+1$ ), the following equations are obtained:

$$\left( \begin{array}{ccc} \underline{K}^{\bar{W}\bar{W}} & \underline{0} & \underline{0} \\ \underline{K}^{\bar{\Phi}\bar{W}} & \underline{K}^{\bar{\Phi}\bar{\Phi}} & \underline{K}^{\bar{\Phi}V} \\ \underline{K}^{V\bar{W}} & \underline{K}^{V\bar{\Phi}} & \underline{K}^{VV} \end{array} \right)_e - \omega^2 \left( \begin{array}{ccc} \underline{M}^{\bar{W}\bar{W}} & \underline{M}^{\bar{W}\bar{\Phi}} & \underline{0} \\ \underline{M}^{\bar{\Phi}\bar{W}} & \underline{M}^{\bar{\Phi}\bar{\Phi}} & \underline{0} \\ \underline{0} & \underline{0} & \underline{M}^{VV} \end{array} \right)_e \begin{bmatrix} \bar{W} \\ \bar{\Phi} \\ V \end{bmatrix}_e = \begin{bmatrix} Q_1 \\ Q_2 \\ Q_3 \end{bmatrix}_e \tag{19}$$

$$\Rightarrow (\underline{K}_e - \omega^2 \underline{M}_e) \underline{u}_e = \underline{Q}_e$$

where:

$$\underline{K}^{\bar{W}\bar{W}} = \int_0^h E_0 \frac{d\underline{\Psi}^{\bar{W}}(\xi)}{d\xi} \frac{d[\underline{\Psi}^{\bar{W}}(\xi)]^T}{d\xi} d\xi \tag{20a}$$

$$\underline{K}^{\bar{\Phi}\bar{W}} = \int_0^h -\frac{G_0}{\chi} \Omega_{21} \underline{\Psi}^{\bar{\Phi}}(\xi) [\underline{\Psi}^{\bar{W}}(\xi)]^T d\xi \tag{20b}$$

$$\underline{K}^{\bar{\Phi}\bar{\Phi}} = \int_0^h E_2 \frac{d\underline{\Psi}^{\bar{\Phi}}(\xi)}{d\xi} \frac{d[\underline{\Psi}^{\bar{\Phi}}(\xi)]^T}{d\xi} + \frac{G_0}{\chi} \Omega_{22} \underline{\Psi}^{\bar{\Phi}}(\xi) [\underline{\Psi}^{\bar{\Phi}}(\xi)]^T d\xi \tag{20c}$$

$$\underline{\underline{K}}^{\bar{\phi}V} = \int_0^h \frac{G_0}{\chi} \underline{\Psi}^{\bar{\phi}}(\xi) \frac{d[\underline{\Psi}^V(\xi)]^T}{d\xi} d\xi \tag{20d}$$

$$\underline{\underline{K}}^{V\bar{W}} = \int_0^h -\frac{G_0}{\chi} \Omega_{21} \frac{d\underline{\Psi}^V(\xi)}{d\xi} [\underline{\Psi}^{\bar{W}}(\xi)]^T d\xi \tag{20e}$$

$$\underline{\underline{K}}^{V\bar{\phi}} = \int_0^h \frac{G_0}{\chi} \Omega_{22} \frac{d\underline{\Psi}^V(\xi)}{d\xi} [\underline{\Psi}^{\bar{\phi}}(\xi)]^T d\xi \tag{20f}$$

$$\underline{\underline{K}}^{VV} = \int_0^h \frac{G_0}{\chi} \frac{d\underline{\Psi}^V(\xi)}{d\xi} \frac{d[\underline{\Psi}^V(\xi)]^T}{d\xi} d\xi \tag{20g}$$

$$\underline{\underline{M}}^{\bar{W}\bar{W}} = \int_0^h m_{11} \underline{\Psi}^{\bar{W}}(\xi) [\underline{\Psi}^{\bar{W}}(\xi)]^T d\xi \tag{20h}$$

$$\underline{\underline{M}}^{\bar{W}\bar{\phi}} = \int_0^h m_{12} \underline{\Psi}^{\bar{W}}(\xi) [\underline{\Psi}^{\bar{\phi}}(\xi)]^T d\xi \tag{20i}$$

$$\underline{\underline{M}}^{\bar{\phi}\bar{W}} = \int_0^h m_{21} \underline{\Psi}^{\bar{\phi}}(\xi) [\underline{\Psi}^{\bar{W}}(\xi)]^T d\xi \tag{20j}$$

$$\underline{\underline{M}}^{\bar{\phi}\bar{\phi}} = \int_0^h m_{22} \underline{\Psi}^{\bar{\phi}}(\xi) [\underline{\Psi}^{\bar{\phi}}(\xi)]^T d\xi \tag{20k}$$

$$\underline{\underline{M}}^{VV} = \int_0^h m_0 \underline{\Psi}^V(\xi) [\underline{\Psi}^V(\xi)]^T d\xi \tag{20l}$$

and:

$$\underline{\underline{Q}}_1 = [-N(0) \quad 0 \quad \dots \quad 0_{n-1} \quad N(h)]^T \tag{20m}$$

$$\underline{\underline{Q}}_2 = [-M(0) \quad 0 \quad \dots \quad 0_{n-1} \quad M(h)]^T \tag{20n}$$

$$\underline{\underline{Q}}_2 = [-T(0) \quad 0 \quad \dots \quad 0_n \quad T(h)]^T \tag{20o}$$

Eqs. (10) and (11) show that the generalized kinematic variables can be expressed in function of the generalized/homogenized ones and vice versa, in such a way their continuity is guaranteed. The continuity of generalized/homogenized variables is imposed by defining the location matrix  $\underline{\underline{L}}_e$  for each finite element. Defining  $\underline{\underline{U}}$  as the vector whose entrances are the nodes displacements and  $\underline{\underline{Q}}$  as the vector containing the internal forces at the nodes, and following the same steps of the classical FE approach, it is possible to obtain:

$$(\underline{\underline{K}} - \omega^2 \underline{\underline{M}}) \underline{\underline{U}} = \underline{\underline{Q}} \tag{21}$$

where:

$$\underline{\underline{K}} = \underline{\underline{L}}_e^T \underline{\underline{K}}_e \underline{\underline{L}}_e \quad \underline{\underline{M}} = \underline{\underline{L}}_e^T \underline{\underline{M}}_e \underline{\underline{L}}_e \quad \underline{\underline{Q}} = \underline{\underline{L}}_e^T \underline{\underline{Q}}_e \quad \underline{\underline{U}} = \underline{\underline{L}}_e^{-1} \underline{\underline{u}}_e \tag{22}$$

By imposing static and kinematic boundary conditions, given Eqs. (10) and Eqs. (13), the system of equations (21) allows to derive the eigenvalues problem able to define the dynamic behaviour of a FGB.

### 4.2 Static Problem

Eqs. (12), simplified for the static case, take the form:

$$-E_0 \frac{d^2 \bar{w}}{dz^2} - q_z = 0 \tag{23a}$$

$$-E_2 \frac{d^2 \bar{\phi}}{dz^2} + \frac{G_0}{\chi} \left( \frac{dv}{dz} - \Omega_{21} \bar{w} + \Omega_{22} \bar{\phi} \right) = 0 \tag{23b}$$

$$-\frac{G_0}{\chi} \left( \frac{d^2 v}{dz^2} - \Omega_{21} \frac{d\bar{w}}{dz} + \Omega_{22} \frac{d\bar{\phi}}{dz} \right) - q_y = 0 \tag{23c}$$

Through the same steps considered previously, the solving equation is obtained as:

$$\underline{\underline{K}} \underline{\underline{U}} = \underline{\underline{F}} + \underline{\underline{Q}} \tag{24}$$

where  $\underline{\underline{K}}, \underline{\underline{U}}, \underline{\underline{Q}}$  are equal to those which appear in Eq. (21);  $\underline{\underline{F}}$  is defined as follows:

$$\underline{\underline{F}} = \underline{\underline{L}}_e^T \underline{\underline{F}}_e \tag{25}$$

and:

$$\underline{\underline{F}}_e = \begin{bmatrix} F_1 \\ 0 \\ F_3 \end{bmatrix} \tag{26a}$$

$$F_1 = \int_0^h \underline{\Psi}^W(\xi) q_z(\xi) d\xi \tag{26b}$$

$$F_3 = \int_0^h \underline{\Psi}^V(\xi) q_y(\xi) d\xi \tag{26c}$$

## 5. Analytical Solutions for Buckling Analysis

In this section the generalized/homogenized displacements are used with the aim of finding analytical solutions for the buckling problem of Timoshenko FGBs. It is noteworthy that some of the analytical solutions set out herein are a novelty in literature; this despite a lot of paper which deal with this problem already exist, for example, [24], [25], [26], [27], [28], and [29].

### 5.1. Buckling Load of a Clamped-Free Beam

In order to investigate the buckling of a generic column subjected to a compressive force  $P$ , Eqs. (12) become:

$$-E_0 \frac{d^2 \bar{w}}{dz^2} = 0 \tag{27a}$$

$$-E_2 \frac{d^2 \bar{\phi}}{dz^2} + \frac{G_0}{\chi} \left( \frac{dv}{dz} + \Omega_{22} \bar{\phi} - \Omega_{21} \bar{w} \right) = 0 \tag{27b}$$

$$-\frac{G_0}{\chi} \left( \frac{d^2v}{dz^2} + \Omega_{22} \frac{d\bar{\phi}}{dz} - \Omega_{21} \frac{d\bar{w}}{dz} \right) + P \frac{d^2v}{dz^2} = 0 \tag{27c}$$

with the boundary conditions:

$$\left[ E_0 \frac{d\bar{w}}{dz} \delta w \right] = 0 \tag{28a}$$

$$\left[ \left( \frac{G_0}{\chi} \left( \frac{dv}{dz} + \Omega_{22}\bar{\phi} - \Omega_{21}\bar{w} \right) - P \frac{dv}{dz} \right) \delta v \right]_0^L = 0 \tag{28b}$$

$$\left[ E_2 \frac{d\bar{\phi}}{dz} \delta \phi \right]_0^L = 0 \tag{28c}$$

Noting that for a clamped-free beam the generalized transversal stress is equal to zero in the free end,  $T(L)=0$ , it is possible to assume  $T(z)=0$  for all the beam. Furthermore, combining Eq.(27a), Eq.(28a) and Eqs.(11),  $\bar{w}(z)=0$  is obtained. Hence, Eq. (28b) allows to give the generalized/ homogenised rotation  $\bar{\phi}$  as a function of the generalized transversal displacement  $v$ :

$$\frac{G_0}{\chi} \left( \frac{dv(z)}{dz} + \Omega_{22}\bar{\phi}(z) \right) - P \frac{dv(z)}{dz} = 0 \Rightarrow \bar{\phi}(z) = \frac{\left( \frac{P - G_0}{\chi} \right) dv(z)}{\frac{G_0}{\chi} \Omega_{22}} \tag{29}$$

Substituting Eq.(29) into Eq.(27b) and deriving with respect to  $z$ , the differential equations governing the buckling problem of a Timoshenko FGB is derived:

$$\frac{d^4v(z)}{dz^4} + \alpha^2 \frac{d^2v}{dz^2} = 0 \quad \alpha = \sqrt{\frac{P\Omega_{22} / E_2}{1 - P / G_0}} \tag{30}$$

This result implies that the buckling load  $P_n$  for this kind of beam is given by:

$$P_n = \frac{P_E}{\Omega_{22} + \frac{\chi P_E}{G_0}} \Leftarrow P_E = \frac{n^2 \pi^2 E_2}{(2L)^2} \tag{31}$$

In order to clarify the transition process between Eqs. (30) and (31), we need to remember that the general solution of Eq. (30) is:

$$v(z) = A \cos \alpha z + B \sin \alpha z + Cz + D \tag{32}$$

By imposing the boundary conditions  $v(0)=0, v(L)=0, dv/dz(0)=0$  (see Eqs. (11a,b-29) with  $w(0)=0$  since the beam is supposed clamped in  $z=0$ ),  $d^2v/dz^2(L)=0$  (see Eqs. (13b-29)); we get the following system in the unknown variables  $A, B, C$  and  $D$ :

$$\begin{cases} A + D = 0 \\ A \cos(\alpha L) + B \sin(\alpha L) + CL + D = 0 \\ B + C = 0 \\ A \cos(\alpha L) + B \sin(\alpha L) = 0 \end{cases} \quad (33)$$

System (33) gives no trivial solution if and only if  $\cos(\alpha L) = 0$ : it follows  $\alpha L = n\pi/2$  then Eq. (31) is achieved.

### 5.2. Buckling Load for a Simply Supported-Simply Supported Beam

In this case, Eqs.(27) and Eqs.(28) continue to hold. Taking into account Eq.(27a), Eq.(28a) and Eqs.(11), it is possible to obtain  $\bar{w}(z) = y_{GE} \bar{\phi}(0)$ . Therefore, deriving Eq. (27b) and adding to it Eq.(27c), it is easy to show that Eq.(30) still holds. This implies that the buckling load is given by:

$$P_n = \frac{P_E}{\Omega_{22} + \frac{\chi P_E}{G_0}} \leftarrow P_E = \frac{n^2 \pi^2 E_2}{L^2} \quad (34)$$

Similar steps as the one just made in Subsection 5.1 needs to be performed.

## 6. Numerical Applications

From here on out, the following acronyms are introduced: S-S for simply supported-simply supported; C-C for clamped-clamped; C-F for clamped-free and C-S for clamped-simply supported.

### 6.1. Natural Frequencies for S-S Beams

Let us consider a S-S Timoshenko FG beam with a rectangular cross of width  $b$ , height  $h$ , length  $L$ , shear correction factor  $\chi$ :

$$h = 5 \times 17.6 \times 10^{-6} \text{ m} \quad b = 2h \quad L = 20h \quad \chi = 1.2 \quad (35)$$

The beam is characterized by an elastic modulus and a density variable along the thickness with an exponential law:

$$E(y) = (E_b - E_a) \left( \frac{y}{h} + \frac{1}{2} \right)^N + E_a \quad (36a)$$

$$\rho(y) = (\rho_b - \rho_a) \left( \frac{y}{h} + \frac{1}{2} \right)^N + \rho_a \quad (36b)$$

where  $E_a = 14400$  MPa,  $E_b = 1440$  MPa,  $\rho_a = 122$  kg/mm,  $\rho_b = 12.2$  kg/mm. The exponent  $N$  defines the composition of the section and, here, it is assumed equal to five different values. The elastic tangential module is given by the usual expression:

$$G(y) = \frac{E(y)}{2(1+\nu)} \quad (37)$$

$\nu$  being the classical Poisson coefficient, here chosen equal to 0.38. The results obtained by the FE approach previously introduced (numerically approximated) are compared with the natural frequencies obtained in accordance with the procedure exposed by Li [11]

(theoretical and numerical approximated). Ten finite elements having the same length have been used; moreover, polynomial interpolating functions of order one for  $\bar{w}$  and  $\bar{\phi}$  and of order two for  $v$  have been applied (This level of refinement is maintained for all numerical applications exposed in this section). The accordance of the values reported in Table 1 ensures the correctness of the methodology applied. Clearly, these FE results could be improved by a p-refinement or a h-refinement.

Table 1. First three natural frequencies (expressed in  $s^{-1}$ ) for a S-S beam with different values of  $N$

N	$\omega_1$ Li	$\omega_1$ FEM	$\omega_2$ Li	$\omega_2$ FEM	$\omega_3$ Li	$\omega_3$ FEM
0.2	0.85	0.85	3.36	3.41	7.41	7.67
0.5	0.81	0.82	3.22	3.27	7.11	7.37
1	0.77	0.78	3.06	3.11	6.77	7.02
5	0.82	0.82	3.25	3.30	7.17	7.43
100	0.93	0.92	3.67	3.67	8.08	8.24

### 6.2. Natural Frequencies for C-C and C-S Beams

The same mechanical and geometrical characteristics assumed in the previous subsection are taken into account. For the beams here considered, no analytical solution exists in the literature. Consequently, the FE method exposed in section 4 has been applied for any examined boundary conditions. Natural frequencies derived for a C-S Timoshenko beam are collected in Table 2, while those derived for a S-S beam are given in Table 1. Table 2 shows the results obtained for the C-C beam. Lastly, the natural frequencies linked to a C-F beam are reported in Table 3.

Table 2. First three natural frequencies (expressed in  $s^{-1}$ ) for C-C and C-S beams with different values of  $N$

$N$	C-C beam			C-S beam		
	$\omega_1$	$\omega_2$	$\omega_3$	$\omega_1$	$\omega_2$	$\omega_3$
0.2	1.98	5.62	11.44	1.33	4.32	9.03
0.5	1.90	5.41	11.03	1.27	4.15	8.69
1	1.81	5.15	10.54	1.21	3.95	8.29
5	1.92	5.45	11.11	1.29	4.19	8.76
100	2.17	6.12	12.36	1.46	4.73	9.82

Table 3. First three natural frequencies (expressed in  $s^{-1}$ ) for the C-F beam with different  $N$

C-F beam			
$N$	$\omega_1$	$\omega_2$	$\omega_3$
0.2	0.30	1.90	5.33
0.5	0.29	1.83	5.12
1	0.28	1.73	4.87
5	0.29	1.84	5.16
100	0.33	2.09	5.82

Eqs. (36a,b) describe the change of material along the cross section of the analysed beam; these laws are functions of a parameter  $N$  which can be considered an indicator of the mixture of the two components that constitute the sample in exam. In detail, when  $N$  tends to infinity then the cross section tends to be homogeneous with the properties of the stiffest component ( $E_a=14400$  MPa,  $\rho_a=122$  kg/mm); on the other hand, when  $N$  tends to

zero then the beam tends to be homogenous with the properties of the weakest one ( $E_b=1440$  MPa,  $\rho_b=12.2$  kg/mm). In light of the above, it is not surprising that in Table 1, 2 and 3 the natural frequencies increase with growing  $N$ .

**6.3. Buckling Loads for S-S and C-F Beams**

Eqs.(31) and Eq.(34) are here applied to the same above considered beams. In this case, the use of the homogenized/generalized displacements makes possible to have exact relations expressing the buckling load of these Timoshenko FGBs. Table 4 shows the numerical results obtained evaluating Eqs. (31) and (34): indeed, buckling loads increases with growing  $N$  since the sample becomes progressively more stiff (same remarks are true for natural frequencies (see Subsections 6.1 and 6.2)

**6.4. Static Bending C-C and C-S Beams**

In this application, the same mechanical and geometrical characteristics used previously are maintained. The static external action is represented by a vertical uniformly distributed load with intensity  $q_y= 10$  N/mm. The coefficient  $N$  appearing in Eqs.(41) is assumed equal to 10. Fig.2 and Fig.3 show the transversal displacements obtained with the FE formulation, here presented, compared with the analytical ones.

Table 4. First three buckling loads (expressed in newton (N)) for S-S and the C-F beam with different values of  $N$

$N$	S-S beam			C-F beam		
	$P_1$	$P_2$	$P_3$	$P_1$	$P_2$	$P_3$
0.2	0.06	0.22	0.47	0.014	0.06	0.12
0.5	0.10	0.39	0.85	0.025	0.10	0.22
1	0.19	0.76	1.67	0.05	0.19	0.43
5	0.28	1.08	2.34	0.07	0.28	0.61
100	0.36	1.42	3.09	0.09	0.36	0.81

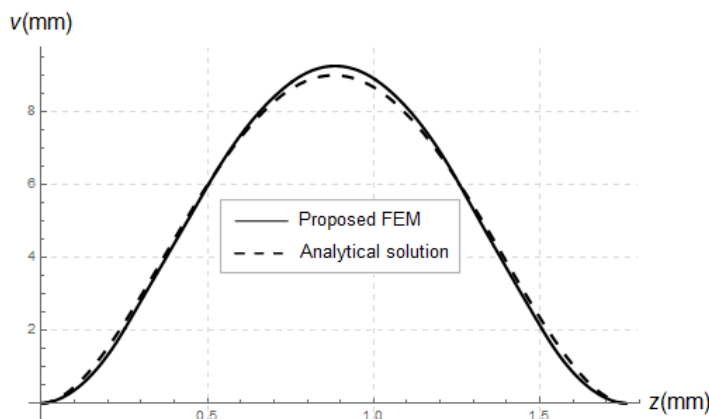


Fig.2 Static transversal deflection (expressed in mm) under constant load for C-C beam with  $N=10$

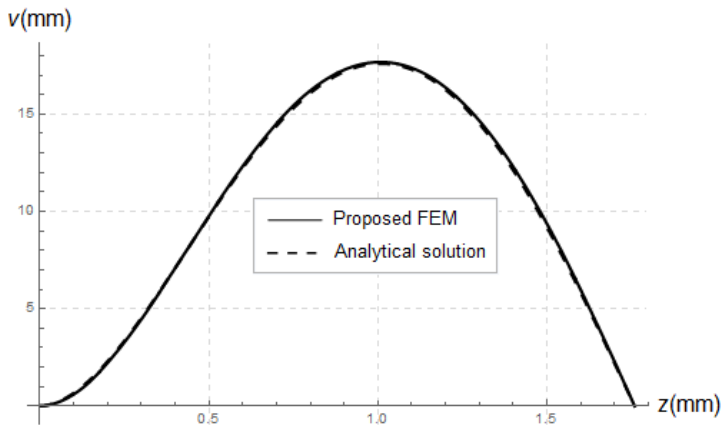


Fig.3 Static transversal deflection (expressed in mm) under constant load for C-S beam with  $N=10$

Fig.2-3 show a higher rate of convergence in the case in which natural (or static) boundary conditions need to be imposed: in the same condition, the accuracy of the numerical solution obtained for the C-S beam (Fig. 3) is better than the one obtained in the C-C case (Fig. 3). This aspect is strictly related to the new approach introduced: the generalized-homogenized displacements aim to create natural boundary conditions equivalent but simpler than the classical ones valid for FG beams. Indeed, the analytical solution is derived following the same procedure shown in the previous paper of the authors [14].

### 7. Conclusions

In the present work, a new theoretical formulation based on some homogenized/generalized displacements has been introduced in order to solve bending, free vibration and buckling problems of Timoshenko FGBs, i.e. mono dimensional elements with constitutive properties that vary gradually along the thickness. The proposed formulation allows the definition of a new FE approach able to uncouple the required boundary conditions and it involves the use of the Navier method for solving dynamic problems: according to the latter, the kinematic variables are approximated as the product of two independent functions. The homogenized/generalized displacements are appropriately defined with the aim of uncoupling the expression of axial, shear and moment stresses generalized to the cross section in the case of FGMs so as to achieve a greater procedural saving. Numerical results are compared, when possible, to the analytical ones obtained by following Li's model and a good match is shown. Different conditions of constraint are analysed to verify the reliability and the physical correspondence of the proposed approach: natural frequencies related to S-S, C-C, C-S, C-F beams and buckling loads for S-S, C-F are compared for different values of an opportune parameter which rules the material composition of the cross section. In accordance with physical intuition, natural frequencies and buckling loads increase with increasing the mean Young's modulus and the mean shear modulus of the cross section. Just for the sake of clarity, transversal numerical displacements are derived only for C-C and C-S beams under static condition of load and they are compared with the exact ones. The performed numerical applications have revealed that the proposed procedure is highly competitive with the most used in literature: moreover, a higher rate of convergence in the case in which natural (or static) boundary conditions need to be imposed is shown. Finally, a closed expression capable of expressing buckling loads linked to FGBs is discovered: it does

not yet exist in literature and it could be considered the natural extension of that valid for homogenous mono-dimensional structures.

## References

- [1] Elishakoff I, Gentilini C. Three-dimensional flexure of rectangular plates made of functionally graded materials, *Journal of Applied Mechanics*, 2005; 72: 788-791. <https://doi.org/10.1115/1.1985429>
- [2] Reddy J N. Analysis of functionally graded plates, *International Journal for Numerical Methods in Engineering*, 2000; 47: 663-684. [https://doi.org/10.1002/\(SICI\)1097-0207\(2000110/30\)47:1/3<663::AID-NME787>3.0.CO;2-8](https://doi.org/10.1002/(SICI)1097-0207(2000110/30)47:1/3<663::AID-NME787>3.0.CO;2-8)
- [3] Huang XL, Shen HS. Nonlinear vibration and dynamic response of functionally graded plates in thermal environments, *International Journal of Solids and Structures*, 2004; 2403-2427. <https://doi.org/10.1016/j.ijsolstr.2003.11.012>
- [4] Reddy JN. Microstructure-dependent couple stress theories of functionally graded beams, *Journal of the Mechanics and Physics of Solids*, 2011; 59, 2382-2399. <https://doi.org/10.1016/j.jmps.2011.06.008>
- [5] Eringen AC. Linear theory of micropolar elasticity, *Journal of Mathematics and Mechanics*, 1966; 15, 909-923. <https://doi.org/10.21236/AD0473723>
- [6] Yang F, Chong ACM, Lam DCC, Tong P. Couple stress based strain gradient theory for elasticity, *International Journal of Solids and Structures*, 2002; 39, 2731-2747. [https://doi.org/10.1016/S0020-7683\(02\)00152-X](https://doi.org/10.1016/S0020-7683(02)00152-X)
- [7] Wu L, Wang QS, Elishakoff I. Semi-inverse method for axially functionally graded beams with an anti-symmetric vibration mode, *Journal of Sound and Vibration*, 2005; 284, 1190-1202. <https://doi.org/10.1016/j.jsv.2004.08.038>
- [8] Sarkar K, Ganguli R. Closed-form solutions for axially functionally graded Timoshenko beams having uniform cross-section and fixed-fixed boundary condition, *Composites Part B*, 2014; 58, 361-370. <https://doi.org/10.1016/j.compositesb.2013.10.077>
- [9] Zhu H, Sankar BV. A combined Fourier series-Galerkin method for the analysis of functionally graded beams, *Journal of Applied Mechanics*, 2004; 71, 421-424. <https://doi.org/10.1115/1.1751184>
- [10] Wang CM, Reddy JN, Lee KH. *Shear deformable beams and plates*, Elsevier, 2000.
- [11] Li XF. A unified approach for analyzing static and dynamic behaviours of functionally graded Timoshenko and Euler-Bernoulli beams, *Journal of Sound and Vibration*, 2008; 318, 1210-1229. <https://doi.org/10.1016/j.jsv.2008.04.056>
- [12] Challamel N. Higher-order shear beam theories and enriched continuum, *Mechanics Research Communications*, 2011; 38, 388-392. <https://doi.org/10.1016/j.mechrescom.2011.05.004>
- [13] Falsone G, Settineri D. An Euler-Bernoulli-like finite element method for Timoshenko beams, *Mechanics Research Communications*, 2011; 38, 12-16. <https://doi.org/10.1016/j.mechrescom.2010.10.009>
- [14] Falsone G, La Valle G. A homogenized theory for functionally graded Euler-Bernoulli and Timoshenko beams, *Acta Mechanica*, 2019; 230, 3511-3523. <https://doi.org/10.1007/s00707-019-02493-w>
- [15] Reddy JN. *Energy Principles and Variational Methods in Applied Mechanics*, second ed. John Wiley & Sons, NY, 2002.
- [16] Reddy JN. *Theory and Analysis of Elastic Plates and Shells*, second ed. Taylor & Francis, Philadelphia, 2007. <https://doi.org/10.1201/9780849384165>
- [17] Heiliger PR, Reddy JN. A higher-order beam finite element for bending and vibration problems. *Journal of Sound and Vibration*, 1988; 126, 309-326. [https://doi.org/10.1016/0022-460X\(88\)90244-1](https://doi.org/10.1016/0022-460X(88)90244-1)

- [18] Antes H. Fundamental solution and integral equations for Timoshenko beams. *Computer and Structures*, 2003; 81, 383-396. [https://doi.org/10.1016/S0045-7949\(02\)00452-2](https://doi.org/10.1016/S0045-7949(02)00452-2)
- [19] Timoshenko SP. On the transverse vibrations of bars of uniform cross section. *Philosophical Magazine*, 1922; 43, 125-131. <https://doi.org/10.1080/14786442208633855>
- [20] Reddy JN. *An Introduction to the Finite Element Method*, 2nd edition. McGraw-Hill, NY, 1993.
- [21] Nickell RE, Secor GA. Convergence of consistently derived Timoshenko beam finite element. *International Journal of Numerical Methods Applied in Engineering*, 1972; 5, 243-253. <https://doi.org/10.1002/nme.1620050210>
- [22] Reddy JN. On locking free shear deformable beam elements. *Computer Methods in Applied Mechanics and Engineering*, 1997; 149, 113-132. [https://doi.org/10.1016/S0045-7825\(97\)00075-3](https://doi.org/10.1016/S0045-7825(97)00075-3)
- [23] Tessler A, Dong SB. On a hierarchy of conforming Timoshenko beam elements. *Computer and Structures*, 1981; 14, 335-344. [https://doi.org/10.1016/0045-7949\(81\)90017-1](https://doi.org/10.1016/0045-7949(81)90017-1)
- [24] Chakraborty A, Gopalakrishnan S, Reddy JN. A new beam finite element for the analysis of functionally graded materials. *International Journal of Mechanical Sciences*, 2003; 45, 519-539. [https://doi.org/10.1016/S0020-7403\(03\)00058-4](https://doi.org/10.1016/S0020-7403(03)00058-4)
- [25] Li SR, Batra RC. Relations between buckling loads of functionally graded Timoshenko and homogeneous Euler-Bernoulli beams. *Composite structure*, 2013; 95, 5-9. <https://doi.org/10.1016/j.compstruct.2012.07.027>
- [26] Şimşek M, H.H. Yurtcu HH. Analytical solutions for bending and buckling of functionally graded nanobeams based on the nonlocal Timoshenko beam theory. *Composite Structures*, 2013; 97, 378-386. <https://doi.org/10.1016/j.compstruct.2012.10.038>
- [27] Chen D, Yang J, Kitipornchai S. Elastic buckling and static bending of shear deformable functionally graded porous beam. *Composite Structures*, 2015; 133, 54-61. <https://doi.org/10.1016/j.compstruct.2015.07.052>
- [28] Ke LL, Yang J, Kitipornchai S, Bradford MA. Bending, buckling and vibration of size-dependent functionally graded annular microplates. *Compos Struct*, 2012; 94, 3250-3257 <https://doi.org/10.1016/j.compstruct.2012.04.037>
- [29] Papargyri-Beskou S, Tsepoura KG, Polyzos D, Beskos DE. Bending and stability analysis of gradient elastic beams. *International Journal of Solids and Structures*, 2003; 40, 385-400. [https://doi.org/10.1016/S0020-7683\(02\)00522-X](https://doi.org/10.1016/S0020-7683(02)00522-X)
- [30] Ma HM, Gao XL, Reddy JN. A microstructure-dependent Timoshenko beam model based on a modified couple stress theory. *Journal of the Mechanics and Physics of Solids*, 2008; 56, 3379-3391. <https://doi.org/10.1016/j.jmps.2008.09.007>
- [31] Ma HM, Gao XL, Reddy JN. A nonclassical Reddy-Levinson beam model based on a modified couple stress theory. *International Journal for Multiscale Computational Engineering*, 2010; 8, 167-180. <https://doi.org/10.1615/IntJMultCompEng.v8.i2.30>



Research Article

## Fresnel calculations of double/multi-layer antireflection coatings on silicon substrates

Al Montazer Mandong<sup>1,a</sup>, Abdullah Uzum<sup>\*1,2,b</sup>

<sup>1</sup>Department of Electrical and Electronics Engineering, Karadeniz Technical University, Trabzon, Turkey

<sup>2</sup>Department of Renewable Energy Resources/Technologies, Karadeniz Technical University, Trabzon, Turkey

### Article Info

#### Article history:

Received 17 Dec 2020

Revised 25 May 2021

Accepted 14 Jun 2021

#### Keywords:

Solar cells;

Fresnel equations;

Antireflection coating;

### Abstract

Reflectance spectra calculations of double and multi-layer antireflection coating (ARC) structures based on Fresnel equations were studied in this work. A detailed explanation of Fresnel equations was presented with different polarization of incoming light for multi-layer antireflection coatings for solar cell applications.  $\text{TiO}_2/\text{SiN}_x$ ,  $\text{MgF}_2/\text{ZnS}$  thin film stacks for double layer ARC and  $\text{SiO}_2/\text{Al}_2\text{O}_3/\text{TiO}_2$ ,  $\text{MgF}_2/\text{SiO}_2/\text{TiO}_2$  thin film stacks for multi-layer ARC were studied. Transfer matrix method and PC1D simulation software were used additionally to simulate crystalline silicon solar cells with considered double and multi-layer ARC films on their front surface with calculated thicknesses. Average reflectance (400-1100 nm) of silicon surface by Fresnel equations with triple layer ARC was around 2.72%. Solar cell performances with each ARC structure were compared to evaluate the achieved output of reflectance of investigated thin films. Simulated short circuit current density of solar cells with tri-layer ARC was  $39.71 \text{ mA/cm}^2$ , was significantly higher than that of the ARC-free solar cells resulting in an efficiency of 19.1%.

© 2021 MIM Research Group. All rights reserved.

## 1. Introduction

Solar cell industry is dominated by crystalline silicon solar cells with a global market share of 93% [1]. The highest confirmed efficiency for monocrystalline and multicrystalline are 26.7% and 22.3% respectively [1,2]. Achieving high efficiencies with low cost is important to expand the use of solar energy based on photovoltaics. To establish high efficiencies of solar cells, numerous researchers and scientists have been looking for various ways in utilizing the basic techniques to improve the efficiency of solar cells. One the most important part of the production of modern high-efficiency solar cell is the integration of antireflection coating [3]. Antireflection coating (ARC) is a thin film layer of dielectric material deposited on top of the surface of solar cell to reduce optical losses due to reflection and increase the transmittance of light, thus improving current generation of solar cell and improve its overall efficiency. Silicon nitride is the most widely used antireflection coating in industrial level production of solar cells due to various advantages such as bulk and surface passivation properties and proven stability [4,5]. As a result, deposition of  $\text{SiN}_x$  using plasma enhanced chemical vapor deposition (PECVD) became an integral part in the production of modern silicon solar cells [4,6]. Other than that, alternative ARCs including  $\text{TiO}_2$ ,  $\text{SiO}_2$ ,  $\text{Al}_2\text{O}_3$ ,  $\text{ZrO}_2$ ,  $\text{HfO}_2$  etc. has been studied and applied to the solar cell structures by a variety of deposition techniques both as a single layer or as in stacks [3,7–11]. On the other hand, solar cell simulation softwares support researchers to design, develop and optimize solar cells. Softwares such as Silvaco TCAD, Sentaurus TCAD and PC1D are used to study the significance of antireflection coating in improving the efficiency of solar cells [12–14]. Lenie et. al demonstrated the effect of  $\text{SiO}_2$  and  $\text{Si}_3\text{N}_4$  as

\*Corresponding author: [auzum@ktu.edu.tr](mailto:auzum@ktu.edu.tr)

<sup>a</sup> orcid.org/0000-0003-3473-9869; <sup>b</sup> orcid.org/0000-0001-5324-8892

DOI: <http://dx.doi.org/10.17515/resm2020.241en1217>

Res. Eng. Struct. Mat. Vol. 7 Iss. 4 (2021) 539-550

ARC on short circuit current ( $J_{sc}$ ), open circuit voltage ( $V_{oc}$ ), fill factor (FF) and efficiency ( $\eta$ ) of silicon solar cell using Silvaco software [9]. Islam et. al used Sentaurus TCAD in simulation of ITO/ $Si_3N_4$ /ZnO:Al as antireflection coating and studied the effect of ARC in  $J_{sc}$ ,  $V_{oc}$  and efficiency of silicon solar cells [8]. These studies of antireflection coatings using simulation softwares have shown a significant increase in  $J_{sc}$ , and  $\eta$  of antireflection coated silicon solar cell when compared to an uncoated solar cell. Due to the vast amount of research data that are compiled in order to make these softwares, they can predict and give accurate output on up to sub-90nm semiconductor manufacturing processes and provide atomic-level accuracy [15].

Various mathematical equations are available for solving the reflectance spectra of solar cells with ARC. The 'transfer matrix method' is the most commonly used equation for solving reflectance spectra of multi-layer thin film stacks due to abundance of available sources [16–18]. For 'N number' layers of thin films deposited on a substrate, multiple reflected and transmitted light are accounted and calculated using a transfer matrix form of each layer. Another way of calculating the reflectance spectra of ARC is through the use of 'Fresnel's equations' using Rouard's Method [19,20]. In this method, the reflectance and transmittance coefficients are calculated using Fresnel's equations which are simplified by Rouard's method. The total reflectance can be calculated by adding all the interacting light waves at the top surface of the ARC. Application of single layer antireflection coating (SLARC) equations using O.S. Heaven's equations, transfer matrix method, and Fresnel equations are available in literature. Besides that, explanations of Fresnel equations for multilayer combinations along with application in solar cells is crucial for simulating its effects for future design of solar cells.

In this work, basic structures and working principles behind double and multi-layer antireflection coatings were presented. Fresnel's equation with the use of Rouard's method were studied and compared with commonly used transfer matrix method in order to solve the reflectance spectra of double and multi-layer ARC. Introduced solutions are valid not only for silicon substrate but also for any type of substrate. Equations regarding the reflectivity of different polarities of light with respect to the incidence angle of the light source were also shown with detailed calculations. Additionally, PC1D simulation software was used to obtain various characteristics and behaviors of a silicon solar cell with up to three layers of antireflection coating which was also used for comparison purposes.

## 2. Simulation Model and Fresnel's Equations

A conventional p-type silicon solar cell consists of <front metallic contacts/antireflection coating/n-type emitter/p-type silicon substrate/p-type back surface field/back contact>. An effective ARC structure has an important role for maximum absorption and minimum reflection of the incoming light. Light is an electromagnetic wave which have both electric and magnetic fields propagating perpendicularly with each other. The light emitted by the sun incident to the Earth's surface is a non-polarized light [21]. The direction of the oscillation of the electric field in an electromagnetic wave determines the polarization direction. S-polarization or sometimes known as 'perpendicular polarization' occurs when the direction of propagation of electric field is perpendicular to the incident surface while P-polarization or 'parallel polarization' occurs when the electric field is parallel to the incident surface [18]. The light emitted by the sun is a combination of different wavelengths and polarization combined with each other which results in a white light that can be seen by the naked eye. When sunlight hits an interface, i.e. silicon, the intensity of reflection will vary depending on the polarization and angle of incidence. Those incoming waves resulting in total wave either by constructively or destructively interfering with each other. Fig. 1a and 1b illustrates the various interacting waves between the substrate and the incident medium for double layer antireflection coating (DLARC) and multi-layer

antireflection coating (MLARC) composed of three layers on silicon substrate. The variable  $n_0$  stands for the refractive index of air while  $n_s$  stands for refractive index of the silicon substrate. The refractive index of antireflection coating in between air and silicon are denoted with subsequent numbers from top to bottom layer.

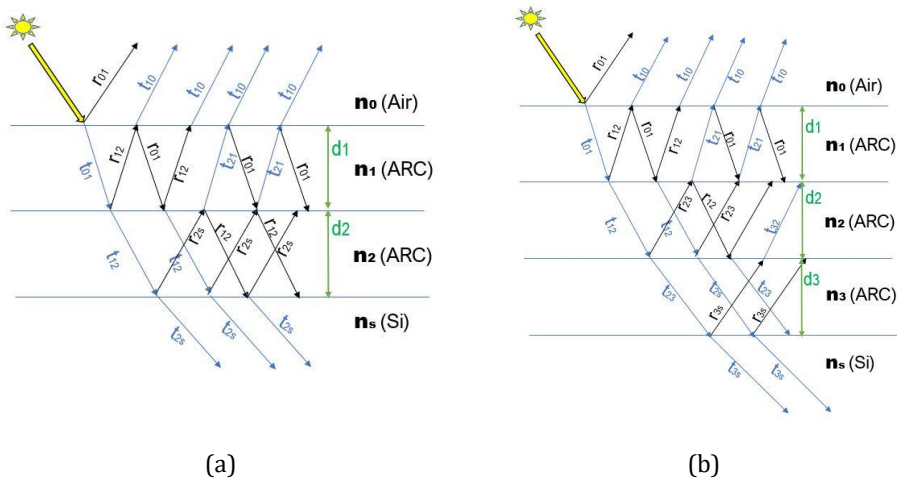


Fig. 1 (a) Interaction of light waves in a silicon, (b) Interaction of light waves in a silicon solar cell with DLARC solar cell with MLARC

When incoming light hits an interface and propagates from one medium to another medium with different refractive index, while a part of the light is transmitted or absorbed into the latter medium, some portion of the light is reflected back, as explained in literature [8,22-24]. During this transaction, the diffraction of transmitted light bends in an angle and changes the angle of propagation. At the end, the sum of all the interacting waves at the top surface figures the total intensity of the reflected light in the solar cell. Therefore, double, and multi-layer ARC can reduce the reflection more effectively than that of the single layer ARC by utilizing destructive interference of waves in multiple interfaces.

### 3. Double and Multi-Layer Anti Reflection Coating (DLARC and MLARC)

A highly efficient solar cell must have very low reflectance in wide range of wavelengths, so it can utilize as much the energy from the sun. SLARC can only achieve near-zero reflection at a specific wavelength. In order to further reduce the reflections in wider range of wavelengths with DLARC and MLARC, a combination of lower refractive index material as the outer layer and higher refractive index at the bottom layer can be stacked to lower average reflectance in wider range of wavelengths compared to SLARC. DLARC and MLARC have more complex reflections which can interfere with other reflected and transmitted waves that results in a lower total reflectance [21]. As a result, detailed calculations are needed to solve the total reflection at the surface of the solar cell due to the multiple interacting waves in a silicon solar cell with DLARC and MLARC (Fig. 1a and 1b).

#### 3.2 DLARC Equations Using Fresnel’s Equation and Rouard’s Method

Rouard’s method simplifies the calculation of the reflectance spectra of any ‘N’ number of dielectric stacks deposited on a substrate. Reflectance spectra of the solar cell with DLARC can be solved by following equations [8,19,24]:

$$\delta_1 = \frac{2\pi n_1 d_1 \cos\theta_1}{\lambda_0} \tag{1}$$

$$\delta_2 = \frac{2\pi n_2 d_2 \cos\theta_2}{\lambda_0} \tag{2}$$

$$r_1 = r_{0,1} + [(t_{0,1}e^{-i\delta_1})(r_{1,2}e^{-i\delta_1})(t_{1,0})] + [(t_{0,1}e^{-i\delta_1})(t_{1,2}e^{-i\delta_2})(r_{2,s}e^{-i\delta_2})(t_{2,1}e^{-i\delta_1})(t_{1,0})] + [(t_{0,1}e^{-i\delta_1})(r_{1,2}e^{-i\delta_1})(r_{1,0}e^{-i\delta_1})(r_{1,2}e^{-i\delta_1})(t_{1,0})] + \dots \tag{3}$$

Simplifying by using Rouard’s method

$$r_2 = \frac{r_{1,2} + r_{2,s}e^{-2i\delta_2}}{1 + r_{1,2}r_{2,s}e^{-2i\delta_2}} \tag{4}$$

$$r_1 = \frac{r_{0,1} + r_2e^{-2i\delta_1}}{1 + r_{0,1}r_2e^{-2i\delta_1}} \tag{5}$$

$$R = \left| \frac{r_{1(s)}^2 + r_{1(p)}^2}{2} \right| + \dots \tag{6}$$

### 3.2. DLARC Equations Using Transfer Matrix Method

The transfer matrix method alternative for double layer ARC can also be calculated by using the following equation:

$$R = \frac{n_0^2 \left[ \cos \delta_1 \cos \delta_2 - \frac{n_2}{n_1} \sin \delta_1 \sin \delta_2 \right]^2 + (n_0 n_3)^2 \left[ \frac{\cos \delta_1 \sin \delta_2}{n_2} + \frac{\cos \delta_2 \sin \delta_1}{n_1} \right]^2 + [n_1 \sin \delta_1 \cos \delta_2 + n_2 \sin \delta_2 \cos \delta_1]^2 + n_3^2 \left[ \cos \delta_1 \cos \delta_2 - \frac{n_1}{n_2} \sin \delta_1 \sin \delta_2 \right]^2 - 2n_0 n_s}{n_0^2 \left[ \cos \delta_1 \cos \delta_2 - \frac{n_2}{n_1} \sin \delta_1 \sin \delta_2 \right]^2 + (n_0 n_3)^2 \left[ \frac{\cos \delta_1 \sin \delta_2}{n_2} + \frac{\cos \delta_2 \sin \delta_1}{n_1} \right]^2 + [n_1 \sin \delta_1 \cos \delta_2 + n_2 \sin \delta_2 \cos \delta_1]^2 + n_3^2 \left[ \cos \delta_1 \cos \delta_2 - \frac{n_1}{n_2} \sin \delta_1 \sin \delta_2 \right]^2 + 2n_0 n_s} \tag{7}$$

### 3.2. MLARC Equations Using Fresnel’s Equation and Rouard’s Method

In order to further reduce the reflectance in a broad spectrum, multi-layer combination of different dielectric materials can be stacked on top of each other. The equation used for solving the total reflectance of MLARC can be calculated using Rouard’s method by:

For k number of layers:

$$\delta_k = \frac{2\pi n_k d_k \cos\theta_k}{\lambda_0} \tag{8}$$

For the k<sup>th</sup> layer:

$$r_k = \frac{(r_{k-1,k}) + (r_{k,k+1})e^{-2i\delta_k}}{1 + (r_{k-1,k})(r_{k,k+1})e^{-2i\delta_k}} \tag{9}$$

For  $k-1$  layer until  $k=2$ :

$$r_k = \frac{(r_{k-1,k}) + (r_k)e^{-2i\delta_k}}{1 + (r_{k-1,k})(r_k)e^{-2i\delta_k}} \quad (10)$$

$$r_1 = \frac{r_{0,1} + r_2e^{-2i\delta_1}}{1 + r_{0,1}r_2e^{-2i\delta_1}} \quad (11)$$

Then the total reflectance at the surface of ARC can be calculated by Eq. (6).  $n_1$  and  $n_2$  are the refractive indexes of the 1<sup>st</sup> and 2<sup>nd</sup> medium, respectively.  $\theta_1$  is the angle of incidence from the source to medium 1,  $\theta_2$  is the angle of light entering from medium 1 to 2,  $r_{s,p}$  is the coefficient of reflection for s and p polarizations,  $t_{s,p}$  is the coefficient of transmission for s and p polarizations.  $d_1$  and  $d_2$  are the thicknesses of the medium 1 and 2, respectively in  $nm$ .  $\delta_1$  is the phase change of the wave,  $\delta_2$  is the phase change at the 2<sup>nd</sup> layer,  $r_1$  is the total reflection coefficient,  $r_2$  is the total reflection coefficient at the 2<sup>nd</sup> layer,  $\lambda_0$  is the wavelength at free space in  $nm$ ,  $r_{a,b}$  is the coefficients of reflection from medium a to b,  $t_{a,b}$  is the coefficients of transmission from medium a to b,  $R$  is the total reflection at the surface of ARC.

#### 4. DLARC and MLARC Simulation Results

Fig. 2 shows the reflectance spectra of silicon surface with DLARC comparing to the SLARC and bare silicon surface calculated by Fresnel equations. The values of refractive index ' $n$ ' and extinction coefficient ' $k$ ' of Silicon [25], TiO<sub>2</sub> [26], MgF<sub>2</sub> [27], ZnS [28] and SiN<sub>x</sub> [29] were also obtained from [30,31]. SiN<sub>x</sub> and ZnS SLARC with various thicknesses were given in Fig. 2a and 2b where a significant decrease of the reflectance is clear comparing to the bare flat silicon surface. Minimum of spectra shifts to the higher wavelengths as the thickness of SLARC increases. Experimental measurement of TiO<sub>2</sub>/SiN<sub>x</sub> DLARC was performed in a polished p-type FZ Silicon wafer and deposited using PECVD at a substrate temperature of 200°C [32]. MgF<sub>2</sub>/ZnS DLARC was deposited using electron beam with a substrate temperature of 125°C for ZnS and 200°C for MgF<sub>2</sub> [33]. These experimental data were used to assess the accuracy of the calculations under consent of related reference. Comparisons found to be relatively in agreement with simulated data in current work. Table 1 shows the average reflectance of each device using various methodologies. Simulated data were in good agreement with the experimental data especially in visible spectrum between 400 nm to 700 nm where the solar intensity is in its maximum. Additionally, spectra of the TiO<sub>2</sub>/SiN<sub>x</sub> and MgF<sub>2</sub>/ZnS DLARC with different thicknesses in stacks were given in Fig. 2e and 2f, respectively. Minimum of the TiO<sub>2</sub>/SiN<sub>x</sub> spectra shifts through the higher wavelengths as the thickness of the stack increases. Reflectance of MgF<sub>2</sub>/ZnS DLARC coated surface in the range of 400-800 nm increases significantly when the thickness of MgF<sub>2</sub> is less than 100 nm in the stack. The one minimum characteristic of TiO<sub>2</sub>/SiN<sub>x</sub> DLARC coated wafers with high average reflectance than that of the wafers coated with MgF<sub>2</sub>/ZnS is due to the high/low ' $n$ ' order of the stack where MgF<sub>2</sub>/ZnS has a gradually increasing order of ' $n$ ' with optimum values from surface to bulk.

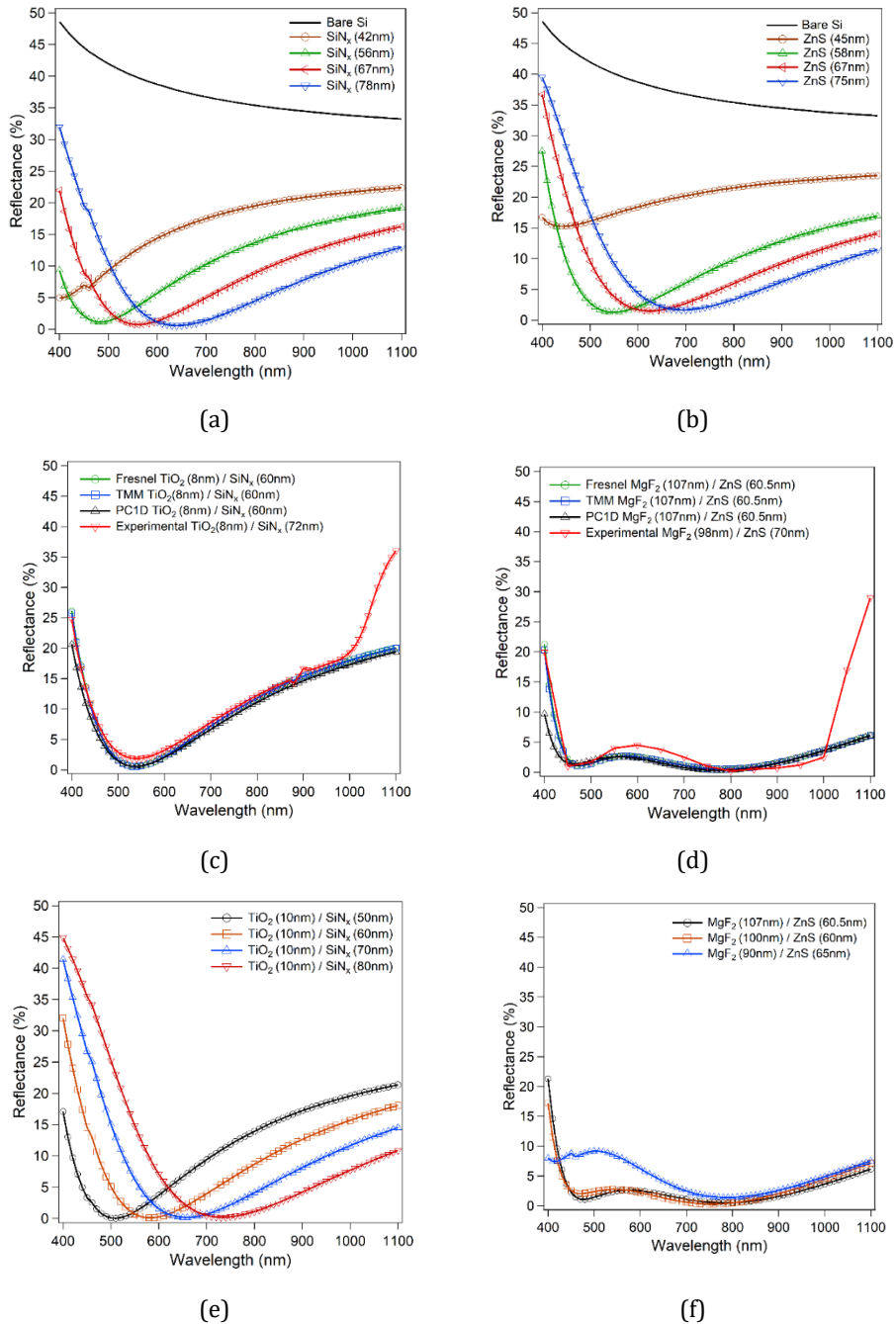


Fig. 2 Reflectance spectra of silicon substrate with (a) SiN<sub>x</sub> SLARC, (b) ZnS SLARC, (c) TiO<sub>2</sub>/SiN<sub>x</sub> DLARC, (d) MgF<sub>2</sub>/ZnS DLARC, (e) TiO<sub>2</sub>/SiN<sub>x</sub> DLARC with various thicknesses, (f) MgF<sub>2</sub>/ZnS DLARC with various thicknesses

Table 1. Average reflectance (400-1100 nm) of silicon substrate with DLARC achieved by using different methods

	Fresnel's Eq.	TMM	PC1D	Experimental
TiO <sub>2</sub> /SiN <sub>x</sub>	10.899	10.848	10.107	12.729
MgF <sub>2</sub> /ZnS	2.802	2.755	2.266	5.973

MgF<sub>2</sub>/ZnS combination provided a 2.2% average reflectance based on simulation with PC1D. Average reflection of MgF<sub>2</sub>/ZnS DLARC was estimated by Fresnel Equations as 2.8% which is slightly closer estimation than that of the TMM method.

Alternative MLARC simulations using combination of three layers of ARC on silicon substrate were shown in Fig. 3a and 3b. Table 2 summarizes the average reflectance of each device using different methodologies.

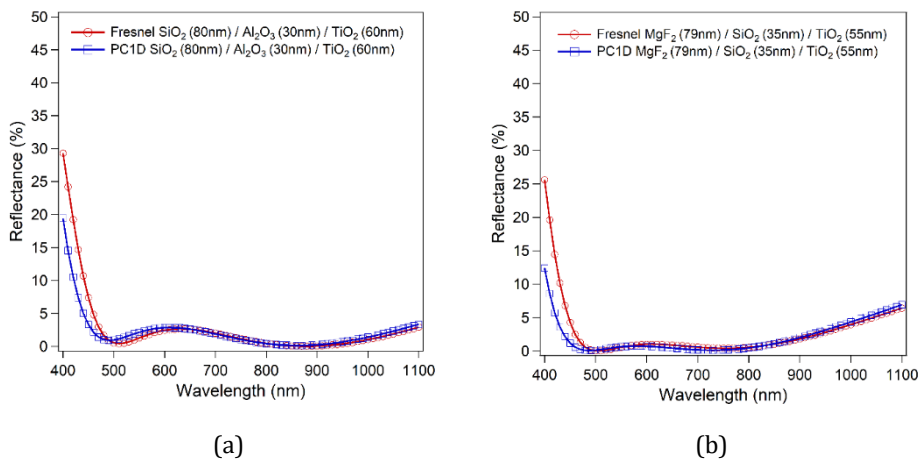
Fig. 3 Reflectance spectra of silicon substrate with (a) SiO<sub>2</sub>/Al<sub>2</sub>O<sub>3</sub>/TiO<sub>2</sub> MLARC and (b) MgF<sub>2</sub>/SiO<sub>2</sub>/TiO<sub>2</sub> MLARC

Table 2. Average reflectance (400-1100 nm) of silicon substrate with MLARC achieved by different methods

	Fresnel's Eq.	PC1D
SiO <sub>2</sub> /Al <sub>2</sub> O <sub>3</sub> /TiO <sub>2</sub>	2.799	2.111
MgF <sub>2</sub> /SiO <sub>2</sub> /TiO <sub>2</sub>	2.720	2.228

TiO<sub>2</sub> with high 'n' of 2.59 (at 550 nm) was used as the bottom layer of the ARC for MLARC where TiO<sub>2</sub> with lower 'n' of 2.11 (at 550 nm) were used for DLARC which can be achieved by different processing conditions [23]. Although MLARC layers provides similar reflection values, MgF<sub>2</sub>/SiO<sub>2</sub>/TiO<sub>2</sub> combination achieved the best results in device performance due to very low reflectance at the peak of solar spectrum with high spectral irradiance. Estimated average reflectance of the silicon surface with SiO<sub>2</sub>/Al<sub>2</sub>O<sub>3</sub>/TiO<sub>2</sub> and MgF<sub>2</sub>/SiO<sub>2</sub>/TiO<sub>2</sub> MLARC were 2.8% and 2.72%, respectively. Reflectance of SiO<sub>2</sub>/Al<sub>2</sub>O<sub>3</sub>/TiO<sub>2</sub> coated wafers provides less reflectivity especially in the range of 800-1100 nm than that of the wafers coated with MgF<sub>2</sub>/SiO<sub>2</sub>/TiO<sub>2</sub>. On the other hand, MgF<sub>2</sub>/SiO<sub>2</sub>/TiO<sub>2</sub> coated wafers have lower reflectivity in the range of 500-800 nm which covers the peak region of solar spectrum.

For the analysis of DLARC and MLARC, both TMM and Fresnel calculations can predict the behavior of reflectance spectra of antireflection coatings with different combinations of dielectric materials. Although, results by Fresnel equations were slightly closer to the experimental values than that of the values achieved by TMM, both techniques were in a good agreement with the experimental measurements. In general, a combination of a lower refractive index materials such as MgF<sub>2</sub> or SiO<sub>2</sub> with refractive index of less than 1.5 can be appropriate for the first layer while higher refractive index materials such as TiO<sub>2</sub> and ZnS are suitable materials at the bottom layer.

In case of double or multi-layer stackings, combination of materials with lower refractive index to higher refractive index in ascending order can have achieve a lower reflectance spectrum on wide range of wavelengths. Various data show the difference in the values of  $n$  and  $k$  of the same material due to different deposition techniques and parameters used such as annealing temperature [27, 28]. The output spectra of the simulation would vary depending on different values of refractive index and extinction coefficients of materials that are used. Due to the gradual refractive indexes and thicknesses of materials in MgF<sub>2</sub>/ZnS structure a reduced overall reflectivity could be achieved in DLARC. Spectra was achieved in W shape which means reflectivity reaches minimum corresponding to two wavelengths and contribute to reduce reflectivity over a broad range of spectrum [34]. MLARC provides further reduced reflectance especially in visible range and in overall spectrum. It is worth to bear in mind that the properties of the materials other than ARC effect plays an important role on silicon solar cell performances as well, such as passivation of defects etc. Therefore, all materials with good ARC may not lead high efficiencies as expected in real devices.

## 5. Silicon Solar Cell Simulations by PC1D

PC1D version 5.9 is a semiconductor modeling software made by UNSW Australia which is widely used in solar cell research [14]. High efficiency silicon solar cell with DLARC and MLARC were simulated with PC1D. Simulations were carried out by fixing the solar cell parameters except of the ARC films. The same ARC films were applied with the same thicknesses as in Figs. 2-3 to investigate the impact of each ARC film on the performance of a silicon based solar cell. Table 3 shows the parameters of the solar cell that were used in the simulation.

Table 3. Solar cell device parameters using PC1D

Front surface texture depth	3 $\mu\text{m}$
Internal optical reflectance	Enabled
Series Resistance	0.8 $\Omega$
Shunt Resistance	50000 $\Omega$
Emitter Sheet Resistance	60 $\Omega/\text{square}$
Thickness	180 $\mu\text{m}$
Front diffusion (N-type)	$2 \times 10^{20} \text{ cm}^{-3}$ peak
Rear diffusion (P-type)	$3 \times 10^{18} \text{ cm}^{-3}$ peak
Front SRV	$1 \times 10^2 \text{ cm/s}$
Rear SRV	$1 \times 10^6 \text{ cm/s}$
Bulk recombination	$\tau_n = \tau_p = 30 \mu\text{s}$
Temperature	25°C

Table 4 presents the electrical performance of each solar cell with and without ARC where relationship of the electrical parameters can be given as  $\eta = (V_{MP} \times J_{MP}) / P_{IN} = (V_{OC} \times J_{SC} \times FF) / P_{IN}$ .  $\eta$  is the conversion efficiency,  $V_{MP}$  and  $J_{MP}$  are the voltage and current at the maximum power point, respectively.  $P_{IN}$  is the standard 1 sun input power for measurements ( $100 \text{ mW/cm}^2$ ). The values of refractive index used in the simulation were obtained [27, 28].  $I$ - $V$  curves of the best solar cells with ARC compared with the simulated solar cell without ARC is shown in Fig. 4. The antireflection effect of DLARC and MLARC layers on the short circuit current density can be clearly confirmed.

Table 4. Performance of solar cells with various layers of ARC

	ARC film (thickness in nm)	$J_{SC}$ (mA/ $\text{cm}^2$ )	$V_{OC}$ (mV)	$J_{MP}$ (mA/ $\text{cm}^2$ )	$V_{MP}$ (mV)	FF (%)	$\eta$ (%)
No ARC	No ARC	26.28	609.7	24.25	517	78.25	12.54
SLARC	SiN <sub>x</sub> (67)	37.03	618.7	35.00	508.1	77.62	17.79
	ZnS (67)	36.18	618.1	33.76	515.2	77.78	17.39
DLARC	TiO <sub>2</sub> (8) / SiN <sub>x</sub> (60)	37.08	618.7	35.03	508.6	77.66	17.82
	MgF <sub>2</sub> (107) / ZnS (60.5)	39.58	620.4	36.96	515.2	77.55	19.04
MLARC	SiO <sub>2</sub> (80)/Al <sub>2</sub> O <sub>3</sub> (30)/TiO <sub>2</sub> (60)	39.45	620.4	36.91	514.3	77.56	18.98
	MgF <sub>2</sub> (79)/SiO <sub>2</sub> (35)/TiO <sub>2</sub> (55)	39.71	620.5	37.01	516.2	77.53	19.10

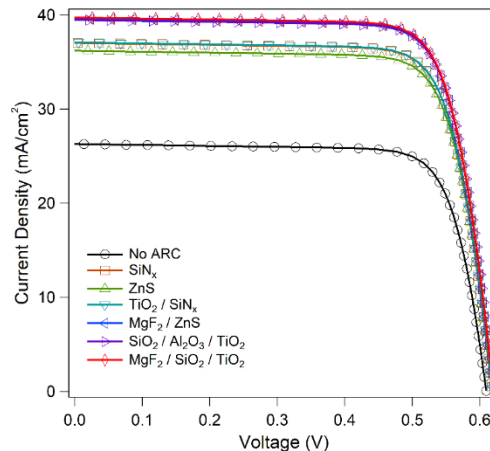


Fig. 4  $I$ - $V$  curve of best solar cells with SLARC, DLARC and MLARC compared with the solar cell without ARC

An uncoated solar cell reflects more than 35% or one third portion of incoming light due to inherent reflective properties of silicon. Increase in conversion efficiency can be confirmed by DLARC and MLARC coated solar cells due to the significant decrease in reflectance. Improvement in solar cell performances were achieved by using MgF<sub>2</sub>/ZnS as DLARC and MgF<sub>2</sub>/SiO<sub>2</sub>/TiO<sub>2</sub> as MLARC. The best  $J_{SC}$  values of the solar cells with MLARC is  $39.71 \text{ mA/cm}^2$  which is significantly higher than the  $J_{SC}$  of uncoated cell ( $26.28 \text{ mA/cm}^2$ ) due to the impact of ARC coatings on trapping the incoming light. As a result of using ARCs,

the best simulated efficiencies for corresponding cells with SLARC was 17.79% with  $\text{SiN}_x$  which was improved up to 19.1% with  $\text{MgF}_2/\text{SiO}_2/\text{TiO}_2$  MLARC. DLARC provided a  $J_{sc}$  of 39.58  $\text{mA}/\text{cm}^2$  leading an efficiency of 19% owing to the reduced reflection in a broad range of spectrum. It is worth to mention that considering the properties of materials and interfaces in the device depend on the source of the materials and the deposition/processing techniques, it is challenging to compare simulation results with real devices based on the antireflection-only effect with exact set of device parameters. However, simulations and experimental results can be compared by the total increment in the conversion efficiency for an estimation. For instance, an increase on efficiency of 6.1% with  $\text{MgF}_2/\text{ZnS}$  DLARC was reported comparing to the solar cells without an ARC [34] which is similar to the results in current work providing the possible increase of 6.32% on efficiency with  $\text{MgF}_2/\text{ZnS}$  DLARC. One of the conclusions can be that a significant reduction of surface reflectance achieved by an optimized DLARC for silicon solar cells would be sufficient for high efficiencies. However, alternative ARC structures can be developed by utilizing Fresnel equations for more complex solar cells such as multijunction, perovskite or other emerging solar cells.

## 6. Conclusion

The reflectance spectra of double and multi-layer antireflection coatings based on Fresnel equations were studied in this work. Various experimental measurements were used to validate the accuracy of the equations besides the comparison of results with transfer matrix method. PC1D simulation results were also added to further validate and measure the overall performance of each combination of ARC. The average reflection of the solar cell without any antireflection coating from 400 to 1100 nm around 37% which results to a huge loss in the overall efficiency of the solar cell due to the reflection of more than 1/3 of incoming light. It was shown that a proper selection of antireflection coating material with optimum thickness can result to such huge decrease of reflectance from the surface and increase in the overall performance of solar cells. And the Fresnel equations can be supportive for estimating the reflectance behavior of coated surfaces. For the  $\text{MgF}_2/\text{ZnS}$  DLARC stack, it was concluded that the thickness of  $\text{MgF}_2$  less than 100 nm is not favorable due to the significant increase of the reflectance of  $\text{MgF}_2/\text{ZnS}$  DLARC coated surface in the range of 400-800 nm, from 2% to up to peak of 10%. Estimated average reflectance of the silicon surface when with  $\text{SiO}_2/\text{Al}_2\text{O}_3/\text{TiO}_2$  and  $\text{MgF}_2/\text{SiO}_2/\text{TiO}_2$  MLARC were 2.8% and 2.72%, respectively.  $\text{SiO}_2/\text{Al}_2\text{O}_3/\text{TiO}_2$  coating wafers provides less reflectivity than that of the wafers coated with  $\text{MgF}_2/\text{SiO}_2/\text{TiO}_2$  especially in the range of 800-1100 nm. On the other hand,  $\text{MgF}_2/\text{SiO}_2/\text{TiO}_2$  coated wafers have lower reflectivity in the range of 500-800 nm which is valuable as it covers the peak region of solar spectrum.  $\text{MgF}_2/\text{SiO}_2/\text{TiO}_2$  MLARC achieved the overall best result with simulated efficiency of 19.1%. Selection and combination of materials are crucial in achieving the reduced reflectance which results to a more efficient device. Therefore, an accurate simulation can be rewarding for researchers and manufacturers in selecting the best combination of materials to optimize their devices.

## References

- [1] Yoshikawa K, Kawasaki H, Yoshida W, Irie T, Konishi K, Nakano K, et al. Silicon heterojunction solar cell with interdigitated back contacts for a photoconversion efficiency over 26%. *Nat Energy*. 2017;2(5). <https://doi.org/10.1038/nenergy.2017.32>
- [2] Benick J, Richter A, Müller R, Hauser H, Feldmann F, Krenckel P, et al. High-Efficiency n-Type HP mc Silicon Solar Cells. *IEEE J Photovoltaics*. 2017;7(5):1171-5. <https://doi.org/10.1109/JPHOTOV.2017.2714139>
- [3] Uzum A, Kuriyama M, Kanda H, Kimura Y, Tanimoto K, Fukui H, et al. Sprayed and Spin-Coated Multilayer Antireflection Coating Films for Nonvacuum Processed Crystalline

- Silicon Solar Cells. Int J Photoenergy. 2017;2017. <https://doi.org/10.1155/2017/3436271>
- [4] El amrani A, Menous I, Mahiou L, Tadjine R, Touati A, Lefgoum A. Silicon nitride film for solar cells. Renew Energy. 2008;33(10):2289-93. <https://doi.org/10.1016/j.renene.2007.12.015>
- [5] Liu B, Zhong S, Liu J, Xia Y, Li C. Silicon nitride film by inline PECVD for black silicon solar cells. Int J Photoenergy. 2012;2012:2-7. <https://doi.org/10.1155/2012/971093>
- [6] Hofstetter J, Cafizzo C, Luque A. Optimisation of SiNx:H anti-reflection coatings for silicon solar cells. 2007;00(c):131-4. <https://doi.org/10.1109/SCED.2007.383961>
- [7] Kanda H, Uzum A, Harano N, Yoshinaga S, Ishikawa Y, Uraoka Y, et al. Al<sub>2</sub>O<sub>3</sub>/TiO<sub>2</sub> double layer anti-reflection coating film for crystalline silicon solar cells formed by spray pyrolysis. Energy Sci Eng. 2016;4(4):269-76. <https://doi.org/10.1002/ese3.123>
- [8] Kanmaz I, Mandong AM, Uzum A. Solution-based hafnium oxide thin films as potential antireflection coating for silicon solar cells. J Mater Sci Mater Electron [Internet]. 2020;31(23):21279-87. <https://doi.org/10.1007/s10854-020-04640-9>
- [9] Uzum A, Kuriyama M, Kanda H, Kimura Y, Tanimoto K, Ito S. Non-vacuum processed polymer composite antireflection coating films for silicon solar cells. Energies. 2016;9(8). <https://doi.org/10.3390/en9080633>
- [10] Abu-Shamleh A, Alzubi H, Alajlouni A. Optimization of antireflective coatings with nanostructured TiO<sub>2</sub> for GaAs solar cells. Photonics Nanostructures - Fundam Appl [Internet]. 2021;43(April 2020):100862. <https://doi.org/10.1016/j.photonics.2020.100862>
- [11] Khan SB, Zhang Z, Lee SL. Single component: Bilayer TiO<sub>2</sub> as a durable antireflective coating. J Alloys Compd. 2020;834. <https://doi.org/10.1016/j.jallcom.2020.155137>
- [12] Islam K, Alnuaimi A, Ally H, Nayfeh A. ITO, Si<sub>3</sub>N<sub>4</sub> and ZnO:Al - Simulation of different anti-reflection coatings (ARC) for thin film a-Si:H solar cells. Proc - UKSim-AMSS 7th Eur Model Symp Comput Model Simulation, EMS 2013. 2013;673-6. <https://doi.org/10.1109/EMS.2013.112>
- [13] Abdullah H, Lennie A, Ahmad I. Modelling and simulation single layer Anti-Reflective Coating of ZnO and ZnS for silicon solar cells using silvaco software. Vol. 9, Journal of Applied Sciences. 2009. p. 1180-4. <https://doi.org/10.3923/jas.2009.1180.1184>
- [14] Clugston DA, Basore PA. PC1D VERSION 5- 32-BIT SOLAR CELL MODELING ON PERSONAL COMPUTERS. 26th IEEE Photovoltaics Spec Conf. 1997;207-10.
- [15] Synopsis. Synopsys TCAD Now Offers Atomic-level Accuracy [Internet]. [cited 2018 Nov 23]. Available from: <https://news.synopsys.com/index.php?s=20295&item=122584>
- [16] Mouchart J. Thin film optical coatings. 1. Optical coating stabilities. Appl Opt [Internet]. 1977;16(9):2486-90. Available from: <http://www.ncbi.nlm.nih.gov/pubmed/20168955> <https://doi.org/10.1364/AO.16.002486>
- [17] Bouhafs D, Moussi A, Chikouche A, Ruiz JM. Design and simulation of antireflection coating for application to silicon solar cells. Sol Energy Mater Sol Cells. 1998;73(1):79-93. [https://doi.org/10.1016/S0927-0248\(97\)00273-0](https://doi.org/10.1016/S0927-0248(97)00273-0)
- [18] Al-turk S. Analytic Optimization Modeling of Anti-Reflection Coatings for Solar Cells Analytic Optimization Modeling of Anti-Reflection Coatings for Solar Cells. Matrix. 2011;
- [19] Lecaruyer P, Maillart E, Canva M, Rolland J, Lecaruyer P, Maillart E, et al. Generalization of the Rouard method to an absorbing thin film stack and application to surface plasmon resonance To cite this version : HAL Id : hal-00664485 Generalization of the Rouard method to an absorbing thin-film stack and application to surface pl. Appl Opt Opt Soc Am. 2006;45:219-23. <https://doi.org/10.1364/AO.45.008419>
- [20] Chehura E, James SW, Tatam RP. Rouard's method as a modelling tool for the sensing characteristics of complex fibre Fabry-Perot interferometers formed between chirped

- fibre Bragg gratings . Proc SPIE. 2005;5855(May):338-41.  
<https://doi.org/10.1117/12.623441>
- [21] Cronin TW, Marshall J. Patterns and properties of polarized light in air and water. Philos Trans R Soc B Biol Sci. 2011;366(1565):619-26.  
<https://doi.org/10.1098/rstb.2010.0201>
- [22] Reithmeier M, Erbe A. Application of thin-film interference coatings in infrared reflection spectroscopy of organic samples in contact with thin metal films. Appl Opt [Internet]. 2011;50(9):C301. Available from: <https://www.osapublishing.org/abstract.cfm?URI=ao-50-9-C301>  
<https://doi.org/10.1364/AO.50.00C301>
- [23] Byrnes SJ. Multilayer optical calculations. 2016;1-20. Available from: <http://arxiv.org/abs/1603.02720>
- [24] Mandong A. Design and simulation of single, double, and multi-layer antireflection coating for crystalline silicon solar cell [Internet]. Karadeniz Teknik Üniversitesi; 2019. Available from: <http://acikerisim.ktu.edu.tr/jspui/handle/123456789/492>
- [25] Green MA. Self-consistent optical parameters of intrinsic silicon at 300 K including temperature coefficients. Sol Energy Mater Sol Cells. 2008;92(11):1305-10.  
<https://doi.org/10.1016/j.solmat.2008.06.009>
- [26] Richards BS. Single-material TiO<sub>2</sub> double-layer antireflection coatings. Sol Energy Mater Sol Cells. 2003;79(3):369-90. [https://doi.org/10.1016/S0927-0248\(02\)00473-7](https://doi.org/10.1016/S0927-0248(02)00473-7)
- [27] Dodge MJ. Refractive index of magnesium fluoride. Appl Opt. 1984;23(12):1980-5.  
<https://doi.org/10.1364/AO.23.001980>
- [28] Siqueiros JM, Machorro R, Regalado LE. Determination of the optical constants of MgF<sub>2</sub> and ZnS from spectrophotometric measurements and the classical oscillator method. Appl Opt. 1988;27(12):2549-53. <https://doi.org/10.1364/AO.27.002549>
- [29] Baker-Finch SC, McIntosh KR. Reflection of normally incident light from silicon solar cells with pyramidal texture. Prog Photovoltaics Res Appl. 2016;19:406-16.  
<https://doi.org/10.1002/pip.1050>
- [30] Polyanskiy MN. RefractiveIndex.INFO Database [Internet]. [cited 2018 Nov 22]. Available from: <https://refractiveindex.info/cite.php>
- [31] Refractive index library [Internet]. [cited 2018 Nov 22]. Available from: <https://www2.pvlighthouse.com.au/resources/photovoltaic-materials/refractive-index/refractive-index.aspx>
- [32] Yang Z-P, Cheng H-E, Chang I-H, Yu I-S. Atomic Layer Deposition TiO<sub>2</sub> Films and TiO<sub>2</sub>/SiN<sub>x</sub> Stacks Applied for Silicon Solar Cells. Appl Sci [Internet]. 2016;6(8):233. Available from: <http://www.mdpi.com/2076-3417/6/8/233>  
<https://doi.org/10.3390/app6080233>
- [33] Cid M, Stem N, Brunetti C, Beloto AF, Ramos CA. Improvements in anti-reflection coatings for high-efficiency silicon solar cells. Surf Coatings Technol. 1998;106(2-3):117-20. [https://doi.org/10.1016/S0257-8972\(98\)00499-X](https://doi.org/10.1016/S0257-8972(98)00499-X)
- [34] Sharma R, Gupta A, Viridi A. Effect of single and double layer antireflection coating to enhance photovoltaic efficiency of silicon solar. J Nano- Electron Phys. 2017;9(2):4-7.  
[https://doi.org/10.21272/jnep.9\(2\).02001](https://doi.org/10.21272/jnep.9(2).02001)
- [35] Ding K, Zhang X, Ning L, Shao Z, Xiao P, Ho-Baillie A, et al. Hue tunable, high color saturation and high-efficiency graphene/silicon heterojunction solar cells with MgF<sub>2</sub>/ZnS double anti-reflection layer. Nano Energy [Internet]. 2018;46(November 2017):257-65. <https://doi.org/10.1016/j.nanoen.2018.02.005>



Research Article

## Case study of the Beirut port explosion using 3D laser scan and nonlinear finite element model

Sahar Ismail<sup>\*1,a</sup>, Wassim Raphael<sup>1,b</sup>, Emmanuel Durand<sup>2,c</sup>

<sup>1</sup>Department of Civil Engineering, the Higher School of Engineering ESIB, Saint Joseph University of Beirut, Lebanon

<sup>2</sup>Amann Engineering, Geneva, Switzerland

### Article Info

### Abstract

#### Article history:

Received 28 Apr 2021

Revised 21 Jun 2021

Accepted 22 Jun 2021

#### Keywords:

*Blast loading;*

*Concrete damage*

*plasticity;*

*Concrete failure;*

*Finite element analysis*

Analysis of the structural failure of the Beirut port silos by the August 4, 2020 explosion is presented in this paper. The structural response of the silos due to the blast loading imposed by the explosion was assessed using 3D laser scan. Then, the silos were modeled using three-dimensional finite element models using Abaqus explicit. The silos' damage and failure were investigated to estimate the blast magnitude and to check the silos structural response against the silos' concrete strength and additional reinforcement and concrete coating added to the silos in 2000. In addition to the effects of reinforcing the ribs between the silos as well as the soil and foundation. Therefore, these parameters were tested after estimating the blast magnitude to check the structural status of the remaining part of the Beirut port silos (if they can be reusable), the role played by the foundation and soil and if the silos' response would have changed if certain parameters were taken differently in the design. In this article, the damage and silos' displacement obtained from the numerical models were compared to the results obtained by the 3D laser scan. The results of this investigated article show that a blast magnitude of 337.5 tons TNT (938 tons of Ammonium Nitrate) best captures the silos' displacement and damage amount. The silos exhibit a tilt between 20 and 30 cm in the direction of the blast. The numerical results indicate that constructing the silos with higher compressive strength would not have affected the silos' damage. Nevertheless, adding the extra concrete coating and reinforcement layer in 2000 to the outer silos decreased the amount of damage in the silos. Moreover, reinforcing the ribs between the silos would have decreased the silos displacement and damage amount. Finally, the soil and the foundation played a positive role in the explosion by absorbing part of the released energy while the silos, in the current state, cannot be reused.

© 2021 MIM Research Group. All rights reserved.

## 1. Introduction

Serious damage to buildings and other infrastructures may be caused by accidental explosions, military explosions, and terrorist attacks [1 - 3]. In addition, failure of structures can occur due to faults in design such as the collapse of Terminal 2E Roissy at Charles de Gaulle airport in 2004 [4], due to large creep and shrinkage of concrete structures [5, 6], or it can be caused by earthquakes [7 - 9] and blast loading such as the 2020 Beirut port silos explosion.

On August 4, 2020, a large fire in warehouse number 12 started at the port of Beirut. The fire was followed by a huge explosion that sent a blast wave which radiated through the city. The explosion caused severe damage all over the city of Beirut and was heard as far away as Cyprus that is about 200 km across the Mediterranean Sea. This explosion left

\*Corresponding author: [sahar.ismail@net.usj.edu.lb](mailto:sahar.ismail@net.usj.edu.lb)

<sup>a</sup> orcid.org/0000-0003-2140-6969; <sup>b</sup> orcid.org/0000-0002-2960-8760; <sup>c</sup> orcid.org/0000-0001-5134-5496;

DOI: <http://dx.doi.org/10.17515/resm2021.286st0428>

Res. Eng. Struct. Mat. Vol. 7 Iss. 4 (2021) 551-577

more than 200 people were killed, and more than 7500 injuries. Moreover, it caused around \$15 billion damage in properties and left more than 300 000 people homeless. The explosion, only few meters away from the Beirut port silos, created a crater approximately 140 m wide, which was then flooded with seawater as shown in Fig. 1. As a result, the blast wave caused extensive damage not only to the city of Beirut but also to the country's grains storage silos: the Beirut port silos (Fig. 2). The cause of explosion was blamed to the detonation of 2750 tons of Ammonium Nitrate that were stored at warehouse 12 in the port.



Fig. 1 The Beirut port silos, a) before August 4, 2020 blast and b) after August 4, 2020 blast [10]

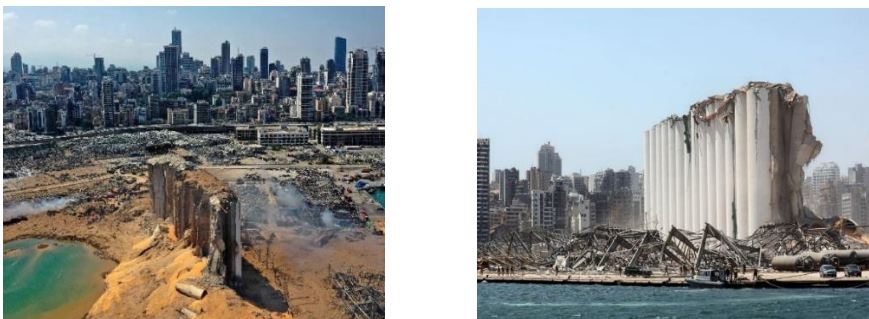


Fig. 2 The damaged grained Beirut port silos, after August 4, 2020 blast [11, 12]

Several blast incidents due to the explosion of Ammonium Nitrate occurred around the world (Table 1) such as in Texas, in the USA in 1947 that left 552 victims [13], in Toulouse, France in 2001 that left 20 victims [14], in Mihailesti Romania in 2004 that left 18 victims [15] and in West Texas, in the USA in 2013 that left 15 victims and more than 260 injuries [16]. As a result, even though Ammonium Nitrate is a common farm and garden fertilizer, it is a hazardous explosive chemical especially when it is contaminated (by intention) with fuel oil, diesel or triggered by a fire [17,18]. It should be noted that Ammonium Nitrate is listed in the European's Seveso Directive that regulates the storage and handling of all hazardous chemicals in Europe [19].

Bauer et al. [24] and King et al. [25] studied the degree of uncertainty associated with the explosive magnitude of Ammonium Nitrate. They found that an uncontaminated Ammonium Nitrate can be very difficult to detonate by any sort of flame, spark or friction under normal storage conditions. Ammonium Nitrate's detonation can only happen when its size is higher than the size of the critical charge and is characterized by a super-sonic pressure wave that travels through a material. Therefore, the initiation of an Ammonium

Nitrate shock wave requires an enormous amount of energy [25]. Nevertheless, the Joint Research Center JRC [26] does not rule out the possibility of Ammonium Nitrate's decomposition under normal storage conditions.

Table 1. Main accidents worldwide caused by Ammonium Nitrate and the corresponding charges

Blast incident location	Date	Casualties	Ammonium Nitrate (tons)
Faversham, Kent, United Kingdom [20]	April 2, 1916	115 deaths	700
Oppau, Germany [21]	September 21, 1921	561 deaths	450
Texas, USA [13]	April 16, 1947	552 deaths	2086 & 870
Brest, France [20]	July 28, 1947	29 deaths	1700-3309
Porgera Gold Mine, Papua New Guinea [22]	August 2, 1994	11 deaths	80
Toulouse, France [14]	September 21, 2001	20 deaths	200-300
Mihalesti, Romania [15]	May 24, 2004	18 deaths	20
West Texas, USA [16]	April 17, 2013	15 deaths	240
Port of Tianjian, China [23]	August 12, 2015	173 deaths	800
Beirut port, Lebanon	August 4, 2020	204 deaths	

In the work presented in this paper, the Beirut port silos blast on August 4, 2020 was analyzed using the 3D laser scan and 3D numerical model. The 3D laser scan was performed by the higher school of Engineering "ESIB" at Saint Joseph University of Beirut in collaboration with the Swiss company "Amann" Engineering. It estimated the amount of damage and deformation of the Beirut port silos. Due to its ability to provide important data, accelerating the workflow, avoiding expensive mistakes, and enhancing work productivity, 3D scan technique is being used in several industries such as engineering and medicine among others [27 - 29]. In this study, the 3D scan results were compared to the FE results, performed using Abaqus explicit. The 3D models allowed us to capture the response and damage of the silos in all its manifestations which provided a better understanding of the blast. Therefore, the objective of this paper is not only to check the Beirut port structural status following the blast, but also to explore and assess the effects and the contribution of several factors to the silos' damage amount. As such, after estimating the blast magnitude, this study examines if the remaining part of the Beirut silos can be reused. Also, it explores the role the soil and the foundation played in the blast and if the silos' response would have changed if certain parameters were taken differently in the design: silos' concrete strength, additional reinforcement and concrete coating added to the silos in 2000 and reinforcing the ribs between the silos.

## 2. Description of the Analyzed Case Study

### 2.1. The Beirut Port Silos History

In 1968, the Lebanese government at a cost of nearly \$2.8 million funded the construction of the Beirut port silos. This project was built by the Czech construction company "Prumstav" along with several Lebanese experts in the civil engineering domain. The Beirut port silos, as shown in Fig. 3, were constructed in three phases. In the first phase, in the late 1960s, 24 silos, formed of 3 rows of 8 silos each (in total 24 silos) were built. Then, in phase 2, also in the late 1960s, another 3 rows of 6 silos each (in total 18 silos) were built. Finally, in 1997, 6 extra silos were constructed to fulfill the country's grains reserves need.

From 2000 to 2002, the 48 m height, 8.5 m diameter silos having a 17 cm wall thickness underwent restoration work due to concrete carbonation. In this work, the internal wall of the outer rows of the silos was increased by 12 cm, i.e the wall thickness of these silos increased from 17 to 29 cm. Therefore, just before the August 4, 2020 blast, the Beirut port silos were able to withhold 123 200 tons of grains. The silos' capacity was divided into 48 big cells of 2000 tons each, as well as 26 smaller cells with 700 tons each and 30 cells with 300 tons each.

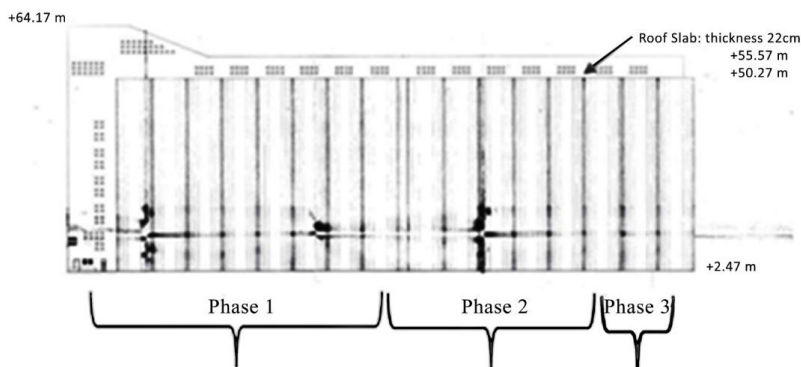


Fig. 3 The construction phases of the Beirut port silos

## 2.2. The 3D Scan and the Equipment Used

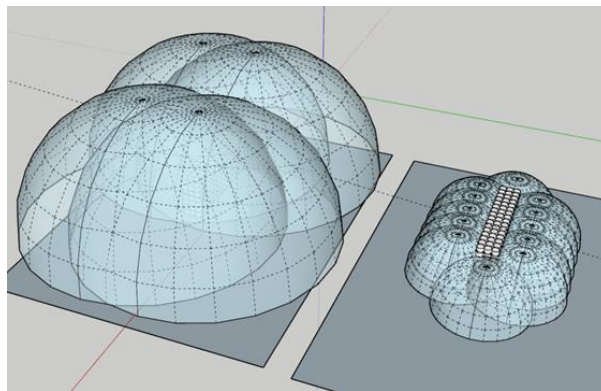
After the August 4, 2020 explosion, the Swiss Company “Amann” Engineering that is based in Geneva offered the Higher School of Engineering “ESIB” at the Saint Joseph University of Beirut free technical assistance to measure the damage in Beirut port silos using 3D scan. 3D scan technique creates high-precision 3D models of real objects by capturing several snapshots of an object and then merging them together. Thus, the 3D model, formed of small triangles or polygons that constitutes the mesh, replicates the object’s geometry within minutes. This copy can be rotated and viewed from different angles. 3D scan technology has been gaining popularity in several industries such as in industrial design, engineering, medicine, forensics, archeology, heritage preservation, art and design, quality inspection, construction, automobile, etc.

After obtaining the permission from the investigation judge and the Lebanese army, the Saint Joseph University of Beirut and the Swiss team, escorted by the Lebanese army, performed the complex mission in two phases. During the first phase in September 2020, the Swiss equipment LEICA BLK360 imaging scanner (Leica geosystems) was used (Fig. 4(a)), while during the second phase in November 2020, the German equipment Z+F Imager 5010X scanner (Zoller & Fröhlich) was used (Fig. 4(b)). The difference between the two equipment lies in the way they acquire the 3D points, the number of points captured per second and the correction of tilt measurements. The LEICA BLK360 allows the acquisition of 3D points with an integrated spherical imaging and a thermography panorama sensor system in up to 360 000 points per second. It provides live image and scanner data stream viewing and editing with automatic tilt measurements. The Z+F Imager comes with a special navigation system that estimates the scanner position and orientation to support the Z+F Laser Control registration software during pre- and post-registration on-site. It includes a dynamic compensator that corrects angular tilts for each pixel during scan acquisition that has a rate of 1 million pixels per second.



a)

b)



c)

Fig. 4 Scanning the Beirut port silos using a) LEICA BLK 360 and b) Z + F Imager 5010 X Imaging scanner and c) Comparing the scope of silos' 3D scan (the left picture concerns the Z+F scope and the right, the Leica scope)

Another difference is the scope range captured by each piece of equipment; i.e the panoramic and thermal camera. The LEICA BLK360 imaging scanner forced the team to stand far from the silos to capture the total silos' height and not be in danger. Whereas the Z+F Imager 5010X allowed the team to sweep a volume 27 times larger per scan in a smaller amount of time since it has a larger scope range than the LEICA BLK360. The Z+F Imager is much more efficient in terms of color rendering as well as calibration between the laser device and the camera. Therefore, the use of the Z+F Imager 5010X in the second phase allowed for a better final 3D scan result. Fig. 4(c) presents a comparison of the scope of the silos' 3D scan using the above equipment. The LEICA BLK360 completes full-dome scan, spherical and thermal 3D images with 6 mm at 10 m and 8 mm at 20 m point accuracy in less than 3 minutes using Waveform Digitizing (WFD) distance measurement system technology. In addition, the camera system is formed of a 15 Mpixel camera system, 150 Mpixel full-dome capture, HDR, LED flash Calibrated 360° X 300° spherical image. While the thermal camera FLIR technology is based on a longwave infrared camera with thermal 360° X 70° panoramic image. The Z+F Imager 5010X scanner comes with an external

thermal camera (Z+F T-Cam) that allows the application of infrared information to the scan. Thus, it generates 360° full-dome thermal panorama scans in a fully automatic process. It records a full panorama (32 images) in 1:45 minutes with a resolution of 382 X 288 pixel and an infrared spectrum of 7.5 to 13  $\mu\text{m}$  as well as a lens' field of view of 62° X 49°. As a result, the term thermo-panorama is scaled to a scan resolution of 2500 pixel at 360° with a working range greater than 1.6 m, a vertical field of view of 284° and a horizontal field of view of 360°. Note that the LEICA BLK360, due to its small size, was used in the slopes of the silos while walking on the grains. On the other hand, although the Z+F Imager 5010X provided more precise images, it was heavier and harder to manipulate than the LEICA BLK360 [30, 31].

As shown in Fig. 5, 752 million points of measure in three dimensions using 25 stations in 360° panorama infrared images were obtained. Therefore, a full panoramic picture of the silos was acquired using the LEICA BLK360 as well as the Z+F Imager 5010X (Fig. 6 and 7 (the video)). The obtained results show that the silos exhibit a general tilt of 20 to 30 cm in the direction of the blast. It should be noted that this tilt is not related to the original silos' construction. The silos, in their current state, do not pass the silos' design codes. The damage in the silos can be explained as follows: either the inner part (inside half cylinder) is damaged and/or the pile head is deformed beyond the elastic range and therefore broken (Fig. 8).

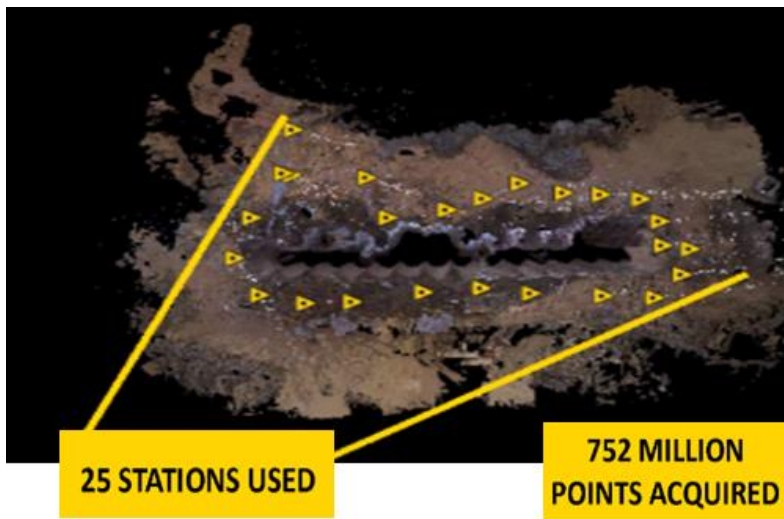


Fig. 5 The Beirut port silos 3D scan, points acquired, and stations used

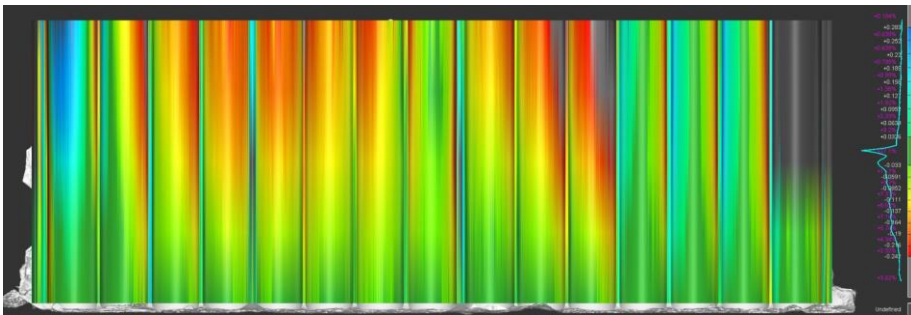
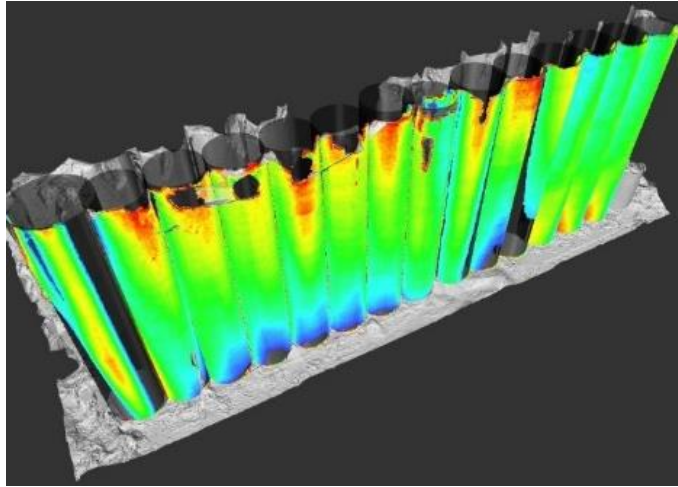


Fig. 6 The Beirut port silos 3D scan (the color shadings red, green and blue refer to a 20, 10 and 0 cm displacement in the direction of the explosion)



Fig. 7 The Beirut Port Silos 3D scan (open the link to access the video)

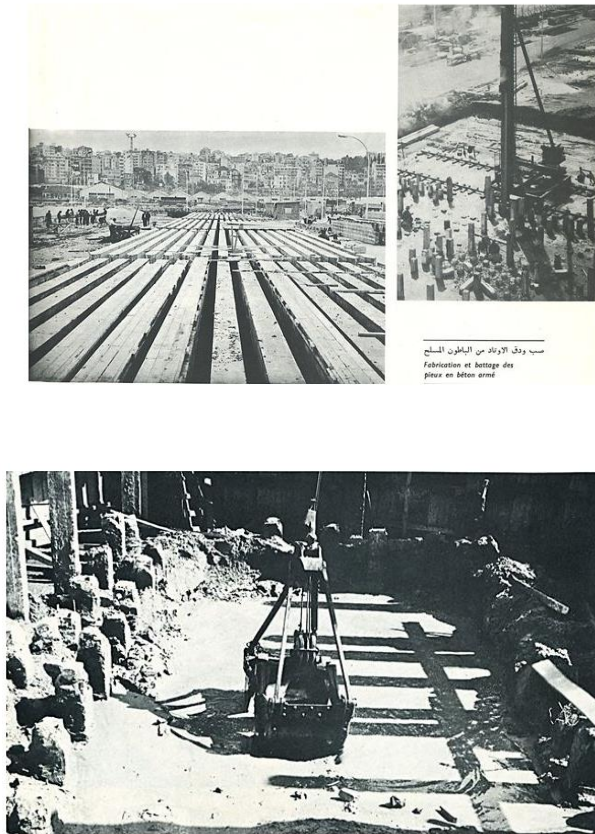


Fig. 8 Grain silos' foundation construction (pile cap and driven piles) and excavation for the base slabs as well exposing the piles head before casting the pile cap (GEER report [32])

### 2.3. The Numerical Model

3D Finite Element model was built to simulate the blast of the Beirut port silos using the FE software Abaqus explicit. The analyses were performed using large strain formulations while incorporating geometric nonlinearity. The simulated 3D models consisted of the reinforcement concrete silos and the grains (Fig. 9). The silos were built using 313 741 4-node doubly curved shell, reduced integration, hourglass control, finite membrane strains S4R shell elements, as detailed in Table 2. In addition, the silos steel reinforcement was defined as layers of reinforcement as part of the silos' shell elements using the rebar command (rebars' layers option) available in Abaqus. The grains: wheat and corn, available at the time of the explosion (Fig. 10) were built using 529 678 8-node linear brick, reduced integration, hourglass control C3D8R solid elements (Table 2).

The 8.5 m diameter modeled reinforced concrete silos were 48 m in height. The restoration work performed in 2000 (concrete and steel reinforcement) were accounted for in the numerical model. Thus, the outer silos had a 29 cm wall thickness while the internal silos had a 17 cm wall thickness. Fig 11 presents the silos geometry and it details the steel reinforcement, adopted in the 1960s (Fig 11, b) and 2000s (Fig 11, c) designs.

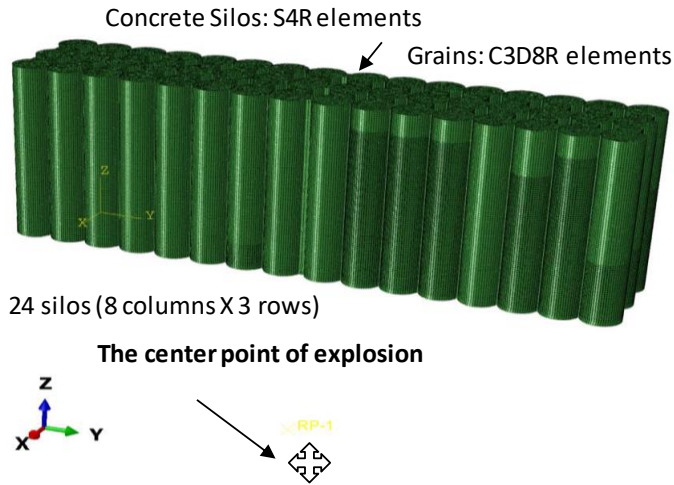


Fig. 9 The FE model

Table 2. Numerical model parts and properties

Part	Material	Element type used	Number of nodes	Number of elements
Silos	Reinforced Concrete	S4R shell elements	302071	313741
Grains	Wheat and Corn	C3D8R solid elements	578970	529678
Pile cap	Reinforced Concrete	S4R shell elements	4800	7902
Driven Piles	Reinforced Concrete	B31 beam elements	20846	17868
Soil Medium	Backfill platform	C3D8R solid elements	37500	30400

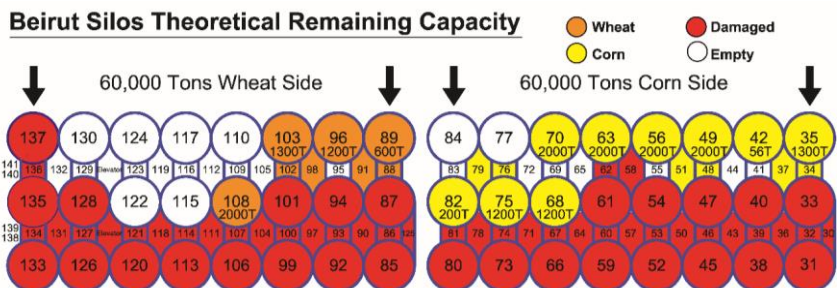


Fig. 10 Beirut silos grains capacity at the time of the blast

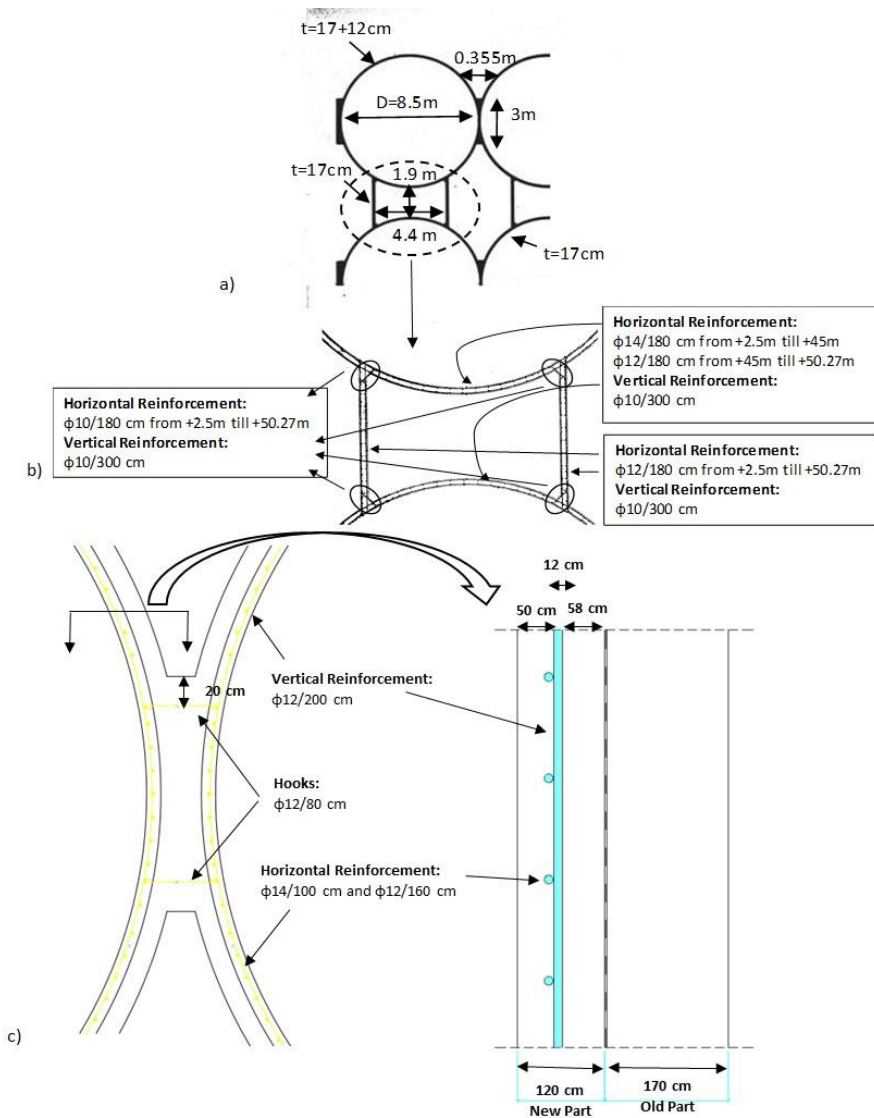


Fig. 11 a) The geometry of the Beirut port silos, b) The steel reinforcement of the Beirut port silos and c) The concrete and steel restoration work of the Beirut port silos

The blast on the silos was modeled using the CONWEP blast loading model in Abaqus explicit. This model simulates, through incident and reflected pressure, the loading effects caused by an explosion of an air blast (spherical waves) or a surface blast (hemispherical incident waves). Noting that the August 4, 2020 blast produced a hemispherical incident wave. The bottom of the silos' boundary was assumed to be fixed while the blast loading was applied at the silos' surface facing the explosion.

The relevant properties of the silos, steel and grains used in the models are presented in Table 3. In this Table,  $\rho$  is the density ( $\text{kg}/\text{m}^3$ ),  $E$  is the Young modulus (GPa),  $\nu$  is the

Poisson’s ratio,  $\sigma_y$  is the yield stress (MPa),  $K$  is the ratio of the second stress invariant on the tensile meridian,  $fb0/fc0$  is the ratio of initial equibiaxial compressive yield stress to initial uniaxial compressive yield stress,  $c$  is the soil cohesion (kPa),  $\Phi$  is the friction angle ( $^\circ$ ),  $\psi$  is the dilation angle ( $^\circ$ ) and  $f_{c,m}$  is the mean concrete compressive strength (MPa). The simplified damage plasticity model was used to define the concrete in the silos [33]. In addition, the inelastic/plastic behavior of the steel reinforcement was simulated using elastic-perfectly plastic material behavior by defining the steel yield stress. Whereas the grains: wheat and corn, were assumed elastic based on EN1991-4 [34] provision. Noting that the grains were also simulated using plastic material. The results show that the permanent displacement at the head of the third row of silos slightly increases from elastic to plastic cases without affecting the amount of damage in the silos. For example, for the 337.5 tons TNT case, the permanent displacement at the head of the third row of silos only increases by 2.18% from elastic to plastic cases. Nevertheless, since the simulation running time of the plastic case needs twice as much as the elastic and the authors in this article wanted to account for the mass and movement of the grains, the grains were modeled using elastic properties.

Table 3. Materials Properties

Steel Properties								
$\rho$ (kg/m <sup>3</sup> )	$E$ (GPa)	$\nu$	$\sigma_y$ (MPa)					
7850	206	0.3	448					
Wheat Properties								
$\rho$ (kg/m <sup>3</sup> )	$E$ (MPa)						$\nu$	
769	20						0.2	
Corn Properties								
$\rho$ (kg/m <sup>3</sup> )	$E$ (MPa)						$\nu$	
721	20						0.32	
Concrete Properties								
$\rho$ (kg/m <sup>3</sup> )	$f_{c,m}$ (MPa)	$\nu$	$\psi$ ( $^\circ$ )	Eccentricity	$fb0/fc0$	$K$	Viscosity parameter	$E$ (GPa)
2400	30	0.2	31	0.1	1.16	0.67	0	26.6

To determine the center point of explosion, i.e. the detonation center point, the aerial photos captured by the Lebanese Army forces as well as the investigation done by Forensic Architecture [35] were used. As shown in Fig. 12, the center point of explosion was located, at about 70 m in front of the silos and 40 m from the side of the silos, in warehouse number 12 which contained the explosive materials.

Since the CONWEP model in Abaqus requires the equivalent mass of explosive materials to be in terms of TNT, the mass of Ammonium Nitrate was transformed into an equivalent mass of TNT by multiplying it by a scaling factor. Note that most finite element software determines the effect of an explosion in terms of the TNT equivalency model [36]. Therefore, the consequence of an explosion is documented in TNT mass equivalent as follows:

$$W_{TNT} = W_{exp} X P_{exp} X \eta \tag{1}$$

where:  $W_{TNT}$  is the equivalent mass of TNT,

$W_{exp}$  is the weight of the explosive substance,

$P_{exp}$  is the explosive magnitude. It is defined by the ratio of the decomposition energy of 1 ton of substance (in J) divided by the detonation energy of 1 ton of TNT (J),

$\eta$  is the efficiency of the explosion. It is defined by the ratio of the real emitted to the theoretical energy of the explosion [37].

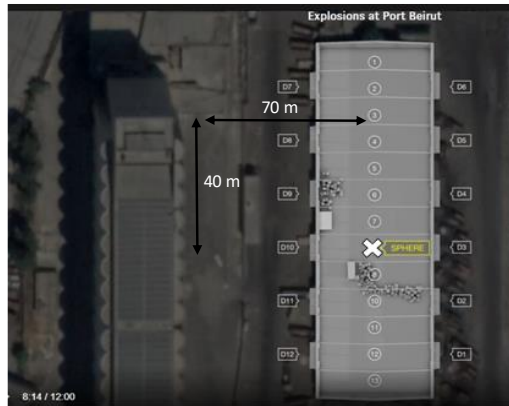


Fig. 12 The center point of explosion in warehouse number 12

Cooper [38] and Locking [39] among other researchers, showed that the TNT equivalency model might present a high degree of uncertainty in terms of explosive magnitude estimation. 20 to 30% errors may be found in TNT equivalency between different studies in the literature. This is related to the various tests adopted such as the “Air Blast” or the “Sand Crush” to determine the TNT equivalency and the conditions associated with these tests. As a result, HSE [37,40] recommends not to accurately measure the explosive field since the explosion is not only related to the mass of explosive substance but also to the state of confinement, storage condition as well as the possibility of the presence of other contaminated materials that may affect the explosion and the amount of released energy. Nevertheless, several researchers in the literature estimated the equivalent mass of TNT by multiplying the quantity of the explosive substance by a scaling factor [14, 37, 41 - 44]. The value of this scaling factor ( $P_{exp} X \eta$ ) varies from a study to another. In this study, a scaling factor of 0.39 was adopted which is based on Krauthammer [44] study and the Lebanese army investigation data. As such, the mass of Ammonium Nitrate used in the CONWEP model was transformed into an equivalent TNT mass by multiplying it by a scaling factor of 0.39.

Finally, to make sure accurate and stable results are obtained in the FE simulations while minimizing the computational speed, a mesh sensitivity analysis was performed in Abaqus. Different meshing options were adopted for the shell silos and the solid grains: 0.25, 0.5 and 1 m, to check the maximum amount of deformation in the least damaged row of silos (row number 3), occurring at the head. The results of the mesh sensitivity analysis, as shown in Fig. 13, indicate that at the head of the third row of silos, the maximum displacement varies on average 3.1 and 2.62% while the permanent displacement varies on average 3.19 and 4.43% between the 0.25 and 0.5 m and between the 0.5 and 1 m cases respectively. Since the computational time of the 0.25 m case is 45 hours while the computational time of the 0.5 m is 23 hours and the deformations at the head of the silos only varies by about 3% between the 0.25 and 0.5 m, the 0.5 m mesh size was adopted in the FE analysis in this article. Also, to validate the FE model and to make sure the model is working correctly, first the artificial energy history was compared to the total energy. The results show that the artificial energy is significantly lower than the total internal energy.

For example, for the 337.5 tons of TNT case, the maximum artificial energy equal to 66.18 MJ is lower than the maximum total internal energy equal to 1053.19 MJ, indicating that the results are trustworthy with small artificial effects. Then, the FE results were compared to the 3D scan results in terms of damage as well as deformations in the silos, as will be detailed in the next section.

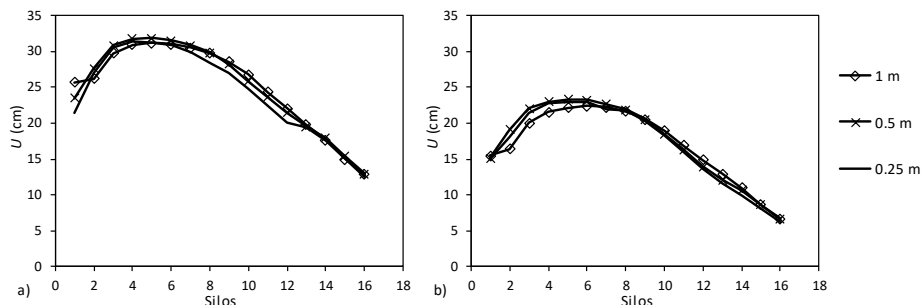


Fig. 13 a) Maximum displacement and b) permanent displacement in the direction of the blast at the head of the silos for different mesh sensitivity analysis

### 3. Comparison Between Site Measurements and the Results of the Numerical Model

To check the structural status of the remaining part of the Beirut port silos (if they can be reusable) and if the silos' response would have changed if certain parameters were taken differently in the design, an estimation of the blast magnitude was first performed. Thus, magnitudes of the blast, expressed in terms of equivalent masses of TNT, of 225, 337.5, 550, 875 and 1100 tons (563, 938, 1375, 2188 and 2750 tons of Ammonium Nitrate) were considered/varied from the baseline case. The baseline case accounts for a mean concrete compressive strength of 30 MPa with all additional concrete coating and steel reinforcement added in 2000 and includes all grains available at the time of the explosion, as described in section 2. Moreover, the blast loading was applied at the silos' surface facing the explosion with the detonation center point as indicated in Fig. 12 in the warehouse which contained the explosive materials. The displacements in the direction of the explosion at the head of the silos in the third row, shown in Fig. 14, clearly demonstrate the significant contribution of the magnitude of the blast. It should be noted that a maximum and a permanent displacement were obtained for each silo. Since a permanent displacement was exceeded, then yield strength was exceeded. Note that the third-row silos' numbering in is indicated in Fig. 15.

For example, in silo 4, as shown in Fig. 14 and 16 and Table 4, the maximum displacement increases from 21.3 to 45.4 cm while the permanent displacement increases from 14.2 to 37.6 cm as the blast magnitude is increased from 225 to 1100 tons TNT. Based on the above, the FE results were henceforth compared to the 3D scan results. Fig. 16 compares the displacement of the silos in the direction of the blast based on the 3D scan and the FE result. The results show that the first silo in the third row (the least damaged row), has lost its geometry. Whereas the other silos in this row have pertained their geometry and their 8.5 m diameter; nevertheless, they tilted around 20 cm. Therefore, the silos in their current state, do not pass the limits set by design codes such as Eurocode [45]. The results of the 3D scan, presented in Fig. 6, points out to a displacement of 20 cm (in red), 10 cm (in green) and 0 cm (in blue) in the direction of the explosion.

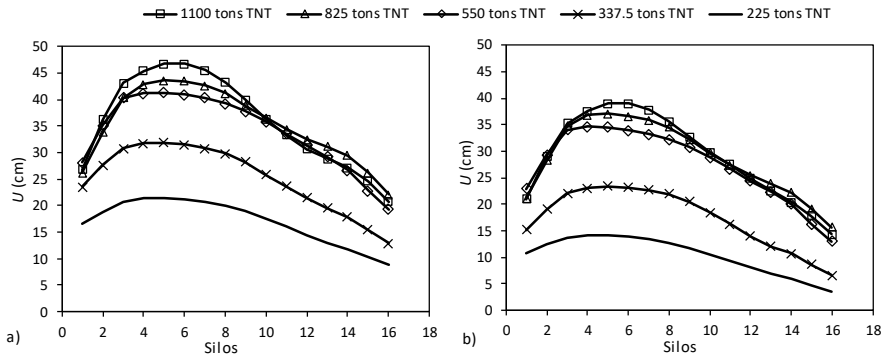


Fig. 14 a) Maximum displacement and b) permanent displacement in the direction of the blast at the head of the silos for different blast magnitudes (baseline case)

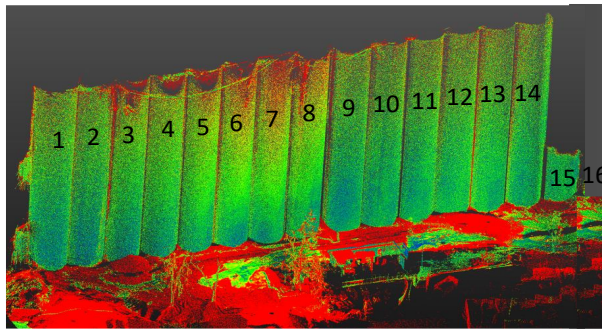


Fig. 15 Silos 1 to 16 in the third row

Comparing the results of Fig. 6 (3D scan) to Fig. 14 and 17 (FE results), we obtain that blast magnitudes of 550, 875 and 1100 tons TNT do not compare favorably to the results obtained from the 3D scan. A blast magnitude of 337.5 tons TNT (938 tons of Ammonium Nitrate) is found to best capture the 3D scan results and therefore, the real silos' displacement and damage. This is clearly illustrated in Tables 4 and 5 and Fig. 6 where silos 2 to 10 present a permanent displacement of around 20 cm while silos 11 to 14 present a permanent displacement of around 10 cm. For example, for silos 4, 5 and 9, the difference between the FE and 3D scan results is equal to 22, 14 and 3% for the estimated 337.5 tons TNT case while it is equal 52, 49 and 39 % for the 1100 tons TNT case. It should be noted that Rigby et al. [46], using empirical formula estimated the magnitude of the blast to an equivalent mass between 550 to 1100 tons TNT. In addition, Diaz [47] using images and videos' recordings of the explosion posted on social media, estimated the magnitude of the blast to be in the order of 1100 tons TNT while Aouad et al. [48] using fireball analysis, estimated the magnitude of the blast to be equivalent to 810 tons TNT. Also, Stennett et al. [49] and Pisman et al. [50] using videos posted on social media in addition to analyzing

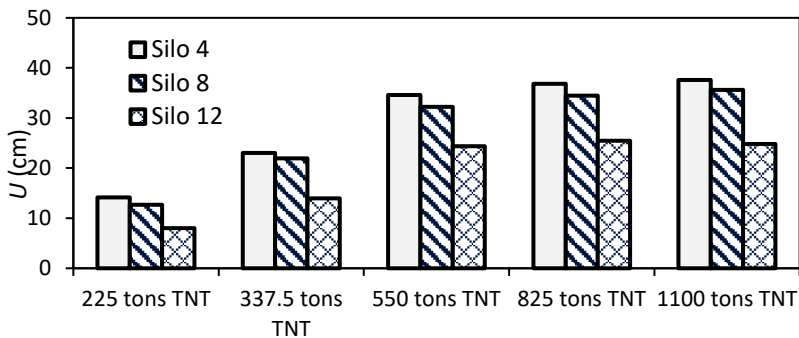


Fig. 16 Maximum permanent displacement in silos 4, 8 and 12 for the different blast magnitudes

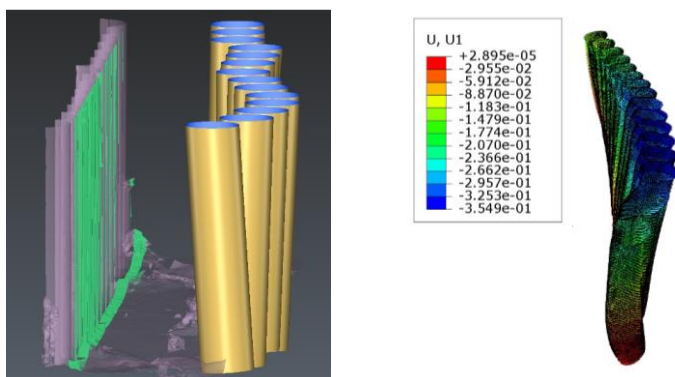


Fig. 17 Displacement of the silos in the direction of the blast a) 3D scan and b) FE results (in m)

the crater formed by the blast [50] estimated the blast magnitude to an equivalent 637 tons of TNT with lower and upper bounds of 407 and 1000 tons and 650 tons of TNT with lower and upper bounds of 300 and 1000 tons respectively. Also, Valsamos et al. [51], based on the geospatial data taken from the open-source world map OpenStreetMap, estimated the blast magnitude to an equivalent 1100 tons TNT. To present the state of damage of the 337 tons TNT estimated case, the silos’ damages in compression and tension are presented in Fig 18. The amount of silos’ damage, extracted from the FE models, presents the degradation of the silos’ elastic stiffness and is described by the compressive damage variable “ $d_c$ ” (damage in compression) and the tensile damage variable “ $d_t$ ” (damage in tension), where these damage variables range from 0: no damage to 1: destruction. Moreover, to show the state of damage of the silos’ elements, the cumulative surface damage rate curves are plotted in Fig. 19. On the ordinate is the percentage of the damaged surface having undergone the amount of damage indicated while on the abscissa is the damage indicator (1 refers to completely damaged elements/surfaces). Finally, the status of damage of the 1100 and 337.5 tons of TNT are shown in Fig 20. As indicated by these figures, for the 1100 tons TNT case, the first and second row of silos are destroyed. On the other hand, for the 337.5 tons of TT case, the first row of silos is destroyed while the second is partially destroyed, similar to reality where part of the second row of silos is still visible after the explosion (Fig 2).

Table 4. Permanent displacement in the direction of the blast (cm)- FE results

FE/different blast magnitudes	1	2	3	4	5	6	7
225 tons TNT	10.87	12.40	13.78	14.18	14.21	13.91	13.31
337.5 tons TNT	15.15	19.07	22.03	23.03	23.35	23.22	22.69
550 tons TNT	22.94	29.31	33.99	34.63	34.50	33.96	33.22
825 tons TNT	21.08	28.22	34.75	36.86	37.01	36.63	35.82
1100 tons TNT	21.02	29.02	35.21	37.59	38.95	38.94	37.79

Table 4 (con.). Permanent displacement in the direction of the blast (cm)- FE results

FE/different blast magnitudes	8	9	10	11	12	13	14	15	16
225 tons TNT	12.65	11.72	10.48	9.26	8.02	6.92	6.02	4.84	3.56
337.5 tons TNT	21.92	20.55	18.44	16.30	13.99	12.10	10.68	8.66	6.57
550 tons TNT	32.21	30.82	28.85	26.63	24.41	22.36	19.97	16.24	13.04
825 tons TNT	34.47	32.25	29.72	27.40	25.43	23.93	22.17	19.18	15.67
1100 tons TNT	35.62	32.66	29.83	27.49	24.83	22.53	20.35	17.86	14.39

Table 5. Comparison between the FE and 3D scan results

	silo	FE (tons TNT)					3D scan
		225 kt	337.5	550t	825	1100	
<i>U</i> (cm)	4	14.2	23.0	34.6	36.9	37.6	18
% difference (3D scan to FE)		-27.0	21.8	48.0	51.2	52.1	-
<i>U</i> (cm)	5	14.2	23.3	34.5	37.0	39.0	20
% difference (3D scan to FE)		-40.7	14.3	42.0	46.0	48.7	-
<i>U</i> (cm)	9	11.7	20.6	30.8	32.2	32.7	20
% difference (3D scan to FE)		-70.7	2.7	35.1	38.0	38.8	-

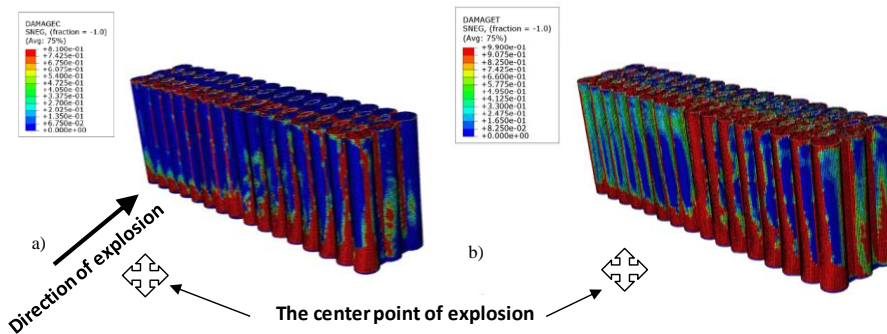


Fig. 18 Damage in a) compression and b) tension- 337.5 tons TNT baseline case (FE) (Damage variables range from 0 (no damage) to 1 (destruction))

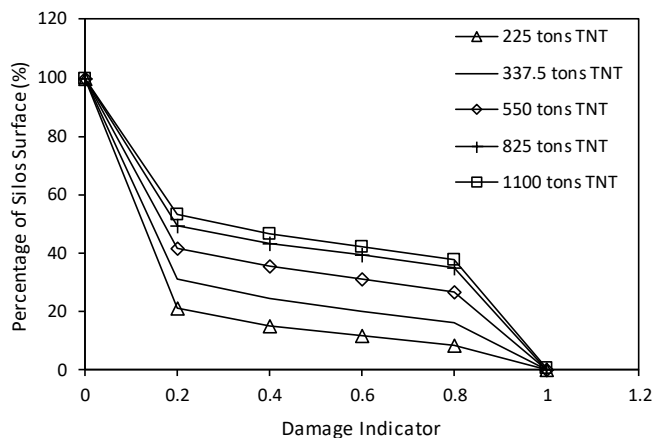


Fig. 19 The cumulative surface damage rate curve

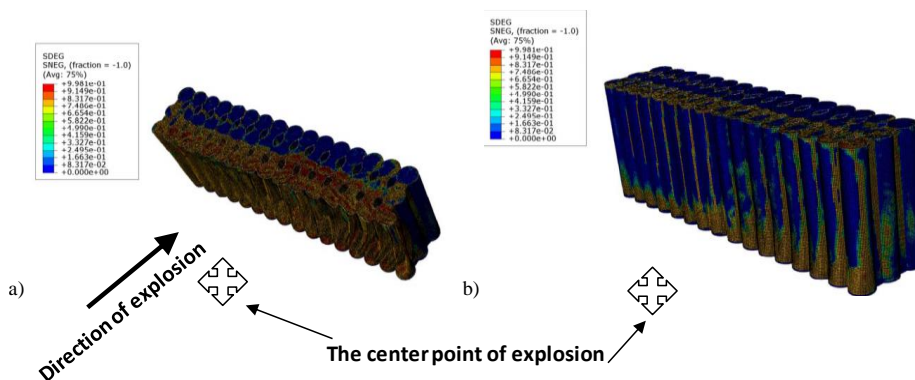


Fig. 20 The SDEG output of the a) 1100 and b) 337.5 tons of TNT simulated cases (Damage variables range from 0 (no damage) to 1 (destruction))

#### 4. Analysis of Additional Parameters Responses to the Blast Loading

##### 4.1. Effect of the Concrete Strength

To study the effect of concrete strength, the displacement response of Beirut port silos was investigated for concrete compressive strengths  $f_{c,m}$ : 30 and 40 MPa starting from the baseline scenario. The results obtained and presented in Fig. 14, 21 and 22 indicate that for low levels of blast magnitude (225 tons and 337.5 tons TNT),  $f_{c,m}$  does not affect the silos' displacement. The average ratio of permanent displacement at the head of the silos for the case of  $f_{c,m}$ =40 MPa to  $f_{c,m}$ =30 MPa in the direction of the explosion is around 1.00 and 1.03 for 225 tons and 337.5 tons TNT respectively. However, as the magnitude of the blast increases from 550 tons to 1100 tons TNT, this ratio increases from 1.09 to 1.36 for the case of  $f_{c,m}$ =40 MPa to  $f_{c,m}$ =30 MPa.

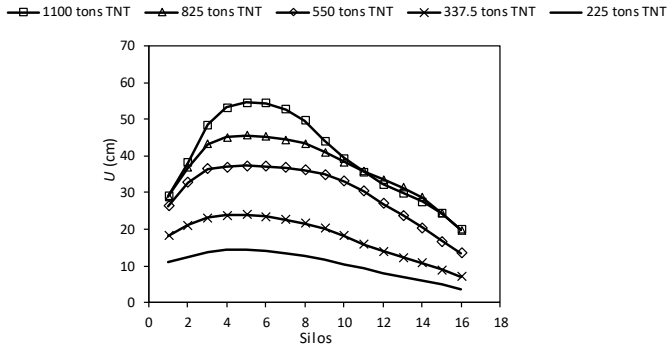


Fig. 21 Permanent displacement in the direction of the blast at the head of the silos for different blast magnitudes in the case of  $f'_{c,m}=40$  MPa

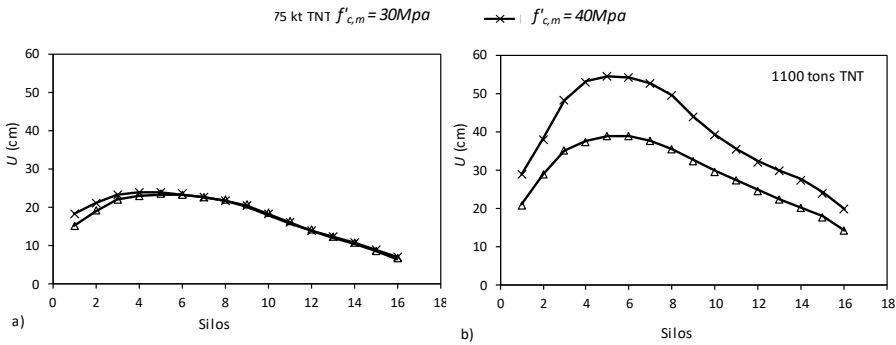


Fig. 22 Permanent displacement in the direction of the blast at the head of the silos for different concrete strength for a blast magnitude of a) 337.5 tons TNT and b) 1100 tons TNT

The significant contribution of concrete compressive strength as the magnitude of the blast increases may be due to the improvement of concrete shear resistance that leads to a reduction in the absorbing capacity of the blast energy. In general, the concrete shear strength increases with the increase in compressive strength. In addition, concrete with higher compressive strengths has greater resistance to blast loading [52]. Therefore, as the compressive strength increases, the concrete becomes stronger and able to withstand more load; in other words, it can withstand more permanent deformation. Noting that the increase in concrete compressive strength makes the latter more ductile, causing the failure of the structure in a brittle manner. This is manifested by the decrease not only in the amount of energies stored in the model under the blast model (the strain energies) but also in a decrease in the total and kinetic energies. For example, as the concrete compressive strength increases from 30 to 40 MPa for the 1100 tons cases, the strain energy decreases from 480.29 to 395.50 MJ and the total energy decreases from 29.60 to 26.14 MJ. The increase in concrete compressive strength also causes a decrease in the amount/level of silos' damage. Nevertheless, for the low level 337.5 tons of TNT estimated blast magnitude, designing silos with higher compressive strength would not have affected the damage obtained in Beirut port silos.

### 4.2. Effect of the Additional Reinforcement and Concrete Coating (ARC) Added in 2000

To assess the contribution of the additional reinforcement and concrete coating (ARC), added from 2000 to 2002 to the outer silos, the damage and displacement behavior of the silos in the case of “no ARC” was compared to the case of “with ARC” (baseline case) for the different blast magnitudes. In the restoration work, the internal wall of the outer rows of the silos was increased by 12 cm and an extra layer of steel reinforcement was added as shown in Fig. 11. The results, presented in Fig. 23 and Table 6, show that the silos with “no ARC” exhibit lower tilting/displacement but a higher amount of damage (in compression and tension) for blast magnitudes greater than 337.5 tons TNT compared to the “with ARC” cases. For example, the ratio of permanent displacement in the direction of the blast for the case “with ARC” compared to the “no ARC” case in silo number 1 is equal to 0.75 for 225 tons TNT, while it is equal to 0.97 and 1.09 for 337.5 tons TNT and 882.5 tons TNT respectively. Similarly, this ratio in silo number 6 is equal to 0.82 for 225 tons TNT, while it is equal to 1.25 and 1.35 for 337.5 tons TNT and 882.5 tons TNT respectively. Therefore, for the estimated blast magnitude 337.5 tons TNT, the case “with ARC” (baseline case) exhibits on average a 5 % greater amount of displacement compared to the “no ARC” case. It should be noted that silos 15 and 16 were destroyed in the blast. For the estimated blast case (337.5 tons TNT), the amount of damage in compression and tension exhibited in the silos is greater in the case of “no ARC” (Fig. 24) compared to the “with ARC” case (Fig. 18). As a result, the FE results indicate that reinforcing the outer silos from 2000 to 2002 played a positive role in the blast by decreasing the amount of the silos’ damage.

Table 6. Ratio of permanent displacement in the direction of the blast (cm) of the cases with ARC to no ARC

Additional reinforcement	Magnitude of the blast (tons TNT)	1	2	3	4	5	6	7
		disp (with ARC)/ disp (no ARC)	225	0.75	0.77	0.82	0.84	0.84
	337.5	0.97	1.06	1.19	1.22	1.24	1.25	1.24
	550	1.52	1.66	1.75	1.68	1.61	1.60	1.61
	825	1.09	1.18	1.35	1.37	1.35	1.35	1.36
	1100	0.98	1.08	1.20	1.22	1.24	1.25	1.23

Table 6 (con.). Ratio of permanent displacement in the direction of the blast (cm) of the cases with ARC to no ARC

Additional reinforcement	Magnitude of the blast (tons TNT)	8	9	10	11	12	13	14	15	16
		disp (with ARC)/ disp (no ARC)	225	0.77	0.73	0.68	0.64	0.61	0.59	0.56
	337.5	1.23	1.20	1.13	1.04	0.94	0.85	0.79	0.69	0.58
	550	1.64	1.70	1.74	1.73	1.75	1.73	1.62	1.41	1.24
	825	1.37	1.41	1.43	1.42	1.46	1.49	1.56	1.53	1.33
	1100	1.20	1.18	1.17	1.17	1.15	1.14	1.12	1.08	0.97

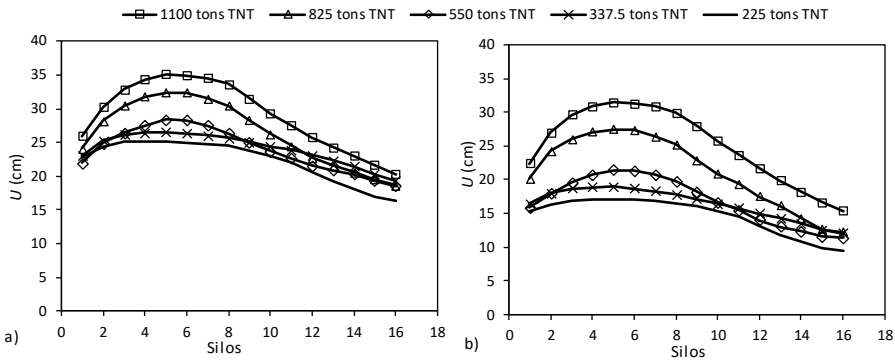


Fig. 23 a) Maximum displacement and b) permanent displacement in the direction of the blast at the head of the silos for different blast magnitudes in the case of no ARC

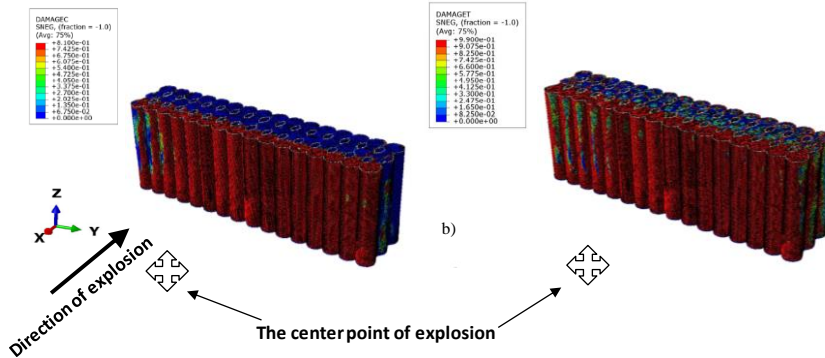


Fig. 24 Damage in a) compression and b) tension 337.5 tons TNT with no ARC (FE)

### 4.3. Effect of Reinforcing the Ribs Between the Silos

To check if reinforcing the ribs between the silos, such as the ARC performed from 2000 to 2002, would have decreased the damage of Beirut port silos, the estimated blast magnitude 337.5 tons of TNT case was simulated for the case without and with additional reinforcement in the ribs. The numerical results, presented in Fig. 25 and 26, show that if the ribs were reinforced, they would have played a significant role in the blast by decreasing the silos displacement as well as damage amount. At the head of the silos and in the direction of the explosion, the maximum and permanent displacements decrease on average by 12% and 20%, respectively for the case with to without additional reinforcement in the ribs. For example, in silos 4 and 5, that exhibit the maximum displacement and damage amount in the direction of the explosion, the permanent displacement decreases from 23.02 and 23.35 cm to 20.60 and 20.49 cm when reinforcing the ribs. As a result, the FE results indicate that reinforcing the ribs would have not only decreased the silos' displacement, but it would have played a positive role in the explosion by absorbing a small part of the released energy. The strain energy (the energy stored in the model under the blast loading), the dissipated energy (the wasted energy outside the model) and the total energy (the sum of all potential energies in the system) released from

the models are 3, 5% and 4% lower in the case when additional reinforcements were added to the ribs.

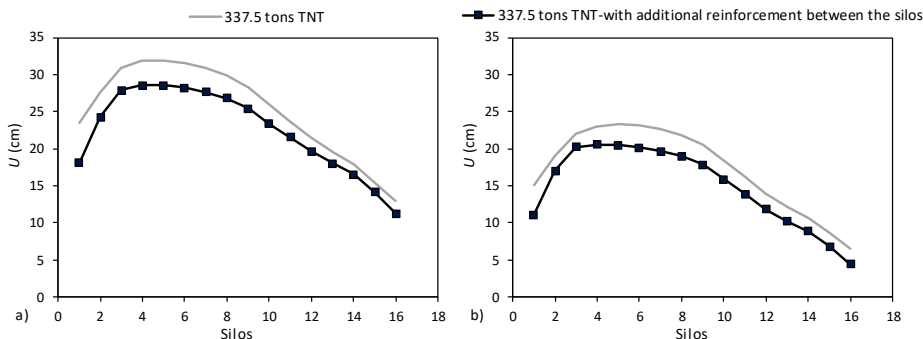


Fig. 25 a) Maximum and b) Permanent displacement in the direction of the blast for the 337.5 tons TNT without and with additional reinforcement in the ribs between the silos

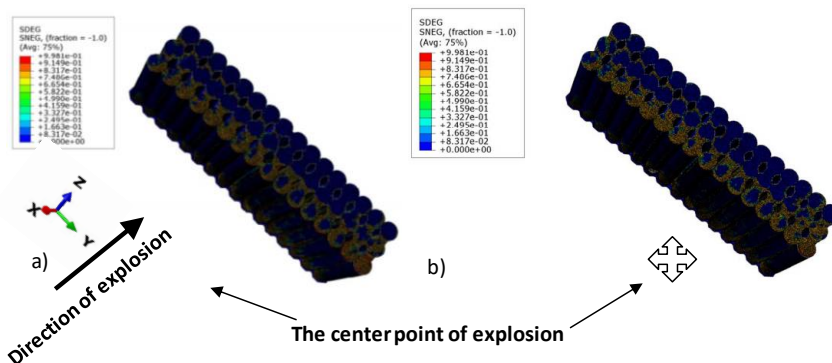


Fig. 26 The SDEG output of the 337.5 tons of TNT simulated cases a) without additional reinforcement and b) with additional reinforcement in the ribs between the silos

#### 4.4. Effect of the Soil and Foundation

The August 4, 2020 explosion released rapid hot gases and produced high temperature and pressure, i.e. enormous amount of energy in only milliseconds. It formed of a blast wave that not only radiated throughout the city, but it radiated in the unbounded soil domain in a form of spherical type wave. Therefore, to check the contribution of the soil and foundation, an extra simulation consisting of the silos, the pile cap, pile foundation as well as the soil medium was simulated for the estimated 337.5 tons TNT blast magnitude (938 tons of Ammonium Nitrate). The displacements at the head, intermediate and near-bottom of the silos were extracted from the FE model. The geometry and properties of the soil and foundation were extracted from the real 1960s plans and designs (Fig. 11). Fig. 27 shows the FE model in flexible-based condition, consisting of the silos, the grains, the 140 X 30 m pile cap, the 2500 30 X 30 cm driven square 15 m length piles as well as the 460 X 200 X 17 m soil medium. In the FE model, and as detailed in Table 2, the pile cap was built using S4R shell elements formed using 7902 elements. Moreover, the pile cap's steel reinforcements were defined as layers of reinforcement as part of the pile cap's shell elements using the rebars command available in Abaqus. Finally, the piles were built using

B31 beam elements using 17868 elements while the soil medium was built using C3D8R solid elements using 30400 elements (Table 2). The typical Mohr-Coulomb model was used to define the plasticity behavior of the soil medium that is formed of a 2 m miscellaneous backfill sand material and 15 m sandy material that presents some levels of gravel and clay (Table 7). In addition, the concrete and steel reinforcements in the silos and pile cap were tied using the tie command in ABAQUS while the silos and the pile cap as well as the pile cap and the piles' interface were modeled by tying the different parts together.

As shown in Fig. 28, that presents the amount of damage the silos exhibited after the blast loading, the numerical results show that in both fixed and flexible-based cases, the first and second row of silos are destroyed while the third row of silos is damaged. Noting that in this row, the last two silos are destroyed (silos 15 and 16). Also, as shown in Fig. 29, silos 4 and 5 exhibit the highest amount of displacement and damage. Therefore, silos 4 and 5 will be used as reference silos in the analysis. The results indicate that, in silos 4 and 5, the maximum relative displacement (head with respect to bottom) only decreases by a ratio of 0.99 while the permanent relative displacement decreases by a ratio of 0.78 from the fixed to the flexible 337.5 tons TNT case. In addition, the average ratio of the maximum and relative displacement from the fixed to the flexible 337.5 tons TNT case at the head level is equal to 1.0 and 0.77, respectively. The increase in silos displacement is also detected at the intermediate level. For example, in silos 4 and 5, the maximum relative displacement (intermediate with respect to the bottom) increases by a small ratio of 1.06 while the permanent relative displacement decreases significantly by a ratio of 0.73 from the fixed to the flexible 337.5 tons TNT case. In addition, at the intermediate level for the 337.5 tons TNT, the average ratio of the maximum and relative silos' displacement fixed to the flexible-based cases is equal to 1.06 and 0.71, respectively.

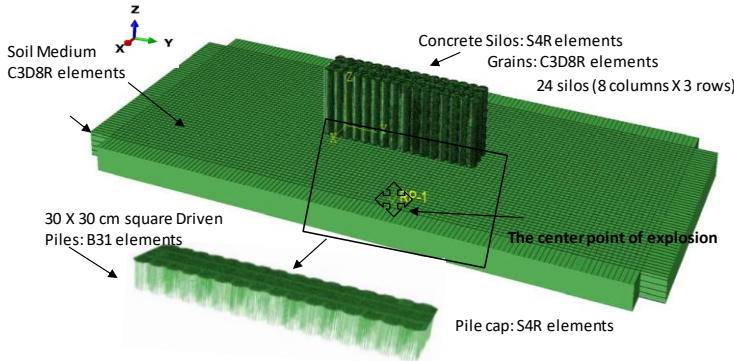


Fig. 27 The FE model (flexible-based model)

Table 7. Soil Properties

	$\rho$ (kg/m <sup>3</sup> )	$E$ (GPa)	$\nu$	$c$ (kPa)	$\Phi$ (°)	$\psi$ (°)
Backfill Material	1500	40	0.25	2	44	2.5
Sandy Soil with some levels of gravel and clay	1700	25	0.25	10	38	10

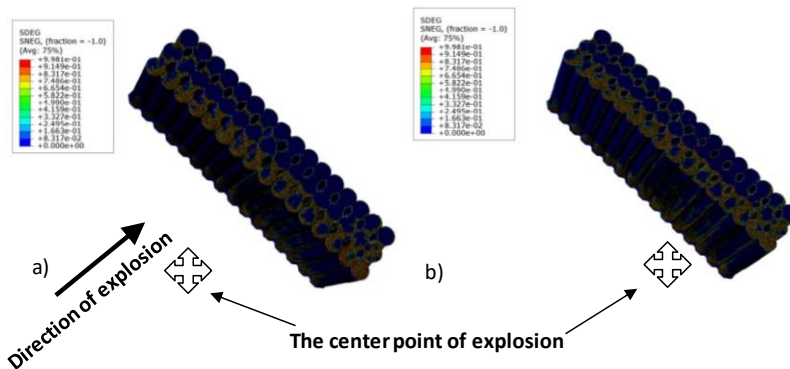


Fig. 28 The SDEG output of the a) fixed and b) flexible-based 337.5 tons of TNT simulated cases

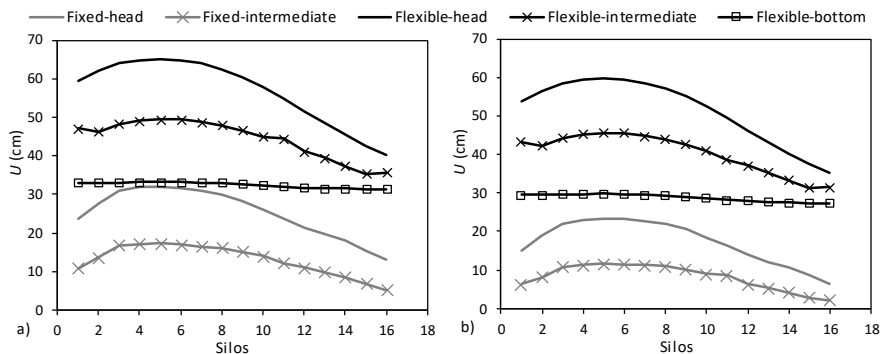


Fig. 29 a) Maximum and b) permanent displacement in the direction of the blast for the 337.5 tons TNT fixed and flexible-based cases

This increase in silos' displacement is caused by the contribution/role played by the soil medium and the pile foundation. Therefore, to examine this contribution, the fixed and flexible numerical models' different types of energies were extracted and compared. The results show that, the decrease in silos' displacement is manifested by a decrease in the amount of strain and damage dissipated energies. These energies decrease by a ratio of 0.82 and 0.78 from the fixed to the flexible-based case, respectively. The strain energy refers to the energy stored in the model while the damage dissipated energy refers to the wasted energy outside the model caused by the blast loading. On the other hand, the total energy released by the model increases by a ratio of 1.32 from the fixed to the flexible-based case while the internal energy, external work and kinetic energy remain almost the same under both models. As a result, even though the silos exhibit a higher amount of displacement when considering the soil and the foundation, the level of damage is very close compared to the fixed-based modeled case. Therefore, the results indicate that the soil and the foundation played a positive role in the explosion by storing more while dissipating less amount of energies. The flexible model absorbed part of the released energy, which only accounts for 0.033% of the total energy released by the August 4, 2021 explosion. The total energy released by the explosion is equal to  $1.84 \times 10^{12}$  J (every 1 ton of TNT releases  $4.184 \times 10^9$  J) while the external work exhibited by the fixed and flexible-based 337.5 tons TNT case is equal to  $590 \times 10^6$  J. This value was calculated by dividing the external work exhibited by the FE model to the explosion released energy. The obtained

results indicate that the silos' base displace 27 to 30 cm while the silos' head displace 40 to 65 cm in the direction of the explosion. These displacements exceed all limits set by design codes such as Eurocode [34,45], indicating that the silos, in the current state cannot be reused.

## **5. Conclusions**

The Beirut port silos' damage followed by the August 4, 2020 explosion was assessed using a three-dimensional laser scan and finite element simulations. The 3D scan was performed by the higher school of Engineering "ESIB" at the Saint Joseph University of Beirut in collaboration with the Swiss company "Amman" Engineering while the numerical models were simulated using Abaqus explicit. The effects of the blast magnitude, silos' concrete strength, additional reinforcement and concrete coating added to the silos in 2000, reinforcing the ribs between the silos and the effect of the soil and the foundation were investigated. The damage and silos' displacement obtained from the 3D FE models were compared to the results obtained by the 3D laser scan that were estimated in two phases using two different equipment: the LEICA BLK360 and the Z+F Imager 5010X.

The 752 million points of measure in three dimensions using 25 stations in 360° panorama infrared images estimated a general tilt of silos between 20 and 30 cm in the direction of the blast. Therefore, comparing the 3D scan to the FE results allowed a precise estimation of the blast magnitude. A blast magnitude of 337.5 tons TNT (938 tons of Ammonium Nitrate) was found to best capture the 3D scan results and therefore, the real silos' displacement and damage.

The numerical results showed that for low levels of blast magnitude such as 337.5 and 225 tons of TNT, concrete compressive strength does not affect the amount of silos' displacement. Nevertheless, as the magnitude of the blast increases, designing the silos with higher concrete compressive strength decreases their damage amount. Nevertheless, for the 337.5 tons TNT estimation blast magnitude, designing the silos with higher compressive strength would not have affected the amount of damage obtained after the August 4, 2020 explosion.

The FE results indicated that the silos with no additional reinforcement and concrete coating (ARC) added from 2000 to 2002 exhibit lower displacement and higher amount of damage (in compression and tension) for blast magnitudes greater than 337.5 tons TNT compared to the "with ARC" cases. Nevertheless, for the estimated blast case (337.5 tons TNT), the amount of damage exhibited in the silos is greater in the case of "no ARC" compared to the "with ARC" case. As a result, reinforcing the outer silos from 2000 to 2002 played a positive role in the blast by decreasing the amount of the silos' damage.

The obtained results proved that if the ribs of the silos were reinforced like the ARC from 2000 to 2002, this reinforcement would have played a positive role in decreasing the amount of silos' displacement and damage and by absorbing a small part of the released energy. Reinforcing the ribs would have decreased the displacement at the head of the silos by 20%.

As for the soil and the foundation, the results pointed out to the positive role they played in the blast. The flexible model absorbed part of the explosion released energy. Even though the level of damage was very close in the fixed and the flexible models, the presence of the soil and the foundation caused an increase in silos' displacements. This increase was manifested by a decrease in the amount of strain and dissipated energies exhibited by the numerical model.

Finally, the 3D scan and FE results showed that the silos' base displaced 27 to 30 cm while the silos' head displace 40 to 65 cm in the direction of the explosion. Thus, the silos

displaced 20 to 30 cm in the direction of the blast. These displacements exceed all limits set by design codes, indicating that the silos, in the current state cannot be reused.

### **Acknowledgement**

The authors would like to acknowledge the support of the Lebanese authorities, Lebanese Army as well as the assistant of the USJ-ESIB-ASCE student chapter, Francois Karam for the drone pictures and Miguel Bandera for the 3D modeling and photogrammetry.

### **References**

- [1] Tang Q, Jiang N, Yao Y, Zhou C, Luo X, Wu T. Safety assessment of buried gas pipeline subject to surface explosion: A case study in Wuhan, China. *Engineering Failure Analysis*, 2021, 120: 105119. <https://doi.org/10.1016/j.engfailanal.2020.105119>
- [2] Luccioni BM, Ambrosini RD, Danesi RF. Analysis of building collapse under blast loads. *Engineering Structures*, 2004, 26:63-71. <https://doi.org/10.1016/j.engstruct.2003.08.011>
- [3] Osteraas JD. Murrah building bombing revisited: a qualitative assessment of blast damage and collapse patterns. *Journal of Performance in Construction Facility*, 2006, 20:330-5. [https://doi.org/10.1061/\(ASCE\)0887-3828\(2006\)20:4\(330\)](https://doi.org/10.1061/(ASCE)0887-3828(2006)20:4(330))
- [4] Raphael W, Faddoul R, Feghaly R, Chateaufneuf A. Analysis of Roissy airport Terminal 2E collapse using deterministic and reliability assessments. *Engineering Failure Analysis*, 2012, 20 : , 1-8. <https://doi.org/10.1016/j.engfailanal.2011.10.001>
- [5] Raphael W, Zgheib E, Chateaufneuf A. Experimental investigations and sensitivity analysis to explain the large creep of concrete deformations in the bridge of Chevire. *Case Studies in Construction Materials*, 2018, 9: e00176. <https://doi.org/10.1016/j.cscm.2018.e00176>
- [6] Raphael W, Faddoul R, Geara F, Chateaufneuf A. Improvements to the Eurocode 2 shrinkage model for concrete using a large experimental database. *Structural Concrete*, 2012, 13: 174-181. <https://doi.org/10.1002/suco.201100029>
- [7] Kawashima K, Takahashi Y, Ge H, Wu Z, Zhang J. Reconnaissance report on damage of bridges in 2008 Wenchuan, China, earthquake. *Journal of Earthquake Engineering*, 2009, 13: 956-998. <https://doi.org/10.1080/13632460902859169>
- [8] Mendez D. Stunned Salvador suffers second deadly quake in a month, The BG News, <http://media.www.bgnews.com/media/storage/paper883/news/2001/02/14/World/Stunned.Salvador.Suffers.Second.Deadly.Quake.In.A.Month-1283510.shtml>, 2001 (accessed Jan. 22, 2008).
- [9] Ozmen HB. A view on how to mitigate earthquake damages in Turkey from a civil engineering perspective, *Journal of Research on Engineering Structures and Materials*, 2021, 7(1): 1-11. <https://doi.org/10.17515/resm2020.231ea1113ed>
- [10] After the blast: Satellite images show destruction in Beirut, The Washington Post, <https://www.washingtonpost.com/world/2020/08/05/beirut-explosions-satellite-images-destruction/?arc404=true>, 2020 (accessed August 5, 2020).
- [11] Beirut explosion: Legendary Palestinian banker envisaged silos that shielded his adopted city from more destruction, The National News, <https://www.thenationalnews.com/world/beirut-explosion-legendary-palestinian-banker-envisaged-silos-that-shielded-his-adopted-city-from-more-destruction-1.1061359#5>, 2020 (accessed August 12, 2020).
- [12] Lebanon's government nears collapse as anger over blast surges, Bloomberg, <https://www.bloomberg.com/news/articles/2020-08-09/global-magnitudes-pledge-aid-to-lebanon-after-beirut-blast>, 2020 (accessed August 9, 2020).
- [13] Stephens, HW. *The Texas City Disaster 1947*, University of Texas Press, Texas, USA, 1997.

- [14] Mannan S. Lees' Loss Prevention in the Process Industries. Hazard Identification, Assessment and Control, Elsevier, Third Ed., Oxford, United Kingdom, 2005.
- [15] Mainiero RJ, Rowland JH. A review of recent accidents involving explosives transport, National Institute for Occupational Safety and Health (NIOSH), Pittsburgh Research Laboratory, 2007.
- [16] REPORT 2013-02-I-TX, U.S. chemical safety and hazard investigation board, investigation report, West fertilizer company fire and explosion, 2016.
- [17] Li X, Hoseki H. Study on the contamination of chlorides in ammonium nitrate, Process Safety and Environmental Protection, 2005, 83: 31-37. <https://doi.org/10.1205/psep.04060>
- [18] Marlair G, Kordek M. Safety and security issues relating to low capacity storage of AN-based fertilizers. Journal of Hazardous Materials, 2005, 123: 13- 28. <https://doi.org/10.1016/j.jhazmat.2005.03.028>
- [19] DIRECTIVE 2012/18/EU, The control of major-accident hazards involving dangerous substances, amending and subsequently repealing Council Directive 96/82/EC, 2012.
- [20] Scott G, Stanley G. Ammonium Nitrate: Its Properties and Fire and Explosion Hazards, U.S. Department of the Interior, Bureau of Mines, 1948.
- [21] Explosion in a nitrogenous fertilizer plant 21 September 1921, Oppau, Germany, N° 14373, French Ministry of Environment, March 2008, [https://www.aria.developpement-durable.gouv.fr/wp-content/files\\_mf/FD\\_14373\\_oppau\\_1921\\_ang.pdf](https://www.aria.developpement-durable.gouv.fr/wp-content/files_mf/FD_14373_oppau_1921_ang.pdf).
- [22] Inquiry Report Department of Mining and Petroleum, Government of Papua New Guinea, 1994.
- [23] Tianjin Port Accident Investigation Report, The State Council of the People's Republic of China, 2016.
- [24] Bauer A, King A, Heater R. The detonation properties of ammonium nitrate perils, Department of Mining and Engineering, Queens University, Canada, 1978.
- [25] King A, Bauer A, Heater R. The explosion hazards of ammonium nitrate and ammonium nitrate based fertilizer compositions, Department of Mining and Engineering, Queen's University report to the Canadian Fertilizer Institute and Contributing Bodies, Canada, 1982.
- [26] Joint Research Centre JRC, Summary Report, Workshop on Ammonium Nitrate, Joint Research Centre, European Commission, Ispra, Italy, 2002.
- [27] Nguyen TA, Nguyen PT, Do ST. Application of BIM and 3D laser scanning for quantity management in construction projects. Advances in Civil Engineering, 2020, 8839923. <https://doi.org/10.1155/2020/8839923>
- [28] Farahani, N, Braun A, Jutt D, Huffman T, Reder N, Liu Z, Yagi Y, Pantanowitz L. Three-dimensional imaging and scanning: current and future applications for pathology. Journal of Pathology Informatics, 2017, 8: 36. <https://doi.org/10.4103/jpi.jpi.32.17>
- [29] Haddad NA. From ground surveying to 3D laser scanner: A review of techniques used for spatial documentation of historic sites. Journal of King Saudi University - Engineering Sciences, 2011, 23: 109-118. <https://doi.org/10.1016/j.jksues.2011.03.001>
- [30] Z+F IMAGER 5010X, <https://www.zf-laser.com/Z-F-T-Cam.150.0.html?&L=1>.
- [31] Leica BLK360 Imaging Laser Scanner, <https://leica-geosystems.com/products/laser-scanners/scanners/blk360>.
- [32] Sadek S, Dabaghi M, Elhadj I, Zimmaro P, Hashash Y, Yun S, O'Donnell T, Stewart J. A report of the NSF-Sponsored geotechnical extreme event reconnaissance association in collaboration with the American University of Beirut, REPORT GEER-070, 2020, <https://doi.org/10.18118/G6C96C>.
- [33] Hafezolzhorani ME, Hijazi F, Vaghei R. Simplified damage plasticity model for concrete. Structural Engineering Journal, 2017, 27. <https://doi.org/10.2749/101686616X1081>

- [34] Eurocode 4, Actions on structures, EN 1991-4, 2006.
- [35] The Beirut Port Explosion, Forensic Architecture, <https://forensic-architecture.org/investigation/beirut-port-explosion>, 2020 (accessed 16 November 2020).
- [36] Alonso FD, Ferradas EG, Perez JFS, Aznar AM, Gimeno JR, Alonso JM. Characteristic overpressure-impulse-distance curves for the detonation of explosives, pyrotechnics or unstable substances. *Journal of Loss Prevention. in the Process Industries*, 2006, 19: 724-728. <https://doi.org/10.1016/j.jlp.2006.06.001>
- [37] HSE, Safety Report Assessment Guide: Chemical warehouses - Hazards, Health and Safety Executive, United Kingdom, 2012.
- [38] Cooper PW. Comments on TNT Equivalence. *Proceedings of 20th Pyrotechnic Seminar*, Colorado Springs, Colorado, USA, 1994.
- [39] Locking PM. The Trouble with TNT Equivalence. *Proceedings of the 26th International Symposium on Ballistics*, Miami, USA, 2011.
- [40] HSE, Storing and Handling Ammonium Nitrate, Health and Safety Executive, United Kingdom, 2004.
- [41] GHD, Orica Mining Services, Report for Kooragang Island Facility Uprate, PHA MOD1 Report, Australia, 2012.
- [42] Kersten RJA, Mak WA. Explosion hazards of ammonium nitrate, how to assess the risks. *Proceedings of the International Symposium on Safety in the Manufacture, Storage, Use, Transport and Disposal of Hazardous Material*, Tokyo, Japan, 2004.
- [43] Nygaard EC. Storage of technical (porous) ammonium nitrate, *International Society of Explosives Engineers*, 2008.
- [44] Krauthammer T. *Modern Protective Structures*, CRC Press, Taylor & Francis Group, 2008. <https://doi.org/10.1201/9781420015423>
- [45] Eurocode 2, Design of concrete structures, EN 1992-1-1, 2004.
- [46] Rigby SE, Lodge TJ, Alotaibi S, Barr AD, Clarke SD, Langdon GS, Tyas A. Preliminary yield estimation of the 2020 Beirut explosion using video footage from social media. *Shock Waves*, 2020. <https://doi.org/10.1007/s00193-020-00970-z>
- [47] Diaz J. Explosion analysis from images: Trinity and Beirut, arXiv preprint, 2020, arXiv:2009.05674. <https://doi.org/10.1088/1361-6404/abe131>
- [48] Aouad C, Chemissany W, Mazzali P, Temsah Y, Jahami A. Beirut explosion: Energy yield from the fireball time evolution in the first 230 milliseconds , arXiv preprint, 2020, arXiv:2010.13537.
- [49] Stennett C, Gaulter S, Akhavan J. An estimate of the TNT-equivalent net explosive quantity (NEQ) of the Beirut Port explosion using publicly-available tools and data, *Propellants, Explosives, Pyrotechnics*. 2020, 45: 1675-1679. <https://doi.org/10.1002/prop.202000227>
- [50] Pasman H, Fouchier C, Park S, Quddus N, Laboureur D. Beirut ammonium nitrate explosion: Are not we really learning anything. *Journal of Process Safety*, 2020, 39: e12203. <https://doi.org/10.1002/prs.12203>
- [51] Valsamos G, Larcher M, Casadei F. Beirut explosion 2020: A case study for a large-scale urban blast simulation. *Journal of Safety Science*, 2021, 137:105190. <https://doi.org/10.1016/j.ssci.2021.105190>
- [52] Na-Hyun Y, Jang-Ho JK, Tong-Seok H, Yun-Gu C, Jang HL. Blast-resistant characteristics of ultra-high strength concrete and reactive powder concrete. *Journal of Construction and Building Materials*, 2012, 28: 694-707. <https://doi.org/10.1016/j.conbuildmat.2011.09.014>

Blank Page



Research Article

## Fatigue life prediction of steel bridge connections using fracture mechanics models

Warda Abdulla<sup>a</sup>, Craig Menzemer<sup>b</sup>

*Department of Civil Engineering, The University of Akron, U.S.A.*

### Article Info

### Abstract

#### Article history:

Received 10 Mar 2021

Revised 16 Jun 2021

Accepted 16 Jun 2021

#### Keywords:

*AFGROW models;*

*Crack growth rate;*

*Fatigue life prediction;*

*Riveted connections;*

*Stress intensity factor;*

*Striation spacing*

Riveted connections used in steel bridges may be subjected to localized fatigue cracking. Experimental data were obtained from coupon fatigue tests for the investigation of the role of the riveting process on fatigue resistance. Fracture mechanics models of both open-hole and riveted A36 steel coupon specimens were used to predict the fatigue life. Stress versus the number of cycles to failure curves (S-N curves) were established based on empirical results and combined with Air Force Grow software (AFGROW) fatigue life estimates and compared. Fatigue crack growth test data was developed and compared with the material library in AFGROW. Fracture surfaces of the specimens were examined and striation spacing measured using Scanning Electron Microscope (SEM) images. Subsequently, stress intensity factors and local crack growth rates were estimated. Estimates of the local crack growth rates and the estimated stress intensity ranges were compared with data obtained from fatigue crack growth test results. Test results demonstrated that fatigue life was improved with the riveting process. In addition, accurate fatigue life predictions required consideration of the compressive residual stresses due to riveting.

© 2021 MIM Research Group. All rights reserved.

## 1. Introduction

One particular design concern is the fluctuation of stress in a component which may cause localized fatigue cracking within a structural system. In general, it is necessary to consider all limit states of a component or structure which includes fatigue [1].

Fatigue cracking generally initiates as a result of localized cyclic plastic deformation, and starts with one or more tiny flaws in the material that grow sub critically until failure occurs. The idea is that even if the nominal stresses are well below the elastic limit, the local stresses may be above yield due to stress concentrations. It is worth noting that prevention of fracture is a significant aspect of design for structures that are subjected to repeated loading or vibration [1, 2].

Mechanically fastened structural connections commonly use either rivets or bolts. In fact, fasteners are often used in components of movable bridges such as in steel grid decks. Bridge decks are exposed to daily traffic load and one significant issue is the design against fatigue cracking induced by repeated cyclic loads. It is well known that connections under such conditions may eventually fail from fatigue cracking even though the maximum applied stress is less than the yield stress. In addition, these failures often occur with small deformation, which makes fatigue cracks difficult to detect until major growth has occurred [3].

<sup>\*</sup>Corresponding author: [wia3@uakron.edu](mailto:wia3@uakron.edu)

<sup>a</sup>orcid.org/0000-0003-4549-4836; <sup>b</sup>orcid.org/0000-0002-6529-085X

DOI: <http://dx.doi.org/10.17515/resm2021.264st0310>

Res. Eng. Struct. Mat. Vol. 7 Iss. 4 (2021) 579-593

Consequently, fatigue life prediction must be considered during the design of structural components [4].

Fracture surfaces of components and test articles subjected to fatigue may contain striations, which represent locations of the crack front(s). Striations can help determine the direction of failure propagation, the local crack growth rate and may help identify the origin of failure. Further, correlations have been developed that establish the relationship between striation spacing or local crack growth rate  $da/dN$  and the stress intensity factor range ( $\Delta K$ ) [5, 6].

In order to understand the fatigue behavior of riveted joints and connections, experimental tests have been conducted and several models proposed over the years. The general idea of testing riveted joints and connections that use smaller rather than full-scale specimens, is simply that it is easier and less costly, but may be limited by scale effects [7].

Fatigue lives exhibit considerable scatter even under constant amplitude loading in controlled laboratory conditions. This phenomenon makes statistical methods indispensable. Further, fatigue life should be predicted at given probability levels of failure for a given detail under defined environment and loading conditions. Generally, the nominal applied stress range is the main parameter for fatigue life, and other loading parameters, such as the mean stress, have a minor effect [8].

Several different studies on the fatigue behavior of steel bridge connections have been performed using different types of analyses. Fatigue damage may also be associated with secondary load effects. Moreover, the interaction between bridge members and load-carrying systems has contributed to fatigue issues [9]. Furthermore, the discontinuities that exist in all fabricated steel structures are a consequence of the manufacturing process of the material and/or the normal fabrication processes of the components. These discontinuities from steel making, as well as various fabrication processes like cutting, drilling, punching, and welding operations provide preferential sites from which fatigue cracks may develop. Usually, lower fatigue resistance for welded joints is expected as compared with bolted or riveted details. It is worth noting that the fatigue behavior of fabricated steel structures is controlled by the detail type, size, shape, and location of the discontinuities, as well as the applied cyclic stresses [10].

As riveting is employed as a joining method in steel construction, fatigue tests and studies of riveted connections are of continued interest. Many of these studies use experimental, numerical, or theoretical analysis for the investigation of fatigue damage. To be specific, the main focus is the evaluation of fatigue life of either open-hole or riveted specimens. Researchers have studied crack initiation by testing open-hole specimens, and fatigue life determined as each specimen was tested to fracture. It has been found that crack growth in the open-hole specimens initiated almost exclusively at the edge of the hole. Through thickness crack development around the edge of the hole appeared to be unsymmetrical in most cases [11]. The fatigue life of riveted sheet metal joints consisting of single as well as specimens with multiple fasteners was investigated. Fatigue testing was conducted on all specimen types and the analysis showed that connections using a stiffened angle design with either two or eight rivets was superior as compared to that of single lap joints with one and four rivets [12].

The goal of this study was to investigate the fatigue behavior of heavy-duty riveted steel grating under a standard AASHTO HL truck, although using coupon samples in order to understand the effect of riveting.

Two types of A36 steel specimens were employed and consisted of both open-hole and riveted samples with dog-bone geometry. The specimens were tested under different stress ranges until failure [13]. To provide a better understanding of the behavior of the

riveted connection, fatigue life prediction using AFGROW was conducted. Moreover, the beneficial residual stresses resulting from the riveting process were taken into consideration in the AFGROW model [13]. Simulating the nature of the riveted connections in the bridge makes this study more realistic.

The open-hole and riveted fracture mechanics models considered in this study are described in detail. Fatigue test results of both the open-hole and riveted coupons subjected to different stress ranges are compared with the AFGROW fatigue life estimates. Fatigue crack growth tests were conducted, and life predictions derived and compared with AFGROW results using a tabular look-up model. Striation spacing measurements taken from four different areas of fracture surfaces of the tested samples were compared to fatigue crack growth test data. Fatigue crack growth rates for stress ratios (R) of 0.1 to 0.4 were derived for the open-hole and riveted models.

## 2. Fatigue Life Prediction Analysis

### 2.1. AFGROW Fracture Mechanics Models

#### 2.1.1. General Background

AFGROW is a fracture mechanics-based software program originally developed by the U.S Air Force. AFGROW was originally developed for evaluating the residual strength and durability of aerospace components. AFGROW was transitioned to a commercial product and has undergone a number of revisions since first introduced. Capabilities include the analysis of crack development, growth, and fracture to predict the behavior of structural systems [14].

#### 2.1.2. Fatigue Life Prediction

A convenient feature within the program is the user's ability to select material properties from a menu, which includes crack growth information. There are multiple models for representing crack growth kinetics. Several of the choices include the Tabular Look-Up and Harter-T methods, also the Forman, Walker, and NASGRO Equations. Crack growth rate data is provided as function of the stress intensity range,  $\Delta K$ , ( $\Delta K = K_{max} - K_{min}$ ) at a given stress ratio ( $R = K_{min}/K_{max}$ ) for  $R \geq 0.0$ . In this study, we employed the NASGRO crack growth rate equation for fatigue life prediction as follows [14]:

$$\frac{da}{dN} = C \left[ \left( \frac{1-f}{1-R} \right) \Delta K \right]^n \frac{\left( 1 - \frac{\Delta K_{th}}{\Delta K} \right)^p}{\left( 1 - \frac{K_{max}}{K_{crit}} \right)^q} \quad (1)$$

Where,  $da/dN$  is the fatigue crack growth rate,  $C$  is the crack growth constant,  $f$  is the crack opening function,  $R$  is the load ratio,  $\Delta K$  is the stress intensity factor range,  $n$ ,  $p$ ,  $q$  are the empirical constants describing the behavior near the threshold,  $\Delta K_{th}$  is the threshold stress intensity factor range for crack propagation and  $K_{crit}$  is the fracture toughness. It is noteworthy that Eq. (1) considers the three stages of fatigue crack growth, which is shown schematically by the curve in Figure 1. Region I is the fatigue threshold region, region II is the Paris region which described by the parameters  $C$  and  $n$  and region III represents rapid-crack propagation while the fracture toughness,  $K_{crit}$ , determines the transition to unstable crack growth [15, 16].

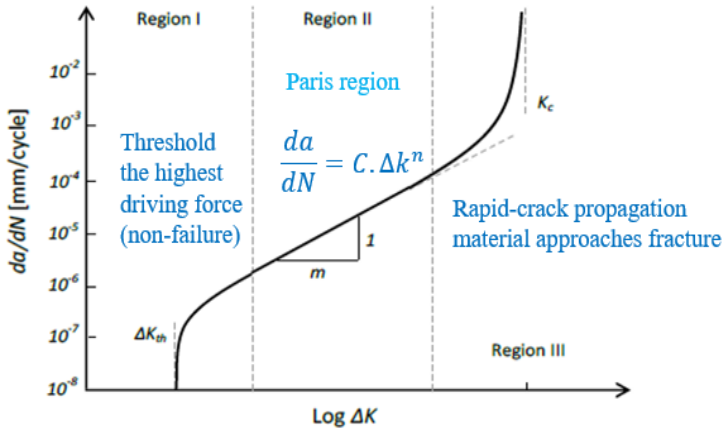


Fig. 1 Crack growth regions [16]

### 2.1.3 Modeling

A fracture mechanics model of a single corner crack at a hole was considered for the fatigue life prediction of the open-hole and the riveted coupon specimens. Two of the parameters considered included the stress ratio (R) and the a/c crack aspect ratio. The parameter  $a_i$  is the crack length and  $c_i$  is the crack depth. To check the model against the laboratory tests, the R-ratio was taken to be 0.1 for both coupon types [17].

#### 2.1.3.1 Open-Hole Fracture Mechanics Model Inputs

The aspect ratio (a/c) for the open-hole coupon, was assumed to be between 0.15 and 0.29. The initial crack size ( $a_i$ ) was assumed to be between (0.0254-0.1016 mm) and the crack depth ( $c_i$ ) was assumed to be between (0.127-0.508 mm) [17].

#### 2.1.3.2 Riveted Fracture Mechanics Model Inputs

For the riveted coupon specimens, the aspect ratio (a/c) was assumed to be between 0.15 and 0.3. The initial crack size ( $a_i$ ) was assumed to vary between (0.0254-0.1016 mm) and the crack depth ( $c_i$ ) was assumed to be between (0.127-0.508 mm). It is noteworthy that residual stress, an estimate of which was obtained from the finite element model analysis, was used as input to simulate the nature of the riveted sample [17]. This was as a result of the compression stress distribution obtained in the area of the corner crack, which has a positive influence on decreasing crack growth rates as reported in [13].

## 2.2. A comparison of AFGROW Calculated Results and Empirical Results

Regression analysis of the laboratory test data is compared with estimates calculated using AFGROW. Figure 2 shows both a lower bound and best-fit S-N curves for all of the study data along with AFGROW calculated results for the open hole configuration. In general, the results calculated using AFGROW are conservative as compared to the test results for lives greater than about 500,000 cycles. Also, design fatigue strength from both the lower bound curve and equation 2 is 111 MPa at 10 million cycles, which is consistent with the experimental fatigue test results.

$$S_r = 70.965N^{-0.092} \tag{2}$$

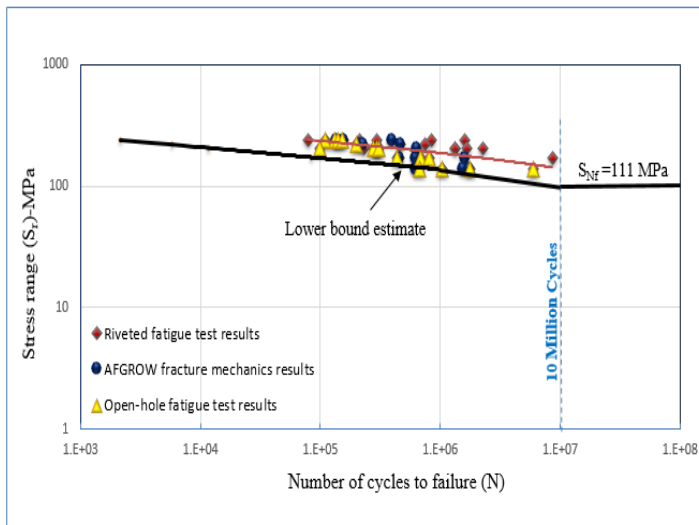


Fig. 2 Regression analysis of fracture mechanics and fatigue test results

Regression analysis of the laboratory test data is compared with estimates calculated using AFGROW. Figure 3 presents lower bound and best-fit S-N curves for all of the test data including the AFGROW results for the riveted configuration. Moreover, the design fatigue strength from both the lower bound curve and equation 3 is 113 MPa at 10 million cycles, which is slightly higher than the experimental fatigue test results.

$$S_r = 72.352N^{-0.092} \tag{3}$$

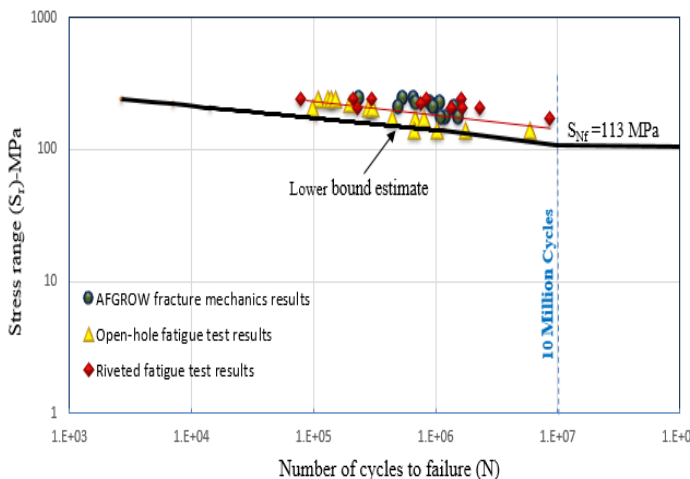


Fig. 3 Regression analysis of fracture mechanics and fatigue test results

### 3. Fatigue Crack Growth Rate Testing

Fatigue crack growth rate analysis helps designers to provide a safe lifetime, also it helps with the inspection process of critical components.

#### 3.1. Fatigue Crack Growth Test Specimens

Fatigue crack growth analysis in the current study is based on A36 steel. The specimen configuration selected for examination is the single edge notched (SEN) depicted in Figure 4. All of the specimens had lengths of 152.4 mm, widths of 25.4 mm and thicknesses of 6.35 mm, with a notch size of 4.50 mm fabricated in the specimen. The advantage of the SEN is to concentrate stress in order to grow a crack from a controlled position. Further, it is relatively easy to fabricate and test.

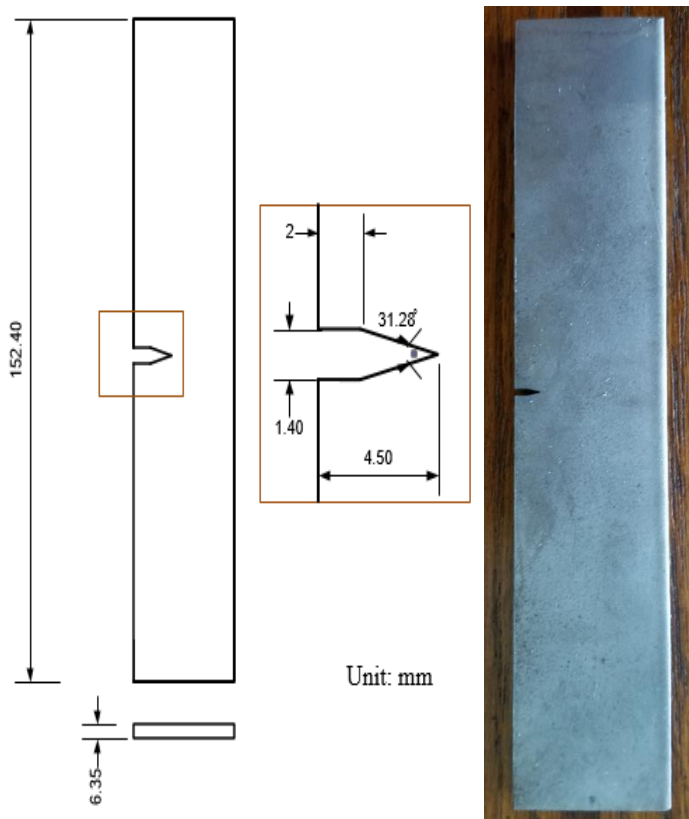


Fig. 4 Details of the single edge notched steel specimen

#### 3.2. Experimental Setup

In order to simulate a natural fatigue crack, nine specimens were pre-cracked in tension. Also, the pre-crack helps ensure that the effect of the machined starter notch is removed from the specimen K-calibration and to obtain suitable test crack growth rate data [18].

Fatigue crack growth tests for nine specimens were conducted using an INSTRON machine with a 50 kN load cell. The specimen was gripped along the top and bottom sides using hydraulic wedge grips. Loading was applied at a frequency of 10 Hz in two steps: (a) the load magnitude was decreased 10% every 2000 cycles starting from 18 kN to obtain the

K-decreasing portion close to the threshold and (b) the load was increased by 10% every 40,000 cycles starting from 18 to 26.6 kN to obtain K-increasing data.

The specimen was subjected to a direct current of 1 Amp through two leads using a Direct Current Potential Drop (DCPD) technique for crack monitoring. As the electrical resistivity changes, it reveals damage initiation and propagation. Consequently, an Agilent 34980a micro Ohmmeter was connected to the leads across the notch as shown in Figures 5 and 6 respectively. Data was recorded using two types of software Agilent and Wave Matrix.

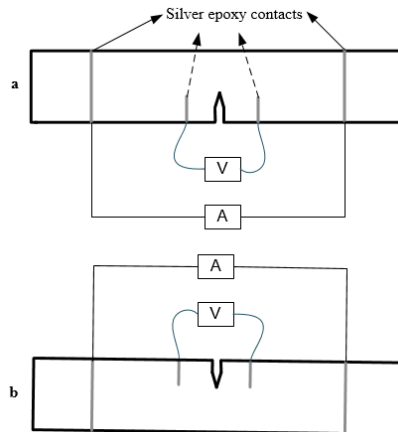


Fig. 5 Specimen configuration (a) front side (b) back side,

Note: A = Amps, V = Volts

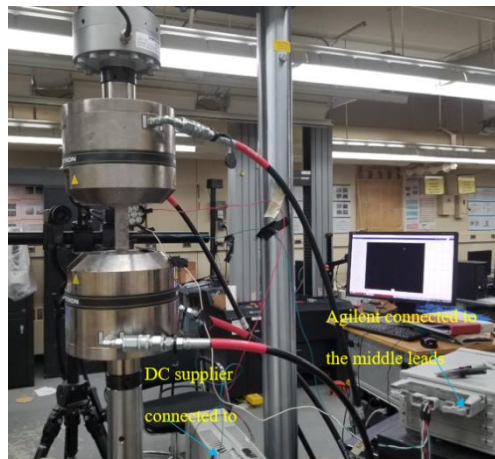


Fig. 6 Experimental setup with sensors position, ER and DC leads

### 3.3. Fatigue Crack Growth Test Results

The data was analyzed using MATLAB and Microsoft Excel, so crack length, time and number of cycles were obtained. The crack growth rate, defined as the change in length of a crack per cycle ( $da/dN$ ) was calculated. Moreover, the stress intensity factor range ( $\Delta k$ )

was calculated in order to correlate with the rate of fatigue crack growth using the following expression:

$$\Delta k = Y\Delta\sigma\sqrt{\pi a} \tag{4}$$

Where Y is a geometry factor,  $\Delta\sigma$  is the stress range and a is the crack length.

Subsequently, Log (da/dN) is plotted versus Log ( $\Delta K$ ) and fatigue crack growth rates curve was obtained.

### 3.3.1. Crack Growth Rate vs. Stress Intensity Factor

Figure 7 presents the relationship between the crack growth rate and stress intensity factor range, which may conveniently be divided into three regions according to the curve shown below. In region I there is a threshold value,  $\Delta k_{th}$  of 9.7 (MPa√m), below which cracks do not propagate, or the growth is too small to measure. It is worthwhile to mention that region I is sensitive to the effects of environment and stress ratio. In region II a linear relation between the Log (da/dN) and Log ( $\Delta K$ ) is commonly referred to as the Paris region. Region II behavior ranges from 11 to 50 (MPa√m). In region III, high values of  $\Delta K$  are present, and there is rapid crack growth. Crack growth is limited by the material toughness,  $k_c$ .

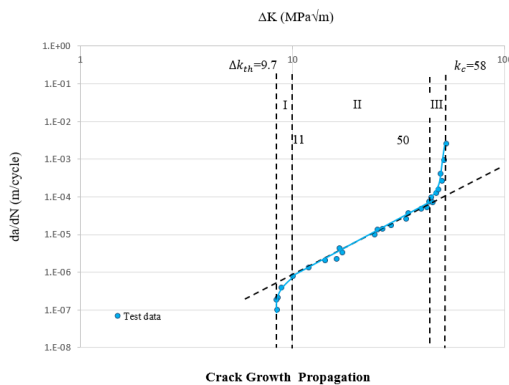


Fig. 7 Fatigue crack growth test results curve

### 3.3.2. A comparison of the Crack Growth Rates between the Experiments and AFGROW Modeling

Based on the experimental data shown on Figure 7, the fatigue threshold was estimated to be 9.7 (MPa√m), which is consistent with a value of 8.2 (MPa√m) used in the material library of AFGROW (Figure 8).

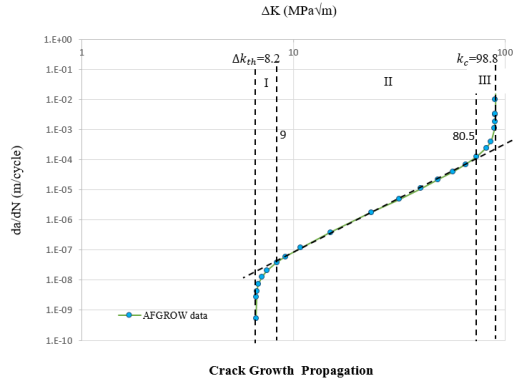


Fig. 8 Fracture mechanics crack growth curve

### 3.3.3. Comparison of Fatigue Crack Growth Test Results

Fatigue crack growth rate curves obtained from the laboratory tests were used as input to AFGROW using a tabular look-up model. Regression analysis of the fatigue test results is compared with estimates calculated using AFGROW. Figure 9 presents a best-fit S-N curve for the open-hole test data along with AFGROW calculated results.

Figure 10 shows a best-fit S-N curve for the riveted test data after adding AFGROW calculated results were for the riveted configuration, which was consistent as compared to the test results.

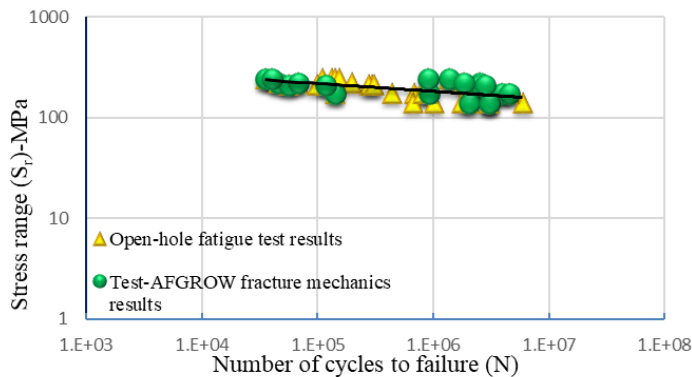


Fig. 9 Regression analysis of fracture mechanics and fatigue test results for the open-hole configuration

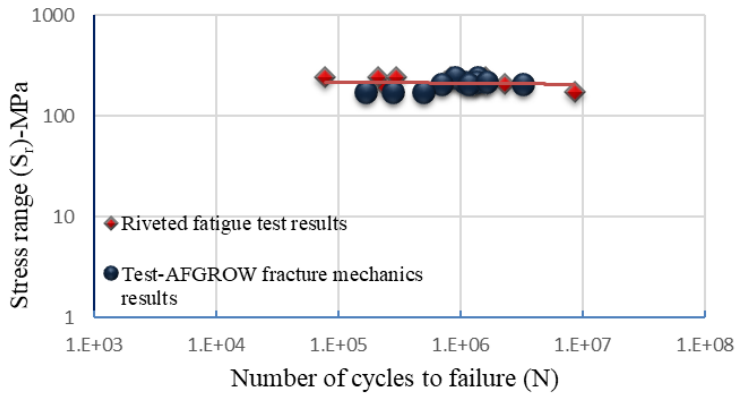


Fig. 10 Regression analysis of fracture mechanics and fatigue test results for the riveted configuration

#### 4. Fatigue Striation Spacing Analysis

##### 4.1. Inspection of Fracture Surfaces

Fatigue tests at a stress range of 206.8 MPa were performed on both open-hole and riveted samples. Fracture surfaces of the fully deformed and failed samples under fatigue loading were examined using Scanning Electron Microscope (SEM) [13].

##### 4.2. A comparison of the Striation Spacing Between the Open-Hole and Riveted Coupons

Striations are features often produced on a fracture surface by fatigue crack growth in ductile materials. In fact, fatigue fracture surfaces are characterized by striations with small ridges perpendicular to crack propagation direction. Additionally, the striations develop at the crack tip because of the presence of slip that is inclined in relation to the fracture plane: when the load decreases, the slip direction turns. It is noteworthy that striations can help to determine the direction of failure propagation and the location of the origin. Striations may be observed and counted using images from the scanning electron microscope [19, 20].

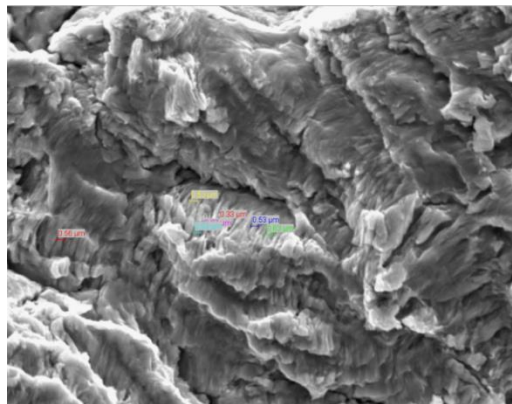


Fig. 11 Striation spacing measurements

One use of the striations is establishing the relationship between fatigue crack growth rate  $da/dN$  and stress intensity factor range ( $\Delta K$ ) [21]. Accordingly, spacing of striations were measured using SEM images (Figure 11). It is noteworthy that the fracture surfaces for each sample were divided into four different areas based on crack growth orientation to ensure accuracy of the spacing measurements. Consequently, stress intensity factors ranges were calculated for the open-hole and riveted samples as summarized in Table 1 and 2 respectively.

Table 1. Fatigue crack growth rate measurements  $\frac{da}{dN}$  ( $\frac{m}{cycle}$ ) and estimated  $\Delta K$  ( $MPa\sqrt{m}$ )

Area	$\frac{da}{dN}$ ( $\frac{m}{cycle}$ )	$\Delta K$ ( $MPa\sqrt{m}$ )
1	5.08E-07	40.5
2	5.08E-07	40.5
3	5.842E-7	42.5
4	7.62E-07	46.4

Striation spacing, for the open-hole specimens vary from 5.08E-07 to 7.62E-07  $\frac{da}{dN}$  ( $\frac{m}{cycle}$ ). Analogous stress intensity factors were calculated to range from 40.5 to 46.4 ( $MPa\sqrt{m}$ ).

Table 2. Fatigue crack growth rate measurements  $\frac{da}{dN}$  ( $\frac{m}{cycle}$ ) and estimated  $\Delta K$  ( $MPa\sqrt{m}$ )

Area	$\frac{da}{dN}$ ( $\frac{m}{cycle}$ )	$\Delta K$ ( $MPa\sqrt{m}$ )
1	3.81E-07	36.8
2	4.06E-07	37.6
3	3.68E-07	36.4
4	3.76E-07	36.7

Also, striation spacing, for the riveted specimens in a similar location vary from 3.68E-07 to 4.06E-07  $\frac{da}{dN}$  ( $\frac{m}{cycle}$ ). Corresponding stress intensity factors were calculated to range from 36.4 to 37.6 ( $MPa\sqrt{m}$ ). Generally, the size of a striation is related to the magnitude of the driving force characterized by the stress intensity factor. The striation's width is indicative of the local crack growth rate. It might be noticed from the previous two tables that striation spacing for the riveted samples are narrower than they are for the open-hole samples. To be more specific, the riveted crack growth rates average is about 16% lower than the open-hole crack growth rates average. Furthermore, the average of the stress intensity factors of the riveted specimens is around 13% less than the open-hole stress intensity factors. It seems the rivet sample performs better, which demonstrates influence of the rivet as well as the installation process.

### 4.3. Correlations Between Crack Growth Rate and Stress Intensity Factor

Figure 12 compares fatigue crack growth rates for the open-hole specimens obtained from the SEM images along with fatigue crack growth test data. In region II, the crack growth rates as measured from the SEM data are consistent with the fatigue crack growth curve. Further, the highest value of  $\Delta K$  obtained from the SEM data is  $46.4(MPa\sqrt{m})$ , which is close to  $50(MPa\sqrt{m})$ , the highest value of  $\Delta K$  obtained from fatigue crack growth test data.

Figure 13 compares fatigue crack growth rates for the riveted specimens obtained from SEM images with fatigue crack growth test results. In region II, the crack growth rates were in reasonable agreement for the SEM and fatigue crack growth test results. Moreover, in region II the highest value of stress intensity factor range,  $\Delta K$ , obtained from SEM data is  $37.6(MPa\sqrt{m})$ , which is about 25% less than the highest value of  $\Delta K$  obtained from fatigue crack growth test data. It appears the rivet influence improved the material behavior.

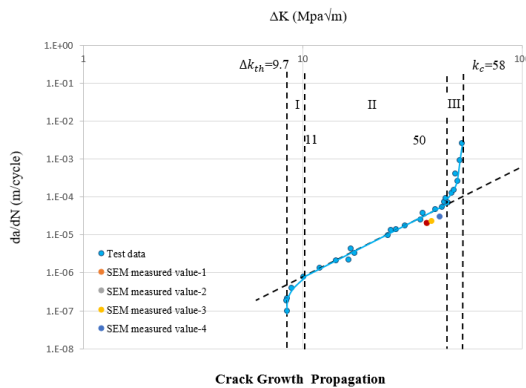


Fig. 12 Fatigue crack growth test results along with SEM open-hole data

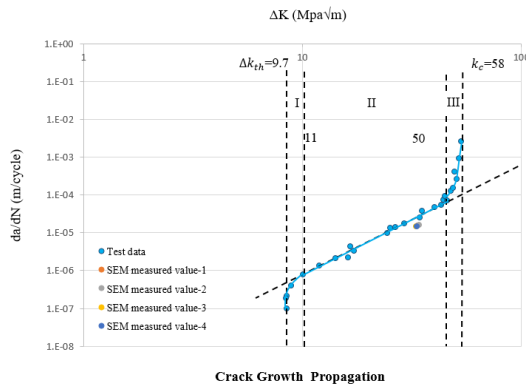


Fig. 13 Fatigue crack growth test results along with SEM riveted data

#### 4.4. Correlations Between Crack Growth Rate and Stress Ratio Using AFGROW

Since fatigue cracks grow during the life of cyclically loaded components, any parameter which affects the growth can have a major effect on the total fatigue behavior of the components. One such parameter that has a significant effect on fatigue crack growth is stress ratio R [22, 23]. To account for the observed effect of stress ratio on crack growth rate, two different models have been proposed for the open-hole and riveted coupons. Generally, with increasing positive stress ratio at a given value of  $\Delta K$ , the fatigue crack growth rate increases.

Figure 14 compares the influence of the R-ratio of 0.1 to 0.4 on the fatigue crack growth rate between the open-hole and the riveted specimens using AFGROW.

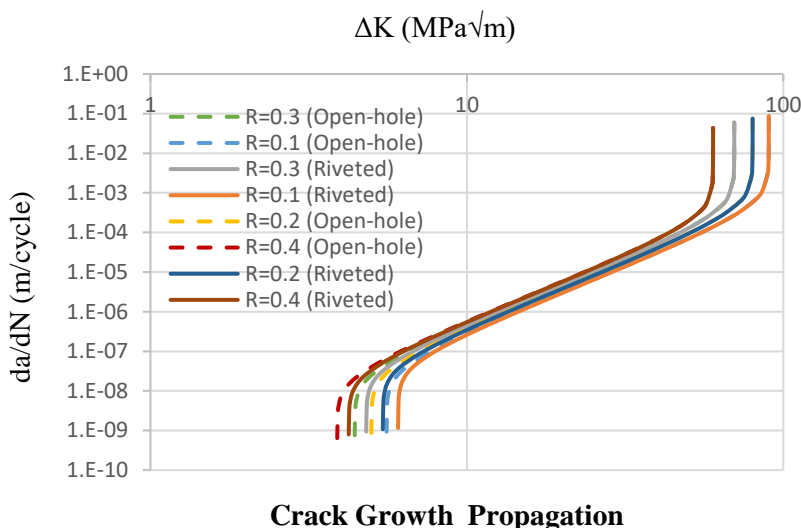


Fig. 14 Fatigue crack growth rate vs. stress intensity factor for different R-ratio

It might be seen that the effect of changing R-ratio for the open-hole and the riveted specimens is simply that the higher R-ratio increases crack growth rates and lowers fatigue life. However, the riveted samples exhibited longer fatigue life at stress ratio of 0.1 as compared with the open hole, which demonstrates the positive effect of the rivet. It is important to note that the riveting process results in a compressive residual stress near the location of the origin of failure.

#### 5. Conclusions

Fatigue has been a design consideration for open grid decks on bridges. In fact, some of the most replaced systems on movable bridges are the deck systems. As a result, fatigue life analysis and design of such systems are necessary. Within the scope of this study, fatigue behavior of the deck focused on the riveted connections in heavy duty riveted steel grates. Therefore, fatigue test results for both open-hole and riveted coupons were compared with life predictions prepared using AFGROW. Fatigue life predictions were close to and consistent with the lower bound curves derived from open-hole test results. However, comparison of the predicted fatigue life of the riveted specimens using the fracture

mechanics model shows that the predicted lives are slightly higher as compared to the test data. These results demonstrate the positive effect of the rivet and the residual stresses resulting from the riveting process.

Fatigue crack growth rate curves obtained from testing of the steel used in grate fabrication are conservative as compared with the corresponding simulations conducted using AFGROW. The Fatigue crack growth threshold based on the experimental test results was compared with the material library in AFGROW. The measured fatigue crack threshold was not identical to, but was similar to that from AFGROW. Based on the fracture mechanics models, the threshold stress intensity of the riveted specimen is about 17% greater than for the open-hole specimen at the same stress range. Reasonable agreement between the striation spacing measurements made from SEM images and the results of crack growth testing was observed. The best-fit S-N curve based on fatigue crack growth data analyzed by AFGROW using the tabular look-up model is in good agreement with the fatigue test results. The fatigue crack growth rate increases with increasing stress ratio at a given value of  $\Delta K$ . The riveted specimens exhibited longer fatigue life, primarily due to the favorable residual stress field induced by the riveting process. This highlights the need to have a carefully controlled riveting process.

## References

- [1] Dowling NE. Mechanical behavior of materials: engineering methods for deformation, fracture, and fatigue. Pearson; 2012.
- [2] Broek D. Elementary engineering fracture mechanics. Springer Science & Business Media; 2012.
- [3] Kulak GL, Fisher JW, Struik JH. Guide to Design Criteria for Bolted and Riveted Joints Second Edition; 2001.
- [4] Santecchia E, Hamouda AM, Musharavati F, Zalnezhad E, Cabibbo M, El Mehtedi M, Spigarelli S. A review on fatigue life prediction methods for metals. *Advances in Materials Science and Engineering*; 2016. <https://doi.org/10.1155/2016/9573524>
- [5] Connors WC. Fatigue striation spacing analysis. *Materials characterization*. 1994 Oct 1; 33(3):245-53. [https://doi.org/10.1016/1044-5803\(94\)90046-9](https://doi.org/10.1016/1044-5803(94)90046-9)
- [6] Sbordone L, Traini T, Caputi S, Scarano A, Bortolaia C, Piattelli A. Scanning electron microscopy fractography analysis of fractured hollow implants. *Journal of Oral Implantology*. 2010 Apr; 36(2):105-11. <https://doi.org/10.1563/AAID-IOI-D-10-90000>
- [7] Åkesson B. Fatigue life of riveted steel bridges. CRC Press; 2010. <https://doi.org/10.1201/b10429>
- [8] Lassen T, Darcis P, Recho N. Fatigue Behavior of Welded Joints Part 1-Statistical Methods for Fatigue Life Prediction. *Welding journal*. 2005 Dec 1; 84(Suppl):183-7.
- [9] Haghani R, Al-Emrani M, Heshmati M. Fatigue-prone details in steel bridges. *Buildings*. 2012 Dec; 2(4):456-76. <https://doi.org/10.3390/buildings2040456>
- [10] Russo FM, Mertz DR, Frank KH, Wilson KE. Design and evaluation of steel bridges for fatigue and fracture-reference manual. National Highway Institute (US); 2016 Dec 1.
- [11] Wang ZY, Li L, Liu YJ, Wang QY. Fatigue property of open-hole steel plates influenced by bolted clamp-up and hole fabrication methods. *Materials*. 2016 Aug; 9(8):698. <https://doi.org/10.3390/ma9080698>
- [12] Urban MR. Analysis of the fatigue life of riveted sheet metal helicopter airframe joints. *International journal of fatigue*. 2003 Sep 1; 25(9-11):1013-26. <https://doi.org/10.1016/j.ijfatigue.2003.08.003>

- [13] Abdulla W, Menzemer C. Fatigue Behavior of a Riveted Connection Detail Used in Steel Bridge Construction; 2020. <https://doi.org/10.12988/ces.2020.91605>
- [14] Harter JA. AFGROW Reference Manual (version 5.3.3.23). Wright-Patterson Air Force Base, AFRL/VASM; 2019.
- [15] Maierhofer J, Pippan R, Ganser HP. Modified NASGRO equation for physically short cracks. *International Journal of fatigue*. 2014 Feb 1; 59:200-7. <https://doi.org/10.1016/j.ijfatigue.2013.08.019>
- [16] Blasón S, Correia JA, Apetre N, Arcari A, De Jesus AM, Moreira PM, Fernández-Canteli A. Proposal of a fatigue crack propagation model taking into account crack closure effects using a modified CCS crack growth model. *Procedia Structural Integrity*. 2016 Jan 1; 1:110-7. <https://doi.org/10.1016/j.prostr.2016.02.016>
- [17] AFGROW, 5.03.05.22, crack growth life prediction software developed by LexTech, Inc., 2018.
- [18] ASTM. Standard Test Method for Measurement of Fracture Toughness. E1820 - 18; 2018.
- [19] Connors WC. Fatigue striation spacing analysis. *Materials characterization*. 1994 Oct 1; 33(3):245-53. [https://doi.org/10.1016/1044-5803\(94\)90046-9](https://doi.org/10.1016/1044-5803(94)90046-9)
- [20] Sbordone L, Traini T, Caputi S, Scarano A, Bortolaia C, Piattelli A. Scanning electron microscopy fractography analysis of fractured hollow implants. *Journal of Oral Implantology*. 2010 Apr; 36(2):105-11. <https://doi.org/10.1563/AAID-JOI-D-10-90000>
- [21] Akhtar K, Khan SA, Khan SB, Asiri AM. Scanning electron microscopy: Principle and applications in nanomaterials characterization. In *Handbook of materials characterization 2018* (pp. 113-145). Springer, Cham. [https://doi.org/10.1007/978-3-319-92955-2\\_4](https://doi.org/10.1007/978-3-319-92955-2_4)
- [22] Hudson CM, Scardina JT. Effect of stress ratio on fatigue-crack growth in 7075-T6 aluminum-alloy sheet. *Engineering fracture mechanics*. 1969 Apr 1; 1(3):429-46. [https://doi.org/10.1016/0013-7944\(69\)90003-4](https://doi.org/10.1016/0013-7944(69)90003-4)
- [23] Musuva JK, Radon JC. The effect of stress ratio and frequency on fatigue crack growth. *Fatigue & Fracture of Engineering Materials & Structures*. 1979 May; 1(4):457-70. <https://doi.org/10.1111/j.1460-2695.1979.tb01333.x>

Blank Page



Research Article

## Behavior of structure type 82/2 (RC frame), during the earthquake of 26 November 2019 in Durrës, Albania

Anjeza Gjini<sup>\*1,a</sup>, Hektor Cullufi<sup>1,b</sup>, Enio Deneko<sup>1,c</sup>, Princ Xhika<sup>2,d</sup>

<sup>1</sup>Faculty of Civil Engineering, Polytechnic University of Tirana, Albania

<sup>2</sup>Structural Engineer, Kastrati Group, Tirana, Albania

### Article Info

#### Article history:

Received 25 May 2021

Revised 21 Jun 2021

Accepted 28 Jun 2021

#### Keywords:

Structure Type 82/2;

Seismic events;

Pushover analysis

### Abstract

On November 26, 2019, an earthquake with magnitude  $M_w = 6.4$  occurred in the city of Durrës, with epicenter about 16 km southwest of Mamurras. This seismic event caused 51 loss of life, hundreds injured and hundreds of damaged buildings. One of the typified structures, identified by the authors with the most cases of damage or even collapse, is the structure Type no. 82/2 built in some areas of the city of Durrës, in the period 1983-1993. The purpose of this study is to analyze the behavior of this type of structure during seismic loading (for two cases, five and six storey, from the same typology), using the non-linear static procedure (Pushover). The obtained results are compared with the damages recorded in the field for these buildings, concluding with their main causes. According to this study it appears that the main cause of failures occurred in this type of building is the reduction of the reinforcement amount from the ground floor to the first floor by 35.5% and percentage of reinforcement required for the given section exceeds the requirements of design standards (Eurocode-2 and KTP-2-89) by around 30%. Also on these failures contribute the low strength of concrete used in construction of some of these buildings (the compressive strength results 50% less than required) and the use of smooth rebar.

© 2021 MIM Research Group. All rights reserved.

## 1. Introduction

Durrës is one of the oldest cities in Albania (known as “Dyrrahum”), with a history of over 2500 years. The region of Durrës is subjected to several strong earthquakes (I0>VIII EMS-98). It can be mentioned the earthquakes in 177 B.C., 334 or 345 A.C., 506, 1273, 1279, 1869 and 1870. The most significant earthquakes of the latest 30 years occur in September and November 2019, with the later one being the most devastating in Durrës region. The earthquake of November 26, 2019 was a 6.4 magnitude earthquake, about 16 km off the coast of Mamurras at 3.54 CET [1]. The most affected area was Durrës and Thumanë, while significant damages were reported in Shijak, Kruja, Tirana, Kamza, Kavaja, Kurbin and Lezha, as well. The earthquake caused 51 fatalities, 913 people injured at least, and the damages of hundreds of buildings [2].

Previous studies are done after this earthquake to identify the damages and their causes for different types of structures. Referring to these studies, most of the inspected buildings sustained severe non-structural damage, because of the combination of flexible structural system and rigid infills. Also, there are some deficiencies in the current Albanian seismic code, that does not provide drift limitations for Damage Limit States. [3] Damage to infills was a widespread issue in Albania after the earthquake. The low lateral stiffness of wide beam – column connections was a likely contributor (in addition to other factors). [4] In

\*Corresponding author: [anjeza.gjini@ftn.edu.al](mailto:anjeza.gjini@ftn.edu.al)

<sup>a</sup> [orcid.org/0000-0002-2258-5332](https://orcid.org/0000-0002-2258-5332); <sup>b</sup> [orcid.org/0000-0001-5238-9992](https://orcid.org/0000-0001-5238-9992); <sup>c</sup> [orcid.org/0000-0002-2029-2042](https://orcid.org/0000-0002-2029-2042);

<sup>d</sup> [orcid.org/0000-0003-4295-2475](https://orcid.org/0000-0003-4295-2475)

DOI: <https://dx.doi.org/10.17515/resm2021.303ea0525>

Res. Eng. Struct. Mat. Vol. 7 Iss. 4 (2021) 595-615

the other hand, the URM structures built of masonry walls have been shown to have low seismic capacity. [5]

After this seismic event, the Construction Institute in cooperation with the academic staff of the Faculty of Civil Engineering in Tirana, organized a more detailed inspection of damaged buildings (in accordance with the DCM no.26, date 15.01.2020) [6] and identifying the extent of their damage. During this inspection in the city of Durrës, the authors (part of the inspection groups) found that one of the typologies with RC frame, named in the project as "Building type 82/2", has suffered significant damage. Two of these buildings collapsed during the November 26 earthquake. Others were assessed as severely damaged, due to significant damage to their structural elements.

Based on these findings and having the necessary data for the study, this article aims to analyze the behavior of building type 82/2, during the November 26 earthquake in Durres.

## 2. Typologies of Constructions in Albania

Buildings in Albania can be classified according to the construction period. Before 1952, the houses were 1-2 storey, built of brick or stone masonry. During the years 1952-1988 began the construction of the residential buildings according to the concept of "Typologies", in fulfillment of the communist ideology, to save construction time and reduce costs. Hence, from the 2-storey houses with a roof (type of 1958) it was transferred to 5-storey buildings (type of 1977) and further to those 6 floors (after 1982). The changes in the "Typology" of projects in different periods consisted not only in their functional and aesthetic requirements, but also in the structural aspect. Thus, from structures with the brick masonry (clay / silicate), the RC frame and the one with shear wall is further developed (after 1980). After 80', began the design and the construction of prefabricated buildings. They were quite prevalent because prefabricated panels permit a larger area of apartments. In 1982 started the construction of 6-storey buildings with elevators and in 1988 the construction of those with shear wall. [7] [8].

After 1993 (in various literatures also refers to 1990, but in this article 1993 is taken as the year of change of the existing legal framework for construction, adapted to the basics of market economy), private investment began to develop in Albania, thus increasing the demand for high-buildings and premises with larger areas.

Referring to the study conducted by INSTAT (until 2011) [9] (Figure 1), it is noticed that 1-2 storey buildings occupy the highest percentage of constructions in the city of Durrës . From 1991 to 2011, the number of buildings more than 6 floors have increased by about 79% and occupy about 3.5% of the total number of constructions in this city.

Figure 2 shows that the number of construction permits approved for buildings more than 3 floors, throughout the territory of Albania, for the period 2016-2020 has increased 3.3 times and occupies about 22% of construction permits issued in this period (it is noted that the study refers only to residential buildings).

High-rise buildings (> 6 floors) designed mainly after 2001 are with RC frame system, with/without shear walls.

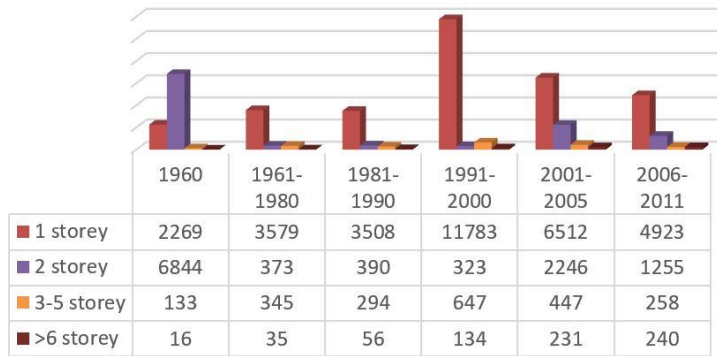


Fig. 1 Number of buildings by floors for the period 1960-2011, in the city of Durrës



Fig. 2 Number of construction permits approved for the period 2016-2020 in the territory of Albania [9]

### 3. November 26, 2019, Durrës Earthquake

On September 21, 2019, in the city of Durrës was recorded the seismic event with magnitude  $M_w = 5.6$ , with epicenter 3 km southwest of Shijak, with a depth of 20 km. The aftershocks continued for several weeks, until on November 26, 2019, the main shock was recorded with magnitude  $M_w = 6.4$ , with an epicenter about 15.6 km southwest of Mamurras [1].

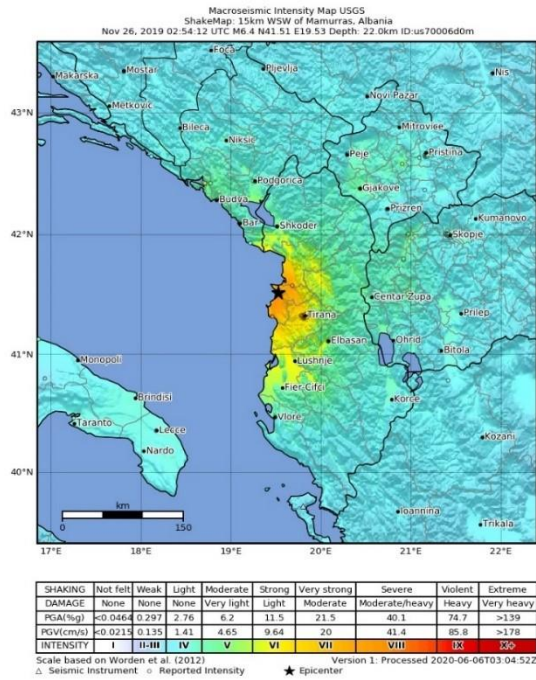


Fig. 3 Macroseismic Intensity Map [1]

Based on the microzoning map (MSK-64), the seismic intensity in the Durrës area is IX, so the seismicity coefficient takes the value 0.42g, for land category III.

The following figure shows the elastic spectra according to EC-8 [10] and KTP-2-89 (Technical Design Code of Albania, published in 1989) [11], as well as the real spectra according to the two main directions E-W and N-S recorded by Institute of Geosciences, Energy, Water and Environment (IGJEUM) at the Durrës station [12].

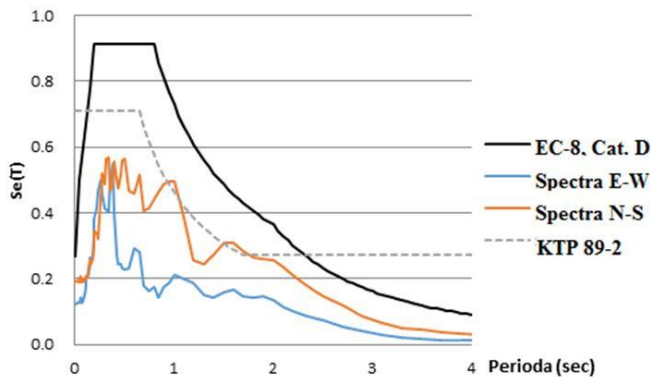


Fig. 4 Elastic spectra according to EC-8 (Cat.D, PGA 0.27g), KTP-2 (Cat.III,  $a_0 = 0.42g$ ) and oscillation spectra recorded for both directions at Durrës station

As can be seen, the real spectra are within the elastic spectrum of Eurocode and almost within that of KTP. At certain points the spectrum in the N-S direction exceeds that of the KTP. This shows that the strongest waves are in this direction. [13]

#### 4. Case Study

The buildings taken in the study, located in the city of Durrës, are of the same typology, respectively type 82/2 (year of design 1982), built in different periods. The structural design of the building Type 82/2, made available by the Central Technical Archive of Construction (AQTN) in Tirana (Figure 5), has been drafted by the Research and Design Institute No. 1 Tirana (ISP). Referring to this project, the building Type 82/2 is conceived as a structure with prefabricated reinforced concrete frames. This building is designed for areas with a seismic intensity IX (according the design notes). This project marks the beginning of the construction of RC frame structure, 5-storey and 6-storey.

Research and Design Bureau (BSP) of the districts had the task of redesigning the project in accordance with the terrain, natural environment, climate, tradition (according to the technical notes of the project). The typology of buildings 82/2 is constructed in Durrës according this design compiled by BSP. Referring to this re-designed project (Figures 6-8) some changes have been made regarding the structural project drafted by the ISP (Research and Design Institute, Tirana), namely:

- The 5 and 6 storey structure is designed as a monolithic reinforced concrete frame;
- The class of concrete has decreased, leading to increased amount of reinforcement of the columns. The studied buildings were constructed according to a project for 5 and 6 floors with monolithic reinforced concrete frame. The structure has no irregularity in plan and in height.

The foundations of the structure are designed with two-stepped footing, with different dimensions (three types). Perimetral footings are connected to the head with prefabricated foundation beams, with dimensions (bxh) 300x400 mm. All columns are located along the parallel axes, with dimensions 300x400 mm (the amount of reinforcement is given in Figure 8). The transverse reinforcement (stirrups) is designed  $\phi 6$ , placed every 100 mm in critical zone and 200 mm in the mid-high of columns. The beams are designed with dimensions (bxh) 300x400 mm. Based on the technical design, the slabs are of prefabricated panels, with holes,  $h=110$  mm (as shown in the Figure 7).

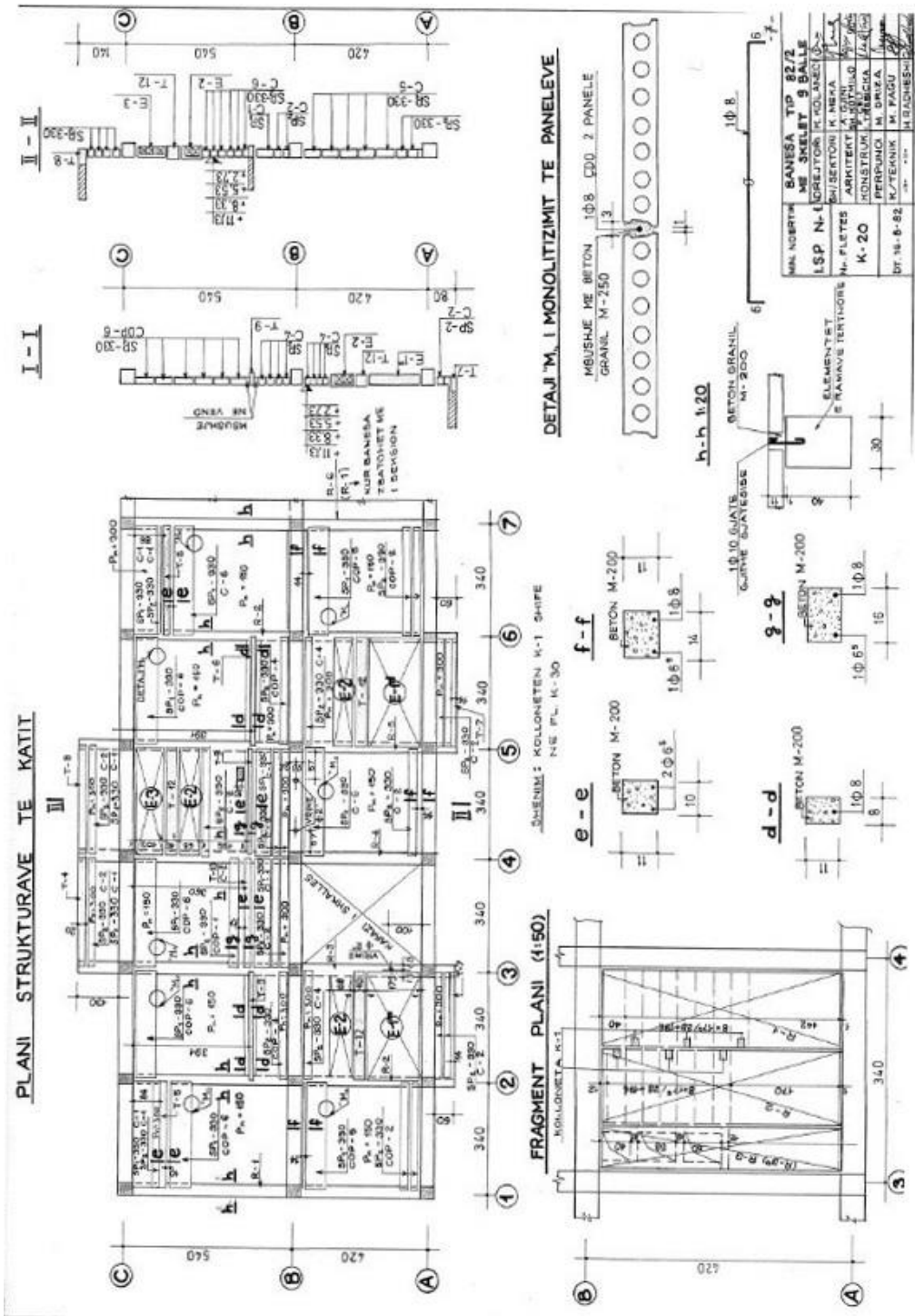


Fig. 5 Structural plan of building type 82/2 (one version), with prefabricated frames, as designed by Research and Design Institute No. 1 Tirana (ISP), (Central Technical Archive of Construction - AQTN)

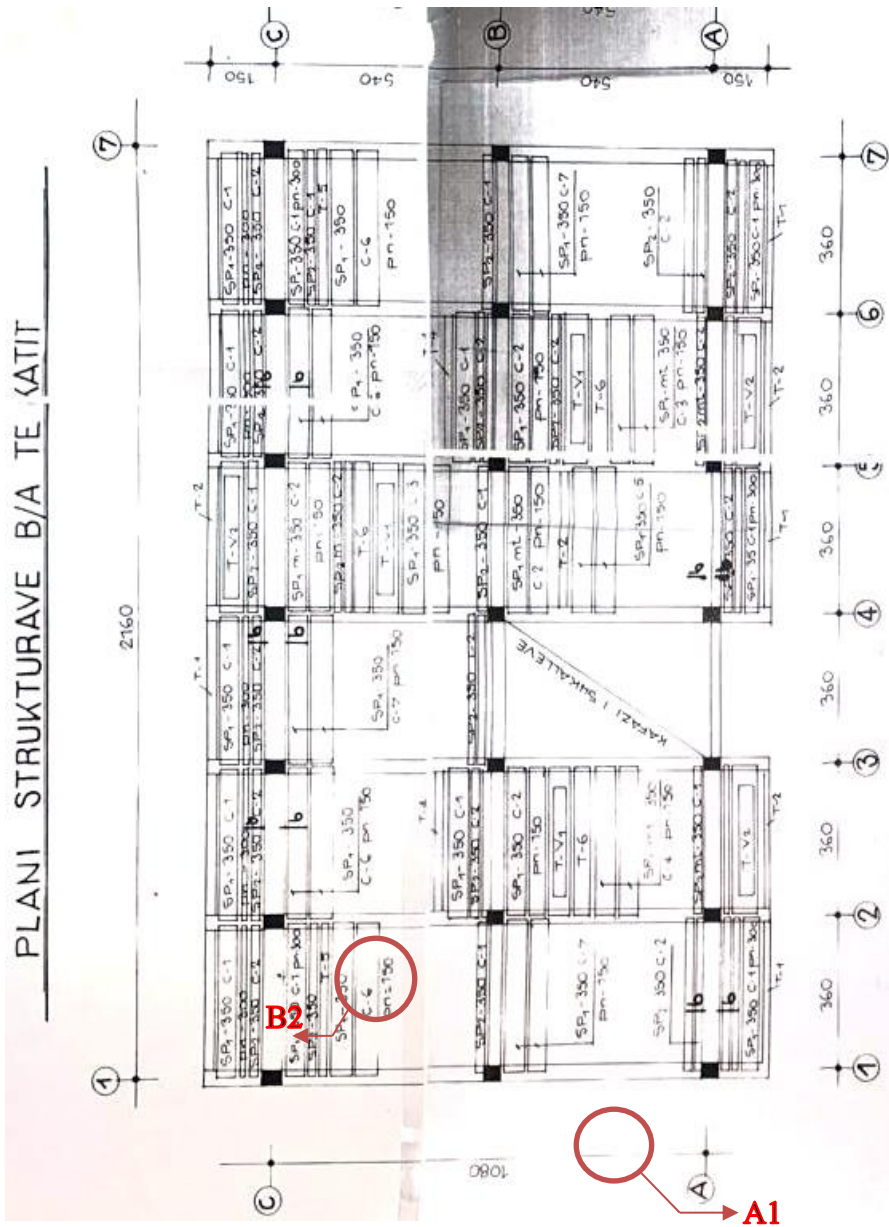


Fig. 6 Structural plan for building type 82/2, with monolithic RC frame system (as constructed)

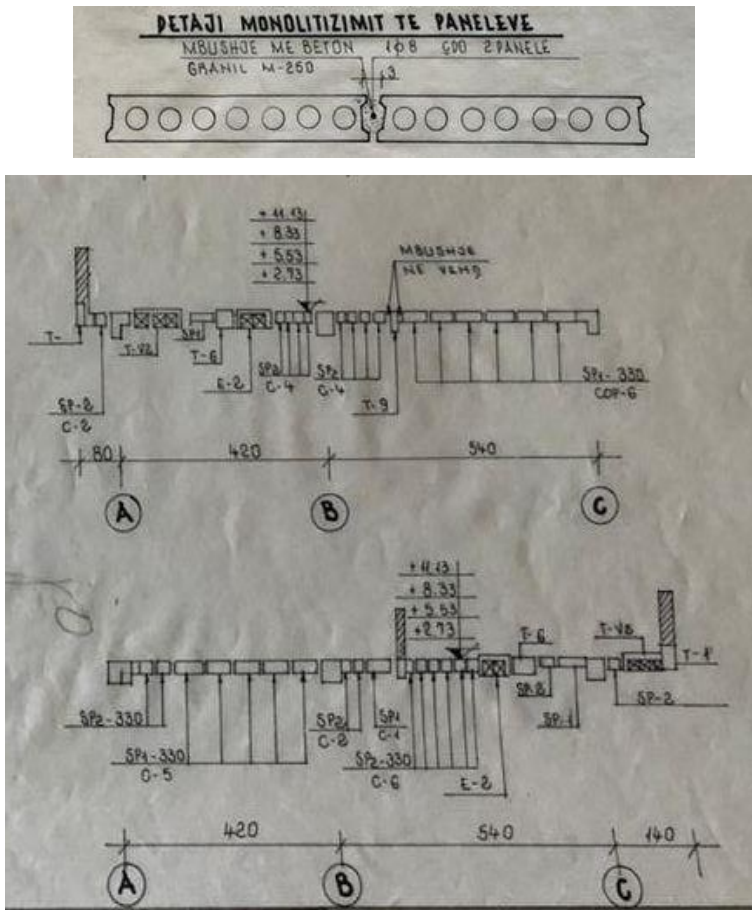


Fig. 7 Details of slabs (as constructed)

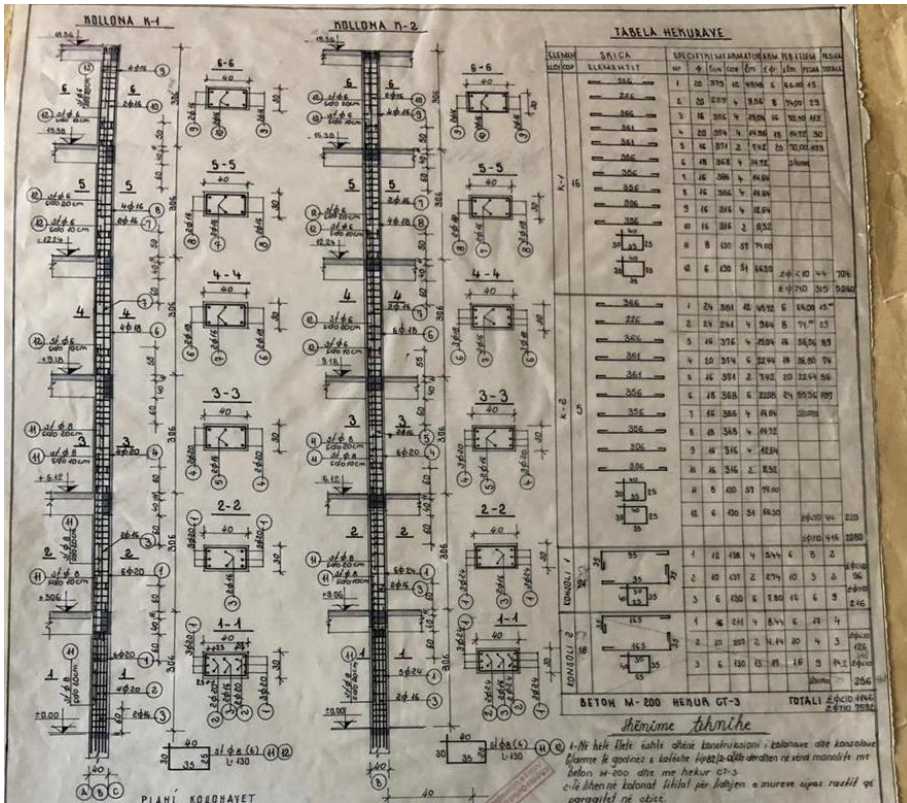


Fig. 8 Details for reinforcement of columns (as constructed)

5. Location

The buildings taken in the study are located in the city of Durrës, respectively in regions no. 3, 4 and 5. The area in which the buildings are positioned has a distance of about 22km southwest from the epicenter of the November 26, 2019 earthquake.



Fig. 9 Location of the studied buildings

## 6. Material Properties

Referring to the technical notes in the structural design of the buildings type 82/2, the class of concrete is M-200 (C16/20), while reinforcing steel is Ç-3 (according to KTP-Albania design code). Below are given the characteristics of these materials.

Table 1. Properties of steel Ç-3

Characteristics of Reinforcing steel	Ç-3
Characteristic yield strength	$f_{yk} = 250 \text{ MPa}$
Characteristic tensile strength	$f_{tk} = 320 \text{ MPa}$
Modulus of elasticity	$E_s = 210\,000 \text{ MPa} = 210 \text{ GPa}$
Partial factor	$\gamma_s = 1,15$
Design yield strength	$f_{yd} = 215 \text{ MPa}$
Design yield for shear	$F_{ywd} = 180 \text{ MPa}$
Poisson's ratio	$\nu = 0.30$

Table 2. Properties of concrete C16/20

Characteristics of concrete	C16/20 MPa
Characteristic compressive cylinder strength	$f_{ck} = 20 \text{ MPa}$
Characteristic cubic strength	$R_{ck} = 16 \text{ MPa (fck,cube)}$
Mean value of concrete cylinder compressive strength (28 days)	$f_{cm} = 28 \text{ MPa}$
Mean value of axial tensile strength of concrete	$f_{ctm} = 2,2 \text{ MPa}$
Characteristic axial tensile strength of concrete	$f_{ctk(5\%)} = 1,5 \text{ MPa}$
Characteristic axial tensile strength of concrete	$f_{ctk(95\%)} = 2,9 \text{ MPa}$
Secant modulus of elasticity of concrete	$E_{cm} = 30 \text{ GPa}$
Design value of modulus of elasticity of concrete	$E_{cd} = 25 \text{ GPa}$
Partial factor for concrete	$\gamma_c = 1,5 \quad \alpha = 0.85$
Design value of concrete compressive strength	$f_{cd} = \alpha * f_{ck} / \gamma_c = 11,3 \text{ MPa}$
Poisson's ratio	$\nu = 0.20$

For investigation purposes, concrete and steel samples were taken and laboratory tests were performed. From the tests performed in one of the building type 82/2 (for the object shown in Figure 21) it results that the compressive strength of concrete samples is less than 50% of design requirements, and out of the requirements of KTP (Albanian design code), as shown in figure 10. Whereas, the properties of the steel, from the laboratory tests, turn out to be acceptable according to the design definition and the technical conditions (Figure 11).

Coring Date / Dt. E Karrotazhit: 12.12.2019  
 Testing date / Data e testimit: 13.12.2019

REZULTATET E TESTIMIT									
Sample No.	Position	Height for test Lartesia per test H [mm]	Diameter for test Diametri per test D [mm]	H/D ratio Raporti H/D	Weight Masa [g]	Density Masa Volumore [g/cm <sup>3</sup> ]	Load Ngarkesa [kN]	Compr. Strength Rez. Shtypje Cubic [MPa]	Note * Shenime
K1	Element beton/arme marre nga mбетjet e objektit te siperpemendur te depozituara prane Rajonit te Policise Shjake	77.0	75.0	1.03	778	2.287	27.9	6.32	
K2		77.5	75.0	1.03	797	2.328	35.6	8.06	

Fig. 10 Concrete test for one of the building type 82/2

Sampling Date / Data e marrjes se mostres: 12/12/19  
 Date of test / Data e Proves: 14/12/19  
 Specimen Nominal Diameter / Diametri Nominal / Mostrove:  $\varnothing = 14.16.22$  mm (Hekura pa vliaska) (No Rebar test bars)

TEST RESULTS / REZULTATET E TESTIT									
NR.	Nominal Diameter Diametri Nominal $\varnothing$ [mm]	Effective Diameter Diametri Efektiv $\varnothing_e$ [mm]	Linear Weight Masa Lineare [kg/m]	SDSS-SDSS Area Sektori Testhor (A <sub>s</sub> ) [mm <sup>2</sup> ]	Yield Strength Niseshanca ne Tereqje (R <sub>e</sub> ) [N/mm <sup>2</sup> ]	Tensile Strength Rezistenca ne Kapulje (R <sub>m</sub> ) [N/mm <sup>2</sup> ]	Tensile Yield Strength Rate Raporti Kapulje/Rebar (R <sub>m</sub> /R <sub>e</sub> )	Uniform Elongation Zgjatimi Relativ [%]	Note Shenime
1	14	14.95	1.377	175.40	267.8	462.1	1.502	32.54	
2	14	9.99	0.614	78.27	337.9	444.0	1.314	-5.00	
1	16	16.27	1.631	207.73	269.8	413.7	1.429	33.75	
2	16	15.87	1.552	197.66	269.4	400.2	1.486	35.00	
1	22	21.87	2.948	375.49	336.5	471.9	1.428	32.27	
2	22	21.91	2.958	376.75	331.8	469.4	1.415	30.00	

Fig. 11 Steel tests for one of the building type 82/2

As can be seen in the figure 10 and 11, only few tests are performed, respectively 2 tests for the concrete and 6 for the steel (in unidentified elements).

Based on Eurocode 1998-3, for assessing the capacity of buildings, this number of tests and their position (the place where the tests were taken) are insufficient for the integral knowledge of the characteristics of these materials used in the structure. It is advisable to test materials for at least 20% of the structural elements when information on the project and construction of the work exists. In cases where this documentation is missing, the number of pieces of evidence should normally be increased [14].

For a reliable structural design of these structures, the proprieties of materials noted in the design papers are considered. From the field inspection (from authors) it was found that in one of the buildings defined for demolition, the concrete of the columns on the ground floor was spalled even with the lightest touch due to the use of sea sand and gravel with large fractions (Figure 12a). This phenomenon has also been influenced by the use of smooth rebar, which reduces the adhesion to concrete (Figure 12b). [15]



Fig. 12 a) Spalling of concrete with hammer (photo by author), b) Smooth rebar for columns reinforcement (photo by author)

### 7. Identification of Damages

Before the year 1990, buildings are designed mainly based on the Albanian Technical Codes KTP-2-89 (which includes the seismic design norms).

The failure observed from Durrës Earthquake for various structures such as RC frame, brick masonry (clay/silicate) or prefabricated structures varied depending on the location, building type and the year of construction. The damages were evident in structural and non-structural elements. The key factors of RC frames damages can be listed:

- Design of high-rise buildings with reinforced concrete frame, without cores or diaphragms, as highly flexible structures with low rigidity. Damages have been identified in non-structural elements such as: out of plan walls, horizontal and diagonal cracks in the walls, etc.
- Differential settlement of the foundation due to the irregularity in plan and height, and seismic actions;
- Design of the structure with hidden beams in the slabs with smaller height, especially the perimetral beams, by reducing the stiffness of the structure.
- Incorrect design of stair beams by reducing the height of the columns and causing the effect of "short columns".
- Absence of piles, even when they are necessary for transmission of vertical forces and seismic action.
- Incorrect design of seismic joint in cases when two sections are built on the same foundation slab or pile, causing the effect of collision.
- Creation of plastic hinges in columns, due to their low strength compared to that of beams.
- Incorrect construction of beam-column joints.

Two of the studied buildings (type 82/2) collapsed, as a result of the earthquake of November 26, 2019, and the others have suffered significant damage to structural elements.

In Figure 13 damages of structural and non-structural elements are shown for various RC structures in Durrës city, taken during the field inspection.



a) Out of plane wall failure (belt beams for infill walls are unlinked with RC columns)



b) Failure of core type shear wall



c, d) Longitudinal reinforcement not fastened by stirrup



e, f) Deflection of the cantiliver beams (cracks in the slabs)



g) Cracks in the stair beam



h) Two buildings type 82/2 near each other, the one on the left did not collapse and on the right totally collapsed



i) Plastic hinge in the upper part of column



j) Out-of-plane wall failure

Fig. 13 Photos of the various damaged buildings in Durrës city (photos by author)

## 8. Model and Analysis

The Type 82/2 structure is modeled with the ETABS Ultimate 19 software for two cases, for the 5-storey building and the 6-storey building. The structure is modeled following the technical notes in the project. The model consists of 3D frame section, with slabs as shell elements. The proprieties of the materials are taken as described in section 5 (concrete and steel). Loadings (dead, live and earthquake) and their combination compliant with KTP-6-78 (Albanian design code) as follows:

$$S_v = S_{g1} + 0.8 \sum S_{p1} + S_{p2} \quad (1)$$

where,  $g_1$ - dead load,  $p_1$ -live loads,  $p_2$ -earthquake

For the seismic loading is taken the spectra recorded in Durrës station during the earthquake of November 26, 2019, as shown in Figure 4 [12] . Live loads are applied as follows [16]:

- Apartment  $p^n_1=150 \text{ daN/cm}^2$
- Hallway  $p^n_1=300 \text{ daN/cm}^2$
- Terraces  $p^n_1=200 \text{ daN/cm}^2$

Using ETABS Ultimate 19 software [17], two types of analysis, namely, response spectrum analysis and non-linear static analysis (Pushover) are conducted. Also, the structure is modelled according Eurocode directives to estimate the amount of reinforcement required by this design code.

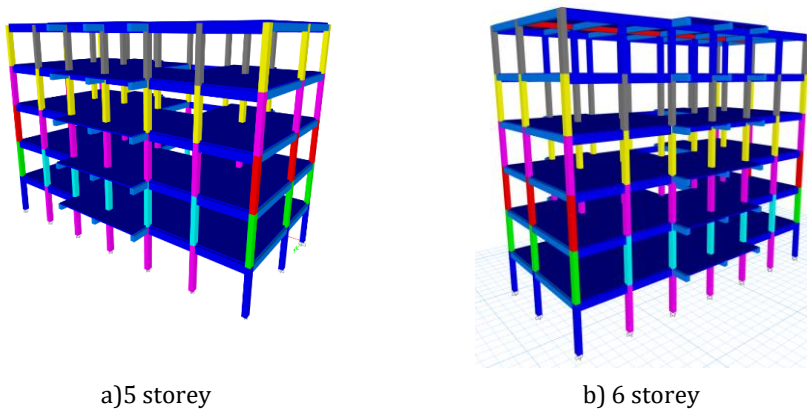


Fig. 14 Geometric models

## 9. Results

Below are shown the results obtained from the two types of analysis, response spectrum analysis and non-linear static analysis (Pushover). A very important parameter to assess the damage of structural and non-structural elements during seismic action, is the inter-storey drift.

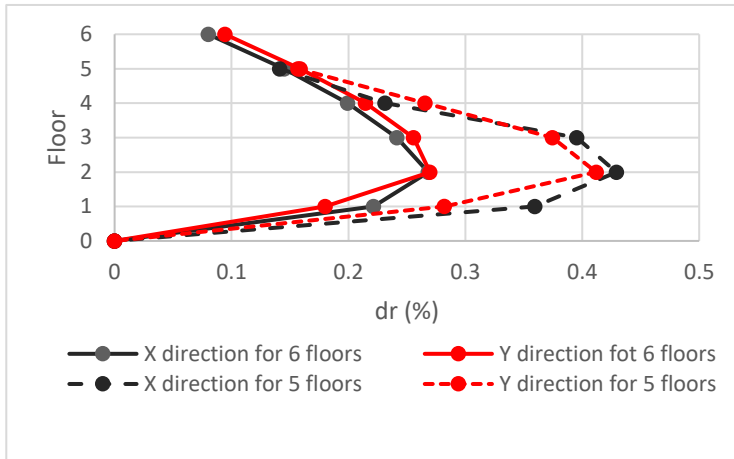


Fig. 15 Maximal drifts

As can be seen from the Figure 15, the interstorey drift reach up to 0.0043 for the 6 storey building and 0.0042 for the 5 storey building. For both studied cases, the requirement of EC-8 and KTP 89-2 are met (according to code maximum drift is 0.0087).

The interstorey drifts are higher in the 2<sup>nd</sup>-3<sup>rd</sup> floors because the amount of the columns reinforcement decreases. Referring to Figure 8, in the ground floor the columns are reinforced with 10 $\phi$ 20+2  $\phi$ 16. In the first floor there is a reduction to 6 $\phi$ 20+2  $\phi$ 16 (35.5% lower), and in the second floor (up to the last floor) it ends with 4 $\phi$ 20+2  $\phi$ 16 (27.4% lower). While, the dimensions of the columns section do not change.

From the nonlinear static analysis (Pushover), the 5-storey building exhibits a seismic capacity that does not fulfill the seismic demand (for y-direction). This phenomenon is also evidenced in the 6-storey building (as shown in Figure 16 and 17).

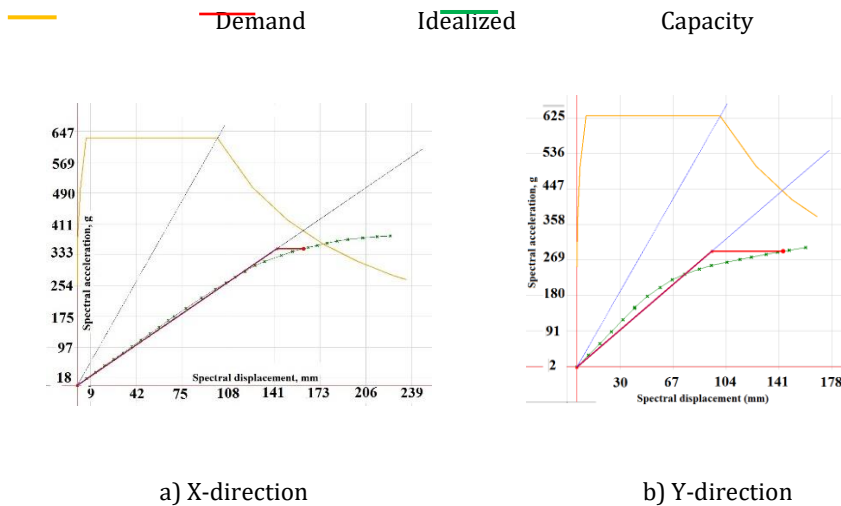


Fig. 16 Capacity diagrams for 5-storey building



The P-M2-M3 interaction generated from response spectrum is represented by a point outside the interaction curve (Figs. 18 and 19). It is clear the reduction of the bending capacity of the ground floor and first floor columns also identified from the damaged state, with the appearance of plastic hinges at their ends. From the development of plastic hinges, it is evidenced that the expected mechanism of collapse develops on the first floor rather than ground floor (Figure 21). This is a reasonable explanation considering the immediate change in the quantity of the longitudinal reinforcement of columns on this floor.

The level of performance is described referring the corresponding damage limit state. In Figure 20, the force-deformation (moment-rotation) curve of a typical plastic hinge is given. Referring to Figure 22 (the plastic hinge distribution), for the 5-storey building the plastic hinge is developed in the first floor, and corresponds to the point B (represents yielding) and in some elements to the point E (represents total failure). For the 6-storey building plastic hinges also develop in the first floor, representing by the point C (ultimate capacity) and E in some elements. Acceptance criteria for deformation or deformation ratios for primary members (P) and secondary members (S) corresponding to the target Building Performance Levels of Collapse Prevention (CP), Life Safety (LS), and Immediate Occupancy (IO) as shown in Figure 20, are given in FEMA 2000 [18].

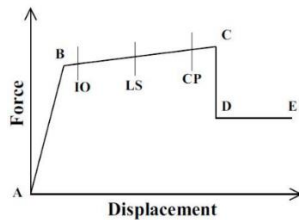


Fig. 20 Force-Deformation relationship of a typical plastic hinge [18]



Fig. 21 Collapse of the first floor in 5 storey building type 82/2

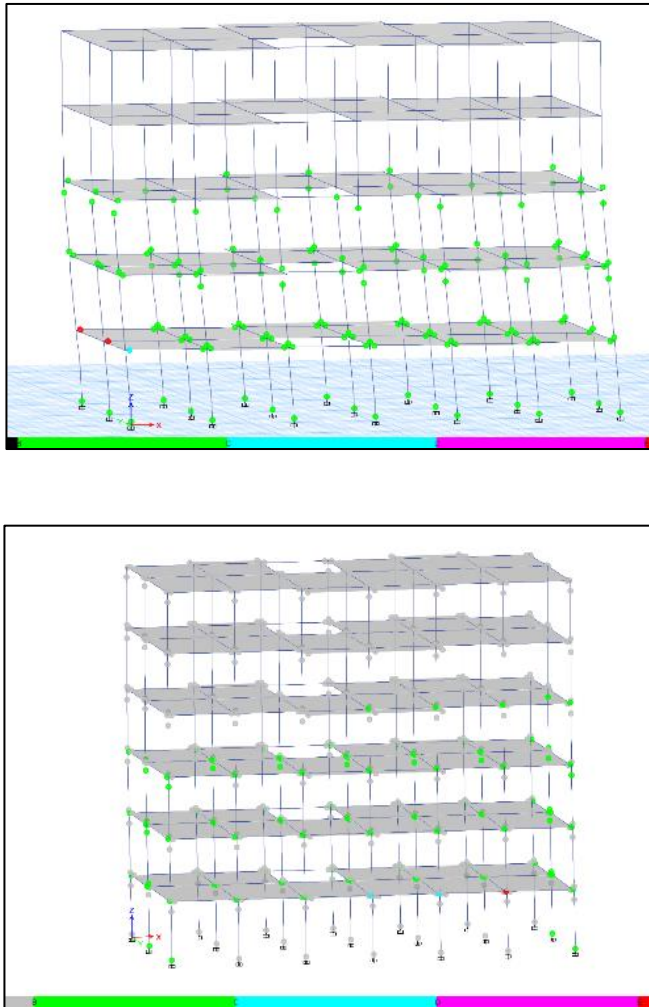


Fig. 22 Development of plastic hinges (generally in state A to B in plastic hinge development curve and a few in the highly plastic, near rupture D region ) from the nonlinear static analysis (Pushover) a) 5-storey and b) 6-storey building

Since ground floor columns in reinforced concrete structures are the most stressed elements during seismic action, in this study a comparison of reinforcement according to the project and structural modeling is made.

It is noticed that even for the 5 floor model, the amount of reinforcement required (obtained from response spectrum analysis) is greater than that referred to the project.

From the modeling of the project according to the current design codes such as Eurocode it can be seen that these elements (with the same concrete sections as given in the design papers) need very high reinforcement, respectively 5.88% and 6.96% (> 4%) which is prohibited according to this code.

Table 3. Comparison of reinforcement area and percentage (as-built project vs design model) for the two types of columns in the ground floor

#	5-storey		6-storey	
	Reinforcement (cm <sup>2</sup> )		Reinforcement (cm <sup>2</sup> )	
	Reinforcement (%)		Reinforcement (%)	
	As-build project	Design model	As-build project	Design model
K-1	35.43 (2.95%)	63.24 (5.27%)	35.43 (2.95%)	70.56 (5.88%)
K-2	49.26 (3.88%)	76.20 (6.35%)	49.26 (3.88%)	83.52 (6.96%)

## 10. Conclusion

The purpose of this study is to analyze the behavior of the designed structure Type 82/2, from the earthquake of November 26, 2019 in the city of Durrës, by comparing the results obtained from the response spectrum analysis (both for design of possible reinforcements and check of existing project) and non-linear static analysis (Pushover). The findings of the study can be stated as follows:

- Comparing the behavior of 5-storey and the 6-storey buildings results that they have the same collapse/failure mechanism.
- From the development of plastic hinges, it is evidenced that the expected collapse/failure mechanism develops on the first floor rather than the ground floor.
- The structural issues seem to be related to strength of elements, in the global and local level, rather than the displacement and drift related.
- For the 5-storey and 6-storey building, the percentage of reinforcement required for the given section exceeds the requirements of Eurocode 2 [19] and KTP by around 30%, meanwhile provided reinforcement is around 56% of required reinforcement by design analysis. Hence, concrete section is insufficient to resist loading.
- The increase of the capacity ratio of the ground floor columns has affected the reduction of the bearing capacity of the structure of the 5-storey building and even more with the addition of the sixth floor.
- The reinforcement area of columns is decreased in the first floor by 35.5% compared to the ground floor and in the second floor by 27.4% compared to the first floor. This explains the high interstorey drifts for the 2<sup>nd</sup>-3<sup>rd</sup> floor.
- There are some deficiencies that affected the low performance of this structure during the Durrës earthquake, causing damage to the load-bearing elements of these buildings. This fact is even more evident by considering the errors during construction, such as: use of transversal reinforcement with diameter and distance in critical zone that does not meet the requirements of design in seismic area, use of smoothed rebar as longitudinal reinforcement, or rather poor quality of the concrete used, justified on the conditions and quality of construction in the years when these structures were built (1983-1993).

## References

- [1] "Earthquake Hazards Program," [Online]. Available: <https://earthquake.usgs.gov/>. [Accessed 30 November 2019].
- [2] Republic of Albania, Council of Ministers, UNDP, "Albania Post-Disaster Needs Assessment Report," Council of Minister, Tirana, 2020.
- [3] Freddi F, Novelli V, Gentile R, Veliu E, Andreev S, Andonov A, Greco F, Zhuleku E. Observations from the 26th November 2019 Albania earthquake: the earthquake engineering field investigation team (EEFIT) mission, Bulletin of Earthquake Engineering, 2021, 19: 2013 - 2044. <https://doi.org/10.1007/s10518-021-01062-8>
- [4] Isufi B, Ramos AP, Baballëku M. Seismic Behavior of Wide Beam - Column Connections: A Literature Review and Observations from the November 26, 2019 Durrës Earthquake, ISDEE-International Symposium on Durrës Earthquakes and Eurocodes, Tirana, 2020.
- [5] Shkodrani N, Bilgin H, Hysenliu M. Influence of interventions on the seismic performance of URM buildings designed according to pre-modern codes, Research on Engineering Structures and Materials, 2021, 7:2 315 - 330. <https://doi.org/10.17515/resm2020.197ea0331>
- [6] Republika e Shqipërisë, VKM, "Për Realizimin e Ekspertizave të Thelluara për objektet e dëmtuara," Këshilli i Ministrave, Tirana, 2020.
- [7] Bego M. Skeda arkitekture 1965-2004 në kronikën e një jete të dallgëzuar: mbi degradimin urban sot., Tirana: Dea, 2009.
- [8] Bilgin H, Hysenliu M. Comparison of near and far-fault ground motion effects on low and mid-rise masonry buildings, Journal of Building Engineering, 2020; 30: 101248. <https://doi.org/10.1016/j.jobbe.2020.101248>
- [9] "Institute of Statistics," [Online]. Available: <http://instat.gov.al/al/temat/censet/censusi-i-popullsis%C3%AB-dhe-banesave/>. [Accessed 2011].
- [10] The European Union, EN 1998-1. Eurocode 8: Design of Structures for Earthquake Resistance - Part 1: General Rules, Seismic Actions and Rules for Buildings., CEN, 2004.
- [11] Akademia e Shkencave, Ministria e Ndërtimit, Kusht Teknik Projektimi per Ndërtimet Antisizmike KTP-2-89, Tirana, Albania: Akademia e Shkencave, 1989.
- [12] "Institute of Geosciences, Energy, Water and Environment," [Online]. Available: <https://www.geo.edu.al/newweb/?fq=bota&gj=gj1&kid=20>.
- [13] Duni L, Theodoulidis N. Short Note on the November 26, 2019 Durrës (Albania) M6.4 Earthquake: Strong Ground Motion with Emphasis in Durrës City, EMSC online report, 2019.
- [14] The European Union, EN 1998-3 (2005) (English): Eurocode 8: Design of structures for earthquake resistance - Part 3: Assessment and retrofitting of buildings., CEN, 2005.
- [15] Işık E, Harirchian E, Bilgin H, Jadhav K. The effect of material strength and discontinuity in RC structures according to different site-specific design spectra, Research on Engineering Structures and Materials, 2021. <https://doi.org/10.17515/resm2021.273st0303>
- [16] Akademia e Shkencave, Ministria e Ndërtimit, "Kritere projektimi. Përcaktimi i ngarkesave në objektet shoqërore ekonomike", KTP-6-78, Tirana, Albania: Akademia e Shkencave, 1978.
- [17] Computers and Structures INC. , Structural and Earthquake Engineering Software- ETABS Ultimate 19, USA: Computers and Structures INC. , 2019.
- [18] Federal Emergency Management Agency, Prestandard and Commentary for Seismic Rehabilitation of Buildings., Washington, D.C. : FEMA, 2000.
- [19] The European Union, Eurocode 2: Design of concrete structures - Part 1-1 : General rules and rules for buildings, CEN, 2004.

Blank Page



Research Article

## Macro-/micro-mechanical interlocking modification on the performance of hybrid friction stir spot welded aluminum/acrylonitrile butadiene styrene joints

Olatunji Oladimeji Ojo

Department of Industrial and Production Engineering, Federal University of Technology Akure, PMB 704, Akure, Nigeria

### Article Info

#### Article history:

Received 08 May 2021

Revised 19 Jun 2021

Accepted 29 Jun 2021

#### Keywords:

Aluminum alloy;

Polymer;

Threaded/unthreaded

hole friction stir spot

welding;

Microstructure;

Mechanical properties

### Abstract

Macro-/micro-mechanical interlocking enhancement of hybrid aluminum/acrylonitrile butadiene styrene (Al/ABS) joint is investigated via the use of joint modification approaches such as pre-fabricated threaded- and unthreaded-hole friction stir spot welding processes. The structure, tensile-shear failure load, and fracture behavior of the as-welded hybrid Al/ABS joints were investigated. Hybrid Al/ABS joint fabricated with threaded hole shows superior tensile-shear failure load due to the combined effects of compressive shearing-induced and threading-induced mechanical interlocks, and adhesion bonding mechanisms. The tensile-shear failure load of the threaded joint improved from 654 to 749 N as the tool rotational speed is increased from 710 to 1120 rpm. A rise in tool rotational speed improves the failure resistance of the hybrid Al/ABS joints (threaded and unthreaded) owing to the enhanced mechanical interlocking, bigger Al anchor/chip, and smaller interfacial gap between the re-solidified ABS and Al anchor. Threading and tool rotational speed have significant impacts on the fracture location and mode of the hybrid Al/ABS joint. The pre-fabricated threaded-hole friction stir spot welding process is thus recommended for the enhanced micro/macro-interlocking in hybrid Al/polymer joints.

© 2021 MIM Research Group. All rights reserved.

## 1. Introduction

Modern industries (such as aerospace and aviation, automotive, and high-speed trains manufacturing industries) continuously seek product design flexibility, cost-saving, high performance, fuel efficiency, high elastic modulus, and specific strength, reduced carbon footprint, and high reliability through the new paradigm shift of using light-weight materials in fabricating engineering structures [1, 2]. Polymers and hybrid metal-polymeric materials offer the potential of achieving the aforementioned goals, especially in drone manufacturing. However, the joining of polymers and metals is difficult through the traditional fusion processes due to the large physiochemical differences between the materials. The available metal/polymer joining processes in literature have been summarized as adhesive bonding, riveting, bolt connections, pin inserts (z-pin), welding (laser, induction, ultrasonic, braze, and resistance welding), and plastic deformation-aided joining processes such as friction stir (spot) welding, hot/self-pierce riveting, and mechanical clinching [3-5]. Susceptibility to environmental conditions (temperature and humidity) and a high disparity between the surface free energies of metal and polymers make adhesive bonding undesirable for metal/polymer joints [6]. Weight addition and induced stress-concentration are also major challenges of mechanically joined metal/polymer materials. Hybrid welding processes such as laser-TIG and diode laser-assisted joining of Al/polymer have recently been investigated by Wang et al. [7], and

Corresponding author: [ojooladimeji90@yahoo.com](mailto:ojooladimeji90@yahoo.com)

orcid.org/0000-0002-6581-1168

DOI: <http://dx.doi.org/10.17515/resm2021.290me0508>

Res. Eng. Struct. Mat. Vol. 7 Iss. 4 (2021) 617-633

Lambiase & Genna [8] respectively. The depth of laser penetration and the induced inherent bubbles were reported to affect the fracture modes and strength of the metal-polymer joints. However, solid-state friction stir (spot) joining of Al/polymers has evolved to be a cost-effective approach (with a process-joint modification capability) for improving the performance and load-bearing capacity of Al/polymer joints. Thus, this paper explores the joint modification-interlocking approach in enhancing the performance of the hybrid Al/ABS joint.

Literature shows that a lot of works on friction stir welding (FSW) of Al/polymer have been studied. For instance, Patel et al. [1] investigated the friction stir welded hybrid AA6061-T6/polycarbonate joints. The occurrence of improved heat concentration and mechanically interlocked Al/polymer (chip interlocking) at the stir zone was reported to improve the tensile strength of the joint to about 14.9 MPa at tool rotational speed and travel speed of 500 rpm and 40 mm/min respectively. Mechanical interlocking also improved the tensile strength of the AA6061/ABS (acrylic) joints to about 7 MPa (at 1000 rpm and 40 mm/min) while plastic deformation-aided hardness rise ensued as the welding speed was increased in the studies of Dalwadi et al. [9]. Macro-level and atomically locked interfaces (with no chemical bond) are established in the friction stir welded Al/polypropylene joint [10]. Liu et al. [11] investigated the interfacial zone of the friction lap welded Al/polyamide 66 joints. It was reported that the formation of Al-O-C bonds at the weld interface improved the resultant joint strength. The shear strength of the Al/PA66 joints was significantly improved by a combination of C-O-Al bonds and mechanical interlocking [12]. The interfacial bonding strength was reported not to be dependent on the induced welding temperature, provided an atomic contact between the Al alloy and PA66 was established. The formation of the interaction layer and internal voids in the AA5754/polymethylmethacrylate (T-joint) was stated to impair the strength and hardness of the joint [13]. However, the defects were cutback by either decreasing the tool travel speed or increasing the tool rotational speed. Derazkola & Elyasi [14] investigated the impact of process parameters on the friction stir welded AA5058/polycarbonate joints. It was revealed that the joint strength and fracture were controlled by the level of the tool rotational speed while the travel speed controlled the Al fragments within the polycarbonate matrix. Excessive heat accumulation induces local thermal degradation (LTD) while the combined effect of LTD and molten state of the polymer affects the lap shear strength of the glass-fabric reinforced polyetherimide/Ti alloy joint [15].

A few modifications of the joining process have also been reported in the literature. Tool modification was studied by Huang et al. [6] while the friction stir lap welding of the AA6061-T6/polyether ether ketone was investigated. It was reported that an increase in the welding speed reduced the adhesion area and the Al anchor with the joint, thereby, producing a deteriorated mechanical interlocking. Ozlati et al. [16] utilized fused deposition modeling (FDM) with polypropylene filament to produce lap joints of Al-Mg/polypropylene. It was stated that the substrate preheating improved the bonding between the polymer sheet/additive part. Hajideh et al. [17] have shown that the introduction of Cu powder to the dissimilar polypropylene/acrylonitrile butadiene styrene joint increased the hardness and tensile strength of the joint by 30 and 36% respectively. Hong et al. [18] investigated the combination of nanoparticle deposition and friction stir spot welding systems in fabricating carbon/Al metal matrix composite joint. This nanoparticle-aided joining approach was reported to improve the toughness and strength of the resultant joint. Derazkola & Simchi [19] employed an in-situ colloidal (nanoparticle) injection technique also known as fed friction stir processing in producing AA6062/ABS joints. Thermal stability was aided through the presence of nanoparticles in the joints while the mechanical properties of the resultant joints were significantly improved when compared with the conventional friction stir processed joints. Bending strength of 56 MPa

(20% improvement), a tensile strength of 60 MPa (14% improvement), and hardness of 79 ShoreD (11% improvement) were obtained with the new fed friction stir processed AA6062/ABS joint. Meng et al. [20] investigated the friction self-riveting of AA2060-T8/polymer matrix composite joints. The combined effect of adhesion and multi-scale mechanical interlocks was reported to produce a maximum tensile strength of about 27 MPa. Liu et al. [21] investigated the hole-clinching of the AA5754/carbon-fiber-reinforced polymer joints. It was revealed that joint delamination was severe in the Al/polymer joints fabricated with complex angle plies. Lambiasi & Paoletti [22] investigated the friction-assisted clinching of Al/carbon fiber-reinforced polymer. This new approach of joining was reported to increase material formability and joint strength.

Surface modification of Al alloy for enhanced interlocking is another approach to improving Al/polymer strength. Improved strength of AA5052/polypropylene joint (up to a factor of 6) was established with an anodizing pre-treatment process (in a sulphuric acid electrolyte) in the works of Aliasghari et al. [23]. Aliasghari et al. [24] employed the plasma electrolytic oxidation (PEO) technique to modify the surface of AA5052 Al alloy before being joined to a polypropylene via the use of friction stir spot welding process. The PEO generated a highly porous and rough surface that favors mechanical interlocking with the polymer. The pretreatment (PEO) technique was reported to have improved the tensile strength of the resultant joint by a factor of 3 (three) when compared to the as-welded FSSW joints. Han et al. [25] studied the friction spot joining of Al/polypropylene via the use of the surface laser pretreatment process. The laser pretreating of the Al surface caused the formation of a deep porous structure on the Al and this occurrence aided mechanical interlocking and changed the reaction features (chemical bonding) between the Al/polypropylene joint. Goushegir et al. [26] reported that sandblasting was suitable to induce surface roughness on AA2024-T3 alloy and this improved the performance of the friction stir spot welded AA2024-T3/poly(phenylene sulfide) joint. Nagatsuka et al. [27] studied the friction stir welding of AA5052 Al alloy and carbon fiber-reinforced polyamide 6 sheets. It was reported the surface grinding of the Al alloy aided the generation of Al(OH)<sub>3</sub> on the alloy which improved the joint strength. The occurrence of the Al/polymer (interfacial) Mg oxide layer aids the joining process.

The latest modification approach of improving Al/polymer joints is the friction stir spot welding (FSSW) approach based on a pre-drilled hole methodology. In this case, a hole is drilled in the Al plate and the molten polymer flows into the pre-drilled hole (during the FSSW process) to establish an interlocking between the Al and the polymer after solidification. This new approach has recently been studied by Paidar et al. [28], Pabandi et al. [29], and Aliasghari et al. [30]. It was reported that the infiltration of polymer into holes provided mechanical keying responsible for improved joint strength in the works of Aliasghari et al. [30]. This paper thus focuses on the use of a pre-drilled hole methodology in producing hybrid Al/ABS joints by examining threaded and unthreaded holes for macro-/micro-mechanical interlocking enhancement. It is necessary to clarify whether a hole or a combination of hole and threading is paramount for enhancing the load-bearing capacity of the Al/ABS joint to save manufacturing costs and time. The microstructure, tensile-shear failure load, and fracture behavior of the as-welded hybrid Al/ABS joints (with threaded and unthreaded holes) are thus clarified in this paper.

## 2. Materials and Method

The base materials employed for this research are 4 mm thick acrylonitrile butadiene styrene (ABS) and AA1050 Al alloy sheets respectively. The as-received polymeric and Al sheets were cleaned with acetone and then cut to the dimensions of 100 mm × 30 mm respectively. Overlapped friction stir spot welding (having an overlapped area of 30 mm × 30 mm) with the Al base material as the upper sheet and the ABS as the lower sheet was

designed for this research. Before the joining process, pre-weld preparations (drilling and threading) were carried on the Al alloy sheets to facilitate the formation of micro-/macro-mechanical interlocking of the Al and polymer sheet during the welding process. The center/middle of the overlapped area of the Al sheet was drilled with a 5 mm drill bit (to produce a through-hole) for some set of Al sheets while the other set of Al sheets were further threaded with an M6.5 mm tap. These pre-processed Al alloys were then placed on the ABS sheets and rigidly clamped to the worktable of the welding machine (MV-2 Maximill Milling Machine) before the joining process. For convenience, the joint obtained with a drilled hole is termed “DH” joint while that of a combination of drilling and threading is termed “DHT” joint in this paper. The schematics of the joining process are shown in Fig.1. The axis of the welding tool coaxially aligns with that of the drilled hole before the commencement of the joining process. This attribute is paramount for the success of the DH and DHT joints. A probeless tool having a 12 mm diameter was fabricated from the heat-treated high-speed steel (HSS) and used for the welding process. The rotating welding tool establishes contact with the top of the Al alloy and penetrates the alloy without reaching the ABS side. The generated in-process temperature rises above the melting point of the ABS and the molten ABS fills the pre-drilled Al hole (threaded and unthreaded) during the welding process. The welding parameters used for this research are tool rotational speed (710-1120 rpm), plunge depth (0.8 - 1.2 mm), and constant dwell time (5 s) respectively.

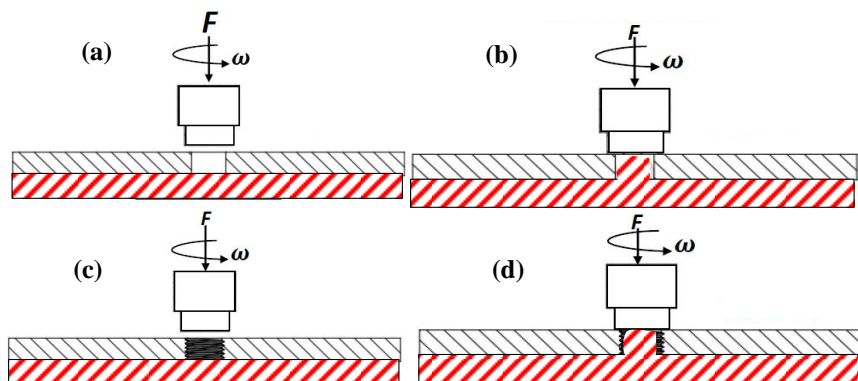


Fig. 1 Schematic of the joining process (a) and (b) DH joining before and after tool plunging, (c) and (d) DT joining process before and after tool plunging

The in-process and local environmental conditions (temperature, and humidity) of the Al/ABS joints were obtained via the use of three K-type thermocouples embedded into the interfacial region of the Al/ABS joints at distances of 10, 15, and 30 mm from the nugget center. The other ends of the thermocouples were connected to a data logger and a computer system for real-time monitoring and in-situ recording of the in-process joining conditions. The cross-section of the DHT and DH joints were prepared according to the ASTM E3-11 standard. The samples were ground with silicon carbide papers (of 200, 400, 600, 800, and 1000 grit numbers), and polished with the aid of diamond pastes having particle sizes of 5 and 1  $\mu\text{m}$ . The Al side of the prepared samples was then etched in Keller's reagent while ethanol was used for the polymeric side of the joint. The samples were then examined under an optical microscope. The tensile strengths of the joints were investigated according to the ASTM E8M-16a standard at a constant strain rate of 0.04  $\text{min}^{-1}$  by employing an INSTRON universal tensile testing machine. The average of three tensile

results was recorded as the actual result in this paper. The fracture surfaces of the joints after tensile loading were examined in a JOEL-JSM 7600F scanning electron microscope to understand the fracture mechanism of the joints.

### 3. Results and Discussion

#### 3.1. Temperature History and Weld Appearance

Fig.2 shows the real time-temperature/humidity graph of the hybrid Al/ABS joint obtained at different tool rotational speeds. AT, RH, TA, TB, and TD represent the atmospheric temperature, relative humidity, and temperature readings of the 1st, 2nd, and 3rd thermocouples respectively. The atmospheric temperature (AT) at which the joining process was carried out was about 30oC (see the red line in Fig.2) while the relative humidity (RH) of approximately 78% was recorded before the commencement of the welding process. The local RH progressively declines while fluctuating during the welding process due to the complex frictionally-induced heat input and heat dissipation into and around the local weld environment (see the blue trendline in Fig.2). The sources of heat input (generation) in a hybrid Al/polymer joint have been stated to include tool-Al alloy contact friction, Al alloy-polymer friction, and plastic deformation of Al and polymer [24]. A sharp temperature rise was recorded as the welding process commenced at different tool rotational speeds. The proximity of the thermocouple to the weld nugget zone is observed to be linearly proportional to the attained peak temperature.

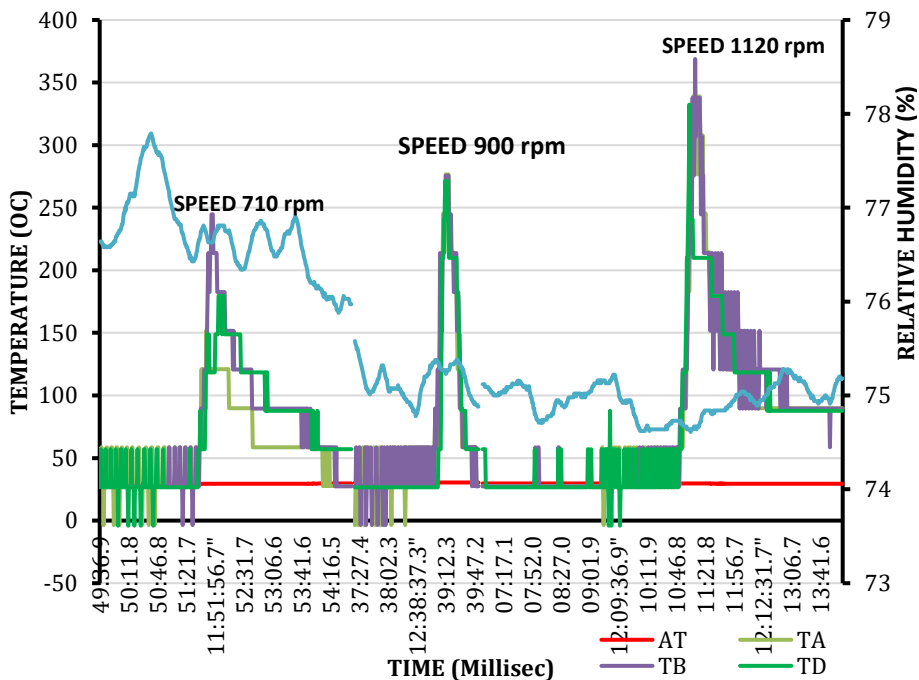


Fig. 2 Real-time – temperature/humidity series graph as a function of variable tool rotational speeds (“AT”: Atmospheric Temperature; “TA”: 1st Thermocouple; “TB”: 2nd Thermocouple; “TD”: 3rd Thermocouple; and “RH”: Relative humidity).

The maximum frictionally and plastic deformation-induced peak temperatures of about 245, 276, 369oC were obtained at tool rotational speeds of 710, 900, and 1120 rpm respectively in Fig.2. This incidence is observed due to the direct interrelationship between

tool rotational speed and heat input [31-33]. The attained peak temperatures at respective tool rotational speeds are lesser than the melting temperature of the pure Al alloy (about 630°C) but are greater than the melting temperature of the ABS polymer (about 160°C). This occurrence indicates that frictionally-aided plastic shear deformation (material flow) is the predominant occurrence at the Al side of the hybrid Al/ABS joint while heat transfer-aided melting of the beneath ABS polymer is an expected outcome. The Al side is a good heat and electrical conductor having a thermal conductivity of approximately 167 W/m/K. This attribute is adjudged to promote the transfer of thermal energy or heat input to the polymer side at the tool under-shoulder region beneath the Al side (or at the faying region between the Al and ABS). The ABS is a poor conductor of heat having a thermal conductivity of about 0.19 W/m/K. This implies that the ABS polymer will act as a local heat sink and this occurrence will aid the local melting of the ABS polymer at the faying region between the base materials. Aliasghari et al. [24] reported that the induced heat input is distributed (via conduction) and melting of the polymer (via absorption or heat sink). The post-weld visual observation of the hybrid Al/ABS joints is thus examined in Fig.3 to understand the role/impact of the inherent frictionally-induced heat input on the ABS side and the hybrid joints.

There is no significant difference between the surface appearance of the DT and DHT hybrid Al/ABS joints obtained at the same level of parameter combination. As a result, the surface outlook associated with the hybrid Al/ABS joints at different tool rotational speeds is provided in Fig.3 irrespective of the type of joint.

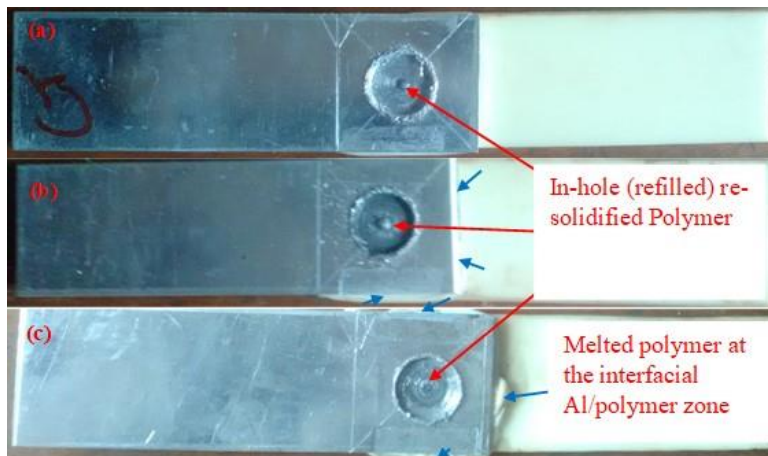


Fig. 3 As-welded Al/ABS joints at (a) 710 rpm, (b) 900 rpm, (c) 1120 rpm

Fig.3a-c shows the in-hole/refilled and re-solidified ABS polymer interlocked with the Al alloy. The local frictionally-induced heat transfer to the ABS polymer beneath the tool shoulder is sufficient to cause the local melting of the ABS polymer (in agreement with Fig.2) as infiltrated or filled (threaded and unthreaded) holes are revealed in Fig.3a-c. The downward axial force of the tool (tool downward plunging) is adjudged to have induced some level of pressure on the local molten pool of the ABS polymer (at the faying region) to force an upward drive of the molten ABS polymer into the pre-drilled holes (empty cavities). The molten ABS matrix thus fills the pre-drilled hole with and without threading in the Al sheets (in Fig.3) to establish mechanical interlocking of the Al alloy and the ABS polymer at the tool rotational speeds of 710, 900, and 1120 rpm respectively. This implies that tool rotational speeds between 710 and 1120 rpm are suitable for establishing efficient in-hole re-solidified polymer in the hybrid Al/ABS joint. However, Fig.3b and c reveal the presence of palpable melted polymer (at the interfacial Al/ABS zone) being

extruded out of the interfacial zone (see the blue arrows in Fig.3). This occurrence is due to the increase in heat input (or peak temperature in Fig.2) as the tool rotational speed is increased. The fluidity of the ABS polymer is enhanced by higher tool rotational speeds and this phenomenon is a major factor for the outstretched flowing of the melted ABS polymer out of the interfacial/faying region. The heat transfer to the ABS sheet beneath the Al alloy at the overlapped and interfacial region (between the Al and the ABS or outside of the tool under-shoulder region) establishes some degree of melting/softening which can favor adhesion between the two materials.

### 3.2. Microstructure

Fig.4 shows the cross-section of the DH and DHT joints with a focus on the hole walls. The interlocking of the re-solidified ABS with the undulating/threaded wall or meshing of the re-solidified ABS polymer matrix with the pitch-crest of the hole wall is revealed in Fig.4a while that of the unthreaded (vertical) hole is revealed in Fig.4b. Evidence of randomly dispersed fine particles of the Al alloy (see the indicated yellow points in Fig.4a and c) entrapped within the re-solidified ABS matrix is observed. The occurrence of these Al particles in the ABS matrix is attributed to the severe plastic deformation and compressive-shearing effect of the Al side. This phenomenon leads to a somewhat fragmentation of the plasticized Al alloy as ABS matrix-embedded fine particles as indicated in Fig.4. A large Al anchor/chips are embedded in the re-solidified ABS matrix as observed in the DH joint (see Fig.4b) due to the downward compressive-shearing of the Al alloy. The hole regions around the tool-shoulder plunged zone are examined in Fig.5 to understand the compressive-shearing effect of the plunging tool on the hole wall.

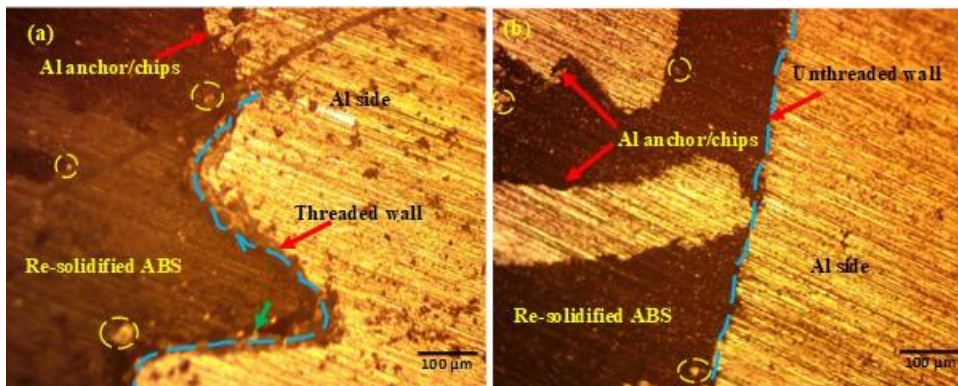


Fig. 4 Pre-fabricated hole wall after welding (a) threaded hole (DHT), (b) unthreaded hole (DH) at 710 rpm

The results of the preliminary experiment reveal that excessive plunging of the welding tool into the Al side reduces the effective (interlocked) hole height, and damages the pre-fabricated threading within the hole. Thus, a shallow plunge depth of 0.8 mm but not exceeding 1.2 mm is recommended for joining the 4 mm thick pre-drilled Al alloy to the ABS polymer via the use of the described novel welding process. Fig.5. reveals the effect of the compressive-shearing effect of the plunging tool on the hole wall in DH and DHT joints. An increase in both the tool plunging depth (0.8 -12 mm) and rotational speed (710 - 900 rpm) increases the compressive-shearing effect on the unthreaded hole wall as revealed in Fig.5a and b. However, more deformation-induced hole wall shearing and plasticized Al fragments ensue in the hybrid Al/ABS joint (DH joint) obtained at higher plunge depth and tool rotational speed (see Fig.5b as compared to Fig.5b). This indicates that Al-ABS

interlocking also emanates from hole wall-shearing at an increased plunge depth and rotational speed. However, the amount of the plasticized Al fragmentation (from the threaded hole) in the re-solidified ABS (see Fig.5c) is greater in the DHT joint obtained at 900 rpm as compared to Fig.5b obtained at the same parameters. This occurrence is due to the presence of wall undulation or pitch-crest wall. It is important to examine the role of tool speed on the shoulder-induced plunge zone of the joint as it has been revealed that mechanical interlocks or Al anchors are greater in the DHT joints at higher plunge depth.

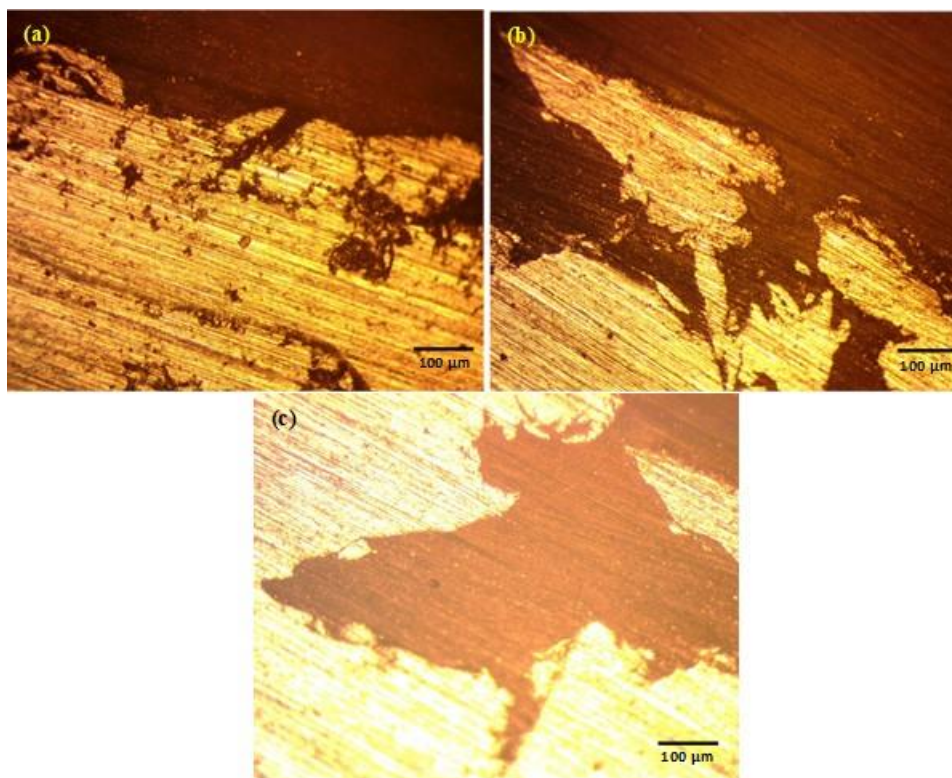


Fig. 5 Hole wall fragmentation around the tool-shoulder plunged zone (a) and (b) unthreaded hole, (c) threaded hole

Fig.6 shows the effect of tool rotational speed on the hybrid Al/ABS joints within the plasticized regions of the pre-fabricated holes (threaded and unthreaded). The combined stirring, compressive-shearing, and frictional effects on the upper Al plate cause a downward deformation-induced material flow and shearing to form Al particles and anchors/chips embedded with the re-solidified ABS matrix (as shown in Fig.6). The amount of the flow-induced Al anchors within the re-solidified ABS matrix establishes a varying degree of mechanical interlocks with the polymer depending on the level of tool rotational speed (see Fig.6a-c). The area of the sheared Al particles and anchors/chips is directly proportional to the level of the tool rotational speed as the percentage of sheared Al anchors/chips is revealed to increase as the tool rotational speed is increased from 900 rpm to 1120 rpm in Fig.6. Large intertwined Al anchors/chips are observed in the hybrid Al/ABS joint obtained at 1120 rpm (see Fig.6c). This occurrence is attributed to the increase in thermal heat input and material flowability. The formation of tangles of trapped metallic fragments/chips in a polymer matrix was also attributed to an increase in tool rotational speed in the studies of Moghanian et al. [34]. The metal tangle/chip

phenomenon was adjudged to have been promoted by structural disparity-aided irregular heat input distribution, a rise in thermal heat-input (at higher rotational speeds), and complex vortex-vertical-horizontal material flows. Besides, the surface area of the re-solidified ABS matrix declines at the stir zone (or at the severely deformed/plasticized zone) of the joint as the tool rotational speed is increased to 1120 rpm. More sheared and dynamically recrystallized Al alloy is obtained at higher tool rotational speed. The large recrystallized and sheared Al alloy (at higher heat-input/rotational speed) occupies a somewhat large area being sandwiched with the melted ABS polymer at the plasticized zone (as revealed in Fig.6).

Apart from the wall difference (in the DH and DHT joints), other inherent regions of the weld have similar observations with no significant difference. Fig.7 shows the adhesive bonded and stirred Al regions of the hybrid Al/ABS joint. The interfacial adhesive bonding occurs due to the wetting of the faying Al surface due to the melted ABS polymer. Upon solidification or cooling, a somewhat bonding is established in this region (see Fig.7a and b) whereas the severe plastic deformation of the Al side induces dynamic recrystallization in the Al side as revealed in Fig.7c. No porosity has been observed in the examined re-solidified ABS regions of the as-welded hybrid Al/ABS joints. It should be noted that the occurrence of oxygen entrapment in the re-solidified polymer is a common feature in hybrid metal/polymer joints. The molten polymer's upward and lateral flows could also have promoted erosion of the Al surface to form Al-O-C interaction layers which can act as a secondary (chemical) bonding mechanism in the hybrid Al/ABS joint.

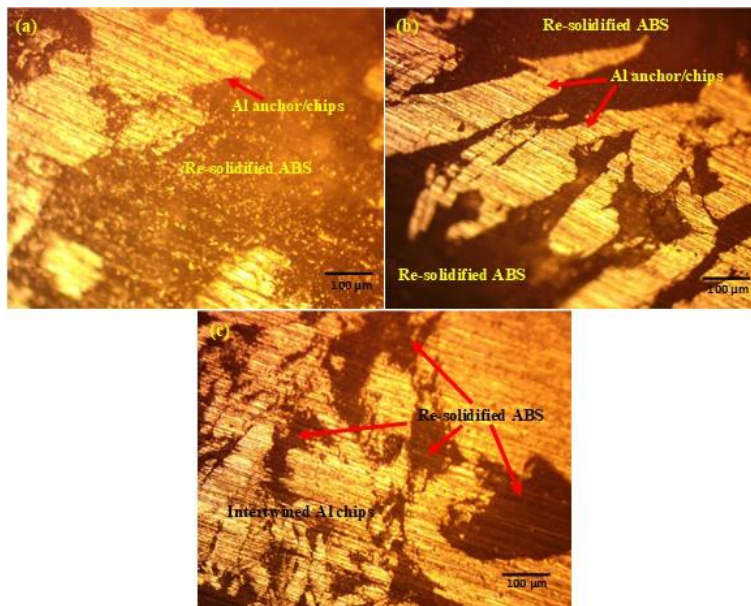


Fig. 6 Tool shoulder-induced mechanical interlocking at the weld nugget (a) 710 rpm, (b) 900 rpm, (c) 1120 rpm

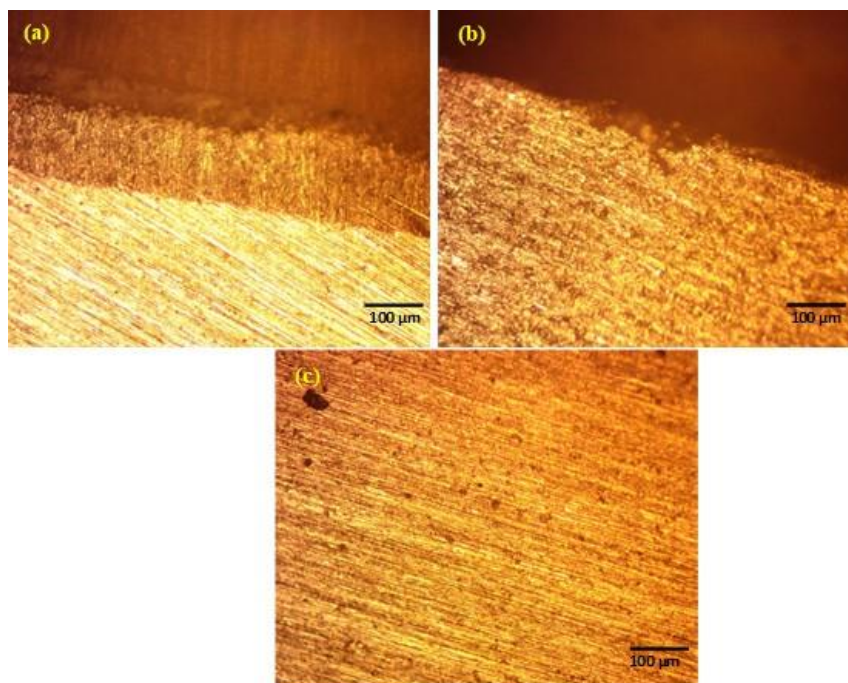


Fig. 7 Other regions of the Al/ABS joints (a) and (b) adhesion bonding, (c) stirred Al

### 3.3. Tensile Strength

Fig. 8 shows the tensile-shear failure loads of the hybrid Al/ABS joints (DH and DHT) obtained at different levels of tool rotational speed and constant plunge depth of 1.2 mm. An increase in the level of the tool rotational speed increases the tensile-shear failure load of the DH and DHT joints (see Fig.8). The rise in the tool rotational speed is adjudged to have increased the localized weld heat-input, polymer flowability [35], wettability of Al surface (at the faying region), and the embedded Al (anchors and threading) for mechanical interlocking in the hybrid Al/ABS joint. The increase in the tool rotational speed favors the wettability of the Al surface and this occurrence is expected to increase the adhesion area (secondary bonding mechanism) of the hybrid Al/ABS joint. The tensile-shear failure loads of the DH and DHT joints consequently improved from 572-705 and 654-749 N respectively as the tool rotational speed is increased from 710-1120 rpm and at a constant plunge depth of 1.2 mm (see Fig.8). This occurrence could also be attributed to the formation of a large-area fraction of Al anchor/chips at higher tool rotational speed (revealed in Fig.6c). Paul et al. [36] described that the size of mechanical interlocking directly affects the tensile force of the metal-polymer joint. The established large Al anchor is considered to have improved mechanical interlocking of the Al in the re-solidified ABS polymer and equally enhanced fracture resistance (tensile-shear failure load) of the joint. This observation is in agreement with the works of Patel et al. [1] as the tool-induced mechanical interlocking behavior was reported as the dominant bonding mechanism in the metal-polymer joint. The presence of a big aluminum anchor in the stir zone of Al/polymer was also described to enhance the mechanical interlocking and shear bond strength of the joint in the works of Huang et al. [6]. The size of the Al anchor and the interfacial gap/width between the re-solidified polymer and Al are reduced/lesser under

lower heat input (low rotational speed). This incidence lowers the load-bearing capability of the Al/ABS joint produced at 710 rpm.

Smaller interfacial gap (between the re-solidified ABS and Al anchor) and bigger Al anchor (high volumetric fraction of Al anchor) are also attributed to be responsible for the improved tensile-shear failure load in the hybrid Al/ABS joint fabricated at higher tool rotational speed. Paidar et al. [28] described that a rise in the tool rotational speed increased the tensile-shear load of the Al/PP-C30S joint due to an increase in the thickness of the reaction layer, a decrease in the unfilled zone, and a substantial mechanically interlocked crest-pitch region. This feature could also have played a significant role in improving the failure load of the hybrid Al/ABS joint as the tool rotational speed is increased. Tool-induced squeezing behavior, improved macro/micro-mechanical interlocking, and inherent oxide layers (for improved adhesive bonding) are reported as attributes for the high-quality heterogeneous metal-polymer joints in the studies of Meng et al. [20]. These phenomena aid multi-scale adhesive bonding and mechanical interlocking in the metal-polymer joints. On the other hand, the threaded (DHT) joint shows an improvement over the unthreaded (DH) joint in Fig.8. This occurrence is attributed to the synergy of the threading and the frictionally induced Al anchor/chips responsible for mechanical interlocking of the re-solidified ABS polymer in the pre-drilled hole of the hybrid Al/ABS joints.

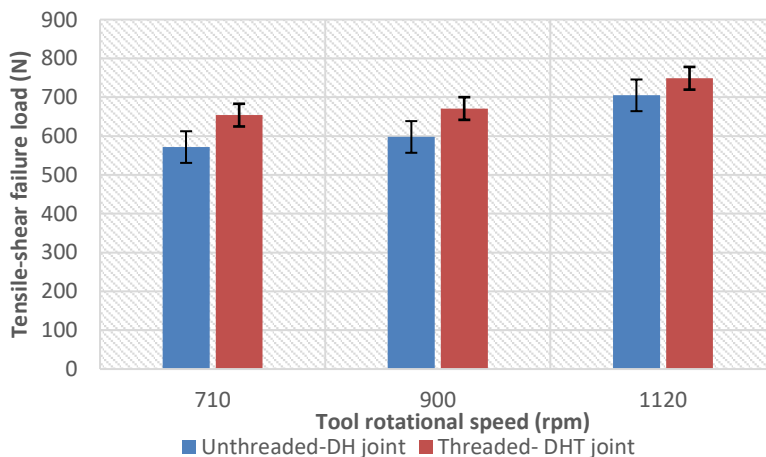


Fig. 8 Tensile-shear failure loads as a function of tool rotational speed at 1.2 mm plunge depth

### 3.4. Fracture

Fig.9 reveals the fracture surfaces of the hybrid Al/ABS joints (DH and DHT joints). The fracture location takes place around the base/root of the infiltrated and re-solidified (ABS) interlocked zones at lower tool speed (710 rpm) in the DHT (see Fig.9a) whereas ABS pullout fracture mode ensues in the DH joint (Fig.9c). The detached threading part is observed in the bottom plate of the DHT joint (see Fig.9a). This occurrence indicates that the threading in the DHT joint inhibits the pullout of the re-solidified ABS polymer from the pre-drilled hole in Fig.9a (at 710 rpm) and thus improves the fracture resistance of the joint. Meanwhile, the absence of threading in the DH joint facilitates the pullout of the inherent re-solidified ABS polymer from the hole during the axial loading process (see Fig.9c). The threading-supported micro/macro interlocking around the base/root of the

in-hole re-solidified ABS polymer is responsible for the improved tensile-shear failure load in the DHT joint as compared to the DH joint. On the other hand, the presence of mechanical Al anchor/interlocking at the upper tool shoulder-plunged zone significantly impacts the hybrid Al/ABS joints at high tool speed in Fig.9b and d (DH and DHT joints). The synergy of Al anchor and threading restrains the fracture of the hybrid Al/ABS joint (DHT joint) at higher tool rotational speed as evidence of Al anchor detachment is observed at the bottom plate of the joint in Fig.9b. This is due to the increase in the percentage deformation-induced Al anchor in the joint at 1120 rpm. Fig.9d also reveals the pullout of the re-solidified ABS polymer from the pre-drilled hole. However, the presence of deformation-induced mechanical interlocking at the tool shoulder-plunged zone or the upper region of the hole (Fig.9d) offers some level of fracture resistance during the loading process (as evidence of fractured Al anchor is seen in the pullout part/bottom plate in Fig.9d).

The observation of the interfacial fracture surface shows that the delamination of the adhesive-bonded zone (circumferential regions around the interlocked zones) of the DHT and DH joints easily occurs during the axial loading process. This makes the interlocked zones act as the major load-bearing region, and the major stress concentration zone is considered to have acted on the interlocked zone of the hybrid Al/ABS joint. The hole threading and Al anchor/chips offer some degree of resistance (mechanical interlocking) to the pull-out of the re-solidified ABS from the pre-drilled hole during the tensile stress-induced nugget rotation process [37,38]. This phenomenon induces crack initiation and propagation at the interlocked regions of the joint. Pullout fracture is predominant in the DH joint with evidence of Al anchor-aided fracture at higher tool rotational speed while the combination of hole-threading and Al anchor fracture-restraining effects ensue in the DHT joint.

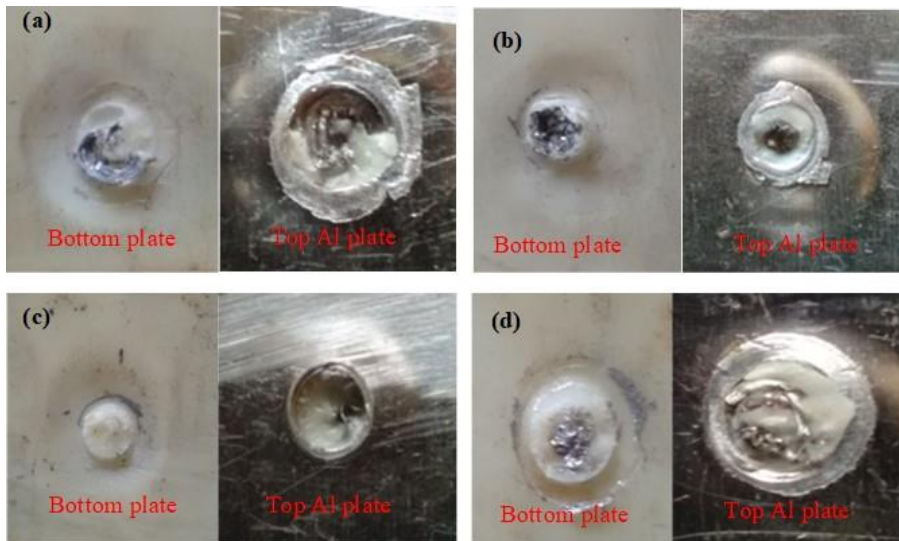


Fig. 9 Views of the fracture surfaces at the faying region of the hybrid Al/ABS joints (a) and (b) DHT joints, (c) and (d) DH joints

Delamination or debonding of the adhesive area of the joint ensues in the hybrid Al/ABS joints as has been observed in Fig.9. Thus, the fracture surfaces of the interlocked region (re-solidified ABS polymer region) are examined under SEM. Fig.10 shows the SEM images of the fracture surfaces of the hybrid Al/ABS joints (DHT and DH joints). Cohesive-adhesive (brittle) fracture is observed in the DHT joint (at low tool rotational speed) in Fig.10a as

evidence of somewhat delaminated facets are present (see the yellow arrows) while brittle-like appearance is observed in the DH joint counterpart in Fig.10c. The fracture appearances in Fig.10a and c justify the reason for low tensile-shear failure loads in the joint fabricated at low tool rotational speeds. This observation also corroborates the works of Huang et al. [4] as the reduced polymer crystallinity, hardness, and load-bearing ability are supported by low heat input (tool rotational speed) or fast cooling rate. On the other hand, fibrous appearance (tearing of polymer) and ductile fracture mode predominate the fracture surface of the DHT joint produced at high tool rotational speed in Fig.10b. The formation of fibrils in the pulling (axial) direction is attributed to the local yielding of the polymer matrix in the works of Abibe et al. [39]. The occurrence of polymer tearing and pullout of fibers has also been reported in the works of Meng et al. [20]. This occurrence is associated with a sufficient amount of inherent mechanical interlocking in the joint. The interlocking offers resistance to polymer (ABS) pullout and it consequently results in some polymer tearing (fibrous appearance) in Fig.10b. Ductile appearance is also observed in the DH joint fabricated at high tool rotational speed in Fig.10d. It can thus be concluded that ductile fracture occurs in the hybrid Al/ABS joint obtained at high tool rotational speed and this attribute justifies the occurrence of high tensile-shear failure load in the joint. Such a high bonding strength was attributed to interfacial atomic contact, Al-O-C bonds, and nylon tearing/fragments in the studies of Liu et al. [12].

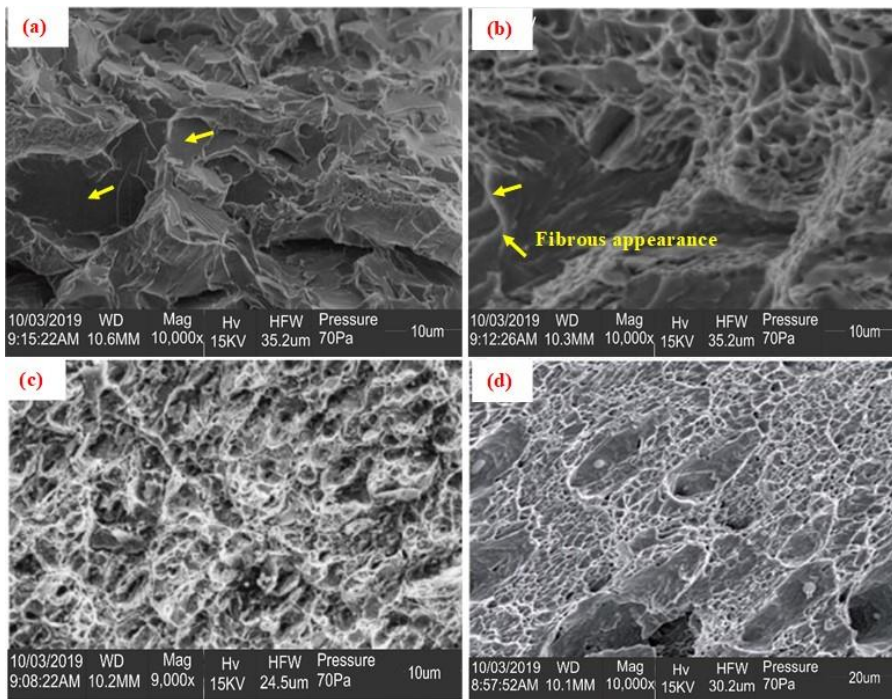


Fig. 10 SEM images of fractured re-solidified ABS matrix of the hybrid Al/ABS joints (a) and (b) DHT joints, (c) and (d) DH joints

## 5. Conclusions

The production of hybrid Al/acrylonitrile butadiene styrene joints was successfully achieved via the use of pre-fabricated threaded- and unthreaded-hole friction stir spot welding approaches. The structure, tensile-shear failure load, and fracture behaviors of the irrespective joints were investigated. The findings of this investigation include:

- Tool rotational speeds of 710-1120 rpm successfully establish in-hole re-solidified ABS polymer (mechanical interlocking) in the pre-drilled unthreaded and threaded holes of the hybrid Al/ABS joint.
- The friction and deformation-induced heat input cause a decline in the local relative humidity of the hybrid Al/ABS joint during the welding process due to local heat dissipation.
- A direct interrelationship exists between the peak temperature and tool rotational speed of the hybrid Al/ABS joint. Maximum peak temperatures of 245, 276, 369°C were obtained at tool rotational speeds of 710, 900, and 1120 rpm respectively.
- Plastic deformation/compressive shearing-induced and threading-induced mechanical interlocks, and adhesion bonding are the bonding mechanisms of the threaded hybrid Al/ABS joint while unthreaded joint is devoid of threading-aided mechanical interlock.
- A rise in the tool rotational speed increases the compressive-shearing effect and the area of embedded Al anchors in the re-solidified ABS polymer.
- Hybrid Al/ABS joint produced with a threaded hole has a higher tensile-shear failure load. An increase in the tool rotational speed (710-1120 rpm) improved the failure load of the unthreaded and threaded hybrid Al/ABS joints from 572-705 and 654-749 N respectively due to enhanced mechanical interlocking, smaller interfacial gap (between the re-solidified ABS and Al anchor), and bigger Al anchor/chip.
- An increase in the tool rotational speed changes the fracture location and modes. Brittle and ductile fracture modes are obtained at low and high tool rotational speeds.

## Acknowledgment

The author acknowledges the assistance of Mr. D. S. Ukanah and Mr. U. F. Etoabasi during the laboratory studies of this work.

## References

- [1] Patel AR, Kotadiya DJ, Kapopara JM, Dalwadi CG, Patel NP, Rana HG. Investigation of Mechanical Properties for Hybrid Joint of Aluminium to Polymer using Friction Stir Welding (FSW). *Materials Today: Proceedings*, 2018; 5: 4242-4249. <https://doi.org/10.1016/j.matpr.2017.11.688>
- [2] Ojo OO, Taban E, Kaluc E. Friction stir spot welding of aluminum alloys: A recent review. *Materials Testing*, 2015; 57: 609 – 627. <https://doi.org/10.3139/120.110752>
- [3] Dawei Z, Qi Z, Xiaoguang F, Shengdun Z. Review on Joining Process of Carbon Fiber-Reinforced Polymer and Metal: Methods and Joining Process. *Rare Metal Materials and Engineering*, 2018; 47(12): 3686-3696. [https://doi.org/10.1016/s1875-5372\(19\)30018-9](https://doi.org/10.1016/s1875-5372(19)30018-9)
- [4] Huang Y, Meng X, Xie Y, Wan L, Lv Z, Cao J, Feng J. Friction stir welding/processing of polymers and polymer matrix composites. *Composites Part A: Applied Science and Manufacturing*, 2018; 105: 235 – 257. <https://doi.org/10.1016/j.compositesa.2017.12.005>

- [5] Kumar R, Singh R, Ahuja IPS, Penna R, Feo L. Weldability of thermoplastic materials for friction stir welding- A state of art review and future applications. *Composites Part B*, 2018; 137: 1-15. <https://doi.org/10.1016/j.compositesb.2017.10.039>
- [6] Huang Y, Meng X, Wang Y, Xie Y, Zhou L. Joining of aluminum alloy and polymer via friction stir lap welding. *Journal of Materials Processing Tech.*, 2018; 257: 148-154. <https://doi.org/10.1016/j.jmatprotec.2018.02.043>
- [7] Wang H, Yang K, Liu L. The analysis of welding and riveting hybrid bonding joint of aluminum alloy and polyether-ether-ketone composites. *Journal of Manufacturing Processes*, 2018; 36: 301-308. <https://doi.org/10.1016/j.jmapro.2018.10.031>
- [8] Lambiase F, Genna S. Experimental analysis of Laser-assisted joining of Al-Mg aluminum alloy with Polyetheretherketone (PEEK). *International Journal of Adhesion and Adhesives*, 2018; 84: 265 – 274. <https://doi.org/10.1016/j.ijadhadh.2018.04.004>
- [9] Dalwadi CG, Patel AR, Kapopara JM, Kotadiya DJ, Patel ND, Rana HG. Examination of Mechanical Properties for Dissimilar Friction Stir Welded Joint of Al Alloy (AA-6061) to ABS (Acrylic). *Materials Today: Proceedings*, 2018; 5: 4761–4765. <https://doi.org/10.1016/j.matpr.2017.12.049>
- [10] Rout A, Pandey P, Oliveira EF, da Silva Autreto PA, Gumaste A, Singh A, Galvao DS, Arora A, Tiwary CS. Atomically locked interfaces of metal (Aluminum) and polymer (Polypropylene) using mechanical friction. *Polymer*, 2019; 169: 148-153. <https://doi.org/10.1016/j.polymer.2019.02.049>
- [11] Liu FC, Dong P, Lu W, Sun K. On formation of Al-O-C bonds at aluminum/polyamide joint interface. *Applied Surface Science*, 2019; 466: 202 – 209. <https://doi.org/10.1016/j.apsusc.2018.10.024>
- [12] Liu FC, Dong P, Pei XA. high-speed metal-to-polymer direct joining technique and underlying bonding mechanisms. *Journal of Materials Processing Tech.*, 2020; 280: 116610. <https://doi.org/10.1016/j.jmatprotec.2020.116610>
- [13] Derazkola HA, Simchi A. An investigation on the dissimilar friction stir welding of T-joints between AA5754 aluminum alloy and poly(methylmethacrylate). *Thin-Walled Structures*, 2019; 135: 376-384. <https://doi.org/10.1016/j.tws.2018.11.027>
- [14] Derazkola HA, Elyasi M. The influence of process parameters in friction stir welding of Al-Mg alloy and polycarbonate. *Journal of Manufacturing Processes*, 2018; 35: 88-98. <https://doi.org/10.1016/j.jmapro.2018.07.021>
- [15] Xiong X, Zhao P, Ren R, Zhang Z, Cui X, Ji S. Enhanced resistance-welding hybrid joints of titanium alloy/thermoplastic composites using a carbon-nanotube lamina. *Diamond & Related Materials*, 2020; 101: 107611. <https://doi.org/10.1016/j.diamond.2019.107611>
- [16] Ozlati A, Movahedi M, Tamizi M, Tartifzadeh Z, Alipour S. An alternative additive manufacturing-based joining method to make Metal/ Polymer hybrid structures. *Journal of Manufacturing Processes*, 2019; 45: 217-226. <https://doi.org/10.1016/j.jmapro.2019.07.002>
- [17] Hajideh MR, Farahani M, Ramezani NM. Reinforced Dissimilar Friction Stir Weld of Polypropylene to Acrylonitrile Butadiene Styrene with Copper Nanopowder. *Journal of Manufacturing Processes*, 2018; 32: 445–454. <https://doi.org/10.1016/j.jmapro.2018.03.010>
- [18] Hong S-T, Das H, Oh H-S, Alam Al Nasim MNE, Chun D-M. Combination of nano-particle deposition system and friction stir spot welding for fabrication of carbon/aluminum metal matrix composite joints of dissimilar aluminum alloys. *CIRP Annals - Manufacturing Technology*, 2017; 66: 261-264. <https://doi.org/10.1016/j.cirp.2017.04.115>
- [19] Derazkola HA, Simchi A. A new procedure for the fabrication of dissimilar joints through injection of colloidal nanoparticles during friction stir processing: Proof concept for AA6062/ABS joints. *Journal of Manufacturing Processes*, 2020; 49: 335-343. <https://doi.org/10.1016/j.jmapro.2019.12.008>

- [20] Meng X, Huang Y, Xie Y, Li J, Guan M, Wan L, Dong Z, Cao J. Friction self-riveting welding between polymer matrix composites and metals. *Composites Part A: Applied Science and Manufacturing*, 2019; 127: 105624. <https://doi.org/10.1016/j.compositesa.2019.105624>
- [21] Liu Y, Zhuang W, Wu S. Damage to carbon fiber reinforced polymers (CFRP) in hole clinched joints with aluminum alloy and CFRP. *Composite Structures*, 2020; 234: 111710. <https://doi.org/10.1016/j.compstruct.2019.111710>
- [22] Lambiase F, Paoletti A. Friction-assisted clinching of Aluminum and CFRP sheets. *Journal of Manufacturing Processes*, 2018; 31: 812–822. <https://doi.org/10.1016/j.jmapro.2018.01.014>
- [23] Aliasghari S, Skeldon P, Zhou X, Hashimoto T. Effect of an anodizing pre-treatment on AA 5052 alloy/polypropylene joining by friction stir spot welding. *Materials Science & Engineering B*, 2019; 245: 107-112. <https://doi.org/10.1016/j.mseb.2019.05.018>
- [24] Aliasghari S, Ghorbani M, Skeldon P, Karami H, Movahedi M. Effect of plasma electrolytic oxidation on joining of AA 5052 aluminum alloy to polypropylene using friction stir spot welding. *Surface & Coatings Technology*, 2017; 313: 274–281. <https://doi.org/10.1016/j.surfcoat.2017.01.084>
- [25] Han SC, Wu LH, Jiang CY, Li N, Jia CL, Xue P, Zhang H, Zhao HB, Ni DR, Xiao BL, Ma ZY. Achieving a strong polypropylene/aluminum alloy friction spot joint via a surface laser processing pretreatment. *Journal of Materials Science and Technology*, 2020; 50: 103-114. <https://doi.org/10.1016/j.jmst.2020.02.035>
- [26] Goushegir SM, dos Santos JF, Amancio-Filho ST. Friction Spot Joining of aluminum AA2024/carbon-fiber-reinforced poly(phenylene sulfide) composite single-lap joints: Microstructure and mechanical performance. *Materials and Design*, 2014; 54: 196–206. <https://doi.org/10.1016/j.matdes.2013.08.034>
- [27] Nagatsuka K, Yoshida S, Tsuchiya A, Nakata K. Direct joining of carbon-fiber-reinforced plastic to an aluminum alloy using friction lap joining. *Composites: Part B*, 2015; 73: 82–88. <https://doi.org/10.1016/j.compositesb.2014.12.029>
- [28] Paidar M, Ojo OO, Moghanian A, Pabandi HK, Elsa M. Pre-threaded hole friction stir spot welding of AA2219/PP-C30S sheets. *Journal of Materials Processing Tech.*, 2019; 273: 116272. <https://doi.org/10.1016/j.jmatprotec.2019.116272>
- [29] Pabandi HK, Movahedi M, Kokabi AH. A New Refill Friction Spot Welding Process for Aluminum/Polymer Composite Hybrid Structures. *Composite Structures*, 2017; 174: 59 – 69. <https://doi.org/10.1016/j.compstruct.2017.04.053>
- [30] Aliasghari S, Skeldon P, Zhou X, Ghorbani M. Influence of PEO and mechanical keying on the strength of AA 5052 alloy/polypropylene friction stir spot welded joints. *International Journal of Adhesion and Adhesives*, 2019; 92: 65–72. <https://doi.org/10.1016/j.ijadhadh.2019.04.002>
- [31] Oladimeji OO, Taban E, Kaluc E. Understanding the role of welding parameters and tool profile on the morphology and properties of expelled flash of spot welds. *Materials & Design*, 2016; 108: 518 – 528. <https://doi.org/10.1016/j.matdes.2016.07.013>
- [32] Ojo OO, Taban E. Hybrid multi-response optimization of friction stir spot welds: failure load, effective bonded size and flash volume as responses. *Sādhanā*, 2018; 43(6): 1-13. <https://doi.org/10.1007/s12046-018-0882-2>
- [33] Ojo OO. Multi-Objective Optimization of Friction Stir Spot Welds of Aluminum Alloy Using Entropy Measurement. *International Journal of Engineering Research in Africa*, 2019; 45: 28 – 41. <https://doi.org/10.4028/www.scientific.net/jera.45.28>
- [34] Moghanian A, Paidar M, Seyedafghahi SS, Ojo OO. Friction stir welding of pure magnesium and polypropylene in a lap-joint configuration: Microstructural and mechanical properties. *International Journal of Minerals, Metallurgy, and Materials*, 2019; 26(6): 766-774. <https://doi.org/10.1007/s12613-019-1784-y>

- [35] Zhao S, Kimura F, Kadoya S, Kajihara Y. Experimental analysis on mechanical interlocking of metal-polymer direct joining. Precision Engineering, 2020; 61: 120 – 125. <https://doi.org/10.1016/j.precisioneng.2019.10.009>
- [36] Paul H, Luke M, Henning F. Combining mechanical interlocking, force fit and direct adhesion in polymer–metal-hybrid structures – Evaluation of the deformation and damage behavior. Composites Part B: Engineering, 2015; 73: 158 – 165. <https://doi.org/10.1016/j.compositesb.2014.12.013>
- [37] Ojo OO, Taban E, Kaluc E. Effect of residual Alclad on friction stir spot welds of AA2219 alloys. Materials Testing, 2018; 60: 979 – 988. <https://doi.org/10.3139/120.111245>
- [38] Ojo OO, Taban E. Assessment of Effective Nugget Size, Nugget Rotation and Failure Mode of Friction Stir Spot Welds of AA2219-O Alloy, Journal of Engineering and Engineering Technology, 2018; 12: 54-62
- [39] Abibe AB, Amancio-Filho ST, dos Santos JF, Hage E. Mechanical and failure behavior of hybrid polymer-metal staked joints. Materials & Design, 2013; 46: 338 – 347. <https://doi.org/10.1016/j.matdes.2012.10.043>

Blank Page

Technical Note

## Development of specially reinforced magnesium composites prepared by squeeze casting process

Akshansh Mishra<sup>\*1,a</sup>, Devarrishi Dixit<sup>2,b</sup>, Raheem Al-Sabur<sup>3,c</sup>

<sup>1</sup>Centre for Artificial Intelligent Manufacturing Systems, Stir Research Technologies, India.

<sup>2</sup>Department of Material Science, Christian-Albrechts-Universität zu Kiel

<sup>3</sup>Department of Mechanical Engineering, University of Basrah, Basra 61001, Iraq

### Article Info

#### Article history:

Received 22 Jun 2021

Revised 11 Aug 2021

Accepted 19 Aug 2021

#### Keywords:

Squeeze Casting;  
Magnesium Matrix  
Composites;  
Carbon Nano Tubes  
(CNTs);  
Titanium Carbide

### Abstract

A wide range of opportunities in the field of automotive and structural applications are being offered by Magnesium matrix composites because of their enhanced mechanical properties. Magnesium alloys based on Metal Matrix Composites (MMCs) are the best candidates for lightweight structural applications due to their improved creep properties. In the present study, three specimens of specially reinforced magnesium composites were manufactured by using the squeeze casting process. Specimen 1 has a composition of 7 % aluminum alloy in addition to 1% zinc and the composition of reinforcement is Titanium Carbide 0.3 % in addition to 1.5% Carbon nanotubes. Specimen 2 has a composition of 12 % aluminum alloy in addition to 1 % zinc and the composition of reinforcement is 2%  $B_4C$  in addition to 2 % Carbon nanotubes. Specimen 3 has a composition of 14 % aluminum alloy in addition to 1 % zinc and the composition of reinforcement is 2 %  $B_4C$  in addition to 2 % Carbon nanotubes. The mechanical properties analysis showed that specimen 2 has a higher hardness value in comparison to other manufactured specimens and it was also observed that specimen 2 possesses a higher tensile strength value in comparison to the other two specimens. Microstructure analysis shows that there was a uniform distribution of the reinforcements in the matrix. So it can be inferred that this uniform distribution causes higher hardness and higher tensile strength in the manufactured specimens.

© 2021 MIM Research Group. All rights reserved.

## 1. Introduction

Metal Matrix Composites (MMCs) can be considered lightweight structural materials that were developed in the 1990s for meeting the requirements in aerospace applications [1–3]. They have a strong potential to replace cast iron and other materials in brakes and engines due to their high strength-to-weight ratio, low density, high fatigue, wear and creep resistance, and at last high-temperature strength retention [4–5]. Magnesium and its alloys have attracted much attention in scientific development and as well as in various commercial applications because of their low density and high specific strength in comparison to other structural metals. In aerospace and automotive applications these properties order to reduce weight, greenhouse emission, and fuel consumption [6–8]. But due to their poor creep resistance behavior at high temperatures, the application of magnesium and its alloys are limited. So to overcome these limitations and to improve the properties, reinforcements are incorporated [9–10]. Dinaharan et al. [11] reinforced titanium particles (0, 7, 14, and 21 vol %) into an AZ31 magnesium alloy by friction stir processing method. The obtained results showed enhanced tensile strength and good ductility in the manufactured composite. Say et al. [12] investigated the corrosion resistance and mechanical properties of AZ91 and AZ61 magnesium matrix composites

\*Corresponding author: [akshansh@stirresearchtech.in](mailto:akshansh@stirresearchtech.in)

<sup>a</sup> orcid.org/0000-0003-4939-359X; <sup>b</sup> orcid.org/0000-0002-5126-6154; <sup>c</sup> orcid.org/0000-0003-1012-7681  
DOI: <http://dx.doi.org/10.17515/resm2021.319me0622n>

reinforced with 0.1, 0.2, and 0.5 wt% carbon nanotubes (CNTs). It was observed that with the increasing amount of carbon nanotubes, the strength of composites increases. Chang et al. [13] used squeeze casting process for manufacturing high-strength and high-modulus  $\text{Al}_{18}\text{B}_4\text{O}_{33\text{W}}/\text{GWZ1031K}$  magnesium matrix composite. The obtained results showed that the Yield Strength (YS), Ultimate Tensile Strength (UTS) and Young's modulus of the material at room temperature resulted  $364 \pm 13$  MPa,  $380 \pm 16$  MPa and  $77.8 \pm 2.1$  GPa. Kumar et al. [14] implemented squeeze casting process for fabricating high-performance aluminum composite material where agro waste reinforcements were used. The results showed that the manufactured composite material has high strength and toughness. Kale et al. [15] studied the tribological and mechanical properties of A7075/ SiC/  $\text{B}_4\text{C}$  hybrid composite which is manufactured by squeeze casting process. The results showed that the fabricated composite has more tensile and compressive strength in comparison to base metal alloy.

In recent work, the squeeze casting process has been used for fabricating the magnesium-based Metal Matrix Composites (MMCs). In the next sections, the experimental procedure and results obtained will be further discussed.

## 2. Material and Methods

Firstly, the ingots of magnesium, aluminum, and zinc weighing in the range of 950 to 990 grams per specimen were taken for composing the matrix purpose. Secondly, the preheating of the ingot mixture consisting of magnesium, aluminum, and zinc is carried out to a temperature of 650 degrees celsius. Thirdly, carbon nanotubes powder with  $\text{B}_4\text{C}$  powder are added as reinforcements then the mixture is taken into an oven and is preheated to a temperature of 300 degrees celsius. After that, by using a funnel these mixtures are poured into a furnace where the mixture is subjected to a stirring process to enhance the homogenous nature in the mixture at a different rotation rate for 10 minutes. The furnace gate is then opened after the stirring process and through the runner molten composite is further transferred to squeeze die arrangement. At a pressure of 40.2 tonnes, compression is performed by the hydraulic press on the obtained composite inside the die. The cooling process is incurred on the composite for 10 minutes inside the die. After cooling, the fabricated composite is taken outside for carrying out the finishing and machining process. Figure 1 shows the specimen after casting and Figure 2 shows the specimen after finishing the operation. Table 1 shows the composition of fabricated specimens.

Table 1. Composition of composite specimens in weight %

Specimen Number	Al	Zn	TiC	$\text{B}_4\text{C}$	Carbon Nanotubes
1	7	1	0.3	-	1.5
2	12	1	-	2	2
3	14	1	-	2	2



Fig. 1 Specimen obtained after casting process



Fig. 2 Specimen obtained after finishing operation

### 3. Results and Discussion

#### 3.1 Microstructure Properties Analysis

For obtaining the clear grain boundaries in the microstructure a proper specimen preparation is needed. Polishing and etching are the two kinds of preparation that are subjected to these specimens as shown in Figure 3 and Figure 4.



Fig. 3 Non-etched and unpolished composite specimen

The specimen surfaces may appear smooth to the human eyes but in reality, it consists of various scratches, irregularities, and grooves that happen when the specimen is subjected to various machining operations. So to increase the surface smoothness of the surface, polishing is done with different grades of emery paper such as 800, 1000, 1200, and 1500. For clear grain boundary observation, the etchant consisted of 92 ml distilled water, 6 ml of nitric acid with 65 % concentration, and 2 ml of hydrofluoric acid with 40 % concentration. The microstructures obtained for specimen 1, specimen 2, and specimen 3 are shown in Figures 5–7.



Fig. 4 Etched and emery polished surface of composite specimen

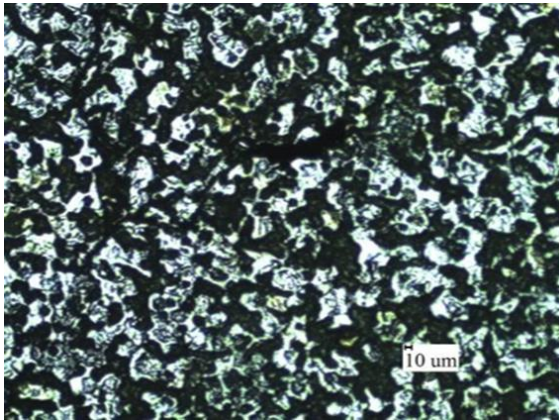


Fig. 5 Microstructure of specimen 1 at the magnification of 100X.

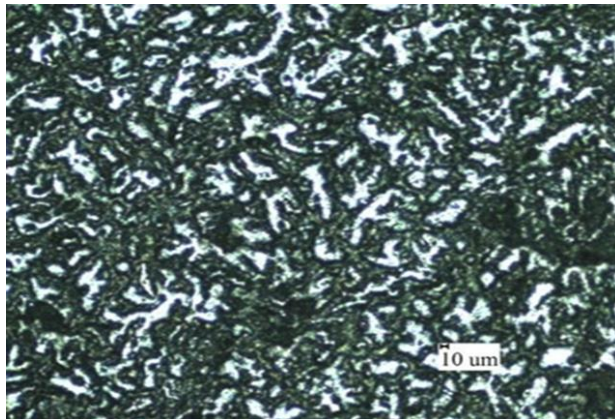


Fig. 6 Microstructure of specimen 2 at the magnification of 100X

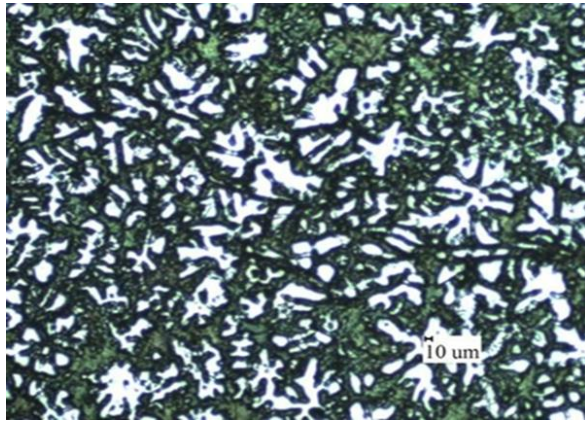


Fig. 7 Microstructure of specimen 3 at the magnification of 100X

From the microstructure analysis of specimen 1, it is observed that there was a non-uniform distribution of the reinforcement in the matrix. It is also observed that due to the existence of slipping between grain boundaries there is a formation of extremely coarse microstructure. From the microstructure analysis of specimen 2, it is observed that there is a uniform distribution of the reinforcement in the matrix and also might be due to less slip occurrence the formation of the microstructure is very fine in comparison to the other two specimens. From the microstructure analysis of specimen 3, it is observed that the reinforcement distribution is slightly non-uniform in nature and it was also observed that in comparison to specimen 1 the microstructure obtained was fine but in comparison to specimen 2 the grain boundaries obtained are coarse due to occurrence of slipping between the grain boundaries. The microstructures obtained from the SEM test for these three specimens are shown in Figures 8-10.

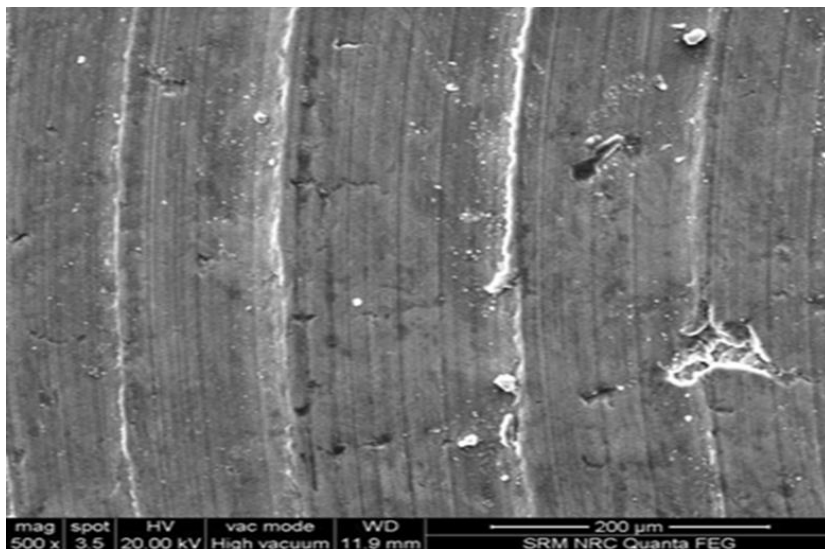


Fig. 8 SEM microstructure of Specimen 1

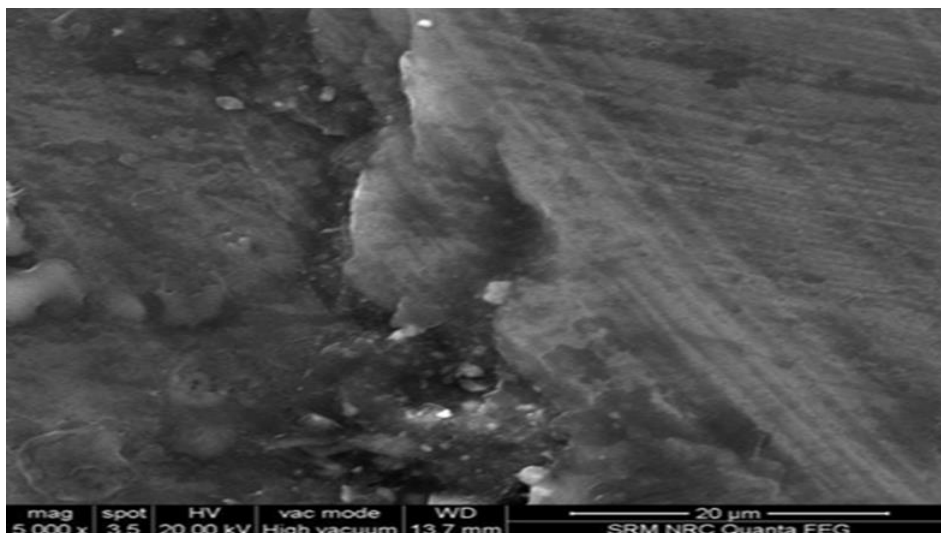


Fig. 9 SEM microstructure of Specimen 2

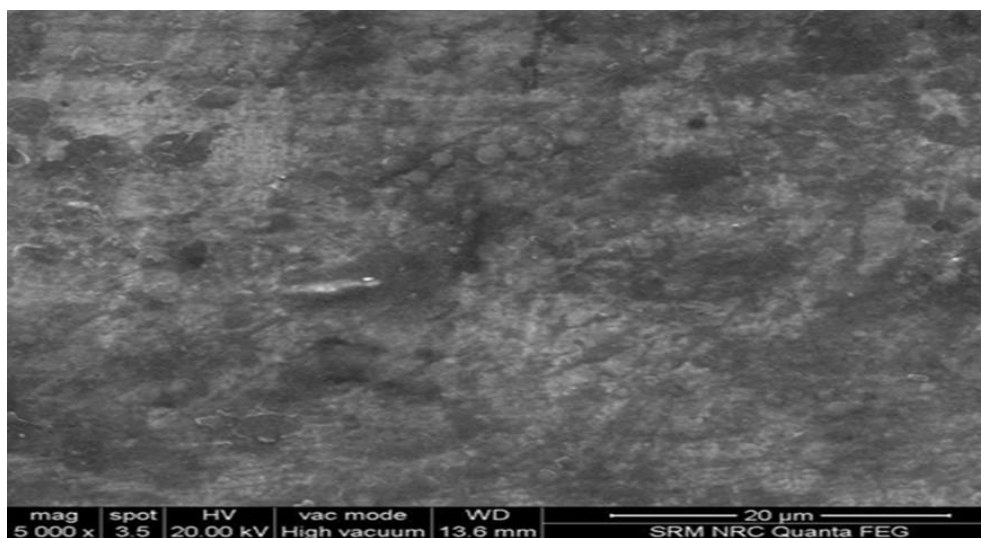


Fig. 10 SEM microstructure of specimen 3

### 3.2 Mechanical Properties Analysis

Tensile test results for specimen 1, specimen 2 and specimen 3 are shown in Figures 11-13 and Tables 2-4.

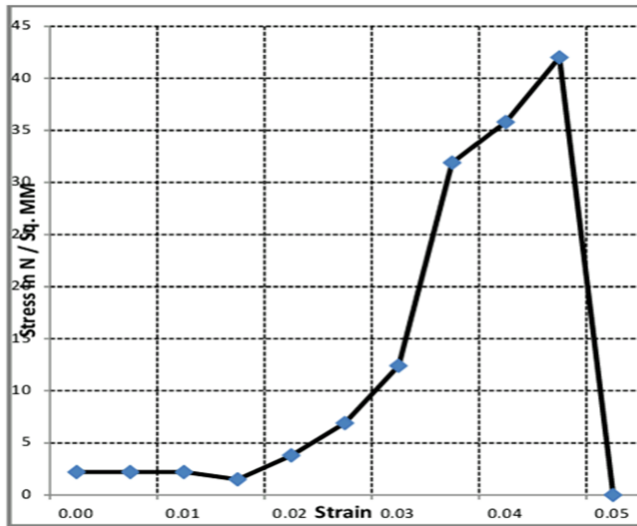


Fig. 11 Tensile test graph plot of specimen 1

Table 2. Tensile Test results of specimen1

Specimen 1	
Part	Tensile MG 01
Material	MG01 GR
Test Mode	Peak/Break
High Limit	20000N
Low Limit	10N
Cross Section Area	12.56 square mm
Sample Length	20.0 mm
Selected Load Cell	20 kN
Test Speed	5.0 mm/min
Peak Load	528 N at length: 0.9 mm
Break Load	450 N at length: 1.0 mm
Peak Displacement	4.5 %
Break Displacement	5.0 %
Tensile/Compressive Stress	42.0 N/sq. mm
Ultimate Tensile Strength	42.0 N/sq. mm

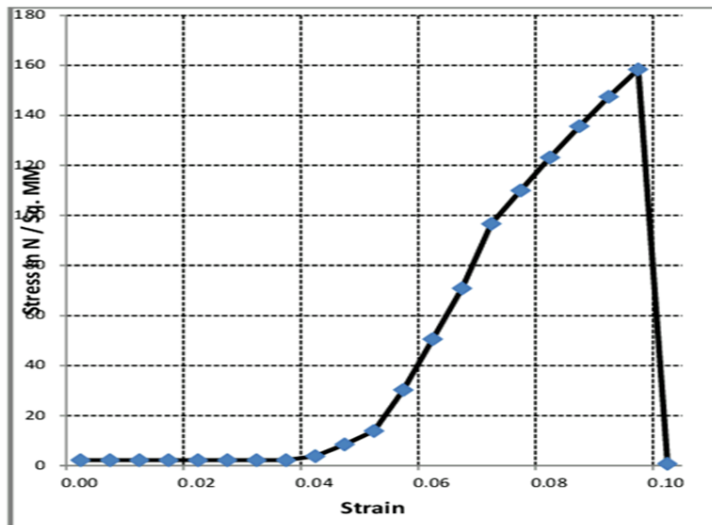


Fig. 12 Tensile test graph plot of specimen 2

Table 3. Tensile Test results of the specimen 2

Specimen 2	
Part	Tensile MG02
Material	MG02 GR
Test Mode	Peak/Break
High Limit	20000 N
Low Limit	10 N
Cross Section Area	12.56 sq. mm
Sample Length	20.0 mm
Selected Load Cell	20 KN
Test Speed	5.0 mm/min
Peak Load	1990 N at length: 1.9 mm
Break Load	1990 N at length: 1.9 mm
Peak Displacement	9.5 %
Break Displacement	9.5 %
Tensile/Compressive Stress	158.4 N/sq. mm
Ultimate Tensile Strength	158.4 N/sq. mm

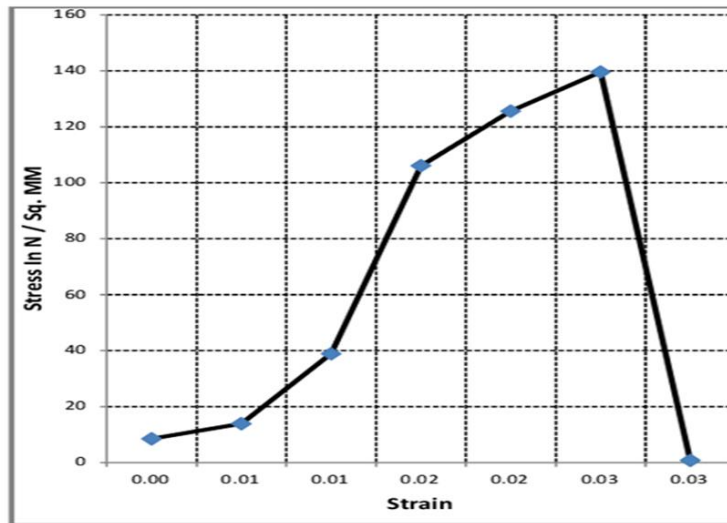


Fig. 13 Tensile test graph plot of specimen 3

Table 4. Tensile Test results of the specimen 3

Specimen 3	
Part	Tensile MG03
Material	MG03 GR
Test Mode	Peak/Break
High Limit	20000 N
Low Limit	10 N
Cross Section Area	12.56 sq. mm
Sample Length	20.0 mm
Selected Load Cell	20 KN
Test Speed	5.0 mm/min
Peak Load	1754 at length: 0.9 mm
Break Load	1754 at length: 1.0 mm
Peak Displacement	2.5 %
Break Displacement	2.5 %
Tensile/Compressive Stress	139.6 N/sq.mm
Ultimate Tensile Strength	139.6 N/sq.mm

From Figure 11 it is observed that the Ultimate Tensile Strength (UTS) of specimen 1 is very less in comparison to the other two specimens. It is also observed that there is a difference between the breaking load and peak load which indicates that specimen 1 has undergone slight yielding as shown in Figure 14 when tensile force was acting on the specimen.



Fig. 14 Fractured specimen 1

From Figure 12 it is observed that the Ultimate Tensile Strength of specimen 2 is higher than specimen 1. It is also observed that both breaking load and peak load are equivalent which means that specimen 2 has not undergone a yielding effect concluding that specimen 2 is brittle as shown in Figure 15.



Fig. 15 Fractured specimen 2

From Figure 13 it is observed that in comparison to specimen 1, specimen 3 has a higher value of Ultimate Tensile Strength due to the presence of higher aluminum content in specimen 3. It is also seen that the breaking load and peak load are equivalent which results in a non-yielding process leading to the presence of brittle behavior in specimen 3 as shown in Figure 16.



Fig. 16 Fractured specimen 3

For the Micro Vickers hardness test, the apparatus was adjusted to apply 100g force on all three specimens. The obtained results are shown in Table 5. At the position of the formation of defects such as micro holes, the hardness value will be less. It can be observed from the result that specimen 2 has a higher value in comparison to the other two specimens.

Table 5. Micro Vickers Hardness test results

Vickers Hardness Value	Specimen 1	Specimen 2	Specimen 3
Reading 1	57.4	77.7	51.8
Reading 2	38.7	87.4	53.5
Reading 3	58.2	53.3	56.5
Mean Value	51.4	72.8	53.9

## 5. Conclusions

In the present research work, three specially reinforced magnesium composites specimen were prepared by using the squeeze casting process. Due to the incorporation of different reinforcements in the magnesium matrix, novel magnesium matrix composites have been manufactured. Specimen 2 has fewer external and internal defects so its Micro Vickers hardness value is greater than the other two specimens fabricated. It is also observed that specimen 2 has a higher value of Ultimate Tensile Strength than specimen 1 and specimen 3. From the microstructure analysis, it can be concluded that uniform distribution of reinforcement particles led to higher values of Ultimate Tensile Strength and Micro Vickers Hardness. The future research work based on this study can be based on the implementation of Machine Learning algorithms such as Artificial Neural Network, Support Vector Machines (SVM), and Decision Tree algorithm for the determination of the mechanical and microstructure properties as well as the geometrical properties analysis of the obtained microstructures by using an image processing algorithm.

## Acknowledgement

The authors acknowledge the availability of open access papers in the domain of the fabrication of composites by casting process.

## References

- [1] Kumar S, Singh R, Hashmi MSJ. Metal matrix composite: a methodological review, *Advances in Materials and Processing Technologies*, 2020; 6:113 - 24. <https://doi.org/10.1080/2374068X.2019.1682296>
- [2] Bahl S. Fiber reinforced metal matrix composites-a review, *Materials Today: Proceedings* 2020. <https://doi.org/10.1016/j.matpr.2020.07.423>
- [3] Bhoi NK, Singh H, Pratap S. Developments in the aluminum metal matrix composites reinforced by micro/nano particles-a review, *Journal of Composite Materials*, 2020; 54:6 813 - 833. <https://doi.org/10.1177/0021998319865307>
- [4] Güler Ö, Bağcı N. A short review on mechanical properties of graphene reinforced metal matrix composites, *Journal of Materials Research and Technology*, 2020; 9:3 6808 - 6833. <https://doi.org/10.1016/j.jmrt.2020.01.077>
- [5] Węglewski W, Pitchai P, Bochenek K, Bolzon G, Konetschnik R, Sartory B, Ebner R, Kiener D, Basista M. Experimental and Numerical Investigation of the Deformation and Fracture Mode of Microcantilever Beams Made of Cr (Re)/Al<sub>2</sub>O<sub>3</sub> Metal-Matrix Composite, *Metallurgical and Materials Transactions A*, 2020; 1 - 14. <https://doi.org/10.1007/s11661-020-05687-3>
- [6] Ramesh P, Nataraj M. Automotive industry application of aluminium-based hybrid metal matrix composite, *International Journal of Heavy Vehicle Systems*, 2020; 27:1-2 18 - 32. <https://doi.org/10.1504/IJHVS.2020.104412>

- [7] Pandian V, Kannan S. Processing and preparation of aerospace-grade aluminium hybrid metal matrix composite in a modified stir casting furnace integrated with mechanical supersonic vibration squeeze infiltration method, *Materials Today Communications*, 2020; 101732. <https://doi.org/10.1016/j.mtcomm.2020.101732>
- [8] Saleh BI, Ahmed MH. Development of functionally graded tubes based on pure Al/Al<sub>2</sub>O<sub>3</sub> metal matrix composites manufactured by centrifugal casting for automotive applications, *Metals and Materials International*, 2020; 26:9 1430 - 1440. <https://doi.org/10.1007/s12540-019-00391-3>
- [9] Singh H, Kumar D, Singh H, Development of magnesium-based hybrid metal matrix composite through in situ micro, nano reinforcements, *Journal of Composite Materials*, 2021; 55:1 109 - 123. <https://doi.org/10.1177/0021998320946432>
- [10] Kumar A, Arafath MY, Gupta P, Kumar D, Hussain CM, Jamwal A. Microstructural and mechano-tribological behavior of Al reinforced SiC-TiC hybrid metal matrix composite, *Materials Today: Proceedings*, 2020; 21: 1417 - 1420. <https://doi.org/10.1016/j.matpr.2019.08.186>
- [11] Dinaharan I, Zhang S, Chen G, Shi Q. Development of titanium particulate reinforced AZ31 magnesium matrix composites via friction stir processing, *Journal of Alloys and Compounds*, 2020; 820: 153071. <https://doi.org/10.1016/j.jallcom.2019.153071>
- [12] Say Y, Guler O, Dikici B. Carbon nanotube (CNT) reinforced magnesium matrix composites: The effect of CNT ratio on their mechanical properties and corrosion resistance, *Materials Science and Engineering: A*, 2020: 798; 139636. <https://doi.org/10.1016/j.msea.2020.139636>
- [13] Chang, Z, Wu Y, Iizuka T, Peng L, Ding W. High-strength and high-modulus Al18B4O33W/GWZ1031K magnesium matrix composite prepared by squeeze casting, *Materials Science and Engineering: A*, 2021: 817; 141393. <https://doi.org/10.1016/j.msea.2021.141393>
- [14] Kumar NS. Fabrication and characterization of Al7075/RHA/Mica composite by squeeze casting, *Materials Today: Proceedings*, 2021: 37; 750 - 753. <https://doi.org/10.1016/j.matpr.2020.05.769>
- [15] Sekar K Mechanical and Tribological Properties of A7075/SiC/B4C Hybrid Composite fabricated by Stir and Squeeze Casting Method, In *Key Engineering Materials*, 2021: 882; 77 - 88. <https://doi.org/10.4028/www.scientific.net/KEM.882.77>



Research Article

## Characterization of low-cost inkjet printed-photonic cured strain gauges for remote sensing and structural monitoring applications

Juho Kerminen<sup>1,a</sup>, Jenny Wiklund<sup>2,b</sup>, Alp Karakoç<sup>1,c</sup>, Kalle Ruttik<sup>1,d</sup>, Riku Jäntti<sup>1,e</sup>, Hüseyin Yiğitler<sup>1,f</sup>

<sup>1</sup> Department of Communications and Networking, Aalto University, 02150 Espoo, Finland

<sup>2</sup> Department of Bioproducts and Biosystems, Aalto University, 02150 Espoo, Finland

### Article Info

#### Article history:

Received 29 Oct 2021

Revised 02 Dec 2021

Accepted 04 Dec 2021

#### Keywords:

Printed electronics;

Strain gauges;

Impedance;

Monitoring and sensing technologies

### Abstract

In the present work, cost-effective strain gauges were fabricated by using inkjet printing and photonic curing on flexible and recyclable PET substrates. Ohmic resistance (a.k.a. DC resistance) ( $R_0$ ) and complex electrical impedance ( $Z$ ) as a function of test frequency were characterized, respectively, with the state-of-the-art electronic testing equipments. For the fabrication process, commercially available silver nanoparticle (AgNP) inks and substrates were used. In order to validate the in-house cantilever beam measurement setup and devices, first, commercially available metallic foil strain gauges (with the provided gauge factor  $GF=2.0$  by the manufacturer) were tested at different locations. Thereafter, the printed strain gauges were investigated with several repetitions at different measurement locations. The measurement results demonstrated an affordable, rapid and tailorable design and repeatable fabrication approach for strain gauges with  $GF_{avg} \sim 6.6$ , which has potential applications in remote sensing and structural monitoring applications.

© 2021 MIM Research Group. All rights reserved.

## 1. Introduction

Strain gauges are electromechanical sensing devices created from thin conductive lines on top of a rigid or flexible substrate, which are then attached to the measurement region [1, 2]. The resistance, capacitance, impedance or piezoelectric characteristics of such devices change when the measurement region is subject to any source of deformation [3, 4]. They can be fabricated by depositing metallic film onto substrates, photolithography, screen printing, aerosol or inkjet printing, to name a few [5, 6, 7]. Due to their cost-effectiveness, tailorable design, high bendability and stretchability, flexible printed strain gauges have been gaining grounds, e.g. in healthcare applications, wearable device technologies, structural health monitoring and intelligent packaging solutions [8, 9, 10].

Despite their advantages and applicability, their electromechanical characteristics may vary a lot due to the fabrication processes, for which the micro-structural variations and fabrication repeatability play critical roles. For instance, in case of inkjet printing, which is based on deposition of ink droplets to create conductive traces with, e.g. silver (Ag) or copper (Cu) nanoparticles (NPs), porosity, thickness and roughness at the boundaries of the traces have dominant effect on both electrical and mechanical characteristics of the designed devices [11, 12, 13]. To be able to improve such characteristics, e.g. strength and electrical conductivity, multiple layers of deposition and sintering methods have been proposed and widely applied in the literature [14, 15]. It has been observed that sintering

\*Corresponding author: [alp.karakoc@aalto.fi](mailto:alp.karakoc@aalto.fi)

<sup>a</sup> [orcid.org/0000-0003-0394-4704](https://orcid.org/0000-0003-0394-4704); <sup>b</sup> [orcid.org/0000-0001-6617-8846](https://orcid.org/0000-0001-6617-8846); <sup>c</sup> [orcid.org/0000-0002-2010-9607](https://orcid.org/0000-0002-2010-9607);

<sup>d</sup> [orcid.org/0000-0002-7365-9194](https://orcid.org/0000-0002-7365-9194); <sup>e</sup> [orcid.org/0000-0002-5398-2381](https://orcid.org/0000-0002-5398-2381); <sup>f</sup> [orcid.org/0000-0002-7794-2763](https://orcid.org/0000-0002-7794-2763)

DOI: [http://dx.doi.org/10.17515/resm2021.360me1029](https://dx.doi.org/10.17515/resm2021.360me1029)

Res. Eng. Struct. Mat. Vol. 7 Iss. 4 (2021) 647-660

effectively agglomerate NPs by densifying and bonding them together while deposition of multiple layers increases the thickness of the conductive traces; hence, the electrical conductivity [16, 17].

Traditionally, strain gauges are fabricated as metallic foils arranged in grid patterns and used in Wheatstone bridge configuration. The bridge usually measures the DC voltage change on the strain gauge exposed to the applied loads  $F$ . For the metallic foil strain gauges, it is sufficient to characterize the initial reference ohmic resistance (a.k.a. DC resistance)  $R_0$  and gauge factor ( $GF$ ), which expresses the sensitivity of the strain gauge, as the resistance change  $\Delta R = R - R_0$  with respect to  $R_0$  and strain  $\varepsilon$ , i.e. [18]

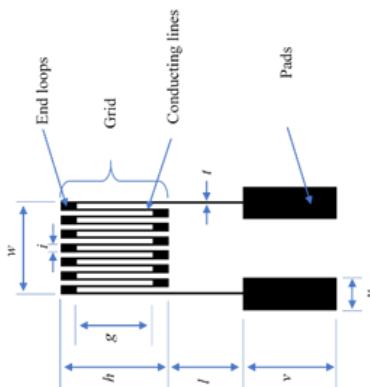
$$GF = \frac{\Delta R/R_0}{\varepsilon} \quad (1)$$

For off-the shelf commercial strain gauges,  $GF \sim 2.0$  is quite common while higher values have been achieved, e.g.  $GF \sim 3.0$  and  $GF \sim 5.0$  with inkjet printing by Rahman et al. and Kravhcuk et al., respectively [19, 20, 21]. Nevertheless, variations exist in electrical characteristics of the printed strain gauges with the frequency shifts when they are deformed as a result of  $F$ . These changes can be explained with the uneven distribution of the conductive ink of the printed patterns resulting in microscopic inductance ( $L$ ) and capacitance ( $C$ ) changes subjected to  $F$ . Hence, this means that the printed strain gauge may function as resonant (LC) circuit with its specific resonant frequency  $\omega_r$ . Therefore, in addition to  $R_0$ , frequency response  $\omega$  and frequency dependent impedance of printed strain gauges  $Z(\omega) = R(\omega) + jX(\omega)$ , which is composed of resistance  $R(\omega)$  and reactance  $X(\omega)$ , should be measured. Such characterization is especially useful for matching the impedance with the circuitry used in passive strain gauge measurement telemetry system, through which the strains can be remotely read [22, 23, 24].

The current study presents a framework for the fabrication and characterization of novel printed strain gauge design, which can function as resonant (LC) circuit and has prospective uses in remote sensing and structural monitoring. For the fabrication process, low-cost inkjet printing equipment was used and the effect of process parameters including number of deposited layers, i.e. trace height, and sintering, which was realized with photonic curing in the present study, on the conductivity was investigated. For the electromechanical characterization, a cantilever beam structure and an impedance analyzer were used to understand the frequency response of the printed strain gauges within the range of 0-500 MHz as function of  $\varepsilon$  due to  $F$  and to compute  $\omega_r$ , which was around 200 MHz for the present design. Therefore, it was possible to compute reliable  $GF$  values by means of the defined frequency bandwidth of 49-50 MHz, which was a distant range from  $\omega_r$ . For the validation of the characterization setup and comparison with the printed strain gauges, commercially available metallic foil strain gauges were used. The validation and comparison studies demonstrated that the printed strain gauges were promising with the  $GF \sim 6.6$  while the commercial ones were measured to have  $GF \sim 1.8$ , out of which 10% measurement error was deduced (in comparison with the provided  $GF = 2.0$  by the manufacturer).

## 2. Materials and Methods

### 2.1. Design, Fabrication of Low-Cost Printed and Photonic Cured Strain Gauges



Parameter	Value
Number of conducting lines	14
Ink	Mitsubishi NBSIJ-MU01 Ag nanoparticle content: 15% Ag nanoparticle diameter: 20 nm
Substrate	Mitsubishi NB-TP-3GU100 Thickness: 135 $\mu\text{m}$ Heat resistance: Max. 120 $^{\circ}\text{C}$
Printer/printer settings	Epson C88+ inkjet printer 5760 x 1440 dpi Matte, Heavyweight Grayscale Best Photo Low speed
Curing	Photonic curing, custom device Linear 400mm Reflector XFTR-L400C (1500W XenonFlash) 15 seconds for each layer
Number of printed layers	3
Grid line (trace) thickness, $b$	$\sim 0.4$ micron [1]
Gage length, $g$	27 mm
Grid height, $h$	34 mm
End loop width, $i$	2 mm
Transition, $l$	15 / 20 / 25 mm
Grid width, $w$	20 mm
Grid line (trace) width, $t$	$\sim 0.35$ mm
Pad width, $u$	7 mm
Pad height, $v$	21 mm

Fig. 1 Geometric and fabrication process parameters of the inkjet printed strain gauge

The strain gauge pattern as designed and represented in Fig. 1 were parametrically created in Mathematica technical computing software and transferred as scalable vector graphics (.svg) to Inkscape open-source drawing software. The generated files were printed onto A4 size Mitsubishi NB-TP-3GU100 transparent polyethylene terephthalate (PET) special media, which has microporous  $\text{Al}_2\text{O}_3$ -PVA single-sided coating and sheet thickness of  $135 \pm 12 \mu\text{m}$ . The conductive ink used on the NB-TP-3GU100 special media was Mitsubishi NBSIJ-MU01 silver nanoparticle (AgNP) inkjet printer ink, which was also purchased from Mitsubishi Paper Mills Ltd. The ink was loaded to the black ink cartridge of Epson Stylus C88+ inkjet printer (5760 dpi x 1440 dpi resolution) (please, see Fig. 2) with the following printer software settings: "Matte Paper - Heavyweight", "best photo" and "gray scale". For

increasing the print quality and registration for the special media and AgNP ink, "High speed printing" option was set off.

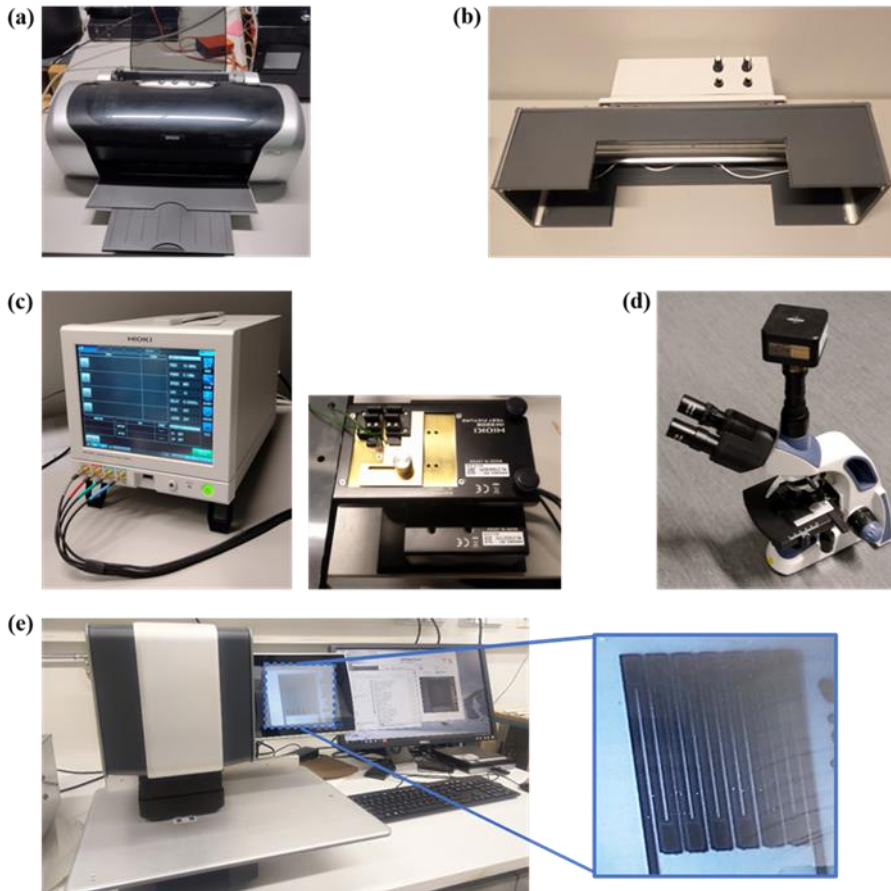


Fig. 2 Printing and measurement devices: (a) Epson Stylus C88+ printer, (b) In-house photonic curing device, (c) HIOKI IM7587 impedance analyzer and IM9202 test fixture, (d) light microscope equipped with 6.3 MP Swiftcam digital camera, (e) height measurement for printed traces with L&W Optitopo system

In order to characterize the conductivity and formulate an optimal printing process, strain gauges were fabricated with one, two and three printed layers, i.e. passes over the same pattern. Moreover, a custom photonic curing system with 1500 W flash device was also assembled, the components of which were purchased from Xenon Flash Tubes LLC ([www.xenonflashtubes.com](http://www.xenonflashtubes.com)), and implemented to sinter AgNPs for approximately 15 seconds immediately after the printing process was over for each layer. The microscopic structure investigations and  $R_0$  measurements (as later provided in Results section) were thereafter carried out. For  $R_0$  measurements, TENMA 72-7745 multimeter was used while 6.3 MP Swiftcam microscope digital camera apparatus was used for the microscopic analysis. In order to measure the printed trace height and generate the height maps, L&W Optitopo surface roughness measurement device was used as depicted in Fig. 2. By means of this device, a pattern of shadows was created by illuminating the sample surface from a small angle. Then, by utilizing two images of the same area illuminated from opposite sides, the height maps for the printed strain gauges were generated in  $\mu\text{m}$  scale. The

measurement area was taken as 32 mm x 32 mm, which is the maximum range achieved with L&W Optitopo, and the resolution and bandpass were 15.625  $\mu\text{m}$  and 0.01-0.5 mm, respectively. In order to analyze the height uniformity, the height profiles were measured over rows (top-center-bottom) on the grids of the printed strain gauges.

## 2.2. Experiment Setup and Measurement System for Characterization

In order to evaluate the performance and understand the characteristics of the printed strain gauges, a slender cantilever beam as schematized in Fig. 3 was built so that only bending moments (eliminating the shear) were taken to be the dominant source of deformation. Here,  $l$  is the distance between the fixed end and applied load  $F$ ;  $x$ ,  $b$  and  $h$  are the distance between the fixed end and strain gauge center, beam breadth and height, respectively. At the free end of the beam, a 3D printed plate was attached with a single screw to provide an easy way of applying load  $F$  at the specified distance  $l=390$  mm. For this purpose, a set of calibration weights was used, and deflections, strains and electrical characteristics of the printed strain gauges and the commercial reference gauges (RS PRO 4 mm 120  $\Omega$  metallic foil strain gauge with the gauge factor  $GF=2$ ) at two different beam locations,  $x=120$  mm and 170 mm, were measured (please, see Fig.3).

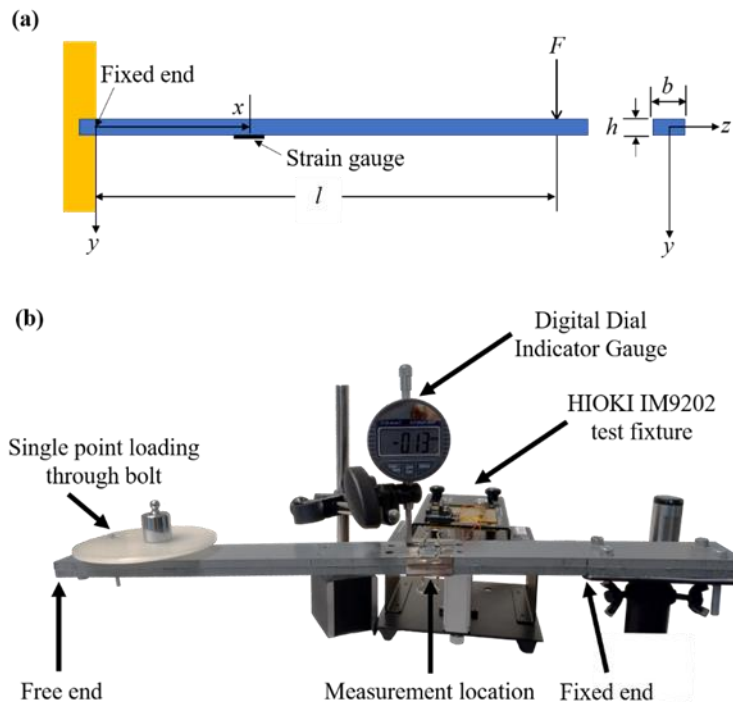


Fig. 3 Cantilever beam: (a) schematic diagram, (b) setup with the test fixture and digital dial indicator gauge

The conductive pads of the printed strain gauges were firmly attached to 10 cm wires with conductive copper tape. Thereafter, the strain gauges were taped to the measurement location  $x$  and pressed with a support plate in order to have a firm grip of the strain gauge and provide correct bending and stretch/contraction over it. The wires were then connected to a Hioki IM9202 test fixture as shown in Fig. 2(c), which was then connected to IM9201 test head used by the Hioki IM7587 impedance analyzer for measuring  $R$  and  $Z$  of the strain gauge. The measurements were carried out by sweeping a signal frequency

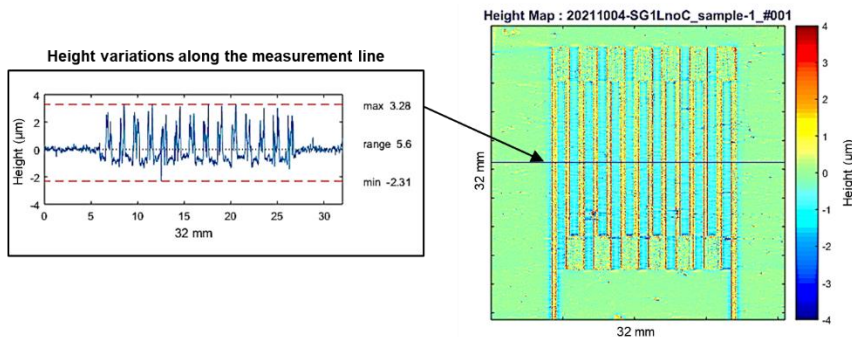
range of 1-120 MHz with LCR-mode on, which was repeated ten times to obtain the average and the standard deviation. The shortest possible frequency interval of 0.1 MHz provided by the device was used while samples were taken with the impedance analyzer application provided by Hioki capable of sweeping and saving the data as .csv file. In all the tests, applied load  $F$  was adjusted in order to provide the beam deflections of  $\delta = \{0, 0.3, 0.6, 0.9, 1.2, 1.5, 1.8, 2.1, 2.4\}$  mm with a tolerance of  $\pm 0.05$  mm at the measurement locations, which were later converted into strains  $\varepsilon$  by using the formula sets provided in the Appendix. As shown in Fig. 3, an RS Pro electronic digital indicator gauge with  $\pm 0.02$  mm accuracy and 25 mm range were used for the deflection measurements.

## Results and Discussion

### 3.1. Effects of Printed Layers and Photonic Curing

In order to understand the conductivity changes with respect to the fabrication parameters and provide repeatable process solutions, a set of measurements were carried out by using  $n=10$  printed strain gauges. Through these measurements, the effects of number of printed layers and photonic curing on the printing quality and resistance of strain gauges were analyzed. For this purpose, one, two and three layers of AgNP ink were deposited onto the substrate, respectively, where the sintering was carried out with photonic curing of 1500 W for approximately 15 seconds. The height profiles depicted in Fig. 4 demonstrates that both printed layers and curing have positive effect on the trace height. However, as a negative effect, the increase in number of printed layers caused spreading of the ink; thus, undesired increase in trace width. In addition to the height profile measurements, as seen in the microscope images of Fig. 5, photonic curing combined with multiple layers of printing was also observed to provide more consistent and denser traces. For instance, Fig. 5(b) for one layer of print without any sintering shows that some of the deposited ink droplets were not connected to the agglomerate. As a result of these unconnected droplets of the printed structure, the resistance was observed to be as high as  $R_0 = 157 \pm 5 \Omega$  for the designed and printed strain gauges. However, after printing and curing the second layer, there was a drastic reduction in the resistance of  $R_0 = 65 \pm 2 \Omega$  on average, which continued to drop to  $R_0 = 45 \pm 1 \Omega$  on average with additional third layer and photonic curing (please, see Fig. 5 (f)). Interestingly, the resulting resistance of three-layer strain gauge is close to  $50 \Omega$  that is common standard for matching different circuits [25]. In addition, the effect of adding more than three layers on the conductivity was obtained to be negligible; thus, three printed layers with photonic curing was taken as the fabrication parameters for the present designed strain gauges.

(a)



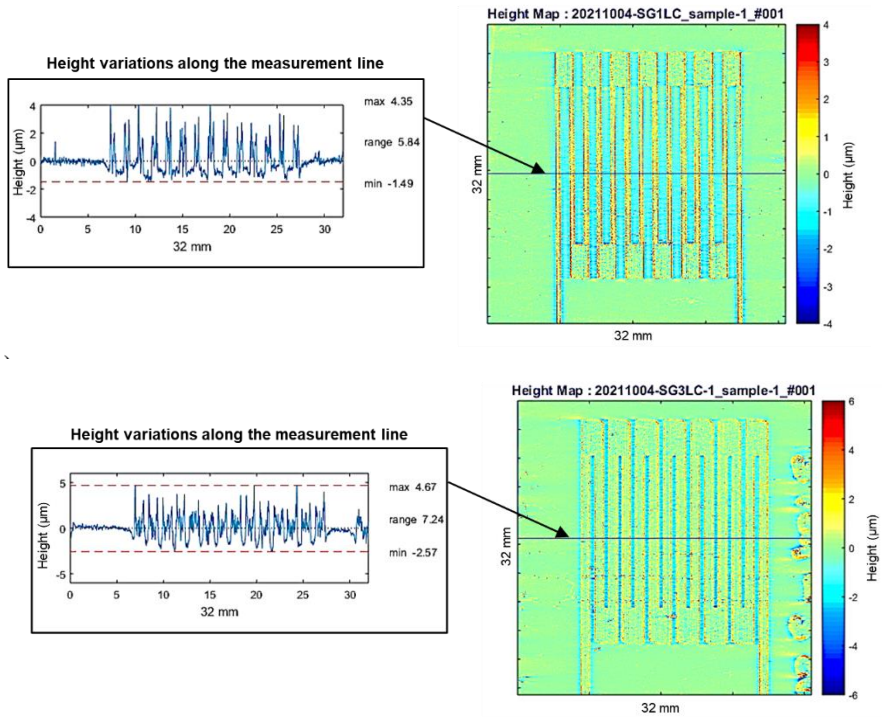
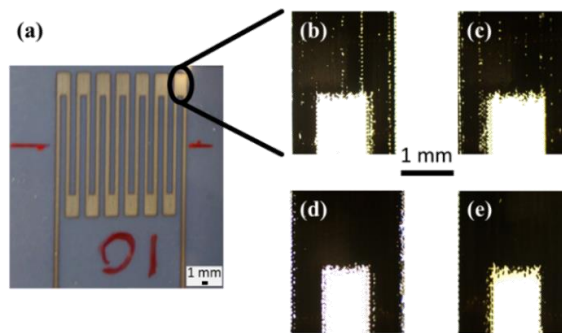


Fig. 4 Effect of printed layers and curing on the strain gauge height profiles: (a) one layer of print no curing (maximum value of  $3.28 \mu\text{m}$ ), (b) one layer of print with curing (maximum value of  $4.35 \mu\text{m}$ ), (c) three layers of print with curing after each layer (maximum value of  $4.67 \mu\text{m}$ ). The scanned area is  $32 \text{ mm} \times 32 \text{ mm}$  while the height profiles are represented in  $\mu\text{m}$  scale, which were obtained by scanning the center rows of the strain gauge grids



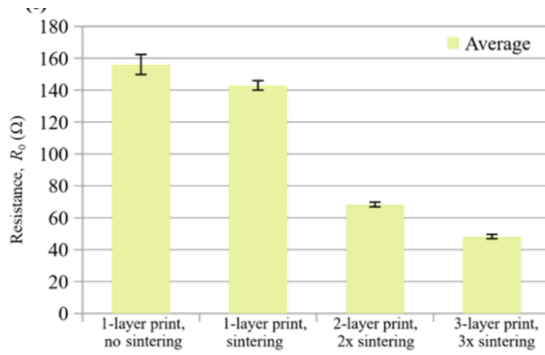


Fig. 5 Printed strain gauge and light microscope images showing the morphological changes due to photonic curing and number of printed layers: (a) digital still, (b) light microscope image for one layer of print without photonic curing, (c) one layer of print and photonic curing, (d) two layers of print and photonic curing, (e) three layers of print and photonic curing, (f) impact of multiple layers and curing on the ohmic resistance  $R_0$  of printed strain gauge

### 3.2. Gauge Factor $GF$

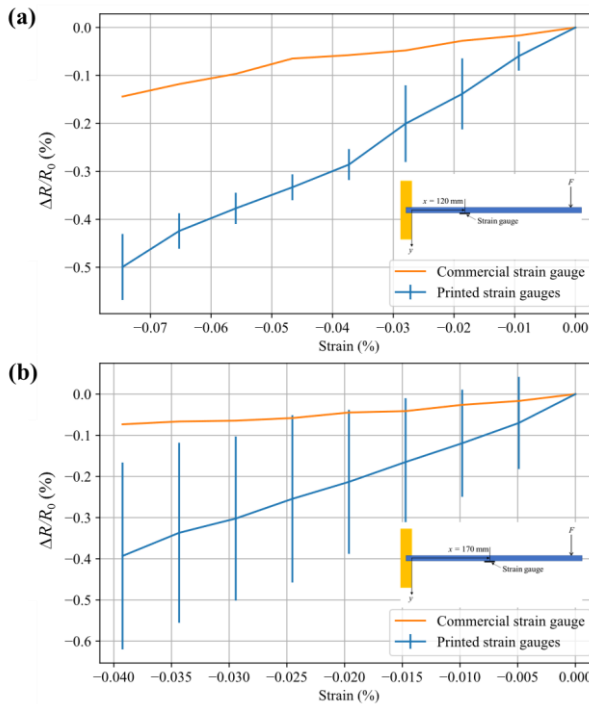


Fig. 6 Resistance change  $\Delta R$  with respect to  $R_0$  of the printed strain gauges as a function of strain within the 49-50 MHz bandwidth: (a) at  $x=120$  mm and (b) at  $x=170$  mm. Error bars refer to the standard deviation while the straight lines represent the mean values

In order to investigate the accuracy of the built setup and determine the  $GF$  of the printed strain gauges, measurements were carried out at two different locations on the cantilever beam, i.e.  $x=120$  mm and  $x=170$  mm (please, see Fig. 6). As the initial step, frequency bandwidth was set to 49-50 MHz for  $GF$  measurements because of great impedance variations near  $\omega_r \sim 200$  MHz (as elaborated in the following sections). The chosen range provided stable results for  $GF$  and beam deflection-impedance correlation.

For the measurement setup and device validation, the measurements were conducted by using the commercially available metallic foil strain gauges with the provided  $GF=2$  by the manufacturer datasheet. The measurements at different locations were conducted one time with the commercial strain gauges while they were repeated 10 times for the printed strain gauges fabricated using three layers and photonic curing process. As a result of the measurements with the commercial strain gauges,  $GF$  was obtained as  $\sim 1.8$ , showing 10% measurement setup and device error. For the printed strain gauges,  $GF=6.6 \pm 0.3$  and  $GF=6.6 \pm 0.9$  were measured for  $x=120$  mm and  $x=170$  mm, respectively. This demonstrates that the printed strain gauges provide repeatable results at different measurement locations with varying beam deflections. It is also noteworthy that the printed strain gauges were obtained to have higher sensitivity when compared with the commercial strain gauge measurements. This also shows the application potentials of the the printed strain gauges, e.g. in detecting tiny vibrations and daily movements of the human body, which can be cumbersome with the conventional gauges [26].

### 3.3. Impedance $Z$ and Frequency Dependency

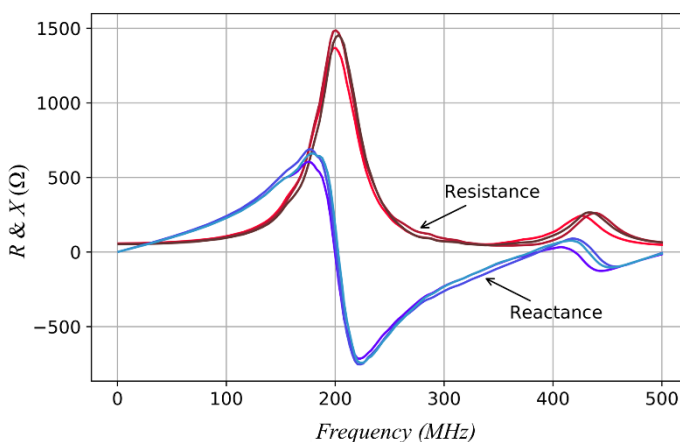


Fig. 7 Resistance  $R$  and reactance  $X$  measurements for three printed strain gauges in unloaded initial configuration, i.e. no bending

The resistance and reactance of the printed strain gauges are depicted in Fig. 7. All three strain gauges have relatively close frequency responses with  $\omega_r$  around 200 MHz. At  $\omega_r$ , the resistance is at its highest value while the reactance changes the phase, which brings forth the impact of the fabrication/printing related differences. As seen in Fig. 7, close to  $\omega_r$ , all the fabrication/printing originated variations are amplified, which makes it more difficult to control the uniformity of the strain gauge behaviour. On the other hand, all the strain gauge have relatively close behaviour well below  $\omega_r$ .

In Figs. 8a and 9a, resistance change  $\Delta R$  and reactance change  $\Delta X$  of a printed strain gauge, which can be elaborated as the differences between the values measured for deformed configuration caused by  $\epsilon$  and initial configuration, are provided for 800 MHz bandwidth. Below  $\omega_r$ ,  $\Delta R$  has negative dependency while above it is vice versa. The closer the frequency

is to  $\omega_r$ , the higher is the  $\epsilon$  sensitivity. Besides, as seen in Fig. 7, variances between the different gauges were observed to be amplified at around  $\omega_r$ . For sufficiently low frequency below  $\omega_r$ , strain gauge resistance has systematic dependency on  $\epsilon$ , which is depicted in the magnified portion of Fig 8b. This indicates that a printed strain gauge does not have to operate only on DC frequency but can also operate on some higher frequency. Around  $\omega_r$  and above, it was deduced that the printed strain gauge has to be calibrated. Such calibration is needed in order to remove printing related variations between the strain gauges and to identify whether there exists negative or positive  $\epsilon$  dependency at particular frequency.

Nonetheless, the results in Fig. 9a indicate that the printed strain gauges can measure deflections not only by  $\Delta R$  but also by  $\Delta X$ . Interestingly,  $\Delta X$  has higher strain sensitivity above  $\omega_r$ . Similar to the  $\Delta R$  measurements, the  $\Delta X$  frequency response is mostly monotonous below  $\omega_r$ , which was similar to the trend obtained for the  $\Delta R$  measurements (please, see Figs. 8b and 9a). However, it is also noteworthy that the  $\Delta X$  values of the printed strain gauges subjected to bending were observed to be changing from positive to negative around 45 MHz, which requires attention in case of reactance based strain measurements.

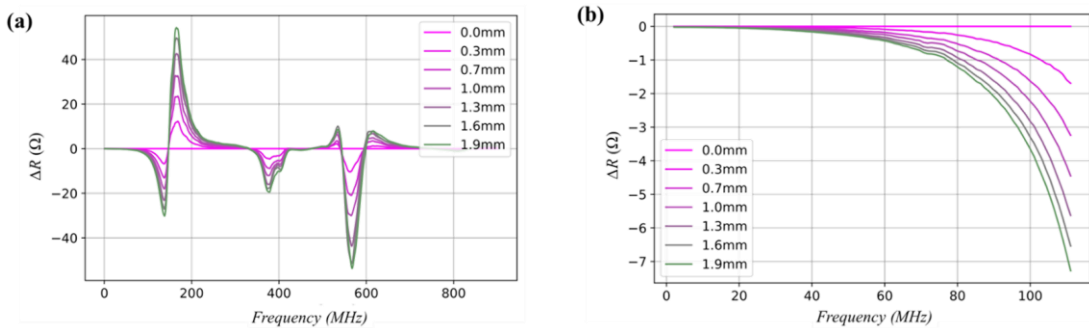


Fig. 8 Resistance change  $\Delta R$  of one strain gauge under deflection: (a) the whole measured bandwidth, (b) restrained bandwidth

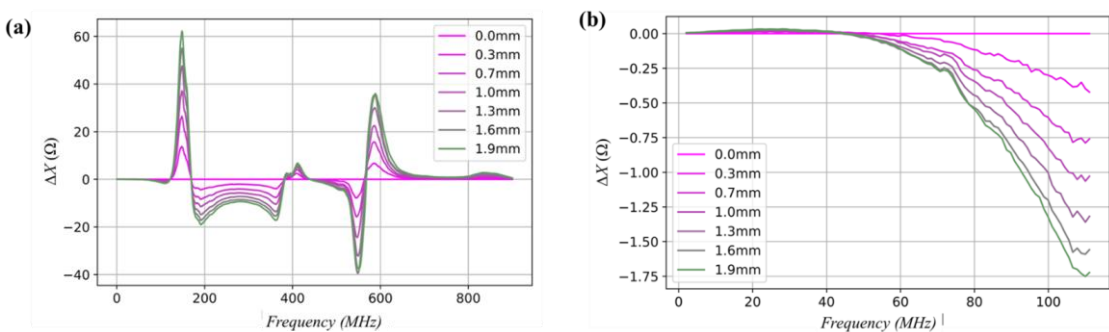


Fig. 9 Reactance change  $\Delta X$  of one strain gauge under deflection: (a) the whole measured bandwidth, (b) restrained bandwidth

In addition to the printed strain gauges, comparative frequency dependent investigations for  $\Delta R$  and  $\Delta X$  was also carried out with commercially available strain gauges, the plots of

which are presented in Fig. 10. For these particular strain gauges, the range of bending dependency was obtained to be in much more smaller range than the one for the printed strain gauges. Similar to the printed strain gauges, the results for the commercial strain gauges in Fig. 10 indicates that there is negative bending dependency of both  $\Delta R$  and  $\Delta X$ .

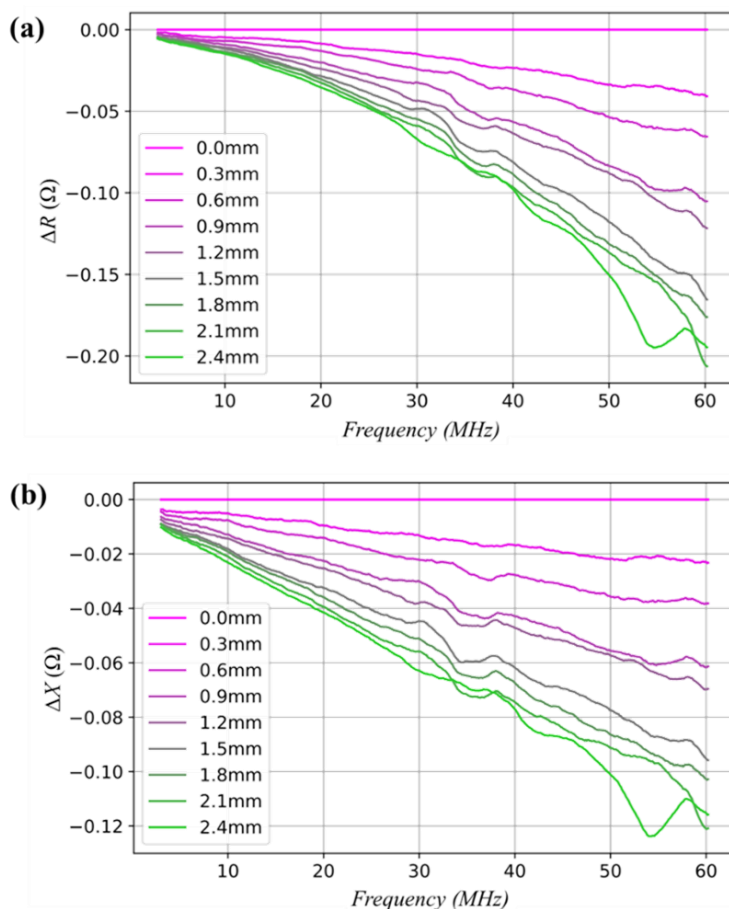


Fig. 10 Commercial strain gauge at x=170 mm position: (a) resistance change  $\Delta R$ , (b) reactance change  $\Delta X$

#### 4. Conclusions

The present study provided a framework for the fabrication and characterization of low-cost inkjet-printed strain gauges,  $\Delta R$  and  $\Delta X$  of which vary with the applied load  $F$  and frequency  $\omega$ . For this purpose, AgNP inks and coated PET substrates manufactured by Mitsubishi Papermills were investigated with a focus on the effect of number of printed layers and curing on the DC resistance  $R_0$ . As a result of this investigation on the fabrication process, the printing parameters such as number of printed layers and curing were found out to have positive effects on the conductivity (with reductions in  $R_0$ ). For instance, one layer printed and non-cured strain gauges were obtained to have  $R_0 = 158 \Omega$  on average, while  $R_0 = 140 \Omega$  on average was reached after photonic curing, which agglomerates the AgNP and increases the conductivity. Moreover, number of printed layers, thus trace

height, was another important printing parameter affecting the conductivity. For instance, three printed layers and photonic-cured strain gauges resulted in  $R_0=45 \Omega$  and  $GF\sim 6.6$  (within the frequency bandwidth of 49-50 MHz) on average, which was obtained to be slightly higher than the  $GF$  values for the strain gauges fabricated with similar inkjet printing strategies in the literature. Therefore, these affordable and easy-to-design printed strain gauges can be an alternative to the commercially available ones with similar dimensions but higher resistance ( $R_0=120 \Omega$ ) and lower gauge factors ( $GF=2$ ). Another important outcome of the printed strain gauges was their electromagnetic characteristics investigated in terms of impedance over a large frequency range up to 800 MHz. It was deduced that they can function as resonant (LC) circuit with their specific resonant frequencies  $\omega_r$ . Therefore, they can be used as flexible and tailorable solutions for remote sensing and structural monitoring, such as in biomedical, seismic or aviation applications, through which the use of heavy-wiring can be minimized. As future studies, degradation and temperature dependency under various operational conditions will be also investigated, which makes such sensors to be robustly utilized in thermal sensing applications such as battery and indoor air temperature monitoring.

### Acknowledgement

The authors gratefully acknowledge the funding from Academy of Finland BESIMAL project (decision number 334197). J.W. also acknowledges the funding from Jenny and Antti Wihuri Foundation. Besides, the authors acknowledge the technical assistance of Timi Lehtola and Juhapekka Hietala.

### References

- [1] KT, Watkins JK, Phero T, Litteken D, Tsai K, Bingham T, Ranganatha KL, Johnson BC, Deng Z, Jaques B, Estrada D. Aerosol jet printed capacitive strain gauge for soft structural materials. *npj Flexible Electronics*, 4:2397-4621, 2020. <https://doi.org/10.1038/s41528-020-00095-4>
- [2] Mitterlehner T, Beisteiner C, Polixmair M, Steinbichler G. Injection molding parts with integrated all-inkjet printed strain gauge for condition monitoring. In ANTECÂ 2018 - Proceedings of the Technical Conference & Exhibition, Orlando, FL, May 7-10, 2018. Society of Plastics Engineers, 2018.
- [3] Yi Y, Wang B, Bermak A. A low-cost strain gauge displacement sensor fabricated via shadow mask printing. *Sensors*, 19(21):4713, 2019. <https://doi.org/10.3390/s19214713>
- [4] Kim J, Kim K, Ham SW, Bae NH, Park MY, Min NK. A hydrogen pressure sensor based on bulk-micromachined silicon strain gauges. *Procedia Engineering*, 168:790-793, 2016. <https://doi.org/10.1016/j.proeng.2016.11.260>
- [5] Shakeel M, Khan WA, Rahman K. Fabrication of cost effective and high sensitivity resistive strain gauge using DIW technique. *Sensors and Actuators A: Physical*, 258:123-130, 2017. <https://doi.org/10.1016/j.sna.2017.03.003>
- [6] Thompson B, Yoon HW. Aerosol-printed strain sensor using PEDOT:PSS. *IEEE Sensors Journal*, 13(11):4256-4263, 2013. <https://doi.org/10.1109/JSEN.2013.2264482>
- [7] Andò B, Baglio S, La Malfa S, L'Episcopo G. All inkjet printed system for strain measurement. In *Sensort*, 2011 IEEE, pages 215-217. IEEE, 2011. <https://doi.org/10.1109/ICSENS.2011.6127295>
- [8] Mantysalo M, Pekkanen V, Kaija K, Niittynen J, Koskinen S, Halonen E, Mansikkamaki P, Hameenoja O. Capability of inkjet technology in electronics manufacturing. In 59th Electronic Components and Technology Conference, pages 1330-1336. IEEE, 2009. <https://doi.org/10.1109/ECTC.2009.5074185>

- [9] Ando B, Baglio S. All-inkjet printed strain sensors. *IEEE Sensors Journal*, 13(12):4874-4879, 2013. <https://doi.org/10.1109/JSEN.2013.2276271>
- [10] Wiklund J, Karakoç A, Palko T, Yiğitler H, Ruttik K, Jäntti R, Paltakari J. A review on printed electronics: Fabrication methods, inks, substrates, applications and environmental impacts. *Journal of Manufacturing and Materials Processing*, 5(3):89, 2021. <https://doi.org/10.3390/jmmp5030089>
- [11] Cummins G, Desmulliez MPY. Inkjet printing of conductive materials: a review. *Circuit World*, 38(4):193-213, 2012. <https://doi.org/10.1108/03056121211280413>
- [12] Özkan M, Dimic-Misic K, Karakoc A, Hashmi SG, Lund P, Maloney T, Paltakari J. Rheological characterization of liquid electrolytes for drop-on-demand inkjet printing. *Organic Electronics*, 38:307-315, 2016. <https://doi.org/10.1016/j.orgel.2016.09.001>
- [17] Özkan M, Hashmi SG, Halme J, Karakoc A, Sarikka T, Paltakari J, Lund PD. Inkjet-printed platinum counter electrodes for dye-sensitized solar cells. *Organic Electronics*, 44:159-167, 2017. <https://doi.org/10.1016/j.orgel.2017.02.015>
- [14] Roshanghias A, Krivec M, Baumgart M. Sintering strategies for inkjet printed metallic traces in 3d printed electronics. *Flexible and Printed Electronics*, 2(4):045002, 2017. <https://doi.org/10.1088/2058-8585/aa8ed8>
- [15] Kuroda K, Nakako H, Inada M, Noudou T, Kumashiro Y. Development of copper materials and processing for printed electronics. *Transactions of The Japan Institute of Electronics Packaging*, 5(1):20-25, 2012. <https://doi.org/10.5104/jiepeng.5.20>
- [16] Saleh E, Vaithilingam J, Tuck C, Wildman R, Hague R, Ashcroft I, Dickens P. 3d inkjet printing of conductive structures using in-situ IR sintering. In *Proceedings of the 26th Annual International Solid Freeform Fabrication Symposium*, pages 1554-1559. University of Texas, 2015.
- [17] German RM. Thermodynamics of sintering. In *Sintering of advanced materials*, pages 3-32. Elsevier, 2010. <https://doi.org/10.1533/9781845699949.1.3>
- [18] Kitzing H. A solid base for precision strain gauge measurements. In *Proceedings of XVI. IMEKO World Congress, Vienna, Austria*, pages 405-408, 2000.
- [19] Heckmann U, Bandorf R, Gerdes H, Lübke M, Schnabel S, Bräuer G. New materials for sputtered strain gauges. *Procedia Chemistry*, 1(1):64-67, 2009. <https://doi.org/10.1016/j.proche.2009.07.016>
- [20] Rahman MT, Moser R, Zbib HM, Ramana CV, Panat R. 3d printed high performance strain sensors for high temperature applications. *Journal of Applied Physics*, 123(2):024501, 2018. <https://doi.org/10.1063/1.4999076>
- [21] Kravchuk O, Reichenberger M. Properties and long-term behavior of nanoparticle based inkjet printed strain gauges. *Journal of Materials Science: Materials in Electronics*, 27, 2016. <https://doi.org/10.1007/s10854-016-5207-9>
- [22] Bona M, Sardini E, Serpelloni M, Andò B, Lombardo CO. Study on impedance behavior of a telemetric system operating with an inkjet-printed resistive strain gauge. In Bruno Andò, Francesco Baldini, Corrado Di Natale, Giovanna Marrazza, and Pietro Siciliano, editors, *Sensors*, pages 258-266, Cham, 2018. Springer International Publishing. [https://doi.org/10.1007/978-3-319-55077-0\\_34](https://doi.org/10.1007/978-3-319-55077-0_34)
- [23] Bona M, Sardini E, Serpelloni M, Andò B, Lombardo CO. Study on a telemetrie system that works with an inkjet-printed resistive strain gauge. In *2016 IEEE Sensors Applications Symposium (SAS)*, pages 1-6, 2016. <https://doi.org/10.1109/SAS.2016.7479869>
- [24] Cheng X, Yu Y, Wang L, Sun C, Tian G. Wireless stress measurement on metal surface based on passive integrated rfid sensor tag. In *2021 IEEE International Instrumentation and Measurement Technology Conference (I2MTC)*, pages 1-6. IEEE, 2021. <https://doi.org/10.1109/I2MTC50364.2021.9460006>
- [25] Yarman BS. A simplified real frequency technique for broadband matching complex. *IIMBO*, 43:529, 1982.

- [26] Yan W, Fuh HR, Lv Y, Chen KQ, Tsai TY, Wu YR, Shieh TH, Hung KM, Li J, Zhang D, Coileáin CÓ, Arora SK, Wang Z, Jiang Z, Chang CR, Wu HC. Giant gauge factor of Van der Waals material based strain sensors. *Nature communications*, 12(1):1-9, 2021. <https://doi.org/10.1038/s41467-021-22316-8>
- [27] Young WC, Budynas RG, Sadegh AM. *Roark's formulas for stress and strain*. McGraw-Hill Education, 2012.

## Appendix

Based on the provided annotations for cantilever beam geometry and applied point load in Fig. 3, the relationship between the beam deflection and strain at the strain gauge location can be expressed as follows [27]:

Deflection at the strain gauge location  $x \in \mathbb{R}^+$

$$\delta = \frac{Px^2}{6EI}(3l-x) \tag{A.1}$$

Point load in terms of deflection

$$P = \delta \frac{6EI}{x^2(3l-x)} \tag{A.2}$$

Stress at x

$$\sigma = \frac{My}{I} = \frac{P(l-x)y}{I} = P \frac{(l-x)h}{2I} \tag{A.3}$$

Stress in terms of deflection

$$\sigma = \delta \frac{3E}{x^2(3l-x)}(l-x)h \tag{A.4}$$

Stress-strain relationship (assuming linear elasticity)

$$\varepsilon = \frac{\sigma}{E} \tag{A.5}$$

Strain in terms of deflection

$$\varepsilon = \delta \frac{3}{x^2(3l-x)}(l-x)h \tag{A.6}$$



Research Article

## London the Shard analysis in the context of parametric and sustainable skyscraper design

Selale Elcin Sungur<sup>a</sup>, Umit Turgay Arpacioğlu<sup>b</sup>, Mustafa Ozgunler<sup>c</sup>

*Department of Architecture, MSGSU Mimar Sinan University, Istanbul, Turkey.*

### Article Info

#### Article history:

Received 01 Nov 2021

Revised 29 Nov 2021

Accepted 08 Dec 2021

#### Keywords:

*Parametric design;  
Sustainability;  
Skyscraper design;  
Tall buildings;  
Wind engineering;  
Engineering analysis*

### Abstract

In this study, London The Shard skyscraper structure was examined under the concepts of sustainability and wind engineering dynamics. The aerodynamic examination of the building in accordance with the wind dynamics principles and the relevant CFD simulations as proof, created. In the simulations carried out in the Matlab CFD environment, the Navier Stokes equation principles with k-omega turbulence model were followed. The skyscraper model 1-1 was created in its original form and simulated under real wind data at its location in London. In the results obtained after the simulations, the velocity increased by V-3V in the first 600-800 meters distance range, in the x direction of the model, created a vortex around the structure. While the speed-vortex effects mechanisms were examined on the model by V-3V, the pressure load P within the first 25 meters in the z direction (structure height) of the model was reached to 5P, up to the limit of 280-300 meters. When it is reached to 300 meters height, a 5-fold increase in pressure was detected. In the x-direction, pressure change of the model tested. The variation of the pressure load at the rate of P - 2P was determined in the first 800-1000 meters of the model in the x-direction, and the pressure exerts a double effect in the first 800-1000 meters of the model. In addition to the norms and regulations of supertall design principles, all risk scenarios of wind, under the effect of velocity and pressure need to be simulated before safe construction.

© 2021 MIM Research Group. All rights reserved.

## 1. Introduction

In this study, the concept of skyscraper construction systems will be discussed through two basic principles. The first of these will be to examine the sustainable energy efficient parameters of the building, which proves that skyscraper structures are also important as being sustainable. The concepts of how much effect it can have on the surrounding structures, and to what extent the vortex power and turbulence created by the structure itself classified, including the center. In the context of this study, both features were examined on the same prototype structure: London The Shard Skyscraper, has been analyzed in detail. The reason for this choice is that "London The Shard" structure is the most qualified skyscraper structure in the Western European building group, as well as the parametric construction systems in its design were placed on a plan base close to the conical by Renzo Piano and the tendency to taper upwards was completed into a high upright pyramid crystal, with tapering [1]. It is an effective and very dynamic plan scheme and is an important feature that distinguishes it from other structures that are both sustainable and parametric. In addition, "London the Shard" structure differs from other structures in terms of the progress of the construction technique during the construction process, the differences in the construction phase, especially in the establishment of its foundations, and the special solutions developed by WSP group. These differences are

<sup>\*</sup>Corresponding author: [selalesungur@gmail.com](mailto:selalesungur@gmail.com)

<sup>a</sup> [orcid.org/0000-0002-8173-0747](https://orcid.org/0000-0002-8173-0747); <sup>b</sup> [orcid.org/0000-0001-8858-7499](https://orcid.org/0000-0001-8858-7499); <sup>c</sup> [orcid.org/0000-0002-5800-3314](https://orcid.org/0000-0002-5800-3314);  
DOI: <http://dx.doi.org/10.17515/resm2021.361st1101>

Res. Eng. Struct. Mat. Vol. 7 Iss. 4 (2021) 661-675

techniques that have been examined so that the structure gains strength by showing effective quality against wind dynamics and is less affected by vortex current intensities.

The differences in the construction system, as well as the different architectural iconic design, which has a crystalline quality in the cross-section process that evolves from a conical base to a high vertical pyramid, [2] and the fact that it is the most qualified skyscraper structure in Western Europe, enabled the analysis of the shard structure to be chosen in this study.

The study was examined in two main sub-headings, in terms of sustainability and wind engineering principles. Considering the sustainability, it has been proven with 5 qualified parameters that, high energy efficiency could be possible even also for a high-tech skyscraper structure, when it is designed with the right decisions & principles.

To focus on the importance of energy efficient principles of skyscraper structures, one of the sustainable architectural solution methods could be choosing the right decisions in terms of aerodynamics concept of design, to build with a lighter construction load bearing-system. To achieve this aerodynamic design envelope, the structure has been handled entirely with the principles of wind engineering dynamics and fluid mechanics simulations.

Evaluations need to be considered for the functions of the changes on the wind speed, vortex measurements, pressure and velocity vectors over the fluid system dynamics of the structure, depending on the distance (x) and height in z direction of the coordinate system.

The effect of physical environmental conditions on the change of velocity and pressure needs to be analyzed. Calculations and measurements have to be created by calculating on the basis of Navier Stokes equations over Matlab CFD Computational Fluid Dynamics systems for safe and aerodynamic high rise building envelope design.

As a result, a high-rise structure over 300+ meters, such as The Shard structure, in focus for this research, has high influence on the wind dynamics and pressure of its own structural load system and also for its surrounding in terms of physical environment conditions on ground and upper-level human comfort and reliability for safe environment.

The ratios and the coefficients of change need to be calculated and pre-estimated before the construction of real design such as the ratios for pressure: P-2P, and velocity of V-3V coefficients in terms of The Shard design simulations, calculated by Computational Fluid Dynamics (CFD), before and after the vortex effect of structure. It has been interpreted and analyzed through the CFD simulations and obtained the correct risk scenarios with the velocity and pressure ratios for safe and sustainable design principles.

The main purpose here is to clearly observe the difference in the distance through the coefficient of variation, and, since the change will still depend on the increase in the coefficient ratio, even if the wind speed changes throughout the year, the distribution and variation can be examined clearly. The simulation data are based on the actual wind speed data for the year and are explained in detail in the methods and methodology. The Shard structure has also been modeled 1-1 in 3D by using the Rhino 3D model system, in a way that would exactly match the real original.

## **2. Sustainable Building Design Evaluation of “London the Shard” Structure**

### **2.1. Difference of Shard in terms of Sustainable High-Tech Design**

When it comes to the design of sustainable building subsystems, it is not only an energy efficient building, but also the design parameters that should be considered in essence. Keeping the sustainability of a building limited to the articulated units such as solar active solar collectors or wind turbines placed in the structure of the building will actually tie the

whole load to the foreign units added after the main structure design. The creative design of the form, by inhibiting the rational design decisions that should be made at the beginning.

As a matter of fact, the changing perception of architecture after 1960, and since Archigram, founded in 1961 by a group of pioneer architects like Peter Cook and Dennis Croptomton, who adopted the futuristic design approach, Plug-in City [3], [4] and Instant City [5] concepts, the use of high technology in architectural design had been futuristically changed. Starting from the first design stages of the building, going to the most suitable structural solutions possible, and the appropriate function, function-form and typology parameters of the building being compatible with the concept, provided with the design had been re-considered after all.

In this study, the structure of London The Shard skyscraper will be analyzed as a pilot application and the unique qualities of the iconic Renzo Piano design and its contribution to sustainability will be examined in the context of sustainable building subsystems.

In the design of The Shard structure, Italian Architect Renzo Piano collaborated with WSP Global in terms of structural solutions. The Technical Director of the Shard, John Parker, defines this meeting with these words, "In general, in every building design, the architect deals with color and aesthetic concerns, and the engineer deals with numerical concerns, and the structure cannot show the desired performance at the point where they cannot communicate. This was not the case at The Shard, Renzo Piano and WSP. He (Renzo Piano) worked in a very good communication, with indefinite and countless meetings. The architect told us about his aesthetic concerns and we, as the engineer, our structural concerns for our architecture, and this communication turned The Shard into reality." [6]

## **2.2. Parameters of the Sustainable Concept of Shard**

The Shard contained 5 very qualified parameters in a sustainable context at the same time.

### *2.2.1. To Decrease the Traffic Load of the City in Terms of CO Emissions*

The first of these is that the structure is located just above the London Main Line Central Station structure and alleviates the traffic load of the city. This approach focused on minimizing the use of private vehicles among home office life in daily routine. Shard design unit, both for those working on their own office floors and the critical Port area and its surroundings, where it is located, the regulation of the traffic routine on behalf of the London Bridge area and the internal solutions established by the ground floor solutions with the London Main Line Station structure bear the burden at the highest level in a sustainable context. To reduce the CO carbon monoxide gas emission of the city, by the way, to provide a positive effect on air quality. (see figure 1, figure 4)

The region where the Shard is built is exactly the definition of the concept of regeneration. The structure has directly affected the general character of the region and has ensured the full integration of the main switchboard station with the economy and finance center of the city. It has inhibited transportation and traffic problems.

### *2.2.2 Steel Spire to Eliminate the 3 Million Pound Damper System*

Secondly, in the creation of the main structural system of the Shard, the main load bearing structure forming the core with the cooperation of the "mace" group and "WSP", with an application that was tried for the first time in the world, was primarily raised.

The form made of glass and steel on it was raised like a tapering mesh made of layers and layers, and the facade design was integrated. The building reached its apex between the 72nd and 95th floors with a steel structure spire placed on it like a crown.

The building, which looks like an olympic torch here, was imagined to be completed just before the London Olympic Games and this spire was designed. With the designed load bearing structure, the apartment and residence floors, reinforced concrete office floors and the viewing terrace were formed as a steel structure.

All these rational design parameters saved the structure from the need to put a 3 million pound damper in the structure and provide aerodynamic resistance. Once again, commitment was a prerequisite, name obtained “Renzo Piano Design”. [6]

### 2.2.3. Triple Glazed Blue Panel Systems

Thirdly, the building has “triple glazed blue glass panels” designed by ARUP and solar active energy conversion systems, which are described as expensive efficiency. (see figure 1, fig2) This triple glazed system is cost-effective, on the other hand, obtained by using 75 million dollars of the 375 million dollars full budget of the building only on the facade, it is an application. [7]

### 2.2.4. Tapering Against the Wind Aerodynamic

The fourth parameter, in fact, should be made at the very beginning of the design decisions, especially in high structures and skyscraper structures of 300 meters and above. Due to the extra load that the active wind speed puts on the building structure, it is necessary to make the aerodynamic resistance decisions of the structure very accurately. Tapering upwards from cube to cone also fully meets the sustainability criteria in terms of inhibiting the wind load on the Shard design, in which the “Tapering” system is actively used, and thus reducing the initial construction costs of the structure. (see figure 5)

### 2.2.5. Reuse of Recycled Materials in Terms of Constrction

Finally, the fifth parameter is the following, the fact that the material used as the building structural material is obtained from 95% recycled material shows that it is suitable for the sustainable design criteria of the Shard in all possible dimensions at the time it was made, according to The Guardian. [8]



Fig. 1 The Shard Facade View[7]

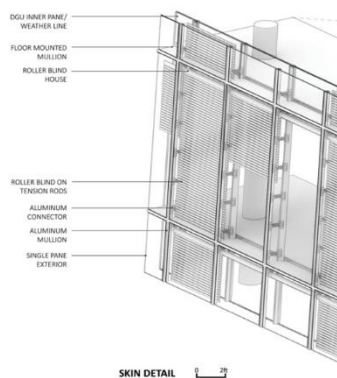


Fig 2 Triple Glazed Detail [7]

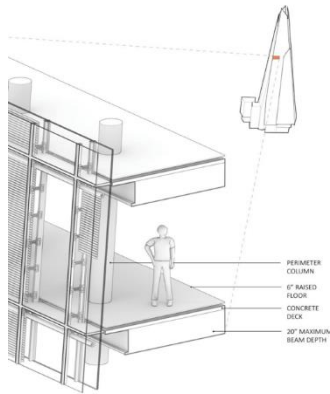


Fig. 3 The Shard Facade, Triple Glazed Detail [7]

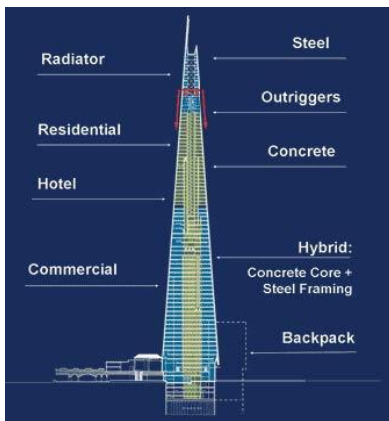


Fig. 4 Construction Technique and Usage Functions According to Shard Floors, Cambridge [9]



Fig. 5 Shard Parametric Facade Design System, a Street View [2]

### 3. The Shard London Analysis in The Context of Parametric Design

#### 3.1. Understanding the Key for CFD Simulations to Evaluate High Rise Structures

Within the scope of this study, London The Shard skyscraper project, which is one of the high-rise building studies designed and implemented with parametric design principles, firstly over the Rhino 3D modeling system, which will enable CFD (Computational Fluid Dynamics) analyzes to be performed, followed by simplification and mass analysis studies, and the data of the wind structure is abundant. Based on basic data such as direction, the structure was modeled in its real condition and subjected to wind tunnel tests.

In this study, which is based on CFD applications, the main purpose and aim to be examined are, built on the basis of parametric design principles, to what extent a 300 meter or more high structure affects the building physics parameters in the surrounding area, how many meters distance, how dense it is in the wind load affects. Turbulence models are the calculation of how much it affects other structures and what the distance of the impact area is.

In the analyzes made, the results of how much the structure is affected by wind load in the context of structural load analyzes on itself will also be examined on the basis of both P wind load pressure, wind speed and vorticity, and effective vortex distributions.



Fig. 6 Building Physics in The Shard London Structure and Its Metropolitan Concept, Its Situation in Environmental Relations, Its Relations with Transportation Networks and Its Relation with Other High Building Stock [10]

#### 4. Methodology and Method for Simulations

##### 4.1. Modelling the Simulation Environment & Procedures

The study proceeded through 2 basic methods, in the first of which, Navier-Stokes flow equations were used with the exact and instantaneous solution method used in "stationary model" static loads - wind turbulence factor analysis. In the second, Time Dependent analyzes were performed and time dependent time-based oscillations were measured in a certain  $\Delta t$  interval.

In the Shard model, where the wind turbulence is tried to be inhibited to design for 300 meters above, tapering upwards technique has been adapted. In terms of CFD simulations, in the time dependent based solution technique, the effect of turbulence on the physical environment of the structure has been analyzed, for the wind vorticity problems, up to how many meters can be calculated mathematically in the model on the coordinate system.

As it is observed in some literature, the structural analysis is based on not only the pressure load, but also " $\rho$ ", the density of the flow on the structure, " $\mu$ ", the viscosity shown against this flow, the creative velocity of the flow and the pressure. In this study, the Navier Stokes equation-based analysis have been examined using the 300 meters and above algebraic and k-omega turbulence models.

Peter Irwin from RWDI Canada group stated that the 300 meter boundary is a critical threshold value in the context of measuring the wind character and the loads on the structure [11] Calculations and standards of high structures depending on the regulations can be used in practice and in a primary sense, but in structures of 300 meters and below [12], [13].

##### 4.2. Necessity for Simulations to Risk Scenario, Losing the Reliability of Norms and Standards above 300 meters

The main point of this theory is the view that when the high structure is designed higher than the 300-meter limit, Irwin supports that norms and standards lose their applicability and reliability. [12] Turbulent flow of 300 meters high and Eddy Vortexes make the effect

of the wind on the structure from being measurable and predictable, to the point of unmeasurable and unpredictable. At this point, the two safest methods available are CFD computer simulations and real wind tunnel testing.

With the simulations made in the context of CFD, wind tunnel designs that make it possible to obtain physical qualifications and suitable wind turbulence models in real wind tunnels. Sensor mechanisms placed in the model (prototype) and instantaneous measurements based on differentials can provide the closest results to the reality and the appropriate risk analysis can be obtained. [14] This argument of Peter Irwin, in the relevant article [11], was also supported in the speech of Ender Ozkan. (a member of the same group, Head of RWDI London and RWDI Europe CEO, on May 29, 2021, in the context of Mimsa Workshop Conference Series.)

While the vortex effects make norms and standards far from safe in structures of 300 meters and above, real tests and simulations against every bad scenario make it necessary to calculate P wind pressure measurements, vorticity, and vortex loads, and oscillations on the basis of risk.

*“The boundary layer models in many building codes and standards have served well for buildings less than about 300m but more realistic models need to be used above 300m.” Peter Irwin – RWDI Canada [11]*

## 5. Results and Discussions

Data analyzes were concluded in this context. As a result of experimental analysis and simulation studies carried out in Matlab environment, 23853 grid cells were assigned on 5039 grid points, data sensitivity should be considered in this context. (Fig.7)

### 5.1. Simulation Environment Model Factor and Mesh Condition

Simulations are provided over

- the minimum grid cell volume of 4.6758,
- 4.2603e+03 (m<sup>3</sup>) mean grid cell volume
- and 1.1788e+04 maximum grid cell volume,
- 0.1695 minimum grid cell quality,
- 0.8532 average grid cell quality
- 6 limit value interfaces.

The 3D mass analysis of the structure has been modeled with real data in the Rhino environment, and it has been made measurable and adaptable to CFD for Matlab simulation.

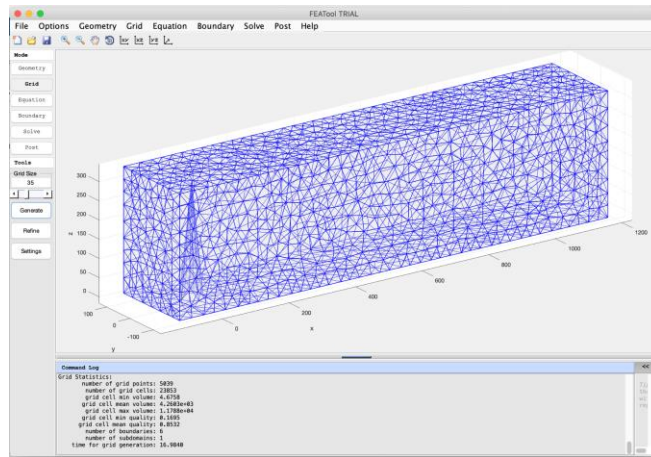


Fig. 7 Matlab Experimental Analysis And Simulation Data Analysis Precision Criteria

## 5.2. Simulation Model for the Velocity Change, k-omega Turbulence Model & Wind Vortex, Velocity Spectrum (x, z - directions)

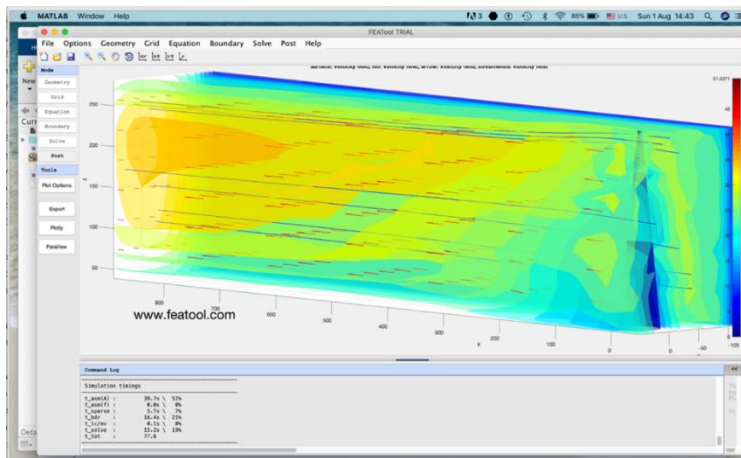


Fig. 8 The Effect of the Shard Structure Around 300 Meters In The Context of the V-3V Velocity

In the results obtained, it has been determined that the normal, ground story speed level influences the building physics and environmental conditions in the first 600-800 meters range after the building itself, 3 times as much, and it increases the current speed vector from  $V$  to  $3V$ .

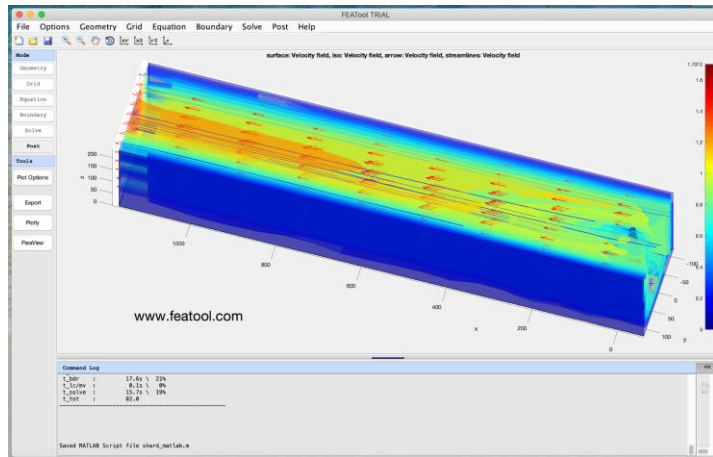


Fig. 9 Vortex And Wind Turbulence Effects of the Structure in the 600-800 Meter Range

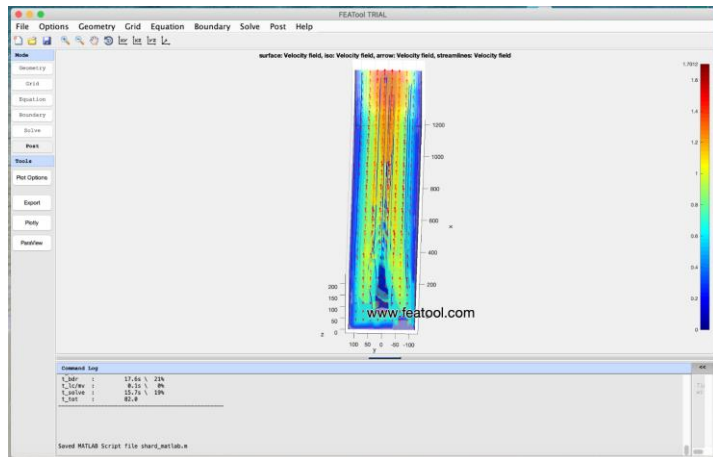


Fig. 10 Vortex and Wind Turbulence Effects of the Structure in the 600-800 Meter Range

Due to the wind turbulence and vortex effects created around the 300 meters above structure, it has been determined that the vortex effect persists in the 600-800 meter distance range closest to the structure. (Fig 9, Fig 10)

### 5.3. Simulation Model for the Time Dependent Scenario- $\Delta t$ interval change & Wind Vortex (x, z -directions)

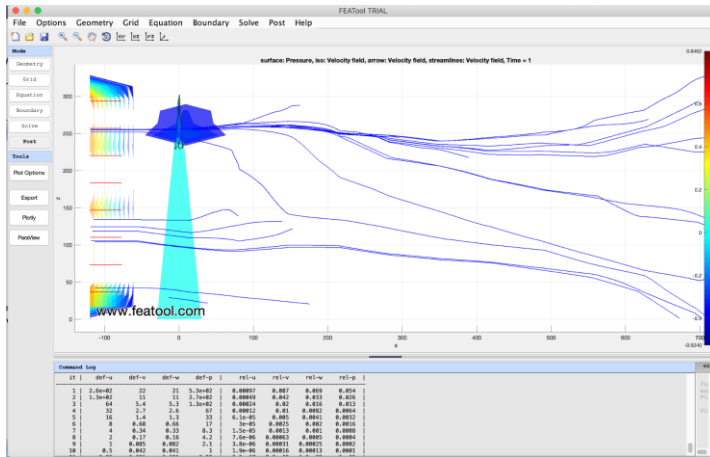


Fig. 11 Measurement of Vortex Effect Distance In The Solution of the Structure in the Simulation Range of Time Dependent Delta T

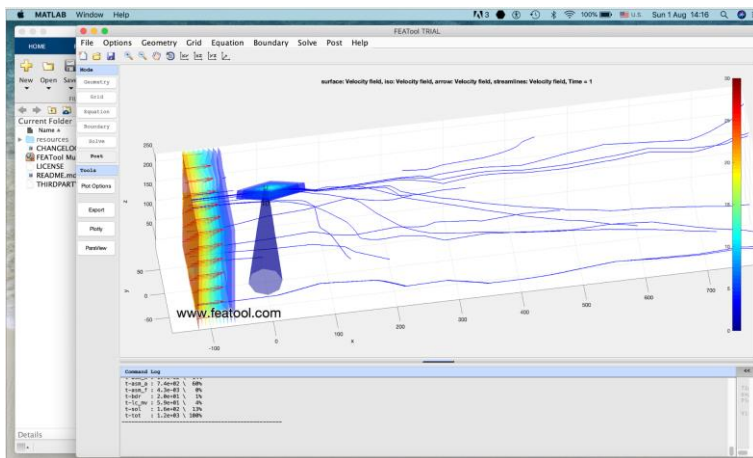


Fig. 12 Measurement of Vortex Effect Distance in the Solution of the Structure in the Simulation Range of Time Dependent Delta T

In the time dependent analyzes used as the second method, the change in the vortex and velocity vector in a certain  $\Delta t$  interval, have been examined. This method supported the first obtained Navier Stokes instantaneous and clear solution data. It has been proven that the effect creates on top of the structure, that is, the highest point, continues until the first 600-800 meters after the flood.

### 5.4. Simulation Model for the k-omega Turbulence Model Scenario- & Wind Vortex and Pressure Spectrum (x, z-direction)

After the analysis of the structure on the velocity and vortex effect mechanisms, the relationship of the structure with the pressure has been examined, and it has been concluded in this analysis that the pressure load on the structure in the range of 280-300 meters have an effect in the context of P-5P pressure change in spectrum.

The pressure load, which is  $P$  in the first 25 meters of the structure, reaches a pressure of  $5P$  in the range of approximately 280-300 meters height of the structure. ( $z$  direction) (Fig 13)

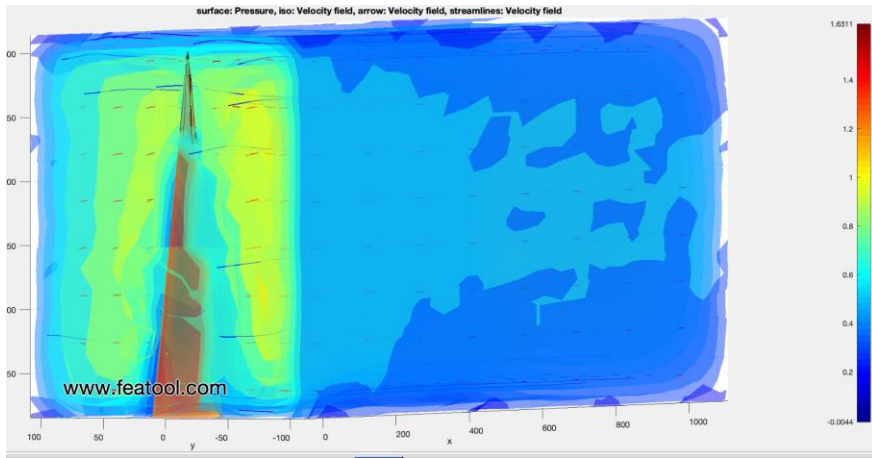


Fig. 13 Analysis of the Pressure Factor, Change Between the First 25 Meters of the Structure and 280-300 Meters Thereafter

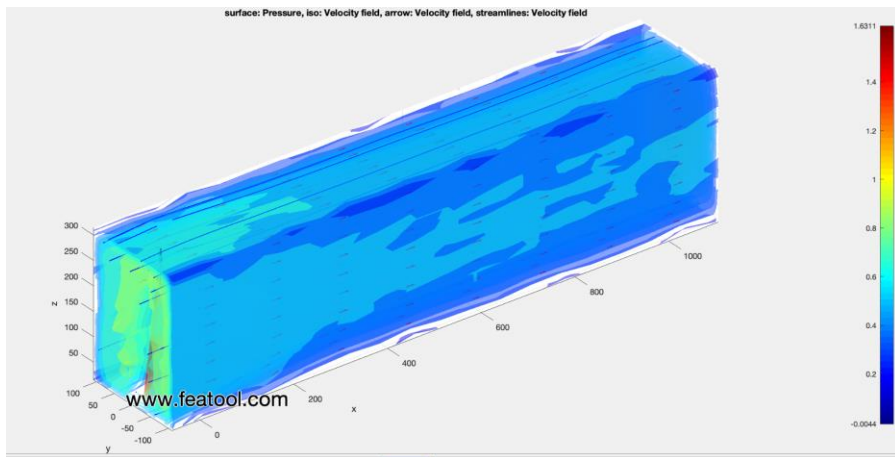


Fig. 14 Analysis of the First 800-1000 Meters Environment Interaction of the Structure and P-2P Pressure Changes (X-Direction)

In addition, when the building physics and safety comfort conditions on the surrounding of the structure are analyzed, it has been determined that the pressure effect on the P-2P scale continues in the first 800-1000 meters after the structure, based on the prevailing wind direction (Fig 14).

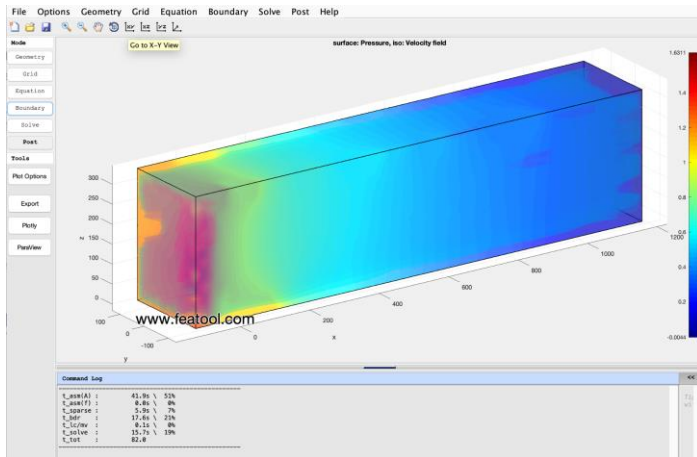


Fig. 15 The Risks of Separation of the Facade from the Structure with the Vortex Effect of the Building Facade Cladding System and the Density Indicators for the First 150 Meters

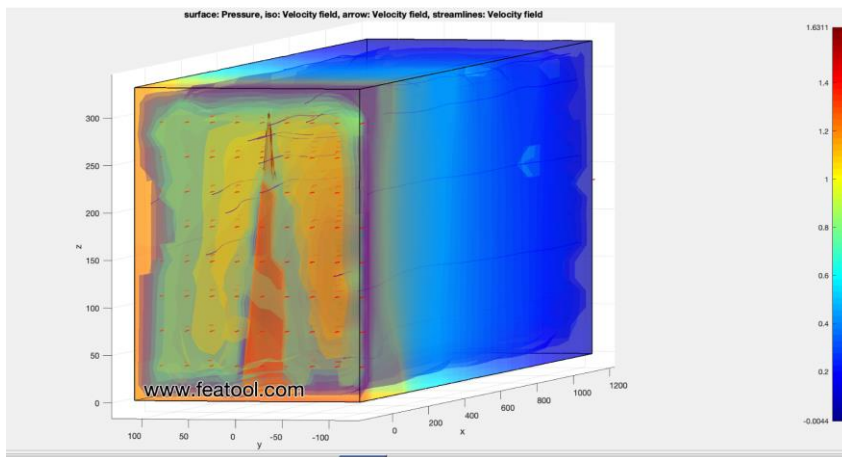


Fig. 16 The Risks of Separation of the Facade from the Structure with the Vortex Effect of the Building Facade Cladding System and the Density Indicators for the First 150 Meters

Based on the structural load, the pressure on the building and especially the risk of separation of the facade from the structure with speed vortices and turbulence on the glass facade system, it is concluded that the wind load on the facade primarily affects the building environment in the first 100-150 meters.

As a result, in the part of what is called “the skyscraper” structures, take their place in the literature as “supertall buildings and skyscrapers” at 300 meters and above, have essential and critic design points to be safe and sustainable. 300 meters and above heights need to be examined differently from the norms and standards. Finding a topic in the world literature as “high-rise design and wind engineering” – “tall building design and wind engineering” is an extreme critical point needs to be simulated in detail both for speed vortex and pressure affects. A serious research area that requires special design principles with both simulations and effective CFD analysis, in turbulent and laminar flow

assumptions, also considering the risks it contains. To mention such as the the risk of facade fall under turbulent flow, could be possible in a negative risk scenario. Unfortunately, became reality in HSBC Headquarter in London. (info on 29 may 2021, conversation with Ender Ozkan, RWDI) Writer's research continues effectively with their original design & models, methods and analyzes for Ph.D. doctorate, in the context of MSGSU Mimar Sinan University - Construction Physics Doctorate Program.

## **6. Conclusions**

In this study, a comprehensive review of the shard skyscraper structure, which is known as the best example of western Europe, was made under the topics of sustainability and wind aerodynamics, to be safe and provide sustainable design. Wind dynamics and fluid mechanics principles have been taken into account in detail. All the calculations performed under the reliability of matlab systems with the Navier Stokes equation on k-omega turbulence model.

### **6.1. Risks and Essentials of Supertall Structures Design**

Skyscrapers are structures that need to be built and tested as prototypes in wind tunnel tests [14] because they are exposed to extra wind load that do not comply with the norms and standards in force during their construction, especially when skyscrapers over 300 meters are considered.

In this context, it is a structure group that is difficult to construct, whose structural calculations must be specially designed for

- both their facade strength and their individual load-bearing systems,
- by pre-determining the risk on them,
- such as the risk of overturning,
- collapse risk,
- damage from the wind,
- or the measurement of the oscillation coefficient.

They are structures that can be constructed by the simultaneous work of architecture and engineering disciplines and producing solutions together.

### **6.2. Success of The Shard London in Terms of Sustainability**

The success of "London The Shard" skyscraper structure, which is one of the best known examples of western Europe, and studied as a prototype in this study, in terms of energy efficient transformation mechanisms and energy efficiency in its initial design, is analyzed. In this concept, with the data obtained from the literature studied on the Shard [8], the recyclable materials used at the rate of 95% in the construction of the structure. Moreover, the use of a 3-million-dollar damper has been waived thanks to the steel crown positioned on top of the structure itself. In aesthetics aspects, it has been also considered to be the flame of the Olympic Games. [6]

Moreover, the location and having the role to be an icon of the the business life of city centre by its location is highly essential. In terms of being the transit point of the city and the relation with the building & office aspects need to be taken into consideration. It has been seen that the building exhibits a successful example in terms of sustainable architecture due to reasons such as being a pioneer-designed high-rise building. With all the explanations and proven cases above, it has been determined that a high-rise building or a skyscraper structure can also be energy efficient with a creative design.

### 6.3. Success of The Shard London in Terms of Aerodynamic Structure Design

The Shard skyscraper structure is modeled in Rhino computer environment, in accordance with the 1-1 architectural features and the original, with the relevant proportions, dimensions and this created model is analyzed with CFD Computational Fluid Dynamics simulations in the Matlab environment.

The technique applied is similar to the techniques studied in skyscraper construction systems, which are built in the real sense, by modeling skyscraper prototype models as models and testing them in wind tunnels, making it possible how this analysis can be done during a Ph.D. doctoral study at the university, academic level.

Model simulations were created by creating appropriate environmental data in a matlab computer environment, processing the relevant scenarios into the model, and the Shard skyscraper structure in real terms and at the location in London, taking into account the characteristics such as wind speed, wind load, pressure factors, and 300 meters above - high structure, with its environmental models were created.

Since the structure over 300 meters is exposed to the vortex effect within the scope of super-high structures, the turbulent flow is solved by using the Navier Stokes equations. Here, in the interface of the matlab program, the data related to the solution are provided as input to the Navier Stokes equation.

In the data obtained from the simulation, the graphs obtained as matlab CFD simulation outputs, vortex diagrams, pressure and velocity controls enable the structure to be evaluated. The difference between the pressure and velocity distributions on and behind the structure observed in 800-1000 meters range, and in this sense, the velocity change of V-3V spectrum, or the pressure change of P-2P spectrum, obtained in x -direction. For z-direction, the pressure change detected with the scope from P to 5P, from first 25 meters to 280 – 300 meters limit, under the effect of height and wind.

Table 1 .Pressure and Velocity Differences on X and X coordinates (Fig 8, 9, 13, 14)

Coordinate	Mean	Dimensions (meters)	P(initial)	P(final)	V(initial)	V (final)
(in ratio and coefficient )						
X	distance	800-1000	P	2P	V	3V
Z	height	280-300	P	5P	Increase regularly by height of the floors	

Finally, as it is, the change of the environmental conditions on the front of the facade and behind the facade of The Shard structure is determined in accordance with the real data, and essentially, by obtaining the necessary ratios in the context of the coefficient. In case, by this way, the total risk scenario can be calculated actively, even during the wind speed and fluctuations throughout the year occur.

#### Acknowledgement

The authors acknowledge that this study is supported by Mimar Sinan University Construction Physics PhD Research Doctorate Programme also the application for TUBITAK 2211-C Doctorate Research Scholarship, with the ID: 1649B032101665

## References

- [1] Cilento K. Renzo Piano- The Shard. 2012; 1–13. Available from: <http://www.bbc.co.uk/programmes/p00tjz3x>
- [2] Maier F. LEAF Awards 2013 Overall Winner : Marsan Mediatheque in France. Detail, September 2013.
- [3] Šenk P. The Plug-In Concept: Technology and Aesthetics of Change. *Architecture and Research*, 2013/1: 42-51;
- [4] Hobson B. Archigram’s Plug-In City shows that “pre- fabrication doesn’t have to be boring”. *Dezeen*, 2020;(373):1–18.
- [5] Hobson B, Cook AP. Next story Follow : Archigram ’ s Instant City concept enables " a village to become a kind of city for a week ". *Dezeen*, 2020;5:1–11
- [6] Mawer R, Parker J. Engineering the Shard. *Eng J. Irl* [Internet]. 2016;20(384):3–5. Available from: <https://www.wsp.com/en-GL/projects/the-shard>
- [7] Brown L. Anatomy of a Skyscraper. University of Kansas USA, 1<sup>ST</sup> edition; 2018
- [8] Press Association. 23 Facts about the Shard. *Guardian*. 2012;16:1–2
- [9] Bogomil E. Burj Khalifa, The Shard and Rivals. *Univ Cambridge , Newnham Coll.* 2009;(March 2012):2–9
- [10] Gibson T. This Tech-Company is Building Photorealistic Models of Cities Around the World. 2021;(July)
- [11] Irwin PA. Wind engineering challenges of the new generation of super-tall buildings. *J Wind Eng Ind Aerodyn.* 2009;97(7–8):328–34. <https://doi.org/10.1016/j.jweia.2009.05.001>
- [12] Irwin BPA. Wind Engineering. *Wind Eng.* 2006;(June):1–4.
- [13] Irwin P. Thought leadership. *RWDI*. 2018;
- [14] Nerberg S. Why this Ontario engineering firm is the go-to for starchitects designing the world ’ s supertall towers. 2019;3



# Research on Engineering Structures & Materials

## In This Issue

- Review Article  
481 **Ismail Luhar, Salmabanu Luhar**  
Valorization of geopolymer paste containing wastes glass
- Research Article  
505 **P.N. Ojha, Amit Trivedi, Brijesh Singh, Adarsh Kumar N. S., Vikas Patel, R.K. Gupta**  
High performance fiber reinforced concrete – for repair in spillways of concrete dams
- Research Article  
523 **Giovanni Falsonea, Gabriele La Valle**  
Dynamic and buckling of functionally graded beams based on a homogenization theory
- Research Article  
539 **Al Montazer Mandong, Abdullah Uzum**  
Fresnel calculations of double/multi-layer antireflection coatings on silicon substrates
- Research Article  
551 **Sahar Ismail, Wassim Raphael, Emmanuel Durand**  
Case study of the Beirut port explosion using 3D laser scan and nonlinear finite element model
- Research Article  
579 **Warda Abdulla, Craig Menzemer**  
Fatigue life prediction of steel bridge connections using fracture mechanics models
- Research Article  
595 **Anjeza Gjini, Hektor Cullufi, Enio Deneko, Princ Xhika**  
Behavior of structure type 82/2 (RC frame), during the earthquake of 26 November 2019 in Durrës, Albania
- Research Article  
617 **Olatunji Oladimeji Ojo**  
Macro-/micro-mechanical interlocking modification on the performance of hybrid friction stir spot welded aluminum/acrylonitrile butadiene styrene joints
- Technical Note  
635 **Akshansh Mishra, Devarrishi Dixit, Raheem Al-Sabur**  
Development of specially reinforced magnesium composites prepared by squeeze casting process
- Research Article  
647 **Juho Kerminen, Jenny Wiklund, Alp Karakoç, Kalle Ruttik, Riku Jäntti, Hüseyin Yiğitler**  
Characterization of low-cost inkjet printed-photonic cured strain gauges for remote sensing and structural monitoring applications
- Research Article  
661 **Selale Elcin Sungur, Umit Turgay Arpacioğlu, Mustafa Ozgunler**  
London the Shard analysis in the context of parametric and sustainable skyscraper design

C  
O  
N  
T  
E  
N  
T